Polish Academy of Sciences

Institute of Fundamental Technological Research

Archives of Mechanics

Archiwum Mechaniki Stosowanej

volume 49 issue 5

Polish Scientific Publishers PWN

Warszawa 1997

ARCHIVES OF MECHANICS IS DEVOTED TO Theory of elasticity and plasticity • Theory of nonclassical continua • Physics of continuous media • Mechanics of discrete media • Nonlinear mechanics • Rheology • Fluid gas-mechanics • Rarefied gas • Thermodynamics

Printed in Poland, Editorial Office: Świętokrzyska 21,
00-049 Warszawa (Poland)

e-mail: publikac@ippt.gov.pl

Arkuszy wydawniczych 13. Arkuszy drukarskich 11,75.
Papier offset. kl. III 70 g. B1. Oddano do składania we wrześniu 1997 r.
Druk ukończono w listopadzie 1997 r.
Skład i łamanie: "MAT - TEX"
Druk i oprawa: Drukarnia Braci Grodzickich, Żabieniec ul. Przelotowa 7

Arch. Mech., 49, 5, pp. 807–814, Warszawa 1997

Numerical simulation of an inviscid transonic flow through a channel with a leap

P. LISEWSKI (WARSZAWA)

A TWO-DIMENSIONAL inviscid transonic channel flow of a perfect gas is considered. The gas of relatively high pressure, flows into a channel through a converging nozzle. The channel geometry is characterised by a discontinuity of cross-section at the nozzle outlet. A fast, explicit differential algorithm based on a two-step Lax–Wendroff scheme is used to solve the set of Euler equations. Results of calculations are compared with the visualised flow and with the measured pressure distributions. The computed steady-state flow field agrees well with measurements.

Notations

a	speed of sound,
e	total energy per unit mass,
$\mathbf{F}$, $\mathbf{G}$	flux vectors,
H	channel height,
J	Jacobian determinant,
k	specific heats ratio,
L	channel length,
p_0	stagnation pressure at the nozzle inlet,
p_{out}	pressure in a large volume at the outlet of the channel,
$R+$	right running Riemann invariant,
$R-$	left running Riemann invariant,
t	time,
u	velocity component in x direction,
v	velocity component in y direction,
T_0	stagnation temperature at the nozzle inlet,
$\mathbf{U}$	flow variable vector,
x, y	coordinates in physical plane,
Δl	distance between two nodes in physical plane,
Δt	time step,
$\Delta\eta$	distance between two nodes in η direction,
$\Delta\xi$	distance between two nodes in ξ direction,
ξ, η	coordinates in computational plane,
ϱ	density,
φ	ratio of the nozzle exit height to channel height.

1. Introduction

TRANSONIC FLOWS through channels with abrupt changes of cross-section can be found in practice in reducing valves or industrial installations. The structure of the flow field depends on the geometry of the channel and on the difference of pressures in the areas situated at the channel inlet and outlet. If the cross-section of the channel changes sharply and the pressure difference is high enough, shock waves may occur in the flow. Determining such flows field seems to be important from practical point of view.

Contemporary techniques of solving transonic flow problems can be grouped generally in two categories. The first contains methods that use central difference approximation applied to spatial derivatives. One can find here both explicit and implicit algorithms of different order of accuracy in time and space. Lax–Wendroff and Beam-Warming approaches are the most popular in this group. The second family of numerical methods for transonic aerodynamics contains the so-called "upwind" schemes. Their nature is closer to physics as they distinguish directions of the propagation of information in the flow. Different approaches of Godunov-type methods can be found in this category.

In the present work, a central difference method based on two-step Lax–Wendroff scheme has been chosen to solve two-dimensional inviscid transonic flow. This method is believed to be simpler to implement as compared with upwind schemes. It requires less arithmetic operations per time step than the explicit upwind algorithms. Hence, it is less time-consuming.

2. Problem description

A two-dimensional, inviscid flow of continuous medium is assumed. The gas flows through a two-dimensional (plane) channel shown schematically in Fig. 1. The first part of the channel consists of a converging nozzle and the second part is a duct of constant cross-section. Air flows into the channel from a large volume characterised by constant stagnation pressure (p_0) and temperature (T_0). At the channel outlet air flows into the surroundings where constant pressure (p_{out}) is assumed. The flow starts after breaking a diaphragm placed at the nozzle inlet.

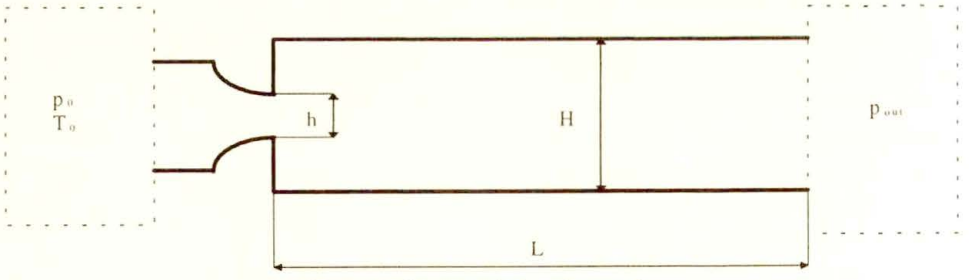

FIG. 1. Shape of the channel.

Air is treated as a perfect gas. A limiting case of steady-state solution is of interest.

3. Mathematical formulation

The inviscid unsteady two-dimensional flow without body forces and heat transfer is described in differential conservative form by Euler equations, i.e. the continuity, momentum and energy equations. This set of equations can be written in a vector form:

$$\frac{\partial \mathbf{U}}{\partial t} + \frac{\partial \mathbf{F}}{\partial x} + \frac{\partial \mathbf{G}}{\partial y} = 0. \tag{3.1}$$

The vectors are:

$$\mathbf{U} = \begin{Bmatrix} \varrho \\ \varrho u \\ \varrho v \\ \varrho e \end{Bmatrix}, \qquad \mathbf{F} = \begin{Bmatrix} \varrho u \\ \varrho u^2 + p \\ \varrho uv \\ u(\varrho e + p) \end{Bmatrix}, \qquad \mathbf{G} = \begin{Bmatrix} \varrho v \\ \varrho uv \\ \varrho v^2 + p \\ v(\varrho e + p) \end{Bmatrix}. \tag{3.2}$$

The total energy per unit mass is expressed by

$$e = \frac{p}{(k-1)\varrho} + \frac{1}{2}\left(u^2 + v^2\right).$$

By knowing the initial and boundary conditions, Eq. (3.1) can be integrated to provide the inviscid solution at a later time. Since the steady flow can be considered as a special case of unsteady flow, the steady-state solution can also be obtained from unsteady Euler equations as an asymptotic case.

For flows in complex geometries it is advantageous to transform the set of Eqs. (3.1) to the generalised, curvilinear coordinate system. General relations between the coordinates in the computational plane of reference and in the physical plane of reference are:

$$\xi = \xi(x, y), \qquad \eta = \eta(x, y). \tag{3.3}$$

After the transformation has been applied, Eq. (3.1) preserves its strong conservation form:

$$\frac{\partial \overline{\mathbf{U}}}{\partial t} + \frac{\partial \overline{\mathbf{F}}}{\partial \xi} + \frac{\partial \overline{\mathbf{G}}}{\partial \eta} = 0, \tag{3.4}$$

where "new" flow variable vector and "new" flux vectors are:

$$\overline{\mathbf{U}} = \frac{\mathbf{U}}{J}, \qquad \overline{\mathbf{F}} = \frac{\xi_x \mathbf{F} + \xi_y \mathbf{G}}{J}, \qquad \overline{\mathbf{G}} = \frac{\eta_x \mathbf{F} + \eta_y \mathbf{G}}{J}. \tag{3.5}$$

The Jacobian of the transformation is given by

$$J = \xi_x \eta_y - \xi_y \eta_x = \frac{1}{x_\xi y_\eta - x_\eta y_\xi}. \tag{3.6}$$

The metrics are:

$$\xi_x = y_\eta \cdot J, \qquad \xi_y = -x_\eta \cdot J, \qquad \eta_x = -y_\xi \cdot J, \qquad \eta_y = x_\xi \cdot J. \tag{3.7}$$

4. Numerical method

As the aim of this work is to investigate transonic channel flow, it is necessary to use a method that captures well the shock waves occurring in the flow. As mentioned in the introduction, a modified two-step differential scheme based on Lax – Wendroff – Richtmyer formulation [1, 3] is used to solve the set of equations (3.1) in the computational plane of reference. The formulation applied in the current work is described below.

During the first step, the values at the intermediate time level are calculated:

$$\begin{aligned} \overline{\mathbf{U}}^{n+1/2}_{i+1/2,j} = {} & \frac{1}{4}\left(\overline{\mathbf{U}}^{n}_{i+1,j} + \overline{\mathbf{U}}^{n}_{i,j} + \overline{\mathbf{U}}^{n}_{i+1/2,j+1/2} + \overline{\mathbf{U}}^{n}_{i+1/2,j-1/2}\right) \\ & - \frac{1}{2}\frac{\Delta t}{\Delta \xi}\left(\overline{\mathbf{F}}^{n}_{i+1,j} - \overline{\mathbf{F}}^{n}_{i,j}\right) - \frac{1}{2}\frac{\Delta t}{\Delta \eta}\left(\overline{\mathbf{G}}^{n}_{i+1/2,j+1/2} - \overline{\mathbf{G}}^{n}_{i+1/2,j-1/2}\right). \end{aligned} \tag{4.1}$$

New values of the flow variable vector $\mathbf{U}$ are obtained from the final step:

$$\overline{\mathbf{U}}^{n+1}_{i,j} = \overline{\mathbf{U}}^{n}_{i,j} - \frac{\Delta t}{\Delta \xi}\left(\overline{\mathbf{F}}^{n+1/2}_{i+1,j} - \overline{\mathbf{F}}^{n+1/2}_{i-1/2,j}\right) - \frac{\Delta t}{\Delta \eta}\left(\overline{\mathbf{G}}^{n+1/2}_{i,j+1/2} - \overline{\mathbf{G}}^{n+1/2}_{i,j-1/2}\right). \tag{4.2}$$

The flux vector $\mathbf{F}$ based on middle nodes is calculated as follows (the flux vector $\mathbf{G}$ is calculated similarly):

$$\begin{aligned} \overline{\mathbf{F}}^{n}_{i+1/2,j+1/2} &= \overline{\mathbf{F}}\left(\frac{\overline{\mathbf{U}}^{n}_{i+1,j} + \overline{\mathbf{U}}^{n}_{i+1,j+1} + \overline{\mathbf{U}}^{n}_{i,j+1} + \overline{\mathbf{U}}^{n}_{i,j}}{4}\right), \\ \overline{\mathbf{F}}^{n+1/2}_{i+1/2,j} &= \overline{\mathbf{F}}\left(\overline{\mathbf{U}}^{n+1/2}_{i+1/2,j}\right). \end{aligned} \tag{4.3}$$

The described algorithm differs from the Ritchmyer's version [1, 3]. Its main advantage is that averaging of flow variables, necessary to calculate the flux vectors at points located between nodes (see (4.1)), takes place only on the basic time level. Values obtained from the intermediate step (4.1) having no physical meaning, serve only for further calculations.

The described integration method is of second-order accuracy in space and time. As it is an explicit method, the maximal time step is limited by the stability

criteria (CFL number). In the present work the size of time step is obtained from the condition

$$\Delta t \leq \min\left(\Delta l/\sqrt{2}\cdot\left(\sqrt{u^2+v^2}+a\right)\right).$$

The method chosen, applied to transonic flow problems, requires artificial damping in order to minimise oscillations produced around the captured shocks. The effect of artificial viscosity has been introduced by adding the third, smoothing step in which the solution obtained from the Lax–Wendroff final step (4.2) is corrected proportionally to the second spatial derivative, separately for ξ and η directions.

5. The physical plane of reference

Because of the symmetry of the steady-state flow, the physical plane of reference can consist only of one half of a real channel. The shape of this area is shown in Fig. 2. It contains two subregions: the first one, corresponding to a converging nozzle and the second, corresponding to the part of the channel of constant cross-section. These two subregions are connected at the nozzle outlet.

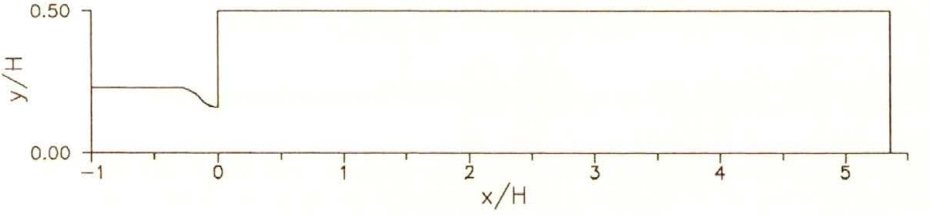

FIG. 2. Physical plane of reference.

6. Numerical implementation of boundary conditions

At the inlet boundary, a quasi-one-dimensional boundary condition is applied. Stagnation pressure p_0 and temperature T_0 are imposed. These values are assumed to be constant over the channel width at the inlet. The energy equation and the Riemann invariant $R-$ (calculated from the interior of the flow field) are used to find static parameters at the nozzle inlet. The value of $R-$ is found with the method of characteristics, assuming linear interpolation of flow variables between nodes.

At the outlet boundary similar treatment is made. Subsonic and supersonic cases are considered separately. At the subsonic outlet, the only variable to be imposed is static pressure.

In the supersonic outflow, no information from outside is coming upstream. In this case both Riemann invariants along suitable characteristics, combined with

the value of entropy along the streamline, are used to calculate flow variables at the channel outlet.

Rigid walls are modelled by superimposing the layer of fictitious nodes placed behind the walls.

At the near axis boundary the symmetry condition is applied.

At the nozzle exit, the exchange of information between two computational subdomains is assured.

7. Sample calculation of the flow field

The calculated steady-state flow field in the wide part of the channel is shown in Fig. 3. The gas flows from the left to the right. The figure presents pressure contours obtained for $\varphi = 0.3$ $L/H = 5.33$ ($L = 160\,\text{mm}$) and $p_{\text{out}}/p_0 = 0.132$.

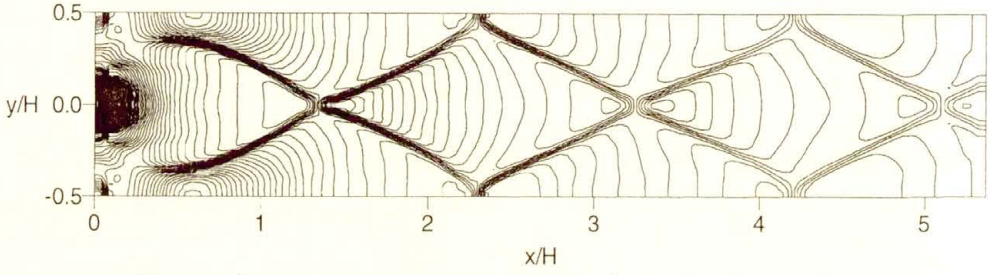

FIG. 3. Calculated steady-state solution (pressure contours).

Figure 4 shows the interferogram obtained from flow visualisation for identical conditions. Results of SZUMOWSKI and MEIER work [4] have been used.

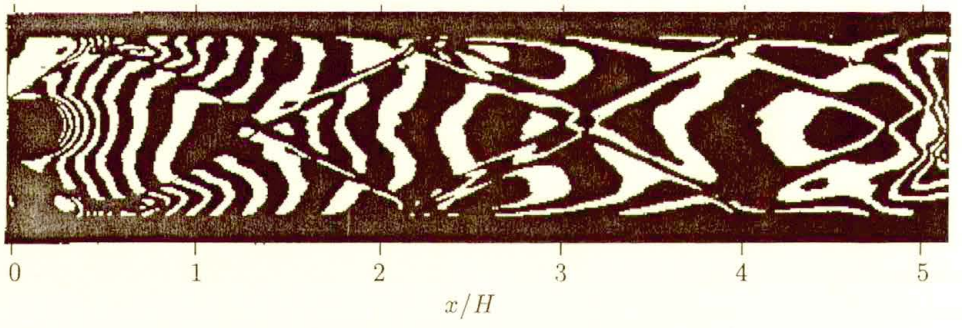

FIG. 4. Interferogram showing transonic channel flow.

As seen in Fig. 3 and Fig. 4, oblique shocks appearing in the flow are captured in the calculation accurately. The calculated structure of the flow agrees well with that observed in the real flow. The effect of a "double" wave seen in the interferogram, where the first shock is reflected from the wall, is a result of shock – boundary layer interaction. Hence, it cannot be obtained from the inviscid model. The first shock seen in the interferogram, is relatively strong and produces a small

separation "bubble". The shock is reflected from the boundary of the separation area rather than from the wall.

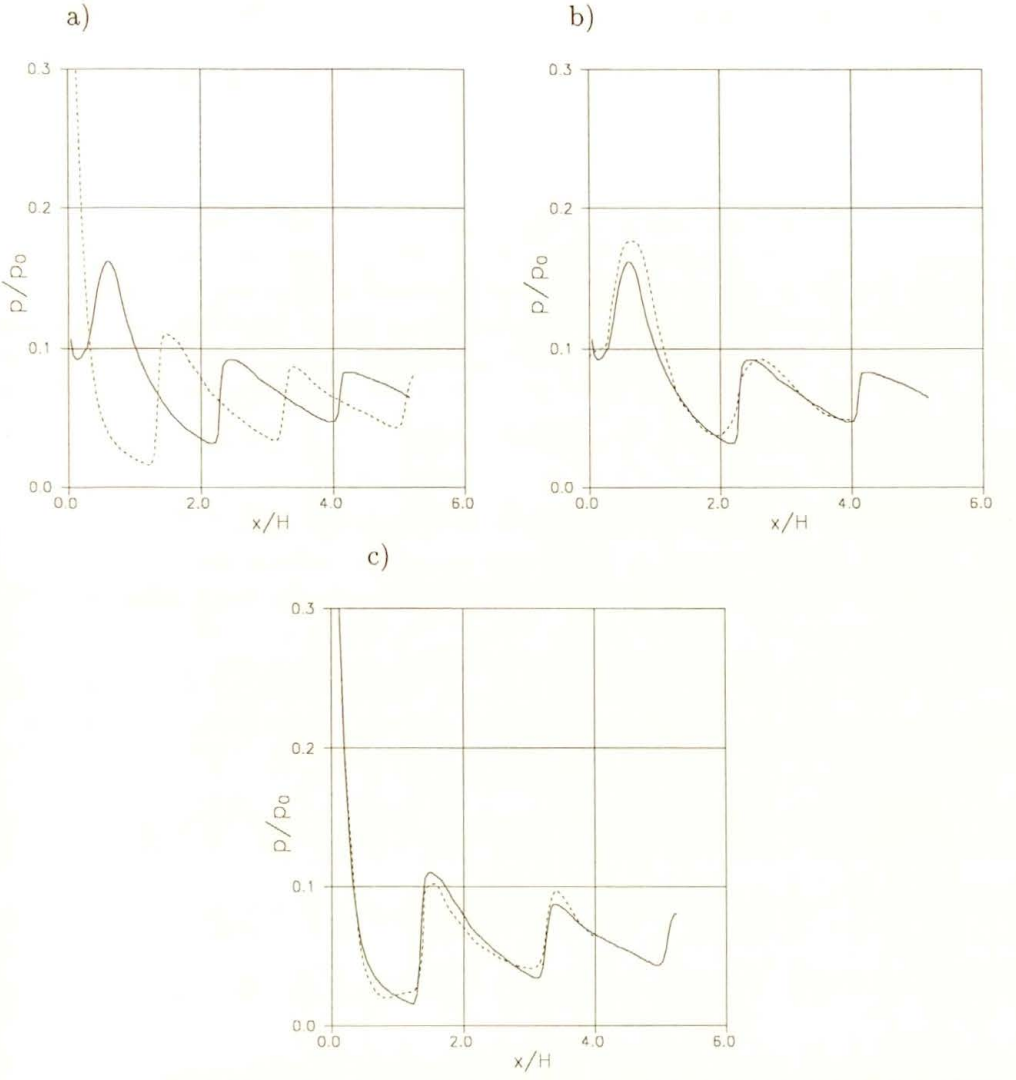

FIG. 5. a. Calculated pressure along the wall (solid line) and the axis (dashed line). b. Pressure along the channel wall: calculated (solid line) and measured (dashed line). c. Pressure along the channel axis: calculated (solid line) and measured (dashed line).

Figures 5 a, b, c show pressure distributions (non-dimensionalized with the inlet stagnation pressure) along the wall and the channel axis. Calculated values (Fig. 5 a) are compared with the measured ones for the wall (Fig. 5 b) and the axis (Fig. 5 c). Experimental data for the chosen case is provided by SZUMOWSKI and MEIER [4].

The calculated pressure distributions confirm the tendency of the shocks to become weaker along the channel. The decrease of shock amplitude is related to the increase of the entropy along the channel length. The largest differences between the calculated and measured pressures are seen for the wall distribution in the region where the supersonic stream hits the wall for the first time.

8. Conclusions

The presented numerical results are in good agreement with experiment. The calculated steady-state flow field properly reflects the presence and positions of oblique shocks occurring in the flow as well as their amplitudes. It is noticed that satisfactory results are obtained with relatively simple modelling of boundary conditions. It can be concluded that the selected numerical method based on two-step Lax – Wendroff algorithm can be effectively used for predicting transonic inviscid channel flows.

References

1. T. CHMIELNIAK, *Transonic flows* [in Polish], Ossolineum, Wrocław 1994.
2. C. HIRSH, *Numerical computation of internal and external flows*, Vol. 2, Wiley, N.Y. 1990.
3. R.D. RICHTMYER and K.W. MORTON, *Difference methods for initial value problems*, Wiley, N.Y. 1967.
4. A. SZUMOWSKI and G. MEIER, *Schwingungen der Überschallströmung in einem Kanal mit Querschnittssprung*, Rep. Max-Planck-Institut fur Strömungsforschung, Göttingen 1978.

INSTITUTE OF AERONAUTICS AND APPLIED MECHANICS
WARSAW UNIVERSITY OF TECHNOLOGY.
e-mail: lis@meil.pw.edu.pl

Received February 7, 1997.

Arch. Mech., 49, 5, pp. 815–829, Warszawa 1997

The velocity of the fluid due to the many-sphere Oseen hydrodynamic interactions

I. PIEŃKOWSKA (WARSZAWA)

WE CONSIDER the velocity field, generated in the incompressible, viscous fluid due to the hydrodynamic interactions between a finite number of solid spheres. The particular properties of the velocity field, due to the convective inertia of the fluid, are examined. The inertia effects are taken into account up to the contributions of the order of 0(Re).

1. Introduction

THE PRESENT PAPER concerns the hydrodynamic interactions of a finite number of solid spheres at small, but finite sphere Reynolds number Re. In the previous paper [1] we have investigated the effects of the hydrodynamic interactions on the friction relations between the spheres. In this paper the respective velocity field of the fluid is studied. In particular, some properties of the velocity field, not to be expected on the basis of the Stokes equation, will be analysed. The analysis is performed in the framework of the Oseen equation of motion of an incompressible fluid. The inertia of the fluid is evaluated up to the contributions of the order of 0(Re), where $\mathrm{Re} = a|\mathbf{U}|/\nu$ (a – the radius of the sphere, $\mathbf{U}$ – the uniform velocity of the fluid at infinity, $\mathbf{U} = (U, \theta, \varphi)$ in spherical polar coordinates, ν – the kinematic viscosity).

Under the condition of vanishingly small Re, the velocity field, generated by the many-sphere hydrodynamic interactions, has been recently considered by DURLOFSKY, BRADY and BOSSIS [12] and by PHILLIPS [13]. In the paper [12], devoted to the dynamic simulation of hydrodynamically interacting particles, it has been shown that the velocity field may be expressed in terms of the propagators, acting on the forces, torques and stresslets, exerted by the particles on the fluid ((2.13), (2.14) in [12]). That representation of the velocity profile is the basis of the dynamic simulation of hydrodynamically interacting spheres in a quiescent second-order fluid, developed in the paper [13], to account for the non-Newtonian behaviour.

The influence of the inertia of the fluid on the hydrodynamic interactions of a cluster of spheres moving in the fluid at small Re has been recently examined both theoretically and experimentally by KUMAGAI [2]. The author has extended the conventional reflection method of the description of the interactions, developed for the Stokes flow regime, to the case of the Oseen flow regime. His numerical results, concerning the inertia effects in the free-fall motion of spheres, show a

good agreement with the experimental results. Earlier approaches to the analysis of the nonlinear effects have been quoted in [1].

In the present paper, we use the multiple scattering approach [3] to the analysis of the hydrodynamic interactions and the velocity field. Starting from the integral formulation for the Oseen flow, the interactions and the velocity field are expressed in terms of the following parameters:

(i) $\sigma = a/R$, describing the dependence of the interactions on the radial distribution of the spheres (R is a typical distance between the centres of two spheres),

(ii) $\kappa = a/P_k$, giving the dependence of the velocity field on the radial distance between the centre of the k-th sphere and the point $\mathbf{r}$ in the fluid,

(iii) RU/ν, P_kU/ν – characterizing the regime of the interactions (the role of the convective inertia effects).

Here we consider the regime specified by the following conditions:

$$\sigma < 1, \qquad \kappa < 1, \qquad RU/\nu < 1, \qquad P_kU/\nu < 1.$$

It means, we regard the intermediate sphere spacing and the velocity field in the region near to the assemblage of the spheres. The spheres are held fixed. No lubrication behaviour is included. The hydrodynamic interactions and the velocity profile are regarded up to a given order with respect to σ and κ. The 0(Re) convective inertia effects are taken into account.

2. Governing equations

The presence of the spheres in the fluid is accounted through the induced forces $\mathbf{f}_j$, $j = 1, ..., N$, distributed on the surfaces of the spheres. In an external Cartesian coordinate system, the centres and the surfaces of the spheres are given, respectively, by $\mathbf{R}_j^0$, and $\mathbf{R}_j$. The fluid velocity $\boldsymbol{\nu}(\mathbf{r})$ and pressure $p(\mathbf{r})$ satisfy the Oseen [8] and continuity equations:

$$\begin{aligned} \varrho \mathbf{U} \cdot \nabla \boldsymbol{\nu} - \mu \Delta \boldsymbol{\nu} + \nabla p &= \sum_{j=1}^{N} \int d\Omega_j \delta\left[\mathbf{r} - \mathbf{R}_j(\Omega_j)\right] \mathbf{f}_j(\Omega_j), \\ \nabla \cdot \boldsymbol{\nu} &= 0, \end{aligned} \tag{2.1}$$

where ϱ and μ are the density and the dynamic viscosity of the fluid, $\delta[\mathbf{r} - \mathbf{R}_j(\Omega_j)]$ indicate the positions of the surfaces of the spheres, $\mathbf{R}_j = \mathbf{R}_j^0 + \mathbf{r}_j$. In the local spherical polar coordinates $\mathbf{r}_j = (a, \Omega_j) = (a, \theta_j, \varphi_j)$. Inside the volumes of the spheres, the respective stress tensors $\mathbf{P}(\mathbf{r}_j)$ satisfy

$$\nabla \cdot \mathbf{P}(\mathbf{r}_j) = 0, \qquad |\mathbf{r}_j| < a. \tag{2.2}$$

On the surfaces of the spheres, we impose the no-slip boundary conditions:

$$\dot{\mathbf{R}}_j(\Omega_j) = \boldsymbol{\nu}(\mathbf{R}_j(\Omega_j)), \qquad \dot{\mathbf{R}}_j(\Omega_j) = 0, \tag{2.3}$$

where $\dot{\mathbf{R}}_j(\Omega_j)$ denotes the velocity of the j-th sphere.

The velocity field in the considered system can be presented in the following form of the convolution integral:

$$\boldsymbol{\nu}(\mathbf{r}) = \mathbf{U} + \int d\mathbf{r}' \mathbf{T}(\mathbf{r}-\mathbf{r}') \cdot \sum_{j=1}^{N} \int d\Omega_j' \delta \left[\mathbf{r}' - \mathbf{R}_j'(\Omega_j')\right] \mathbf{f}_j'(\Omega_j'), \tag{2.4}$$

where $\mathbf{T}(\mathbf{r}-\mathbf{r}')$ is the free-space Green tensor.

Its space-Fourier transform reads [4]:

$$\mathbf{T}(\mathbf{r}) = \int \frac{d^3\mathbf{k}}{(2\pi)^3} \frac{\exp(i\mathbf{k}\cdot\mathbf{r})(1-\hat{\mathbf{k}}\hat{\mathbf{k}})}{\mu(k^2 + i\nu^{-1}\mathbf{U}\cdot\mathbf{k})}, \tag{2.5}$$

where $\hat{\mathbf{k}} = \mathbf{k}/|\mathbf{k}|$, $\mathbf{k}(k,\chi,\eta)$ in spherical polar coordinates.

The second term on the r.h.s. of (2.4) describes the disturbance of the uniform fluid velocity $\mathbf{U}$ due to the hydrodynamic interactions of the spheres. To perform the integrations over the surfaces of the spheres, appearing in this term, we expand the induced forces $\mathbf{f}_j$, $\exp(i\mathbf{k}\cdot\mathbf{P}_k)$ and $\exp(i\mathbf{k}\cdot\mathbf{r}_j)$ in terms of the normalized surface spherical harmonics Y_l^m [5]:

$$\mathbf{f}_j(\mathbf{r}_j) = \frac{1}{\sqrt{4\pi}} \sum_{lm} \mathbf{f}_{j,lm} Y_l^m(\Omega_j), \qquad l \geq 0, \quad |m| \leq l, \tag{2.6}$$

$$\begin{aligned} \exp(i\mathbf{k}\cdot\mathbf{P}_k) &= 4\pi \sum_{lm} i^l j^l(P_k k) Y_l^m(\chi_k,\eta_k) Y_l^{-m}(\chi,\eta), \\ \exp(i\mathbf{k}\cdot\mathbf{r}_j) &= 4\pi \sum_{lm} i^l j^l(ak) Y_l^m(\theta_j,\phi_j) Y_l^{-m}(\chi,\eta), \end{aligned} \tag{2.7}$$

where j_l is the spherical Bessel function, $\mathbf{P}_k = \mathbf{R}_k^0 - \mathbf{r} = (P_k, \chi_k, \eta_k)$ in spherical polar coordinates. Finally, we arrive at the following representation

$$\boldsymbol{\nu}(\mathbf{r}) = \mathbf{U} + \sum_{k=1}^{N} \sum_{l_2 m_2} \mathbf{C}^{l_2 m_2}(\mathbf{P}_k) \cdot \mathbf{f}_{k,l_2 m_2}, \tag{2.8}$$

giving the velocity field in terms of the $(l_2 m_2)$ components of the induced forces $\mathbf{f}_k$. The second order tensors $\mathbf{C}^{l_2 m_2}(\mathbf{P}_k)$ are called the velocity field tensor. They are introduced to examine the disturbance of the velocity field $\mathbf{U}$ due to the hydrodynamic interactions of the k-th sphere in the presence of the $N-1$ other

spheres. For further consideration, the tensors are written down in the following form:

$$\mathbf{C}^{l_2m_2}(\mathbf{P}_k) = \sum_{l_3m_3} \mathbf{C}^{l_2m_2}_{l_3m_3}(P_k) Y^{m_3}_{l_3}(\chi_k, \eta_k), \tag{2.9}$$

where

$$\mathbf{C}^{l_2m_2}_{l_3m_3} = \frac{i^{-l_2-l_3}}{\mu\pi\sqrt{\pi}} \int \frac{d^3\mathbf{k}}{(2\pi)^3} \frac{(\mathbf{1} - \hat{\mathbf{k}}\hat{\mathbf{k}})}{k^2 + i\nu^{-1}\mathbf{U}\cdot\mathbf{k}} Y^{m_2}_{l_2} Y^{-m_3}_{l_3} j_{l_2}(ak) j_{l_3}(P_k k). \tag{2.10}$$

We note that the properties of the velocity field tensors follow the properties of the Green tensor $\mathbf{T}(\mathbf{r})$. In the description of the velocity profile, the role of the velocity tensors is similar to the role of the propagators, introduced by DURLOFSKY, BRADY and BOSSIS [12]. In what follows, the dependence of the tensors on the parameters κ and Re will be discussed.

3. Properties of tensors $\mathbf{C}^{l_2m_2}_{l_3m_3}(P_k)$

It is shown in the Appendix that the tensors $\mathbf{C}^{l_2m_2}_{l_3m_3}(P_k)$ can be presented in the following form (A.7):

$$\begin{aligned} \mathbf{C}^{l_2m_2}_{l_3m_3} = \pm 4\pi \sum_{m=0}^{\infty} \beta_m(l_2, l_3) i^{|l_2+2m-l_3|} \\ \cdot \sum_{m_4,m_5} R(l_2, m_2, m_4) R(l_3, -m_3, -m_5) d^{m_4}_{l_2} d^{-m_5}_{l_3} \\ \cdot \int_0^1 d\xi \left[\frac{2}{3}\delta_{m_4,m_5} - \sqrt{\frac{2\pi}{15}} \sum_{m_6,m_7} \delta_{m_7+m_4,m_5} \mathbf{K}_{m_6} R(2, m_6, m_7) d^{m_7}_2 P^{m_7}_2(\xi) \right] \\ \cdot P^{m_4}_{l_2}(\xi) P^{-m_5}_{l_3}(\xi) I_{\tilde{z}}(P_k\alpha\xi) K_{\tilde{\varrho}}(P_k\alpha\xi), \end{aligned} \tag{3.1}$$

where the signs $\{\pm\}$ refer to the cases $l_2+l_3 = 2n$, $l_2+l_3 = 2n+1$, respectively, the quantity $\beta_m(l_2, l_3)$, depending on P_k, is given by the formula (A.3), the quantities $R(l_i, m_i, m_j)$ describe the rotation of the coordinate system, the functions Y^m_l are written down in the form:

$$Y^m_l = d^m_l P^m_l e^{im\varphi},$$

$I_{\tilde{z}}$, $K_{\tilde{\varrho}}$ are the modified Bessel functions, $\alpha = U/\nu$, $\tilde{z} = \max(l_2+2m+1/2, l_3+1/2)$, $\tilde{\varrho} = \min(l_2 + 2m + 1/2,\ l_3 + 1/2)$.

We note the appearance of the parameter P_kU/ν (in the arguments of the modified Bessel functions), characterizing the regime of the disturbances of the velocity field $\mathbf{U}$. The above formula is valid for arbitrary values of that parameter.

In what follows we are going to discuss the properties of the above tensors in the range $P_k U/\nu < 1$, referring to the weak inertia effects in the velocity profile. In this range, the products of the modified Bessel functions behave as follows:

$$I_{\tilde{z}}(P_k\alpha\xi)K_{\tilde{\varrho}}(P_k\alpha\xi) = \left(\frac{1}{2}\right)^{\tilde{z}-\tilde{\varrho}+1} \frac{\Gamma(\tilde{\varrho})}{\Gamma(\tilde{z}+1)}(P_k\alpha\xi)^{|l_2+2m-l_3|} + \dots . \tag{3.2}$$

From (3.2) it follows that for the case considered we have two kinds of the velocity field tensors:

(i) the Stokes velocity field tensors (disregarding the role of the inertia of the fluid);

(ii) the 0(Re) Oseen velocity field tensors (taking into account the weak inertia effects).

We see that the leading order contributions to the velocity tensors, which do not depend on Re, are equal to

$$\begin{aligned} \mathbf{C}_{l_3 m_3}^{l_2 m_2} = \pm 4\pi \sum_{m=0}^{\infty} \beta_m(l_2, l_3) \sum_{m_4, m_5} R(l_2, m_2, m_4) R(l_3, -m_3, -m_5) d_{l_2}^{m_4} d_{l_3}^{-m_5} \\ \cdot \int_0^1 d\xi \left[\frac{2}{3}\delta_{m_4,m_5} - \sqrt{\frac{2\pi}{15}} \sum_{m_6,m_7} \delta_{m_7+m_4,m_5} \mathbf{K}_{m_6} R(2, m_6, m_7) d_2^{m_7} P_2^{m_7}(\xi)\right] \\ \cdot P_{l_2}^{m_4}(\xi) P_{l_3}^{-m_5}(\xi) \left(\frac{1}{2}\right)^{\tilde{z}-\tilde{\varrho}+1} \frac{\Gamma(\tilde{\varrho})}{\Gamma(\tilde{z}+1)} . \end{aligned} \tag{3.3}$$

The integrals over the associated Legendre functions are different from zero for the following sets of the indices l_i [6]:

$$l_2 = l_3 \qquad \text{and} \qquad l_2 = l_3 - 2. \tag{3.4}$$

Hence the leading order contributions to the considered tensors are characterized by the following parameters:

$$\begin{aligned} &\text{(i)} \qquad m = 0, \qquad l_2 = l_3 ; \\ &\text{(ii)} \qquad m = 1, \qquad l_2 = l_3 - 2. \end{aligned} \tag{3.5}$$

The tensors exhibit the characteristic dependence on the inverse powers of the distances P_k:

$$\begin{aligned} &\text{(i) they are of the leading order of } \left(\frac{a}{P_k}\right)^{l_2+1} ; \\ &\text{(ii) the tensors with } m=1 \text{ contain the contributions of the order of } \left(\frac{a}{P_k}\right)^{l_2+3} . \end{aligned} \tag{3.6}$$

For example, the velocity tensors of low indices assume the following form:

(i) diagonal with respect to l_i ($m = 0$):

$$\mathbf{C}_{00}^{00}(P_k) = \frac{1}{3\sqrt{\pi}\mu P_k}\mathbf{I}; \tag{3.7}$$

(ii) off-diagonal with respect to l_i ($m = 1$):

$$\mathbf{C}_{2m_3}^{00}(P_k) = \frac{\sqrt{2}}{8\sqrt{15\pi}\mu P_k}\left[1 - \left(\frac{a}{P_k}\right)^2\right]\mathbf{K}_{m_3}. \tag{3.8}$$

The leading order contributions to the velocity tensors, given by (3.3), will be used to describe the velocity field past N spheres, provided the inertial effects are negligible.

In the considered range $P_k U/\nu < 1$ the second group of the velocity tensors, being of our interest, are the tensors of the order of 0(Re). It follows from (3.2) that they are equal to

$$\begin{aligned}\mathbf{C}_{l_3 m_3}^{l_2 m_2} = \pm 4\pi i \sum_{m=0}^{\infty} \beta_m(l_2, l_3) \sum_{m_4, m_5} R(l_2, m_2, m_4) R(l_3, -m_3, -m_5) d_{l_2}^{m_4} d_{l_3}^{-m_5} \\ \cdot \int_0^1 d\xi \left[\frac{2}{3}\delta_{m_4, m_5} - \sqrt{\frac{2\pi}{15}} \sum_{m_6, m_7} \delta_{m_7+m_4, m_5} \mathbf{K}_{m_6} R(2, m_6, m_7) d_2^{m_7} P_2^{m_7}(\xi)\right] \\ \cdot P_{l_2}^{m_4}(\xi) P_{l_3}^{-m_5}(\xi) \left(\frac{1}{2}\right)^{\tilde{z}-\tilde{\varrho}+1} \frac{\Gamma(\tilde{\varrho})}{\Gamma(\tilde{z}+1)} P_k \alpha \xi + \dots .\end{aligned} \tag{3.9}$$

Taking again into account the properties of the integrals over ξ we deduce that the tensors, belonging in that group, are characterized by the following sets of their indices:

$$\begin{aligned} &\text{(i)} && m = 0, && l_3 = l_2 - 1, \\ &\text{(ii)} && m = 0, 1, && l_3 = l_2 + 1, \\ &\text{(iii)} && m = 1, 2, && l_3 = l_2 + 3. \end{aligned} \tag{3.10}$$

It follows from (3.9) that the above tensors are built up of the contributions of the following orders with respect to (a/P_k):

$$\begin{aligned} \mathbf{C}_{l_2-1 m_3}^{l_2 m_2} &\sim \left(\frac{a}{P_k}\right)^{l_2}, \\ \mathbf{C}_{l_2+1 m_3}^{l_2 m_2} &\sim \left(\frac{a}{P_k}\right)^{l_2}, \left(\frac{a}{P_k}\right)^{l_2+2}, \\ \mathbf{C}_{l_2+3 m_3}^{l_2 m_2} &\sim \left(\frac{a}{P_k}\right)^{l_2}, \left(\frac{a}{P_k}\right)^{l_2+2}, \left(\frac{a}{P_k}\right)^{l_2+4}. \end{aligned} \tag{3.11}$$

Here we list, for example, a few low indices 0(Re) tensors, for the particular case of $\hat{U}(0,0,1)$:

(i) $l_3 = l_2 - 1, \quad m = 0,$

$$\mathbf{C}_{00}^{1m_2}(P_k) = -\frac{\mathrm{Re}}{9\sqrt{3\pi}\,\mu P_k}(-1)^{(m_2-|m_2|)/2}\left\{\delta_{m_2,0} - \frac{3}{2\sqrt{5}}\sum_{m_6=-2}^{2}\delta_{m_2+m_6,0}(-1)^{(m_6-|m_6|)/2}\begin{pmatrix}2 & 1 & 1\\ m_6 & m_2 & 0\end{pmatrix}\mathbf{K}_{m_6}\right\}; \tag{3.12}$$

(ii) $l_3 = l_2 + 1, \quad m = 0,\ 1,$

$$\mathbf{C}_{1m_3}^{00}(P_k) = \frac{\mathrm{Re}}{6\sqrt{3\pi}\,a\mu}(-1)^{(-m_3-|m_3|)/2}\left\{-\delta_{m_3,0} + \frac{9}{8\sqrt{5}}\sum_{m_6=-2}^{2}\delta_{m_3,m_6}(-1)^{(m_6-|m_6|)/2}\begin{pmatrix}2 & 1 & 1\\ m_6 & -m_3 & 0\end{pmatrix}\mathbf{K}_{m_6}\right\} + 0\left(\left(\frac{a}{P_k}\right)^2\right); \tag{3.13}$$

(iii) $l_3 = l_2 + 3, \quad m = 1,\ 2,$

$$\mathbf{C}_{3m_3}^{00}(P_k) = \frac{\sqrt{5}\mathrm{Re}}{56\sqrt{2\pi}\,a\mu}\sum_{m_6=-2}^{2}\delta_{m_3,m_6}\begin{pmatrix}2 & 3 & 1\\ m_6 & -m_3 & 0\end{pmatrix}\mathbf{K}_{m_6} + 0\left(\left(\frac{a}{P_k}\right)^2\right), \tag{3.14}$$

where the Wigner 3-j symbols $\begin{pmatrix}l_1 & l_2 & l_3\\ m_1 & m_2 & m_3\end{pmatrix}$ are given by the formula (3.7.11) from [6].

In view of the properties of the Bessel functions $I_{1/2}$ and $K_{1/2}$, the contributions linear in Re appear also in the series expansion of the tensor $\mathbf{C}_{00}^{00}$ with respect to P_kU/ν. It follows from (A.8) that the tensor $\mathbf{C}_{00}^{00}(P_k)$ can be presented in the following form:

$$\mathbf{C}_{00}^{00}(P_k) = \mathbf{C}_k + \mathbf{C}_k^1 + \dots\,, \tag{3.15}$$

where $\mathbf{C}_k$ denote the Stokes contributions (3.7), $\mathbf{C}_k^1$ are the 0(Re) contributions, equal to:

$$\mathbf{C}_k^1 = \frac{\mathrm{Re}}{16\sqrt{6\pi}\,a\mu}\sum_{m_6=-2}^{2}R(2,m_6,0)\mathbf{K}_{m_6}\,, \tag{3.16}$$

and the quantity $R(2,m_6,0)$ is defined by (A.4).

We note that the leading order contributions to $\mathbf{C}_{1m_3}^{00}(P_k)$, $\mathbf{C}_{3m_3}^{00}(P_k)$ and $\mathbf{C}_k^1$ are independent of P_k. In the paper [7] we have discussed an analogous lack of $|\mathbf{R}_{jk}|$ in the leading order contributions to the mutual interaction tensors

$\mathbf{T}^{l_2m_2}_{l_1m_1}(\mathbf{R}_{jk})$ ($\mathbf{R}_{jk} = \mathbf{R}^0_k - \mathbf{R}^0_j$, the formula (4.20) in [7]). The above contributions to the velocity tensors, acting on the component $\mathbf{f}_{k,00}$ of the induced forces, give rise to the P_k-independent terms in the expression (2.8) for the velocity field.

That type of the independence has been reported, for example, in the paper by PROUDMAN and PEARSON [14], concerning the flow past one sphere. The authors have considered the velocity field in the framework of the Navier–Stokes equations, applying the method of the matched asymptotic expansions. The above contributions to the velocity field, being proportional to Re, vanish at the Stokes conditions.

4. The components $\mathbf{f}_{j,l_2m_2}$ of the induced forces

The hydrodynamic interactions between the spheres are treated as the multiple scattering events, describing the scattering of the disturbances of the velocity field due to the presence of the spheres. The approach leads to the following formula, providing the representation for the components $\mathbf{f}_{j,l_2m_2}$ in terms of the relative velocity of the fluid with respect to the spheres $\mathbf{V}_{j,lm}$:

$$\mathbf{f}_{j,l_1m_1} = \sum_{l_2m_2} \tilde{\mathbf{T}}^{l_2m_2}_{l_1m_1}(\mathbf{O}_j)\cdot\Bigg[\mathbf{V}_{j,l_2m_2} - \sum_{k\neq j}\sum_{l_im_i} \mathbf{T}^{l_3m_3}_{l_2m_2}(\mathbf{R}_{jk})\cdot\tilde{\mathbf{T}}^{l_4m_4}_{l_3m_3}(\mathbf{O}_k)\cdot\mathbf{V}_{k,l_4m_4} + \sum_{k\neq j}\sum_{k\neq k_1}\sum_{l_im_i} \mathbf{T}^{l_3m_3}_{l_2m_2}(\mathbf{R}_{jk})\cdot\tilde{\mathbf{T}}^{l_4m_4}_{l_3m_3}(\mathbf{O}_k)\cdot\mathbf{T}^{l_5m_5}_{l_4m_4}(\mathbf{R}_{kk_1})\cdot\tilde{\mathbf{T}}^{l_6m_6}_{l_5m_5}(\mathbf{O}_{k_1})\cdot\mathbf{V}_{k_1,l_6m_6} - \dots\Bigg], \tag{4.1}$$

where $i = 2,3,4,5,6$,

$$\mathbf{V}_{j,lm} = \left\{\begin{array}{ll} -\mathbf{U}, & l=0 \\ 0, & l\geq 1 \end{array}\right\}. \tag{4.2}$$

$\tilde{\mathbf{T}}^{l_2m_2}_{l_1m_1}(\mathbf{O}_j)$ and $\mathbf{T}^{l_3m_3}_{l_2m_2}(\mathbf{R}_{jk})$ are respectively the inverse self- and mutual interaction tensors; their properties have been analysed in the author's previous paper [1], under the assumption $R_{jk}U/\nu < 1$. For example, we list below a few hydrodynamic interaction tensors with the lowest indices, including the contributions up to 0(Re):

(i) self-interaction tensors:

$$\mathbf{T}^{00}_{00}(\mathbf{O}_j) = \mathbf{T}_j + \mathbf{T}^1_j + \dots,$$

where

$$\mathbf{T}_j = \frac{1}{6\pi\mu a}\mathbf{I}, \qquad \mathbf{T}^1_j = \frac{1}{6\pi\mu a}\left[-\frac{3}{16}\mathrm{Re}\left(3\mathbf{I} - \hat{\mathbf{U}}\hat{\mathbf{U}}\right)\right];$$

(ii) inverse self-interaction tensors:

$$\tilde{\mathbf{T}}^{00}_{00}(\mathbf{O}_j) = \tilde{\mathbf{T}}_j + \tilde{\mathbf{T}}^1_j + \dots, \tag{4.3}$$

where

$$\tilde{\mathbf{T}}_j = 6\pi\mu a\mathbf{I}, \qquad \tilde{\mathbf{T}}_j^1 = 6\pi\mu a\left[\frac{3}{16}\mathrm{Re}\left(3\mathbf{I} - \hat{\mathbf{U}}\hat{\mathbf{U}}\right)\right];$$

(iii) mutual-interactions tensors:

$$\mathbf{T}_{00}^{00}(\mathbf{R}_{jk}) = \mathbf{T}_{jk} + \mathbf{T}_{jk}^1 + \dots,$$

where

$$\mathbf{T}_{jk} = \frac{1}{8\pi\mu R_{jk}}\left[\mathbf{1} + \hat{\mathbf{e}}_{jk}\hat{\mathbf{e}}_{jk} + \frac{2a^2}{R_{jk}^2}\left(\frac{1}{3}\mathbf{I} - \hat{\mathbf{e}}_{jk}\hat{\mathbf{e}}_{jk}\right)\right],$$

$$\hat{\mathbf{e}}_{jk} = \frac{\mathbf{R}_{jk}}{|\mathbf{R}_{jk}|},$$

$$\mathbf{T}_{jk}^1 = -\frac{\mathrm{Re}}{32\pi\mu a}\left(3\mathbf{I} - \hat{\mathbf{U}}\hat{\mathbf{U}}\right) + \sum_{m_3}\mathbf{T}_{00,1m_3}^{00}Y_1^{m_3} + \sum_{m_3}\mathbf{T}_{00,3m_3}^{00}Y_3^{m_3} + \dots,$$

$$\mathbf{T}_{00,1m_3}^{00} \sim 0(\mathrm{Re}), \qquad \mathbf{T}_{00,3m_3}^{00} \sim 0(\mathrm{Re}), \qquad \mathrm{R_{jk}U}/\nu < 1.$$

The first contributions to the above tensors describe the Stokes interactions, the second terms, respectively, the 0(Re) Oseen interactions. Taking into account the properties of the tensors $\mathbf{T}_{l_1m_1}^{l_2m_2}$, the formula (4.1) yields the series expansion of the $\mathbf{f}_{j,l_1m_1}$ with respect to σ and Re. For example, the components $\mathbf{f}_{j,00}$ are equal to:

(i) for the case of the flow past one sphere:

$$\mathbf{f}_{j,00} = -\left[\tilde{\mathbf{T}}_j + \tilde{\mathbf{T}}_j^1 + \dots\right]\cdot\mathbf{U} = \mathbf{f}_j + \mathbf{f}_j^1 + \dots, \tag{4.4}$$

where $\mathbf{f}_j$ denotes the Stokes drag force, $\mathbf{f}_j^1$ – the 0(Re) Oseen force;

(ii) for the case of the flow past N spheres:

$$\begin{aligned}\mathbf{f}_{j,00} = -\tilde{\mathbf{T}}_{00}^{00}(\mathbf{O}_j)\Bigg\{1 - \sum_{k\neq j}\Bigg[\mathbf{T}_{00}^{00}(\mathbf{R}_{jk})\cdot\tilde{\mathbf{T}}_{00}^{00}(\mathbf{O}_k) + \sum_m \mathbf{T}_{00}^{1m}(\mathbf{R}_{jk})\cdot\tilde{\mathbf{T}}_{1m}^{00}(\mathbf{O}_k)\Bigg] \\ + \sum_{k\neq j}\sum_{l\neq k}\mathbf{T}_{00}^{00}(\mathbf{R}_{jk})\cdot\tilde{\mathbf{T}}_{00}^{00}(\mathbf{O}_k)\cdot\mathbf{T}_{00}^{00}(\mathbf{R}_{kl})\cdot\tilde{\mathbf{T}}_{00}^{00}(\mathbf{O}_l) \\ - \sum_{k\neq j}\sum_{l\neq k}\sum_{n\neq l}\mathbf{T}_{00}^{00}(\mathbf{R}_{jk})\cdot\tilde{\mathbf{T}}_{00}^{00}(\mathbf{O}_k)\cdot\mathbf{T}_{00}^{00}(\mathbf{R}_{kl})\cdot\tilde{\mathbf{T}}_{00}^{00}(\mathbf{O}_l)\cdot\mathbf{T}_{00}^{00}(\mathbf{R}_{ln})\cdot\tilde{\mathbf{T}}_{00}^{00}(\mathbf{O}_n)\Bigg\}\cdot\mathbf{U} \\ + \sum_{k\neq j}\sum_m \tilde{\mathbf{T}}_{00}^{1m}(\mathbf{O}_j)\cdot\mathbf{T}_{1m}^{00}(\mathbf{R}_{jk})\cdot\tilde{\mathbf{T}}_{00}^{00}(\mathbf{O}_k)\cdot\mathbf{U} + \dots,\end{aligned} \tag{4.5}$$

where, taking into account (4.3), the Stokes $\mathbf{f}_j$ and the 0(Re) $\mathbf{f}_j^1$ contributions can be separated. The above expression is written down up to the terms of the

order of $0(\sigma^2)$ in inverse sphere spacing. In that approximation, the four body effects enter the formula (4.5). Hence, to analyse that range of the interactions, a pairwise additivity assumption cannot be used. The more detailed discussion of the properties of $\mathbf{f}_{j,lm}$ can be found in the paper [1].

5. The velocity field in the range $\mathrm{Re} < 1$, $(\mathrm{Re}/\kappa) < 1$

It follows from (2.8) that the velocity field can be presented as the sum of the contributions, generated by each sphere in the presence of $(N-1)$ other spheres. In view of the properties of the velocity tensors, the contributions exhibit different features in the regions near to and far from the assemblage of the spheres. The velocity of the fluid in the region, characterized by $P_k U/\nu < 1$, assumes the form of the sum of the Stokes (linear in $\mathbf{U}$) and the Oseen (quadratic with respect to $\mathbf{U}$) terms.

Within the considered approximation (i.e. including the contributions up to $0(\kappa^2)$), the Stokes terms can be expressed by means of the four Stokes velocity tensors ($\mathbf{C}^{00}_{00}$, $\mathbf{C}^{00}_{2m_3}$, $\mathbf{C}^{1m_2}_{1m_3}$, $\mathbf{C}^{1m_2}_{3m_3}$), whereas the description of the 0(Re) terms requires, in addition, the tensors $\mathbf{C}^{00}_{1m_3}$, $\mathbf{C}^{00}_{3m_3}$, $\mathbf{C}^{1m_2}_{00}$, $\mathbf{C}^{1m_2}_{2m_3}$ and $\mathbf{C}^{1m_2}_{4m_3}$. Below we continue the list of the relevant tensors (comp. (3.7), (3.8), (3.12), (3.13), (3.14)):

(i) the Stokes velocity tensors:

$$\mathbf{C}^{1m_2}_{1m_3}(P_k) = \frac{1}{6\sqrt{\pi}a\mu}\left(\frac{a}{P_k}\right)^2 (-1)^{(m_2-m_3-|m_2|-|m_3|)/2}\left\{-\frac{2}{3}(-1)^{m_3}\delta_{m_2,m_3} + \sqrt{\frac{1}{5}}\sum_{m_6=-2}^{2}\delta_{m_2+m_6,m_3}(-1)^{(m_6-|m_6|)/2}\begin{pmatrix}2 & 1 & 1\\ m_6 & m_2 & -m_3\end{pmatrix}\mathbf{K}_{m_6}\right\}, \tag{5.1}$$

$$\mathbf{C}^{1m_2}_{3m_3}(P_k) = -\frac{\sqrt{3}}{8\sqrt{10\pi}a\mu}\left(\frac{a}{P_k}\right)^2 (-1)^{(m_2-m_3-|m_2|-|m_3|)/2}\sum_{m_6=-2}^{2}\delta_{m_2+m_6,m_3} \cdot (-1)^{(m_6-|m_6|)/2}\begin{pmatrix}2 & 1 & 3\\ m_6 & m_2 & -m_3\end{pmatrix}\mathbf{K}_{m_6} + 0\left(\left(\frac{a}{P_k}\right)^4\right); \tag{5.2}$$

(ii) the 0(Re) velocity tensors (for the case of $\hat{U}(0,0,1)$):

$$\mathbf{C}^{1m_2}_{2m_3}(P_k) = \frac{\sqrt{2}\mathrm{Re}}{18\sqrt{\pi}a\mu}\left(\frac{a}{P_k}\right)(-1)^{(m_2-m_3-|m_2|-|m_3|)/2}\left\{\delta_{m_2,m_3} \cdot \begin{pmatrix}1 & 2 & 1\\ m_2 & -m_3 & 0\end{pmatrix} - \frac{\sqrt{3}}{5}\sum_{m_6}\delta_{m_2+m_6,m_3}(-1)^{(m_6-|m_6|)/2}\left[-\frac{9}{4\sqrt{7}} \cdot \begin{pmatrix}1 & 2 & 3\\ m_2 & -m_3 & m_6\end{pmatrix} + \frac{1}{\sqrt{10}}\begin{pmatrix}1 & 2 & 1\\ m_2 & -m_3 & m_6\end{pmatrix}\right]\mathbf{K}_{m_6}\right\} + 0\left(\left(\frac{a}{P_k}\right)^3\right), \tag{5.3}$$

$$(5.4)\qquad \mathbf{C}^{1m_2}_{4m_3}(P_k) = \frac{\sqrt{7}\mathrm{Re}}{60\sqrt{6\pi}a\mu}\left(\frac{a}{P_k}\right)(-1)^{(m_2-m_3-|m_2|-|m_3|)/2}\sum_{m_6}\delta_{m_6+m_2,m_3}$$
$$\cdot(-1)^{(m_6-|m_6|)/2}\begin{pmatrix}3 & 1 & 4\\ m_6 & m_2 & -m_3\end{pmatrix}\mathbf{K}_{m_6} + 0\left(\left(\frac{a}{P_k}\right)^3\right).$$

The Stokes and the 0(Re) contributions to the velocity field are expressed in terms of the listed velocity tensors, acting on the respective components of the induced forces. The components are the results of the many-sphere hydrodynamic, non-additive interactions. Up to the contributions of the order of $0(\sigma^2)$, the non-additive interactions of three and four spheres enter the description of the velocity of the fluid. In Table 1 we have written down the admissible (from

Table 1. The velocity field ($\boldsymbol{\nu}(\mathbf{r}) - \mathbf{U}$, cf. (2.8)) near to N spheres ($P_kU/\nu < 1$), including terms up to $0(\kappa^2)$ and $0(\sigma^2)$, $j = 1, ..., N$.

	Stokes contributions	Oseen contributions
κ^0	–	$\sum_j \mathbf{C}^1_j Y^0_0 \cdot \mathbf{f}_j$ $\sum_j \sum_{m_3} \mathbf{C}^{00}_{1m_3} Y^{m_3}_1 \cdot \mathbf{f}_j$ $\sum_j \sum_{m_3} \mathbf{C}^{00}_{3m_3} Y^{m_3}_3 \cdot \mathbf{f}_j$
κ^1	$\sum_j \mathbf{C}_j Y^0_0 \cdot \mathbf{f}_j$ $\sum_j \sum_{m_3} \mathbf{C}^{00}_{2m_3} Y^{m_3}_2 \cdot \mathbf{f}_j$	$\sum_j \mathbf{C}_j Y^0_0 \cdot \mathbf{f}^1_j$ $\sum_j \sum_{m_3} \mathbf{C}^{00}_{2m_3} Y^{m_3}_2 \cdot \mathbf{f}^1_j$ $\sum_j \sum_{m_2} \mathbf{C}^{1m_2}_{00} Y^0_0 \cdot \mathbf{f}_{j,1m_2}$ $\sum_j \sum_{m_2,m_3} \mathbf{C}^{1m_2}_{2m_3} Y^{m_3}_2 \cdot \mathbf{f}_{j,1m_2}$ $\sum_j \sum_{m_2,m_3} \mathbf{C}^{1m_2}_{4m_3} Y^{m_3}_4 \cdot \mathbf{f}_{j,1m_2}$
κ^2	$\sum_j \sum_{m_2,m_3} \mathbf{C}^{1m_2}_{1m_3} Y^{m_3}_1 \cdot \mathbf{f}_{j,1m_2}$ $\sum_j \sum_{m_2,m_3} \mathbf{C}^{1m_2}_{3m_3} Y^{m_3}_3 \cdot \mathbf{f}_{j,1m_2}$	$\sum_j \sum_{m_3} \mathbf{C}^{00}_{1m_3} Y^{m_3}_1 \cdot \mathbf{f}_j$ $\sum_j \sum_{m_3} \mathbf{C}^{00}_{3m_3} Y^{m_3}_3 \cdot \mathbf{f}_j$ $\sum_j \sum_{m_2,m_3} \mathbf{C}^{1m_2}_{1m_3} Y^{m_3}_1 \cdot \mathbf{f}_{j,1m_2}$ $\sum_j \sum_{m_2,m_3} \mathbf{C}^{1m_2}_{3m_3} Y^{m_3}_3 \cdot \mathbf{f}_{j,1m_2}$

the point of view of the properties of the velocity tensors and of the components $\mathbf{f}_{j,lm}$) sequences of the hydrodynamic interactions.

We note the following qualitative properties of the velocity profile, due to the inertia of the fluid:

(i) the velocity exhibits the stronger, than under the Stokes conditions, dependence on the non-additivity of the interactions (at the Stokes regime the non-additive interactions of three spheres enter);

(ii) the components $\mathbf{f}_{j,00}$ generate the contributions to the velocity field starting from the terms of the order of $0(\kappa^0)$ (at the Stokes regime, respectively, from the terms of $0(\kappa^1)$);

(iii) the components $\mathbf{f}_{j,1m}$ generate the analogous contributions, starting from the terms of the order of $0(\kappa^1)$ (at the Stokes conditions, respectively, from the terms of $0(\kappa^2)$);

(iv) there appear the contributions, expressed in terms of the functions Y_1^m and Y_3^m, which describe the lack of the fore-aft symmetry.

We note that for the particular case of one sphere, the tensor $\mathbf{C}_j$ and $\mathbf{C}_{2m_3}^{00}$, acting on the component $\mathbf{f}_j = -6\pi\mu a\mathbf{U}$, give the classical Stokes velocity profile. To our knowledge, the description of the velocity field past N spheres, involving the Oseen hydrodynamic interactions between more than two spheres, is at present not available in the literature. Summing up, in the present paper it has been investigated to what extent the weak convective inertia of the fluid increases the role of the hydrodynamic interactions and modifies the symmetry properties of the generated velocity field.

Appendix. Series expansion of the tensors $\mathbf{C}_{l_3m_3}^{l_2m_2}$ with respect to P_kU/ν

The tensors $\mathbf{C}^{l_2m_2}(\mathbf{P}_k)$ describe the effect of the component $\mathbf{f}_{k,l_2m_2}$ of the force, induced on the surface of the k-th sphere, on the velocity field of the fluid. The tensors $\mathbf{C}_{l_3m_3}^{l_2m_2}(P_k)$ concern the respective radial properties. To examine these properties, we start with the integration over $|\mathbf{k}|$ in the expression (2.10). To this end we use the properties of the Bessel functions $J_{l+1/2}$, expressed by the formula (7) on the page 45, and by the formula (7) on the page 99 of [9], and we apply the expansion of $\mathbf{1} - \hat{\mathbf{k}}\hat{\mathbf{k}}$ in terms of Y_2^m [5]:

$$\mathbf{1} - \hat{\mathbf{k}}\hat{\mathbf{k}} = \frac{2}{3}I - \sqrt{\frac{2\pi}{15}} \sum_{m_6=-2}^{2} \mathbf{K}_{m_6} Y_2^{m_6}, \tag{A.1}$$

where

$$\begin{aligned}
\mathbf{K}_0 &= \sqrt{\frac{2}{3}}\left(-\mathbf{e}_x\mathbf{e}_x - \mathbf{e}_y\mathbf{e}_y + 2\mathbf{e}_z\mathbf{e}_z\right), \\
\mathbf{K}_{\pm 1} &= \mathbf{e}_x\mathbf{e}_z + \mathbf{e}_z\mathbf{e}_x \mp i\mathbf{e}_y\mathbf{e}_z \mp i\mathbf{e}_z\mathbf{e}_y, \\
\mathbf{K}_{\pm 2} &= \mathbf{e}_x\mathbf{e}_x - \mathbf{e}_y\mathbf{e}_y \mp i\mathbf{e}_x\mathbf{e}_y \mp i\mathbf{e}_y\mathbf{e}_x.
\end{aligned}$$

As a result, we obtain the following expression:

$$\mathbf{C}_{l_3 m_3}^{l_2 m_2} = \sum_{m=0}^{\infty} \beta_m(l_2, l_3) \int d\Omega_k \left[\frac{2}{3} I - \sqrt{\frac{2\pi}{15}} \sum_{m_6=-2}^{2} \mathbf{K}_{m_6} Y_2^{m_6} \right] Y_{l_2}^{m_2} Y_{l_3}^{-m_3} \cdot \int d\tilde{k} \frac{\tilde{k} - iP_k \alpha \xi}{\tilde{k}^2 + (P_k \alpha \xi)^2} J_{l_2+1/2+2m}(\tilde{k}) J_{l_3+1/2}(\tilde{k}), \tag{A.2}$$

where

$$\beta_m(l_2, l_3) = \frac{i^{l_2 - l_3}}{2a\mu} \left(\frac{a}{P_k} \right)^{l_2+1} \cdot (l_2)! \sum_{n=0}^{l_2} \frac{(-1)^n (2l_2 - 2n + 1) \left(l_2 + \frac{1}{2} + 2m \right) \Gamma \left(l_2 + \frac{1}{2} + m \right)}{n!(2l_2 - n + 1)! \Gamma \left(l_2 - n + \frac{3}{2} \right) \Gamma \left(-l_2 + n + \frac{1}{2} \right) m!} \cdot F_4 \left[-m, l_2 + \frac{1}{2} + m; l_2 - n + \frac{3}{2}, \ -l_2 + n + \frac{1}{2}; \left(\frac{a}{2P_k} \right)^2, \left(\frac{a}{2P_k} \right)^2 \right], \tag{A.3}$$

F_4 is the hypergeometric series,

$$\alpha = U/\nu, \qquad \hat{U} = \mathbf{U}/U, \qquad \xi = \cos(\hat{U}, \hat{k}), \qquad \tilde{k} = P_k k .$$

To perform the $\tilde{k}$ integration, we apply a rotation of the coordinate system by the linear transformation, $\hat{\mathbf{k}} = \mathbf{A} \cdot \hat{\mathbf{y}}$, letting the new axis 3 coincide with $\mathbf{U}$. Then, taking into account the properties of the functions Y_l^m:

$$Y_l^q(\hat{k}) = \sum_{|n| \le l} R(l, q, n) Y_l^n(\hat{y}), \tag{A.4}$$

and using the formula (6.577) from [10], we obtain:

$$\mathbf{C}_{l_3 m_3}^{l_2 m_2} = \pm \sum_{m=0} \beta_m(l_2, l_3) \int\limits_{\xi > 0} d\Omega_y \{...\} i^{|l_2 + 2m - l_3|} I_{\tilde{z}}(P_k \alpha \xi) K_{\tilde{\varrho}}(P_k \alpha \xi) + \sum_{m=0}^{\infty} \beta_m(l_2, l_3) \int\limits_{\xi \le 0} d\Omega_y \{...\} i^{|l_2 + 2m - l_3|} I_{\tilde{z}}(P_k \alpha |\xi|) K_{\tilde{\varrho}}(P_k \alpha |\xi|), \tag{A.5}$$

where $(+)$ refers to the cases $l_2 + l_3 = 2n$, and $(-)$ – to the cases $l_2 + l_3 = 2n + 1$, $I_{\tilde{z}}$ and $K_{\tilde{\varrho}}$ denote the modified Bessel functions, $\tilde{z} = \max(l_2 + 1/2 + 2m, \ l_3 + 1/2)$, $\tilde{\varrho} = \min(l_2 + 1/2 + 2m, \ l_3 + 1/2)$, and the expression in the parentheses reads:

$$\{...\} = \sum_{m_4, m_5} R(l_2, m_2, m_4) R(l_3, -m_3, -m_5) \left[\frac{2}{3} I - \sqrt{\frac{2\pi}{15}} \sum_{m_6, m_7} \mathbf{K}_{m_6} R(2, m_6, m_7) \cdot Y_2^{m_7}(\hat{y}) \right] Y_{l_2}^{m_4}(\hat{y}) Y_{l_3}^{-m_5}(\hat{y}). \tag{A.6}$$

Carrying out the integrations over the meridional angle, we arrive at:

$$\text{(A.7)}\qquad \mathbf{C}_{l_3 m_3}^{l_2 m_2} = \pm 4\pi \sum_{m}^{\infty} \beta_m(l_2, l_3) i^{|l_2+2m-l_3|} \cdot \sum_{m_4,m_5} R(l_2, m_2, m_4) R(l_3, -m_3, -m_5) d_{l_2}^{m_4} d_{l_3}^{-m_5} \cdot \int_0^1 d\xi \left[\frac{2}{3}\delta_{m_4,m_5} - \sqrt{\frac{2\pi}{15}} \sum_{m_6,m_7} \delta_{m_7+m_4,m_5} \mathbf{K}_{m_6} R(2, m_6, m_7) d_2^{m_7} P_2^{m_7}(\xi) \right] \cdot P_{l_2}^{m_4}(\xi) P_{l_3}^{-m_5}(\xi) I_{\tilde{z}}(P_k\alpha\xi) K_{\tilde{\varrho}}(P_k\alpha\xi),$$

where the coefficients d_l^m read:

$$d_l^m = (-1)^{(m-|m|)/2} \sqrt{\frac{(2l+1)(l-m)!}{4\pi(l+m)!}}\,.$$

$P_l^m(\xi)$ are the associated Legendre functions [cf. [6], formulae (2.5.17) and (2.5.18)].

Taking into account the properties of $P_l^m(\xi)$, we can accomplish the integration with the help of the formula 1.11.3.2 from [11]:

$$\text{(A.8)}\qquad \int_0^1 d\xi\, \xi^{\lambda} I_{\tilde{z}}(P_k\alpha\xi) K_{\tilde{\varrho}}(P_k\alpha\xi) = \frac{\pi}{2\sin\tilde{\varrho}\pi} \left[\frac{(P_k\alpha/2)^{\tilde{z}-\tilde{\varrho}}}{(\lambda+\tilde{z}-\tilde{\varrho}+1)\Gamma(\tilde{z}+1)\Gamma(-\tilde{\varrho}+1)} \cdot {}_3F_4\left[\frac{\lambda+\tilde{z}-\tilde{\varrho}+1}{2}, \frac{\tilde{z}-\tilde{\varrho}+1}{2}, \frac{\tilde{z}-\tilde{\varrho}+2}{2}; \tilde{z}+1,\ -\tilde{\varrho}+1,\ \tilde{z}-\tilde{\varrho}+1,\ \frac{\lambda+\tilde{z}-\tilde{\varrho}+3}{2};\ (P_k\alpha)^2 \right] - \frac{(P_k\alpha/2)^{\tilde{z}+\tilde{\varrho}}}{(\lambda+\tilde{z}+\tilde{\varrho}+1)\Gamma(\tilde{z}+1)\Gamma(\tilde{\varrho}+1)} \cdot {}_3F_4\left[\frac{\lambda+\tilde{z}+\tilde{\varrho}+1}{2}, \frac{\tilde{z}+\tilde{\varrho}+1}{2}, \frac{\tilde{z}+\tilde{\varrho}+2}{2}; \tilde{z}+1,\ \tilde{\varrho}+1,\ \tilde{z}+\tilde{\varrho}+1,\ \frac{\lambda+\tilde{z}+\tilde{\varrho}+3}{2};\ (P_k\alpha)^2 \right] \right],$$

where the parameter λ depends on the $P_l^m(\xi)$ involved, and the following condition should be fulfilled:

$$\lambda + \tilde{z} + \tilde{\varrho} > -1.$$

The last integration leads to the representation of the velocity field tensors in terms of the linear combinations of the ${}_3F_4$ functions. That representation is valid for the arbitrary values of Re. We are going to examine the particular regime of the hydrodynamic interactions, which is described by the velocity tensors, having arguments $P_k\alpha < 1$.

References

1. I. PIEŃKOWSKA, Arch. Mech., **48**, 231, 1996.
2. T. KUMAGAI, JSME Int. J., Ser. B, **38**, 563, 1995.
3. P. MAZUR and W. VAN SAARLOOS, Physica A, **115**, 21, 1982.
4. P. MAZUR and A.J. WEISENBORN, Physica A, **123**, 209, 1984.
5. T. YOSHIZAKI and H. YAMAKAWA, J. Chem. Phys., **73**, 578, 1980.
6. A.R. EDMONDS, *Angular momentum in quantum mechanics*, Princeton University Press, 1974.
7. I. PIEŃKOWSKA, Arch. Mech., **45**, 665, 1993.
8. R. BERKER, *Encyclopedia of Physics*, vol. VIII/2, S. FLÜGGE, Springer, 1963.
9. A. ERDÉLYI, *Higher transcendental functions*, vol. II, New York 1953.
10. I.S. GRADŠTEIN and I.M. RYZHIK, *Tables of integrals, series and products* [in Russian], Moskva 1962.
11. A.P. PRUDNIKOV, YU.A. BRYČKOV and O.I. MARIČEV, *Integrals and series, special functions* [in Russian], Nauka, 1983.
12. L. DURLOFSKY, J.F. BRADY and G. BOSSIS, J. Fluid Mech., **180**, 21, 1987.
13. R.J. PHILLIPS, J. Fluid Mech., **315**, 345, 1996.
14. I. PROUDMAN and J.R.A. PEARSON, J. Fluid Mech., **2**, 237, 1957.

POLISH ACADEMY OF SCIENCES
INSTITUTE OF FUNDAMENTAL TECHNOLOGICAL RESEARCH
e-mail: ipienk@ippt.gov.pl

Received March 5, 1997.

Arch. Mech., 49, 5, pp. 831–846, Warszawa 1997

Transverse Stokes flow through a square array of cylinders

A. ZACHARA (WARSZAWA)

THE WORK PRESENTS results of calculations of the transverse Stokes flow through a square array of cylinders. The new functional basis has been derived and the solution is sought in the form of series expansions in this basis, the terms of which are given explicitly as functions of the volume fraction φ. The presented method enabled us to evaluate the expression for the drag force of high accuracy using symbolic computations.

1. Introduction

SLOW FLOW of a viscous fluid through an array of cylinders is observed in many technical applications such as heat exchangers, fibre filters and bundles of man-made fibres in spinning processes. In this paper we shall study the flow through a square array of cylinders in a direction transverse to the cylinder axes. This problem was first studied in 1959 by HAPPEL who calculated the Stokes flow, taking into account the periodic structure of the array with the aid of a so-called free surface model [1–2]. As a result, he got an expression for the drag force F' exerted by the fluid on a unit length of a cylinder. The drag force was a function of the volume fraction φ of cylinders for a given mean velocity U of the fluid. The volume fraction φ is defined as

$$\varphi = \frac{\pi a'^2}{A}, \tag{1.1}$$

where a' is the cylinder radius and A is the cross-sectional area of the array per single cylinder. In the case of a square area it takes the form

$$A = l^2, \tag{1.2}$$

l being the distance between the cylinder axes.

The expression for the drag force F' may be presented in the following general form which involves approximations of various order

$$\frac{F'}{\mu U} = \frac{1}{K(\varphi)}, \tag{1.3}$$

where

$$K(\varphi) = \frac{1}{8\pi}\left[\ln(1/\varphi) + T^{(n)}(\varphi)\right], \tag{1.4}$$

$$T^{(n)}(\varphi) = \sum_{i=0}^{n} T_i \varphi^i, \tag{1.5}$$

and μ is the dynamic viscosity of the fluid.

The approximation of HAPPEL [1–2] was rather rough and the results obtained were of a reasonable accuracy merely for very dilute arrays ($\varphi \ll 1$). At the same time, an alternative approach to the investigation of a viscous fluid flow through periodic arrays of particles was proposed by HASIMOTO [3]. Using Fourier series expansions, he obtained spatially periodic fundamental solutions of the Stokes flow for arrays of spheres as well as of cylinders. Lattice sums which appeared in this method were calculated using rapidly converging Evald's technique. He introduced then two functions S_1 and S_2 with the aid of which it was possible to construct the infinite system of algebraic equations, in which one of unknown quantities was the drag force. After truncation the system was solved and the expression for $K(\varphi)$ (1.4) has been obtained with the accuracy of $O(\varphi)$. The method of Hasimoto was then developed by SANGANI and ACRIVOS [4] who obtained the expression for $K(\varphi)$ to $O(\varphi^3)$. It is also worth to mention the paper of DRUMMOND and TAHIR [5]. They calculated $K(\varphi)$ using the method of singularities, matching a solution outside a cylinder to a sum of solutions inside each cylinder in an infinite array. The obtained expression for $K(\varphi)$ was determined with the accuracy up to $O(\varphi^4)$.

SANGANI and ACRIVOS [6] made also numerical calculations of a Stokes flow past a periodic array of cylinders and evaluated the drag force F' in a wide range $0.05 < \varphi < 0.75$. The results [6] may then be treated as reference data for analytical approximations.

The expressions derived for the drag force may be used to calculate filtration flow through the array of cylindrical rods, treated as a porous medium [7]. It can be shown that the force F' is related to the mean pressure gradient exerted on the fluid in the array of cylinders [1–2]

$$\frac{F'}{A} = -\frac{dp'}{dx}. \tag{1.6}$$

Inserting (1.6) to (1.3) we obtain the relation

$$U = -\frac{A}{\mu} K(\varphi) \frac{dp'}{dx}, \tag{1.7}$$

which has the form of a linear Darcy equation, where $K(\varphi)$ (1.4) plays the role of a permeability coefficient [7].

These results, together with the results for the parallel case [1–2], were applied by SZANIAWSKI and ZACHARA [8, 9] for calculation of filtration flow through a bundle of man-made fibers in a formation processes. It allowed them to obtain velocity and pressure distribution inside the bundle of fibers.

In the present paper, the approach of Hasimoto as well as of Sangani and Acrivos has been modified. A new functional basis has been derived. It allowed to derive explicit expressions for matrix components of the infinite system of equations and its solution could be obtained using symbolic computations [10].

The system was truncated and as an example, the coefficient $K(\varphi)$ was calculated with the accuracy of $O(\varphi^5)$. This procedure can be easily extended to solutions of higher accuracy.

2. Governing equations

We consider the slow flow of a viscous fluid through a square array of cylinders, each of them of radius a'. They are infinitely long, so the problem may be treated as two-dimensional. With respect to the periodicity of the array, we shall limit ourselves to a unit cell which is repeated throughout the system (Fig. 1). The dimension of a unit cell is l. To describe the problem, we shall use both the Cartesian (x_1', x_2') and cylindrical (r', θ) coordinate systems. Position of the cylinder axes in the plane $x_1'x_2'$ are given by the vector

$$\mathbf{n}' = l(n_1\mathbf{a}_{(1)} + n_2\mathbf{a}_{(2)}), \qquad n_1,\ n_2 = 0, \pm 1, \pm 2, \dots , \tag{2.1}$$

where $\mathbf{a}_{(1)}$ and $\mathbf{a}_{(2)}$ are basic unit vectors in x_1' and x_2' direction, respectively. We assume that the fluid flows in x_1' direction with the mean velocity U. According to the assumption that the Reynolds number is very small, the flow may be described by the Stokes equations which are given below in a non-dimensional form

$$\frac{\partial^2 u_i}{\partial x_k \partial x_k} = \frac{\partial p}{\partial x_i}, \tag{2.2}$$

$$\frac{\partial u_k}{\partial x_k} = 0, \tag{2.3}$$

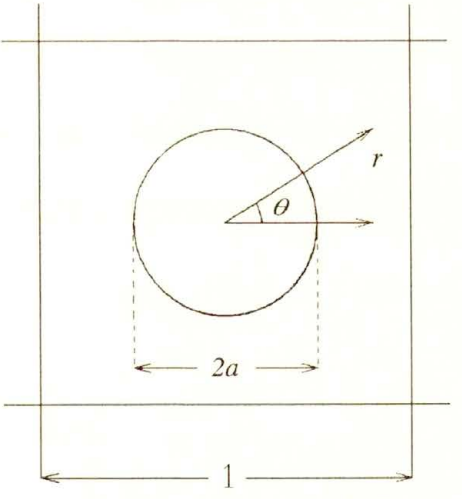

FIG. 1. Unit cell of a square array of cylinders.

where u_i is the velocity component of the fluid and p_i is the pressure. The coordinates have been non-dimesionalized with l and velocity components with U. The non-dimensional pressure p is determined as

$$p = \frac{p' \cdot l}{U \cdot \mu}.$$

The velocity field must satisfy the periodicity conditions and the no-slip boundary condition at the cylinder surface

$$\begin{aligned} \mathbf{u}(\mathbf{r}+\mathbf{n}) &= \mathbf{u}(\mathbf{r}), \\ \mathbf{u}(a,\theta) &= 0. \end{aligned} \tag{2.4}$$

Following the approach of HASIMOTO [3] and SANGANI and ACRIVOS [4], we first consider the Stokes flow through the periodic system where cylindrical particles have been replaced with singular multipole force distributions located at their axes. In this case, the Stokes equations may be presented in the following form:

$$\begin{aligned} \frac{\partial^2 v_i}{\partial x_k \partial x_k} &= \frac{\partial q}{\partial x_i} + F_i \sum_{\{n\}} \delta(\mathbf{r}-\mathbf{n}), \\ \frac{\partial v_k}{\partial x_k} &= 0, \end{aligned} \tag{2.5}$$

where $\delta(\mathbf{r}-\mathbf{n})$ is Dirac's delta function, while v_i and q are velocity component and pressure, respectively. The components F_i are $F_1 = F$, $F_2 = 0$.

The non-dimensional drag force F acting on a unit length of the cylinder is determined by

$$F = \frac{F'}{U\mu}.$$

The symbol $\{n\}$ at the sign $\sum$ in $(2.5)_1$ denotes summation in the directions x_1 and x_2 to infinity,

$$\sum_{\{n\}}^{\infty} = \sum_{n_1=-\infty}^{\infty} \sum_{n_2=-\infty}^{\infty}.$$

HASIMOTO [3] found the periodic fundamental solution of Eq. (2.5) in the form

$$v_i = U_0 \delta_{i1} - \frac{F}{4\pi}\left[S_1 \delta_{i1} - \frac{\partial^2 S_2}{\partial x_1 \partial x_i}\right], \tag{2.6}$$

$$\frac{\partial q}{\partial x_i} = F\left[-\delta_{i1} + \frac{1}{4\pi}\frac{\partial^2 S_1}{\partial x_1 \partial x_i}\right]. \tag{2.7}$$

The functions S_1 and S_2 which are periodic throughout the lattice are as follows [11]:

$$S_1 = \frac{1}{\pi}{\sum_{\{n\}}}' \frac{\exp[-2\pi i(\mathbf{n}\cdot\mathbf{r})]}{|\mathbf{n}|^2}, \tag{2.8}$$

$$S_2 = -\frac{1}{4\pi^3}{\sum_{\{n\}}}' \frac{\exp[-2\pi i(\mathbf{n}\cdot\mathbf{r})]}{|\mathbf{n}|^4}, \tag{2.9}$$

where i is an imaginary unit and the prime ($'$) over the summation symbol indicates that the term $|\mathbf{n}| = 0$ is excluded.

They are solutions of the equations

$$\nabla^2 S_1 = -4\pi \left[\sum_{\{n\}} \delta(\mathbf{r} - \mathbf{n}) - 1\right], \tag{2.10}$$

$$\nabla^2 S_2 = S_1, \tag{2.11}$$

what may be proved by the finite Fourier transforms.

Now we choose the unit cell of the array, indicated by the point $\mathbf{n} = 0$ at its centre. The functions S_1 and S_2 (2.8)–(2.9) are here calculated using the Evald summation [3] and expanded in planar harmonics near $r = 0$. The corresponding expressions are as follows

$$S_1 = -2\ln r - C_0 + \pi r^2 + 2\sum_{m=4}^{\infty} A_m r^m \cos m\theta, \tag{2.12}$$

$$S_2 = \frac{1}{2}r^2(1 - \ln r) - C_0\frac{r^2}{4} + \frac{\pi r^4}{16} + \sum_{m=4}^{\infty}\left[A_m/(2(m+1))r^2 + B_m\right] r^m \cos m\theta, \tag{2.13}$$

where

$$r = (x_1^2 + x_2^2)^{1/2},$$
$$\theta = \tan^{-1}(x_2/x_1).$$

Both the functions (2.12)–(2.13) fulfil Eqs. (2.10), (2.11) in the unit cell $\mathbf{n} = 0$ where the Dirac's delta $\delta(0)$ corresponds to the properties of $\ln r$ and its derivatives at $r = 0$. The function S_1 is simply related to the Wigner potential and the first non-vanishing coefficients A_m are evaluated in [12]. With respect to the symmetry of the square array, the coefficients A_m and B_m are different from zero only for m which are multiples of 4. The method of evaluation and numerical values of A_m, B_m and C_0 are given in the Appendix 1.

The importance of these results exceeds the frames of the fluid dynamics since S_1 is equivalent to the electrostatic potential in a periodic system of charge particles embedded in a neutralizing uniform background [12]. It is worth to note that this background corresponds to the mean pressure gradient which is able to balance the drag of the cylinders in the flow. The approach of Hasimoto was also successfully applied to the calculation of the effective conductivity of composite materials of a regular structure [13–16].

The fundamental solution (2.6) is a starting point to construct a general solution of Eqs. (2.2)–(2.3) where velocity components u_1 and u_2 defined for $r \geq a$ satisfy the no-slip boundary condition on the cylinder surface $r = a$ with the required accuracy. To this end, following [3] and [4], we add to the solution (2.6) the even derivatives of v_i and S_1 multiplied by unknown coefficients. This operation satisfies the symmetry conditions of the periodic flow through the array and leads to the following expressions for the velocity components u_1 and u_2:

$$u_1(r,\theta) = U_0 - \frac{1}{4\pi}\left[\mathbf{G}\left(S_1 - \frac{\partial^2 S_2}{\partial x_1^2}\right) + \mathbf{H}\frac{\partial^2 S_1}{\partial x_1^2}\right], \tag{2.14}$$

$$u_2(r,\theta) = \frac{1}{4\pi}\left[\mathbf{G}\frac{\partial^2 S_2}{\partial x_1 \partial x_2} - \mathbf{H}\frac{\partial^2 S_1}{\partial x_1 \partial x_2}\right], \tag{2.15}$$

where $\mathbf{G}$ and $\mathbf{H}$ are differential operators

$$\begin{aligned} \mathbf{G} &= \sum_{n=0}^{\infty} P_n \frac{\partial^{2n}}{\partial x_1^{2n}}, \\ \mathbf{H} &= \sum_{n=0}^{\infty} Q_n \frac{\partial^{2n}}{\partial x_1^{2n}}, \end{aligned} \tag{2.16}$$

and

$$U_0 = 1 + Q_0. \tag{2.17}$$

We perform differentiation of $S_1(r,\theta)$ and $S_2(r,\theta)$, Eqs. (2.12)–(2.13), with respect to x_1 and x_2 in (2.14)–(2.16) using operators

$$\begin{aligned} \frac{\partial}{\partial x_1} &= \cos\theta \frac{\partial}{\partial r} - \frac{\sin\theta}{r}\frac{\partial}{\partial \theta}, \\ \frac{\partial}{\partial x_2} &= \sin\theta \frac{\partial}{\partial r} + \frac{\cos\theta}{r}\frac{\partial}{\partial \theta}. \end{aligned} \tag{2.18}$$

To calculate the coefficients P_n and Q_n we make use of the no-slip boundary condition on the surface of the cylinder $(2.4)_2$. Thus we have

$$u_1(a,\theta) = 0, \qquad u_2(a,\theta) = 0. \tag{2.19}$$

Hence Eqs. (2.14)–(2.19) lead to the system of algebraic equations for the coefficients P_n and Q_n. If we compare (2.6), (2.14) and $(2.16)_1$ we can see that the force F exerted by the fluid on the cylinder is equal to the coefficient P_0,

$$F = P_0\,, \tag{2.20}$$

and from (1.3) we have

$$K(\varphi) = 1/P_0\,. \tag{2.21}$$

3. The basis functions

It is useful to define and derive the basis functions which may help to carry out calculations of the coefficients P_n and Q_n in an efficient and tractable way. These functions, which appear in (2.14) and (2.15) are

$$U^1 = S_1 - \frac{\partial^2 S_2}{\partial x_1^2}\,, \qquad U^2 = \frac{\partial^2 S_1}{\partial x_1^2}\,, \tag{3.1}$$

$$V^1 = \frac{\partial^2 S_2}{\partial x_1 \partial x_2}\,, \qquad V^2 = \frac{\partial^2 S_1}{\partial x_1 \partial x_2}\,, \tag{3.2}$$

where S_1 and S_2 are determined by (2.12) and (2.13). Performing differentiation of S_1 and S_2 with the use of operators (2.18), we get expressions for the function (3.1) and (3.2) given below

$$U^1(r,\theta) = \frac{1}{2}\left[\ln 1/r^2 - C_0\right] + \frac{\pi r^2}{2} + \frac{1}{4}(2 - \pi r^2)\cos 2\theta + \sum_{m=0}^{\infty} A_m E_m(r,\theta) - \sum_{m=0}^{\infty}(m+2) D_{m0}(r) E_m(r,\theta), \tag{3.3}$$

$$U^2(r,\theta) = 2\pi + \frac{2\cos 2\theta}{r^2} + 2\sum_{m=0}^{\infty} A_{m+2}\frac{(m+2)!}{m!} E_m(r,\theta), \tag{3.4}$$

$$V^1(r,\theta) = -\frac{1}{4}(2 - \pi r^2)\sin 2\theta - \sum_{m=1}^{\infty}(m+2) D_{m0}(r) F_m(r,\theta), \tag{3.5}$$

$$V^2(r,\theta) = \frac{2\sin 2\theta}{r^2} - 2\sum_{m=1}^{\infty} A_{m+2}\frac{(m+2)!}{m!} F_m(r,\theta). \tag{3.6}$$

The auxiliary functions which appear in (3.3) – (3.6) are defined as follows:

$$D_{mn}(r) = \frac{1}{2} A_{m+2n+2} r^2 + (m+1) B_{m+2n+2}\,, \tag{3.7}$$

$$E_m(r,\theta) = r^m \cos m\theta\,, \tag{3.8}$$

$$F_m(r,\theta) = r^m \sin m\theta\,. \tag{3.9}$$

The even derivatives of the basis functions which appear in the operators (2.16) are denoted by the following symbols

$$
\begin{aligned}
U_n^1 &= \frac{\partial^{2n} U^1}{\partial x_1^{2n}}, \qquad U_n^2 = \frac{\partial^{2n} U^2}{\partial x_1^{2n}}, \\
V_n^1 &= \frac{\partial^{2n} V^1}{\partial x_1^{2n}}, \qquad V_n^2 = \frac{\partial^{2n} V^2}{\partial x_1^{2n}},
\end{aligned} \tag{3.10}
$$

where $n = 1,\ 2,\ 3, \ldots$.

After differentiation of the basis functions (3.3) – (3.6), we obtain the expressions for their derivatives (3.10) which are

$$
\begin{aligned}
U_n^1 = \frac{\pi}{2}\delta_{n1} + \frac{1}{2r^{2n}}\left[(2n)!\cos 2(n+1)\theta - 2(n-1)(2n-1)!\cos 2n\theta\right] \\
- \sum_{m=0}^{\infty} \frac{(m+2n+2)!}{(m+1)!} D_{mn}(r) E_m(r,\theta) \\
- (n-1)\sum_{m=0}^{\infty} A_{m+2n}\frac{(m+2n)!}{m!} E_m(r,\theta), \qquad \text{for} \quad n \geq 1,
\end{aligned} \tag{3.11}
$$

while

$$
U_0^1 = U^1,
$$

$$
\begin{aligned}
U_n^2 = 2\pi\delta_{n0} + \frac{2(2n+1)!}{r^{2(n+1)}}\cos 2(n+1)\theta \\
+ 2\sum_{m=0}^{\infty} A_{m+2n+2}\frac{(m+2n+2)!}{m!} E_m(r,\theta) \qquad \text{for} \quad n \geq 0,
\end{aligned} \tag{3.12}
$$

$$
\begin{aligned}
V_n^1 = \frac{(2n)!}{2r^{2n}}\left[\sin 2n\theta - \sin 2(n+1)\theta\right] - n\sum_{m=1}^{\infty} A_{m+2n}\frac{(m+2n)!}{m!} F_m(r,\theta) \\
- \sum_{m=1}^{\infty} \frac{(m+2n+2)!}{(m+1)!} D_{mn}(r) F_m(r,\theta) \qquad \text{for} \quad n \geq 1,
\end{aligned} \tag{3.13}
$$

while $V_0^1 = V^1$,

$$
\begin{aligned}
V_n^2 = \frac{2(2n+1)!}{r^{2n+2}}\sin 2(n+1)\theta \\
- 2\sum_{m=1}^{\infty} A_{m+2n+2}\frac{(m+2n+2)!}{m!} F_m(r,\theta) \qquad \text{for} \quad n \geq 0.
\end{aligned} \tag{3.14}
$$

4. Calculation of the drag force

The drag force F (2.20) can be calculated from the system of Eqs. (2.19) where the velocity components u_1 and u_2 are determined by (2.14) and (2.15). The differential operators **G** and **H** (2.16) act on the functions (3.3) – (3.6). The system of equations (2.19) may thus be written

$$\mathbf{G}U^1 + \mathbf{H}U^2 = 4\pi U_0\,, \tag{4.1}$$

$$\mathbf{G}V^1 - \mathbf{H}V^2 = 0. \tag{4.2}$$

Using (2.16) – (2.18) we present Eqs. (4.1) – (4.2) in the form

$$\sum_{i=0}^{\infty}\left[P_i U_i^1 + Q_i\left(U^2 i - 4\pi\delta_{i0}\right)\right] = 4\pi\,, \tag{4.3}$$

$$\sum_{i=0}^{\infty}\left[P_i V_i^1 - Q_i V_i^2\right] = 0. \tag{4.4}$$

The basis functions (3.3) – (3.6) and their derivatives (3.11) – (3.14) may be presented in a form of $\cos 2i\theta$ and $\sin 2i\theta$ expansions whose coefficients are elements of a matrix Z_{lm}. Thus we have the following expansions of U_n^k and V_n^k,

$$\begin{aligned} U_n^k(a,\theta) &= \sum_{i=0}^{\infty}\left(4\pi\delta_{i0}\delta_{n0}\delta_{k2} + Z_{2i+1,2n+k}\right)\cos 2i\theta\,, \\ V_n^k(a,\theta) &= -(-1)^k\sum_{i=1}^{\infty} Z_{2i,2n+k}\sin 2i\theta\,, \end{aligned} \tag{4.5}$$

where $k = 1$ and 2, $n = 0,\ 1,\ 2,\ 3\ldots$.

Now we insert the basis function expansions (4.5) to Eqs. (4.3) – (4.4) and collect terms of Eq. (4.3) containing $\cos 2i\theta$ and terms of Eq. (4.4) containing $\sin 2i\theta$. Then, after some rearrangement we present Eqs. (4.3) – (4.4) in the following form:

$$\sum_{i=0}^{\infty}\sum_{j=1}^{\infty}\left(Z_{2i+1,j}X_j\right)\cos 2i\theta = 4\pi\,, \tag{4.6}$$

$$\sum_{i=1}^{\infty}\sum_{j=1}^{\infty}\left(Z_{2i,j}X_j\right)\sin 2i\theta = 0. \tag{4.7}$$

Here X_j are unknown quantities related to P_i and Q_i

$$X_{2n+1} = P_n\,, \qquad X_{2n+2} = Q_n\,, \tag{4.8}$$

while the coefficients Z_{ij} are known elements of the matrix evaluated from the basis functions (3.3) – (3.6) and their derivatives (3.11) – (3.14). The details are

given in the Appendix 2. Thus we can transform Eqs. (4.6), (4.7) to the infinite system of algebraic equations where X_j are unknown components of the vector $\mathbf{X}$ and Z_{ij} are known elements of the matrix $\hat{Z}$,

$$\hat{Z}\mathbf{X} = 4\pi\mathbf{I}, \tag{4.9}$$

where $\mathbf{I}$ is a column vector whose first component is 1 and all other components are equal to zero.

We can see from (4.8) and (2.20) that the drag force F is equal to X_1. For calculation of X_1 it is useful to separate from the matrix Z_{ij} the logarithmic term included in $U^1(a,\theta)$ (3.3), which we denote by K_0

$$K_0 = \ln 1/a^2 - C_0\,. \tag{4.10}$$

Thus we can present the elements of the matrix $\hat{Z}$ in the form

$$Z_{ij} = \frac{1}{2}K_0\delta_{1i}\delta_{1j} + W_{ij}\,, \tag{4.11}$$

while the elements of the matrix $\hat{W}$ are given in the Appendix 2.

The unknown X_1 can be written formally as

$$X_1 = \frac{4\pi|\hat{Z}^S|}{|\hat{Z}|}\,, \tag{4.12}$$

where the superscript S denotes a submatrix of the original matrix, corresponding to its first element (1,1).

It follows from (4.11) that

$$|\hat{Z}| = \frac{1}{2}K_0|\hat{Z}^S| + |\hat{W}|, \tag{4.13}$$

and

$$\hat{Z}^S = \hat{W}^S. \tag{4.14}$$

Inserting (4.13) – (4.14) to (4.12) we get

$$X_1 = \frac{8\pi}{K_0 + \beta}\,, \tag{4.15}$$

where

$$\beta = 2/Y_1\,, \tag{4.16}$$

while Y_1 is the first component of the vector $\mathbf{Y}$ which is the solution of the equation

$$\hat{W}\mathbf{Y} = \mathbf{I}. \tag{4.17}$$

According to (2.21), (4.8) and (4.15) we have

$$K(\varphi) = \frac{1}{X_1} = \frac{1}{8\pi}(K_0 + \beta). \tag{4.18}$$

5. Results

The infinite system of equations (4.17) was truncated to five equations and solved with matrix elements W_{ij} taken from the Appendix 2. The solution Y_1, which is the subject of our interest, has been obtained with the accuracy of $O(a^{10})$. Inserting Y_1 to (4.16) we get the following expression

$$\beta = \frac{2}{Y_1} = C_1 a^2 + C_2 a^4 + C_3 a^6 + C_4 a^8 + C_5 a^{10}, \tag{5.1}$$

where the coefficients C_n have the following numerical values:

$$\begin{aligned} C_1 &= 2\pi\,, \\ C_2 &= -\left(\frac{\pi^2}{2} + 1152\, B_4^2\right), \\ C_3 &= -1536\, A_4\, B_4\,, \\ C_4 &= 576\pi A_4 B_4 - 520 A_4^2\,, \\ C_5 &= 384\pi A_4^2\,. \end{aligned} \tag{5.2}$$

Numerical values of C_0, A_4 and B_4 are given in the Appendix 1.

The expressions $(5.2)_{1-3}$ are completely equivalent to those used by SANGANI and ACRIVOS [4] who calculated β to $O(a^6)$. The expression $(5.2)_4$ cannot be directly compared with the corresponding one of DRUMMOND and TAHIR [5] since they used a different calculation method than ours, and these expressions are of a quite different form. We shall come back to this question later and compare the numerical values of the coefficients with the literature data.

It is however more convenient to express the force F as a function of the volume fraction φ (1.1) which is related to the non-dimensional radius a as

$$\varphi = \pi a^2. \tag{5.3}$$

Inserting (5.3) into (5.1) and then combining (5.1), (4.10) and (4.18), we obtain the expression for $K(\varphi)$ presented in Sec. 1 (1.4), where $T^{(n)}(\varphi)$ is a power function expansion in φ (1.5). The drag force is related to $K(\varphi)$ according to (1.3)

$$F = \frac{1}{K(\varphi)}\,. \tag{5.4}$$

The initial coefficient of the expansion $T^{(n)}$ is

$$T_0 = \ln \pi - C_0 = -1.47633597. \tag{5.5}$$

The other coefficients are related to the coefficients C_i of (5.1) using expression (5.3)

$$T_i = \frac{C_i}{\pi^i}\,. \tag{5.6}$$

Table 1.

i	T_i
0	−1.47633597
1	2.00000000
2	−1.77428264
3	4.07770444
4	−4.84227403
5	2.44662267

The numerical values of all these coefficients $T_0 - T_5$ are collected in Table 1.

We can now compare the numerical values of the coefficients from Table 1 with the values obtained by the previous authors [4] and [5]. The coefficients of SANGANI and ACRIVOS [4], calculated up to four decimal places in frames of the approximation to $O(\varphi^3)$, i.e. for $i = 3$, are equivalent to the corresponding values from Table 1. The coefficients of DRUMMOND and TAHIR [5] ($i = 4$) are equal to those from Table 1 up to nine decimal places, although they were evaluated by different procedures, as it was previously indicated. It seems to confirm the conclusion that both the procedures are equivalent, and calculations in [5] and in the present paper were carried out correctly. The coefficient T_5 is a new value

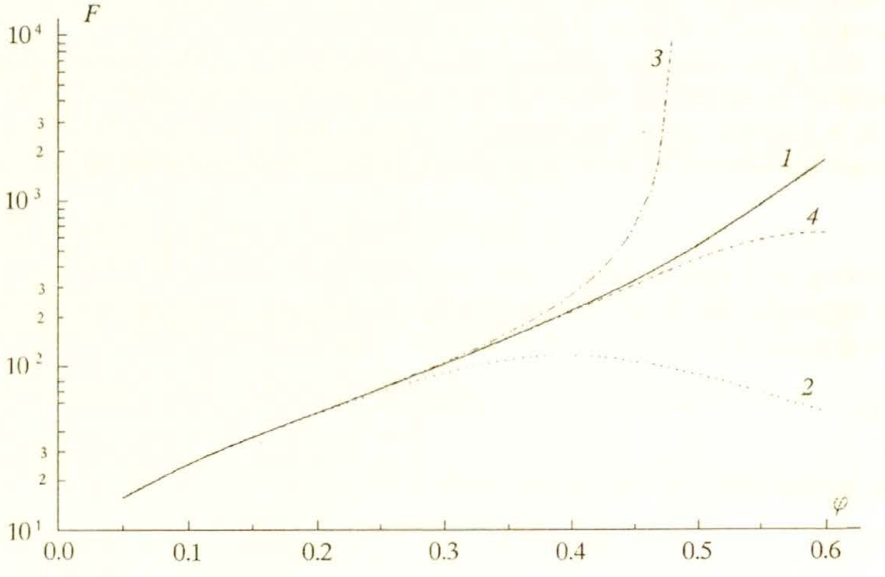

FIG. 2. The non-dimensional drag force F vs. the volume fraction φ. Comparison of the numerical reference data of SANGANI and ACRIVOS [6], (line 1) with various approximations. Line 2 – Sangani and Acrivos to $O(\varphi^3)$ [4], line 3 – Drummond and Tahir to $O(\varphi^4)$ [5], line 4 – the present results to $O(\varphi^5)$.

obtained in the frames of the present approximation corresponding to $O(\varphi^5)$. The results of [4] and [5] were collected and presented in the monograph of P. ADLER [7]. The literature data concerning approximations of higher order than that of DRUMMOND and TAHIR, of $O(\varphi^4)$, are not known to the author.

We calculated the drag force $F(\varphi)$ from (5.4) for approximations of various order using coefficients from Table 1. The results are presented in Fig. 2. The results of SANGANI and ACRIVOS [6] are here included as the reference data. They were obtained by numerical integration of the Stokes equations in a range of φ from 0.05 up to 0.75. It is almost the full range of φ since the maximum value of φ, which corresponds the case of touching cylinders, is $\varphi_{\max} = \pi/4 = 0.785398...$. We can see how the accuracy of calculations increases with the order of approximation. The expression (5.4) with the series expansion $T^{(3)}(\varphi)$ estimates the drag force within the error of about 2% at $\varphi = 0.2$. This error is kept with $T^{(4)}(\varphi)$ at $\varphi = 0.3$ and with $T^{(5)}(\varphi)$ at $\varphi = 0.4$. For $\varphi > 0.4$ all these expressions diverge and a new formula of better accuracy is needed.

6. Conclusions

A new functional basis derived in this paper enabled us to obtain expressions for matrix elements W_{ij} (see Appendix 2). The matrix is involved in Eq. (4.17) which is subjected to truncation of a chosen order, and its solution enters the formula (4.15) for a drag force. The explicit form of the expressions W_{ij} makes the calculations very tractable and allows to derive the solution using symbolic computations of *Mathematica* [10]. This procedure was here applied to the system of five equations and the results obtained to $O(\varphi^5)$ were of higher accuracy than the results of the previous authors. Extension of these calculations for larger systems of equations is straightforward.

Appendix 1

We present below numerical values of the first non-vanishing coefficients A_m and B_m as well as the constant C_0, which appear in (2.12) and (2.13). The coefficients were evaluated from the expressions derived in [4] and adopted here for the square array.

$$\text{(A1.1)} \qquad A_m = \frac{\alpha(2\pi)^m}{2^m(m)!}\left[\alpha^{-(m+1)}\sum_{\{n\}} E_m(|n|,\theta)\Phi_{m-1}\left(\frac{\pi}{\alpha}|n|^2\right) + \sum_{\{n\}} E_m\left(|n|,\theta\right)\Phi_0(\pi|n|^2\alpha)\right],$$

$$\text{(A1.2)} \qquad B_m = \frac{-\alpha^2(2\pi)^m}{\pi 2^{m+1} m!}\left[\alpha^{-(m+1)}\sum_{\{n\}} E_m(|n|,\theta)\,\Phi_{m-2}\left(\frac{\pi|n|^2}{\alpha}\right) + \sum_{\{n\}} E_m(|n|,\theta)\,\Phi_0(\pi|n|^2\alpha)\right],$$

$$\text{(A1.3)} \qquad C_0 = \gamma + \ln(\pi/\alpha) + \alpha - \sum_{\{n\}} \Phi_{-1}(\pi|n|^2/\alpha) - \alpha\sum_{\{n\}} \Phi_0(\pi|n|^2\alpha).$$

We used here the following notation:

$$\Phi_\nu(x) = \int_1^\infty e^{-xt} t^\nu\, dt$$

is the incomplete gamma function. In particular we have

$$\Phi_{-1}(x) = -Ei(-x) = -\gamma - \ln x + \sum_{n=1}^{\infty} \frac{x^n}{n\,n!}(-1)^{n+1},$$

where $\gamma = 0.5772156649...$ is the Euler constant. The functions $\Phi_\nu(x)$ of higher rank can be obtained from the recurrence formula

$$x\,\Phi_\nu = e^{-x} + \nu\Phi_{\nu-1}.$$

Arguments of the functions can be calculated by taking $|n| = (n_1^2 + n_2^2)^{1/2}$, a modulus of the vector $\mathbf{n} = \mathbf{n}'/l$, (2.1),

$$\theta = \begin{cases} \text{Arctan}\,(n_2/n_1), & n_1 \neq 0, \\ \pi - \text{sgn}\,(n_2)\pi/2, & n_1 = 0. \end{cases}$$

The parameter α which appears in (A1.1) – (A1.3) is a moderate constant involved in Evald's summation method, and is of a very small influence on the final result of calculations.

The constants evaluated from (A1.1) – (A1.3) are as follows:

$$\begin{aligned} A_4 &= 0.7878030005, & A_8 &= 0.5319716294, \\ A_{12} &= 0.3282374177, & A_{16} &= 0.2509809396, \\ B_4 &= -1.044856181\ 10^{-1}, & B_8 &= -4.031710210\ 10^{-2}, \\ B_{12} &= -1.469973805\ 10^{-2}, & B_{16} &= -8.399042320\ 10^{-3}, \\ C_0 &= 2.6210658523. \end{aligned}$$

The coefficients A_m are related to the Rayleigh sums S_m

$$A_m = \frac{S_m}{m},$$

which were evaluated up to five decimal places and presented in [16]. Numerical values of the coefficients B_m, as far as it is known to the present author, were not presented in literature except the coefficient B_4 [4], the value of which given there is however not correct.

Appendix 2

In this section the expressions are presented which enable us to calculate elements W_{ij} of the matrix $\hat{W}$. They have been derived from Eqs. (4.11), (4.5), and (3.11) – (3.14). The expressions W_{ij} are different for odd and even subscripts j corresponding to the matrix columns. To simplify the form of expression for odd j, we exclude here elements of the first column ($j = 1$).

Matrix elements W_{ij} for $j = 1$:

$$\text{(A2.1)} \qquad W_{i1} = \frac{\pi a^2}{2}\delta_{i1} + \frac{1}{4}(2 - \pi a^2)(\delta_{i3} - \delta_{i2}) + A_{i-1}a^{i-1} - (i+1)\left[\frac{1}{2}A_{i+1}a^2 + iB_{i+1}\right]a^{i-1} - (i+2)\left[\frac{1}{2}A_{i+2}a^2 + (i+1)B_{i+2}\right]a^i.$$

Matrix elements W_{ij} for other odd subscripts $j = 3,\ 5,\ 7, \ldots$:

$$\text{(A2.2)} \qquad W_{ij} = \frac{\pi}{2}\delta_{i1}\delta_{j3} + \frac{(j-1)!}{2a^{j-1}}(\delta_{i,j+2} - \delta_{i,j+1} + \delta_{i,j-1}) - \frac{(j-3)(j-2)!}{2a^{j-1}}\delta_{ij} - \frac{(j-3)(i+j-2)!}{2(i-1)!}A_{i+j-2}a^{i-1} - \frac{(j-1)(i+j-1)!}{2i!}A_{i+j-1}a^i - \frac{(i+j)!}{i!}\left[\frac{1}{2}A_{i+j}a^2 + iB_{i+j}\right]a^{i-1} - \frac{(i+j+1)!}{(i+1)!}\left[\frac{1}{2}A_{i+j+1}a^2 + (i+1)B_{i+j+1}\right]a^i.$$

Matrix elements W_{ij} for even subscripts $j = 2,\ 4,\ 6, \ldots$:

$$\text{(A2.3)} \qquad W_{ij} = -2\pi\delta_{i1}\delta_{j2} + \frac{2(j-1)!}{a^j}(\delta_{i,j+1} - \delta_{ij}) + \frac{2(i+j-1)!}{(i-1)!}A_{i+j-1}a^{i-1'} + \frac{2(i+j)!}{i!}A_{i+j}a^i.$$

References

1. J. HAPPEL, *Viscous flow relative to arrays of cylinders*, AIChE J., **5**, 174–177, 1959.
2. J. HAPPEL and H. BRENNER, *Low Reynolds number hydrodynamics*, Nordhoff International Publ., Leyden 1973.

3. H. HASIMOTO, *On the periodic fundamental solutions of the Stokes equations and their application to viscous flow past a cubic array of spheres*, J. Fluid Mech., **5**, 317–328, 1959.
4. A.S. SANGANI and A. ACRIVOS, *Slow flow through a periodic array of spheres*, Int. J. Multiphase Flow, **8**, 4, 343–360, 1982.
5. J.E. DRUMMOND and M.I. TAHIR, *Laminar viscous flow through regular arrays of parallel solid cylinders*, Int. J. Multiphase Flow, **10**, 5, 515–540, 1984.
6. A.S. SANGANI and A. ACRIVOS, *Slow flow past periodic arrays of cylinders with application to heat transfer*, Int. J. Multiphase Flow, **8**, 193–206, 1982.
7. P.M. ADLER, *Porous media*, Butterworth - Heinemann, 1992.
8. A. SZANIAWSKI and A. ZACHARA, *Penetration of spinning bath into the filament bundle* [in Polish], Polimery, **19**, 143, 1974.
9. A. ZACHARA, *How to estimate the flow characteristics in multifilament spinning*, ATI Fiber World, Part I, May, 13–17, and Part II, July, 52–60, 1987.
10. S. WOLFRAM, *Mathematica. A system for doing mathematics by computer*, Addison-Wesley Publ. Co., 1991.
11. B. CICHOCKI and B.U. FELDERHOF, *Periodic fundamental solution of the linear Navier–Stokes equations*, Physica, **A 159**, 19–27, 1989.
12. B. CICHOCKI and B.U. FELDERHOF, *Electrostatic interactions in two-dimensional Coulomb systems with periodic boundary conditions*, Physica, **A 158**, 706–722, 1989.
13. M. ZUZOVSKY and H. BRENNER, *Effective conductivities of composite materials composed of cubic arrangements of spherical particles embedded in an isotropic matrix*, ZAMP, **28**, 6, 979–992, 1977.
14. A.S. SANGANI and A. ACRIVOS, *The effective conductivity of a periodic array of spheres*, Proc. R. Soc. London, **A 386**, 263–275, 1983.
15. S. MAY, S. TOKARZEWSKI, A. ZACHARA and B. CICHOCKI, *Continued fraction representation for the effective conductivity coefficient of a regular two-component composite*, Int. J. Heat Mass Transfer, **17**, 2165–2173, 1994.
16. W.T. PERRINS, D.R. MCKENZIE and R.C. MCPHEDRAN, *Transport properties of regular arrays of cylinders*, Proc. R. Soc. London, **A 369**, 207–225, 1979.

POLISH ACADEMY OF SCIENCES
INSTITUTE OF FUNDAMENTAL TECHNOLOGICAL RESEARCH
e-mail: azachara@ippt.gov.pl

Received December 11, 1996; new version March 3, 1997.

Arch. Mech., 49, 5, pp. 847–863, Warszawa 1997

A yield-vertex modification of two-surface models of metal plasticity

H. PETRYK (WARSZAWA) and K. THERMANN (DORTMUND)

A PHENOMENOLOGICAL MODEL of elastoplastic behaviour of metal polycrystals is proposed which combines the features of micromechanical models with the classical flow theory of plasticity. The standard equation of a smooth loading surface describes here an outer limit surface which is never reached. The actual inner yield surface possesses a vertex at the current loading point, interpreted as the point of intersection of active yield surfaces for plastic flow mechanisms at a micro-level. The incremental response of the material at the vertex is defined in terms of the position of the current stress relative to the outer surface. In the computational version of the model, the effects of partial unloading and of physical and constraint hardening are represented by separate constitutive functions.

1. Introduction

THE CLASSICAL FLOW THEORY of time-independent plasticity is based on the assumption of a smooth yield surface and of a flow rule that prescribes the direction of the plastic part of strain-rate in the current state. On the contrary, micromechanical models of elastoplastic polycrystals invariably predict (cf. [1–4]) the formation of a vertex on the yield surface at the current loading point, as well as the existence of a whole range of admissible plastic strain-rate directions, the actual one being dependent on the current stress-rate.

Accordingly, two separate classes of time-independent phenomenological constitutive models for polycrystalline metals in the plastic range have been proposed: of the classical type and of the corner (or vertex) type. The former have a simpler structure in the incremental form and can in principle be constructed using the accumulated knowledge of experimental yield surfaces, while the latter are closer to micromechanical predictions and are expected to simulate better the material response after an abrupt change of the direction of straining. In calculations, the J_2 corner theory of plasticity formulated in [5] was most frequently used among relatively few phenomenological corner models proposed so far for metal polycrystals [6–14].

The purpose of this paper is to develop a phenomenological model of elastoplastic behaviour of metal polycrystals which combines the features of the above two classes of constitutive description. A *given* model of the classical type is modified in order to improve the consistency with general conclusions drawn from a micromechanical analysis [3]. Accordingly, the classical smooth yield surface plays here the role of an outer *extremal* (limit or target) surface which is

never reached, while the related inner yield surface (a boundary of the actual elastic domain) possesses a vertex at the current loading point. The extremal surface may be interpreted as a locus of *asymptotic* stress states approached when physical hardening is imagined to be suspended [3]. A considerable simplification in the proposed computational model, and also the difference in relation to the previous corner theories, is that the incremental response of the material is defined in terms of the position of the current stress point with respect to the *extremal* surface, independently of evolution of the latter, e.g. according to an isotropic/kinematic hardening law. In turn, the fundamental distinction from plasticity models with two or more loading surfaces [15–18] is that the inner surface is here no longer smooth. The derivation of the incremental law at the vertex of the inner yield surface also appears to be novel. In the first approximation, the simplest assumption of mutually independent internal mechanisms of plastic deformation at a micro-level has been explored.

2. Two-surface model of plasticity with a vertex on the inner yield surface

The small-strain formulation is given first; an extension to a geometrically exact description at finite strain will be given in Sec. 4. The standard yield condition of the Huber–Mises type:

$$\bar{\tau} = k, \qquad \bar{\tau} \equiv \left(\frac{1}{2}(\boldsymbol{\sigma}' - \boldsymbol{\alpha})\cdot(\boldsymbol{\sigma}' - \boldsymbol{\alpha})\right)^{1/2} \tag{2.1}$$

is adopted here as an equation of the *extremal* surface in the sense of HILL [3]. $\boldsymbol{\sigma}$ denotes the Cauchy stress([1]), $\boldsymbol{\sigma}'$ its deviator, $\boldsymbol{\alpha}$ denotes the deviatoric backstress and k is the yield shear stress. $\boldsymbol{\alpha}$ and k can vary with the plastic deformation according to prescribed rules which are left arbitrary here. (2.1) can be replaced by a more general equation of a smooth surface without changing the remaining part of this section. However, the specifications in the next section are only given for the form (2.1).

Contrary to classical elastoplasticity, the surface (2.1) is not allowed to be reached, and plastic deformation can take place when the current stress lies inside the surface (2.1). During plastic flow, the current stress point $\boldsymbol{\sigma}$ constitutes a vertex on the inner yield surface which is a boundary of the current elastic domain (Fig. 1 a). The vertex is interpreted as an intersection point of individual smooth yield surfaces (transformed to the *macroscopic* stress space) for a large or infinite number of internal plastic deformation mechanisms at a micro-level,

([1]) In the standard symbolic notation employed, bold-face letters denote second- or fourth-order tensors, a dot between two tensor symbols denotes full contraction, a tensor product is denoted by $\otimes$, and $|\dot{\boldsymbol{\sigma}}| = (\dot{\boldsymbol{\sigma}}\cdot\dot{\boldsymbol{\sigma}})^{1/2}$ denotes a norm of the stress-rate. Throughout the paper, only symmetric second-order tensors are used.

cf. [3]. Such a mechanism can be identified, for instance, with crystallographic slipping on some system in some grain in a polycrystalline aggregate. We restrict ourselves to examining the case when the matrix of hardening moduli, which represents mutual interactions between the mechanisms either within the same grain or in different grains, is symmetric and positive definite. A well known consequence is that the fourth-order tensor of macroscopic plastic compliances, denoted below by $\mathbf{M}^{\mathrm{p}}$, is diagonally symmetric and at least positive semi-definite.

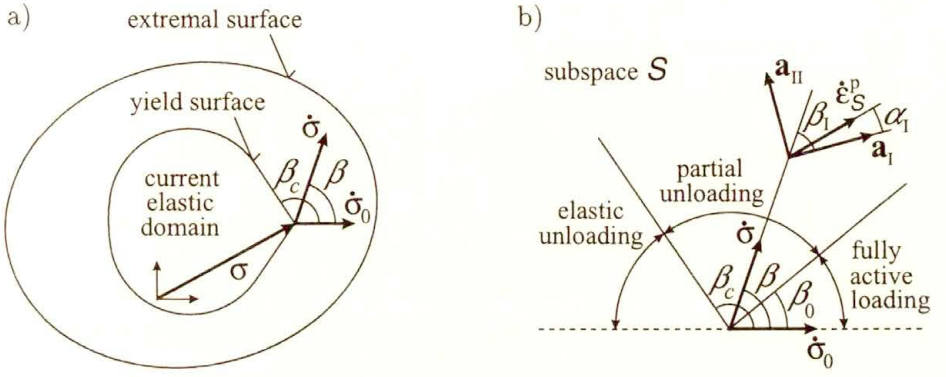

FIG. 1. (a) Two-surface model of plasticity where the inner yield surface has a vertex at the current loading point and the outer extremal surface is smooth. (b) Overall structure of the incremental plastic constitutive law at the yield-vertex, within a two-dimensional subspace $\mathcal{S}$.

As long as unloading is absent or partial so that the elastic domain is not penetrated, a phenomenological constitutive relationship at the vertex may be defined without specifying the entire form of the elastic domain but merely the directions tangent to the corner of the elastic domain at $\boldsymbol{\sigma}'$. In a given state of the material, a macroscopic plastic strain-rate $\dot{\boldsymbol{\varepsilon}}^{\mathrm{p}}$ is assumed to be a single-valued, positively homogeneous of degree one, continuous and (except at $\dot{\boldsymbol{\sigma}} = \mathbf{0}$) at least piecewise-continuously differentiable function of a macroscopic stress-rate $\dot{\boldsymbol{\sigma}}$. It is emphasized that a dot over a symbol denotes the *forward* rate. We will examine that function restricted to a two-dimensional subspace $\mathcal{S}$ of the Euclidean space of symmetric second-order tensors, and denote by $\dot{\boldsymbol{\varepsilon}}^{\mathrm{p}}_{\mathcal{S}}$ the orthogonal projection $\mathbf{P}_{\mathcal{S}} \cdot \dot{\boldsymbol{\varepsilon}}^{\mathrm{p}}$ of $\dot{\boldsymbol{\varepsilon}}^{\mathrm{p}}$ on $\mathcal{S}$[2]. By the Euler theorem, the homogeneous incremental plastic law can be written down as

$$
\begin{aligned}
&\dot{\boldsymbol{\varepsilon}}^{\mathrm{p}} = \mathbf{M}^{\mathrm{p}}(\dot{\boldsymbol{\sigma}}) \cdot \dot{\boldsymbol{\sigma}}\,, \qquad \mathbf{M}^{\mathrm{p}} = \frac{\partial \dot{\boldsymbol{\varepsilon}}^{\mathrm{p}}}{\partial \dot{\boldsymbol{\sigma}}}\,, \\
&\dot{\boldsymbol{\varepsilon}}^{\mathrm{p}}_{\mathcal{S}} = \mathbf{M}^{\mathrm{p}}_{\mathcal{S}}(\dot{\boldsymbol{\sigma}}) \cdot \dot{\boldsymbol{\sigma}}\,, \qquad \mathbf{M}^{\mathrm{p}}_{\mathcal{S}} = \mathbf{P}_{\mathcal{S}} \mathbf{M}^{\mathrm{p}} \mathbf{P}_{\mathcal{S}}\,, \qquad \text{if} \quad \dot{\boldsymbol{\sigma}} \in \mathcal{S}\,.
\end{aligned} \tag{2.2}
$$

The diagonal symmetry of $\mathbf{M}^{\mathrm{p}}$ implies that $\mathbf{M}^{\mathrm{p}}_{\mathcal{S}}$ is a diagonally symmetric operator within $\mathcal{S}$. From the spectral decomposition theorem for fourth-order

[2] If $(\mathbf{a},\mathbf{b})$ with $\mathbf{a}\cdot\mathbf{b} = 0$, $|\mathbf{a}| = |\mathbf{b}| = 1$ is an orthonormal basis in $\mathcal{S}$ then $\mathbf{P}_{\mathcal{S}} = \mathbf{a}\otimes\mathbf{a} + \mathbf{b}\otimes\mathbf{b}$.

diagonally symmetric tensors (cf. [19]), we obtain that $\mathbf{M}^{\mathrm{p}}_{\mathcal{S}}$, henceforth assumed to be positive definite, has the following representation

$$\begin{aligned} &\mathbf{M}^{\mathrm{p}}_{\mathcal{S}} = M_{\mathrm{I}}\mathbf{a}_{\mathrm{I}} \otimes \mathbf{a}_{\mathrm{I}} + M_{\mathrm{II}}\mathbf{a}_{\mathrm{II}} \otimes \mathbf{a}_{\mathrm{II}}\,, \\ &\mathbf{a}_{\mathrm{I}}\,,\ \mathbf{a}_{\mathrm{II}} \in \mathcal{S}\,, \qquad \mathbf{a}_{\mathrm{I}} \cdot \mathbf{a}_{\mathrm{II}} = 0\,, \qquad |\mathbf{a}_{\mathrm{I}}| = |\mathbf{a}_{\mathrm{II}}| = 1\,, \end{aligned} \tag{2.3}$$

with principal directions $\mathbf{a}_{\mathrm{I}}$, $\mathbf{a}_{\mathrm{II}}$ and positive principal compliances M_{I}, M_{II}. Let $\dot{\boldsymbol{\sigma}}_0 \neq \mathbf{0}$ define a distinctive direction within $\mathcal{S}$, and β denote an angle of inclination of a nonzero $\dot{\boldsymbol{\sigma}}$ to $\dot{\boldsymbol{\sigma}}_0$,

$$\cos\beta = \frac{\dot{\boldsymbol{\sigma}} \cdot \mathbf{a}_0}{|\dot{\boldsymbol{\sigma}}|}\,, \qquad \mathbf{a}_0 = \frac{\dot{\boldsymbol{\sigma}}_0}{|\dot{\boldsymbol{\sigma}}_0|}\,. \tag{2.4}$$

The considerations below are limited to $\dot{\boldsymbol{\sigma}} \in \mathcal{S}$ lying on one side of $\dot{\boldsymbol{\sigma}}_0$ where $\beta \in [0, \pi]$; the other side can be examined analogously.

Each quantity in (2.3) depends in general on β. An admissible function $\mathbf{M}^{\mathrm{p}}_{\mathcal{S}}(\beta)$, if discontinuous, must ensure the continuity of $\dot{\boldsymbol{\varepsilon}}^{\mathrm{p}}_{\mathcal{S}}(\dot{\boldsymbol{\sigma}})$, and at every differentiability point it must satisfy the additional condition

$$\frac{d\mathbf{M}^{\mathrm{p}}_{\mathcal{S}}}{d\beta} \cdot \dot{\boldsymbol{\sigma}} = \mathbf{0} \tag{2.5}$$

obtained by differentiation of (2.2). On substituting (2.3), the condition (2.5) is easily transformed to

$$\begin{aligned} \frac{dM_{\mathrm{I}}}{d\beta} \cos\beta_{\mathrm{I}} &= \left(\frac{d\beta_{\mathrm{I}}}{d\beta} - 1\right)(M_{\mathrm{I}} - M_{\mathrm{II}}) \sin\beta_{\mathrm{I}}\,, \\ \frac{dM_{\mathrm{II}}}{d\beta} \sin\beta_{\mathrm{I}} &= \left(\frac{d\beta_{\mathrm{I}}}{d\beta} - 1\right)(M_{\mathrm{I}} - M_{\mathrm{II}}) \cos\beta_{\mathrm{I}}\,, \end{aligned} \tag{2.6}$$

where β_{I} is an angle between $\dot{\boldsymbol{\sigma}}$ and $\mathbf{a}_{\mathrm{I}}$ with

$$\cos\beta_{\mathrm{I}} = \frac{\dot{\boldsymbol{\sigma}} \cdot \mathbf{a}_{\mathrm{I}}}{|\dot{\boldsymbol{\sigma}}|}\,, \qquad \sin\beta_{\mathrm{I}} = \frac{\dot{\boldsymbol{\sigma}} \cdot \mathbf{a}_{\mathrm{II}}}{|\dot{\boldsymbol{\sigma}}|}\,. \tag{2.7}$$

From (2.3) we also find that β_{I} is connected with an angle α_{I} between $\dot{\boldsymbol{\varepsilon}}^{\mathrm{p}}_{\mathcal{S}}$ and $\mathbf{a}_{\mathrm{I}}$ through

$$\tan\alpha_{\mathrm{I}} = \frac{M_{\mathrm{II}}}{M_{\mathrm{I}}} \tan\beta_{\mathrm{I}}\,. \tag{2.8}$$

It can be seen that if *one* scalar function from the triple $\{M_{\mathrm{I}}(\beta), M_{\mathrm{II}}(\beta), \beta_{\mathrm{I}}(\beta)\}$ defining $\mathbf{M}^{\mathrm{p}}_{\mathcal{S}}(\beta)$ is prescribed then the two other have to satisfy two differential

equations (2.6), with appropriate boundary conditions. That restriction is related to the existence of a stress-rate potential $\Psi^{\mathrm{P}}(\dot{\boldsymbol{\sigma}})$,

$$\dot{\boldsymbol{\varepsilon}}^{\mathrm{P}} = \frac{\partial \Psi^{\mathrm{P}}}{\partial \dot{\boldsymbol{\sigma}}}, \qquad \Psi^{\mathrm{P}} = \frac{1}{2}\dot{\boldsymbol{\varepsilon}}^{\mathrm{P}} \cdot \dot{\boldsymbol{\sigma}} \qquad \text{and} \qquad \Psi^{\mathrm{P}} = \frac{1}{2}\dot{\boldsymbol{\sigma}} \cdot \mathbf{M}^{\mathrm{P}}_{\mathcal{S}} \cdot \dot{\boldsymbol{\sigma}} \quad \text{if} \quad \dot{\boldsymbol{\sigma}} \in \mathcal{S}, \tag{2.9}$$

which is a consequence of the diagonal symmetry of $\mathbf{M}^{\mathrm{P}}$. If more than one scalar constitutive function in a subspace $\mathcal{S}$ is assumed, as in [12, 14], then the potentiality property is generally lost.

Further considerations are restricted to the case $0 < \beta_{\mathrm{I}} < \pi/2$ illustrated in Fig. 1 b. Moreover, we will assume that $M_{\mathrm{I-II}} \equiv M_{\mathrm{I}} - M_{\mathrm{II}} > 0$ and that $0 < d\beta_{\mathrm{I}}/d\beta \leq 1$. Then (2.6) holds if and only if either

$$\frac{d\beta_{\mathrm{I}}}{d\beta} = 1, \qquad \frac{dM_{\mathrm{I}}}{d\beta} = 0, \qquad \frac{dM_{\mathrm{II}}}{d\beta} = 0, \tag{2.10}$$

or

$$\begin{gathered} \frac{d\beta}{d\beta_{\mathrm{I}}} - 1 \equiv r \in (0, \infty), \\ \frac{dM_{\mathrm{I}}}{d\beta_{\mathrm{I}}} = -rM_{\mathrm{I-II}} \tan\beta_{\mathrm{I}}, \qquad \frac{dM_{\mathrm{II}}}{d\beta_{\mathrm{I}}} = -rM_{\mathrm{I-II}} \cot\beta_{\mathrm{I}}. \end{gathered} \tag{2.11}$$

In the former case $\mathbf{M}^{\mathrm{P}}_{\mathcal{S}}(\beta) = \text{const}$. In the second case, the following differential equation for $M_{\mathrm{I-II}}$ is obtained:

$$\frac{dM_{\mathrm{I-II}}}{d\beta_{\mathrm{I}}} = 2rM_{\mathrm{I-II}} \cot 2\beta_{\mathrm{I}}. \tag{2.12}$$

This defines a class of constitutive relationships corresponding to different functions $r(\beta_{\mathrm{I}})$. A particular solution

$$M_{\mathrm{I-II}} = 2\overline{M} \sin^{r} 2\beta_{\mathrm{I}} \tag{2.13}$$

is obtained for r independent of β_{I}, with $\overline{M} > 0$ being a positive integration constant.

Suppose that there exists a stress-rate $\dot{\boldsymbol{\sigma}}_0$ codirectional with the principal direction of $\mathbf{M}^{\mathrm{P}}(\dot{\boldsymbol{\sigma}}_0)$ associated with the *maximum* principal plastic compliance; in particular, $\dot{\boldsymbol{\sigma}}_0$ is then codirectional with $\dot{\boldsymbol{\varepsilon}}^{\mathrm{P}}(\dot{\boldsymbol{\sigma}}_0)$. To cover all directions in the stress-rate space, it suffices to consider the two-dimensional subspaces $\mathcal{S}$ that contain $\dot{\boldsymbol{\sigma}}_0$ as the common distinctive stress-rate used to determine the angle β from (2.4). If $\mathbf{M}^{\mathrm{P}}_{\mathcal{S}}$ varies continuously with β then from (2.10) and (2.11) it follows that the principal plastic compliances $M_{\mathrm{I}}(\beta)$, $M_{\mathrm{II}}(\beta)$ are non-increasing functions which attain maximum values at $\beta = \beta_{\mathrm{I}} = 0$. If (2.10) holds for $\beta < \beta_0$, say, then that interval of β can be identified with the angular range of fully active loading

in the current state, while an interval of validity of (2.11), $\beta_0 < \beta < \beta_c$ say, can be identified with the transitory range of partial unloading, cf. [3]. We shall assume that $(-\dot{\boldsymbol{\sigma}}_0)$ lies within the current elastic unloading cone corresponding to $\beta_c < \beta \leq \pi$, cf. Fig. 1 b.

To *derive* a constitutive function in the transitory range rather than to define it arbitrarily, we propose the following simplifying procedure. The effect of physical hardening within the grains in a polycrystalline aggregate is included into a hardening rule for the *extremal* surface, e.g. into an evolution rule for $\boldsymbol{\alpha}$ and k in (2.1). The interaction (in the stress-space formulation) between micro-mechanisms of plastic deformation in different grains is imagined to be represented, at least partially, by variations of $\overline{M}$ inside the extremal surface (see below). Finally, a phenomenological relationship between the plastic strain-rate and stress-rate at the vertex on the inner yield surface, which includes the effect of partial unloading, is constructed as for mutually independent mechanisms of plastic deformation. For comparison, in the well-known theories of BATDORF and BUDIANSKY [1] or KOITER [6], the effects of interaction between the plastic deformation mechanisms were fully neglected, while here they are taken into account in an indirect manner.

Under that assumption, the range of fully active loading becomes a prolongation of the elastic unloading range, so that $\beta_0 = \pi - \beta_c$. Both ranges suffer a *right-hand* discontinuous change in time if $\dot{\boldsymbol{\sigma}}$, the current right-hand rate of stress, induces partial unloading. Then, $\dot{\boldsymbol{\sigma}}$ constitutes one limiting ray of the *new* angular range of fully active loading([3]), while the second limiting ray of that range is regarded as varying continuously in time. The key simplifying assumption is that $\mathbf{a}_{\mathrm{I}}(\beta)$ corresponding to any direction of loading (total or partial) within $\mathcal{S}$ always bisects *the right-hand limit* (in time) of the angular range of elastic unloading. It follows that in the range of partial unloading, $\mathbf{a}_{\mathrm{I}}$ rotates continuously with increasing β so that (cf. (2.13))

$$r = 1, \qquad M_{\mathrm{I-II}} = 2\overline{M} \sin 2\beta_{\mathrm{I}}, \tag{2.14}$$

with a parameter $\overline{M}$ independent of β_{I}. It may be noted that (2.14) gives $d(M_{\mathrm{I}} + M_{\mathrm{II}})/d\beta_{\mathrm{I}} = -4\overline{M}$. To obtain a smooth transition to elastic unloading, we assume that M_{I} tends to zero as $\beta \to \beta_c$. On using the condition of continuity of $\dot{\boldsymbol{\varepsilon}}^{\mathrm{p}}_{\mathcal{S}}(\dot{\boldsymbol{\sigma}})$, we obtain the following solution to (2.11) in the transition range:

$$\begin{aligned} &\beta \in [\beta_0, \beta_c], \qquad \beta_c = \pi - \beta_0, \qquad \beta_{\mathrm{I}} = \frac{1}{2}(\pi - \beta_c + \beta) = \frac{1}{2}(\beta_0 + \beta), \\ &M_{\mathrm{I}} = (\pi - 2\beta_{\mathrm{I}} + \sin 2\beta_{\mathrm{I}})\overline{M}, \qquad M_{\mathrm{II}} = (\pi - 2\beta_{\mathrm{I}} - \sin 2\beta_{\mathrm{I}})\overline{M} \end{aligned} \tag{2.15}$$

([3]) Fully active loading means that each plastic deformation mechanism that is potentially active (i.e. stressed to its yield point in the current state) is actually active. After partial unloading, some of previously potentially active mechanisms become inactive, so that the angular range of fully active loading increases discontinuously. For infinitely many mechanisms, $\dot{\boldsymbol{\sigma}}$ corresponding to partial unloading will generally induce neutral loading for some mechanism(s), i.e. will constitute the limiting ray as stated above; cf. also [20].

and in the range of fully active loading:

$$
\begin{aligned}
&\beta \in [0, \beta_0], && \beta_{\mathrm{I}} = \beta, \\
&M_{\mathrm{I}} = (\pi - 2\beta_0 + \sin 2\beta_0)\overline{M}, && M_{\mathrm{II}} = (\pi - 2\beta_0 - \sin 2\beta_0)\overline{M}.
\end{aligned} \tag{2.16}
$$

For convenience, the basic relationship between M_{I}, M_{II} and β_0 or β_{I} for fully or partially active loading, respectively, is visualized in Fig. 2.

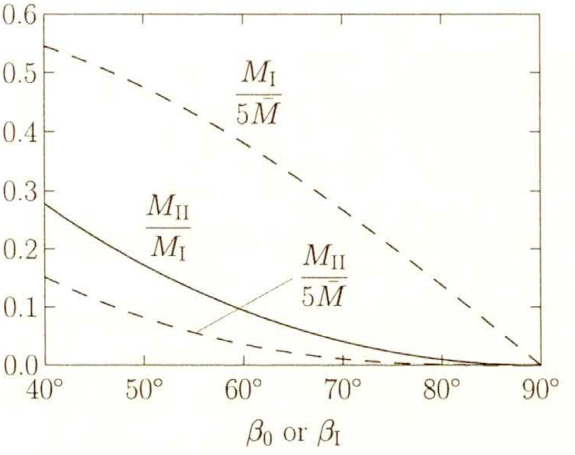

FIG. 2. Principal plastic compliance ratio, $M_{\mathrm{II}}/M_{\mathrm{I}}$, as a function of β_0 for fully active loading or of β_{I} after partial unloading. Broken lines show the respective variations of the principal plastic compliances scaled down by $5\overline{M}$.

From elementary geometry it follows that $\dot{\boldsymbol{\varepsilon}}^{\mathrm{p}}_{\mathcal{S}}$ makes an angle $(\pi - \beta_{\mathrm{I}} - \alpha_{\mathrm{I}})$ or $(\pi - \beta_0 - \alpha_{\mathrm{I}})$ in the range of partially or fully active loading, respectively, with the limiting ray of the elastic unloading range in the respective subspace $\mathcal{S}$, cf. Fig. 1 b. It can be checked by using (2.8), (2.15) and (2.16) that this angle decreases monotonically from β_c to $\pi/2$ as β increases from zero to β_c. Hence, $\dot{\boldsymbol{\varepsilon}}^{\mathrm{p}}_{\mathcal{S}}$ lies within the range generated by the outward normals to the limiting rays of the elastic unloading range in $\mathcal{S}$, in agreement with the generalized normality rule at a yield-surface vertex.

Once the elastic unloading cone in $\dot{\boldsymbol{\sigma}}$-space has been specified in the current state, then the elastic unloading range within each $\mathcal{S}$ is known along with its internal angle $2\beta_0$, external angle $2\beta_c$ and outward bisector $\mathbf{a}_0$. Finally, the constitutive relationship between $\dot{\boldsymbol{\varepsilon}}^{\mathrm{p}}$ and $\dot{\boldsymbol{\sigma}}$ is fully determined, after substituting (2.15) and (2.16) into (2.3) and next into (2.9), by the geometry of the current elastic unloading cone and by the scalar parameter $\overline{M}$ dependent on the material state and on $\mathcal{S}$. Of course, when performing the partial differentiation in (2.9), the dependence of the parameters $\overline{M}$ and β_0 on the subspace $\mathcal{S}$ must be taken into account in general. That dependence is absent from the simplest version of the model discussed in the next section.

3. A simple computational version of the model

Suppose first that the current state of the material has been reached by proportional loading from a virgin unstressed state with $\boldsymbol{\alpha} = \mathbf{0}$; this condition will later be relaxed. Under the usual assumption of an incompressible and pressure-insensitive plastic flow, the following specifications (cf. Fig. 3) are made in the incremental constitutive law from Sec. 2:

(i) The deviatoric stress-rate space and its two-dimensional subspace $\mathcal{S}'$ are substituted in place of $\dot{\boldsymbol{\sigma}}$–space and $\mathcal{S}$.

(ii) The elastic unloading cone has a symmetry axis codirectional with $(\boldsymbol{\sigma}' - \boldsymbol{\alpha})$, and β is defined by (2.4) with

$$\mathbf{a}_0 = \frac{\boldsymbol{\sigma}' - \boldsymbol{\alpha}}{|\boldsymbol{\sigma}' - \boldsymbol{\alpha}|}. \tag{3.1}$$

(iii) The parameters β_0 and $\overline{M}$ are independent of $\mathcal{S}'$ and depend on the placement of $\boldsymbol{\sigma}'$ relative to the extremal surface.

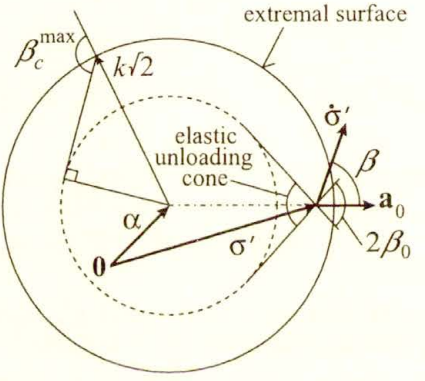

FIG. 3. Construction of the elastic unloading cone in the computational version of the two-surface model.

The relationship between the plastic strain-rate and stress-rate at the vertex $\boldsymbol{\sigma}'$ on the inner yield surface becomes fully defined by two state-dependent scalar parameters β_0 and $\overline{M}$ being functions of the current values of $\boldsymbol{\alpha}$, k and $\boldsymbol{\sigma}'$. In the potential form, the incremental plastic constitutive law is given by

$$\dot{\boldsymbol{\varepsilon}}^{\mathrm{p}} = \frac{\partial \Psi^{\mathrm{p}}}{\partial \dot{\boldsymbol{\sigma}}}, \qquad \Psi^{\mathrm{p}} = \frac{1}{2} F(\beta) |\dot{\boldsymbol{\sigma}}'|^2, \tag{3.2}$$

$$F(\beta) = \overline{M} \cdot \begin{cases} \pi - 2\beta_0 + \sin 2\beta_0 \cos 2\beta & \text{for } 0 \le \beta \le \beta_0 \quad \text{(total loading)}, \\ \pi - (\beta + \beta_0) + \dfrac{1}{2} \sin 2(\beta + \beta_0) & \text{for } \beta_0 \le \beta \le \pi - \beta_0 \quad \text{(partial unloading)}, \\ 0 & \text{for } \pi - \beta_0 \le \beta \le \pi \quad \text{(total unloading)}. \end{cases} \tag{3.3}$$

In an explicit form, it reads([4])

$$
\begin{aligned}
\dot{\boldsymbol{\varepsilon}}^{\mathrm{p}} &= \overline{M}(A(\beta)|\dot{\boldsymbol{\sigma}}'|\mathbf{a}_0 + B(\beta)\dot{\boldsymbol{\sigma}}'), \\
A(\beta) &= 2\cos\beta\sin 2\beta_0\,, \\
B &= \pi - 2\beta_0 - \sin 2\beta_0 \qquad \text{for } \beta \le \beta_0\,, \\
A(\beta) &= \sin^2(\beta+\beta_0)/\sin\beta\,, \\
B(\beta) &= \pi - (\beta+\beta_0) - \sin\beta_0\sin(\beta+\beta_0)/\sin\beta \qquad \text{for } \beta_0 \le \beta \le \pi - \beta_0\,, \\
A &= 0, \\
B &= 0 \qquad \text{for } \pi - \beta_0 \le \beta \le \pi\,.
\end{aligned}
\tag{3.4}
$$

This can be complemented by the standard equation for the elastic part of strain-rate, viz.

$$
\dot{\boldsymbol{\varepsilon}} = \dot{\boldsymbol{\varepsilon}}^{\mathrm{e}} + \dot{\boldsymbol{\varepsilon}}^{\mathrm{p}}, \qquad \dot{\boldsymbol{\varepsilon}}^{\mathrm{e}} = \mathbf{M}^{\mathrm{e}}\cdot\dot{\boldsymbol{\sigma}}\,,
\tag{3.5}
$$

with $\mathbf{M}^{\mathrm{e}}$ being the compliance tensor of the linear theory of isotropic elasticity.

Finally, specification of the parameters β_0 and $\overline{M}$ and of evolution equations for k and $\boldsymbol{\alpha}$ completes the set of constitutive equations of the model. The evolution rule for the extremal surface is left arbitrary here since the equations are proposed as a refinement of a given model of the classical type. β_0 and $\overline{M}$ are assumed to depend on the relative distance of the current deviatoric stress $\boldsymbol{\sigma}'$ from the extremal surface. For instance, they can be expressed in terms of the ratio $\bar{\tau}/k$ as

$$
\beta_0 = \arcsin\frac{k\sin\beta_c^{\max}}{\bar{\tau}}\,, \qquad \frac{\bar{\tau}}{k} \in (\sin\beta_c^{\max}, 1), \qquad \beta_c^{\max} = \text{const} \in \left(\frac{\pi}{2}, \pi\right),
\tag{3.6}
$$

$$
\overline{M}(\beta_0) = \frac{1}{E}\,\frac{2}{1 - \chi(\beta_0)/\chi(\pi - \beta_c^{\max})}\,, \qquad \chi(\beta_0) = \frac{\pi - 2\beta_0 - \sin 2\beta_0}{\sin\beta_0}\,,
\tag{3.7}
$$

where $\beta_c^{\max}$ is a material constant and E is the elastic Young modulus. In comparison with the standard elastoplastic model, that specification of the yield-vertex modification requires only one additional material constant $\beta_c^{\max}$. Formula (3.6) means that generators of the elastic unloading cone are tangent to a sphere with centre $\boldsymbol{\alpha}$ and radius $k\sqrt{2}\sin\beta_c^{\max}$ in $\boldsymbol{\sigma}'$-space, cf. Fig. 3. During proportional loading in the range $\bar{\tau}/k \le \sin\beta_c^{\max}$, we substitute $\overline{M} = 0$ with β_0 undefined. On the other hand, the inner sphere shown in Fig. 3 by a broken line is only used to

([4]) A closer inspection of Eq. (3.4) shows a resemblance to the equation obtained in [9] in a different way and without considering its potential form. The present equation is more general since $\overline{M}$ is a function of state rather than a constant. The distinction is essential since constant $\overline{M}$ would be inconsistent with the existence of a fixed unattainable extremal surface when physical hardening within the grains is suspended. To have consistency, $1/\overline{M}$ must tend to zero when a fixed extremal surface is approached.

define the current elastic unloading cone at $\boldsymbol{\sigma}'$ and need not be identified with the boundary of the current elastic domain.

The function (3.7) has been chosen to fit approximately the tensile stress/plastic strain curves calculated for micromechanical models of a polycrystal [4]; the approximation will further be discussed in the next section. Of course, one could also take another function $\overline{M}$ in place of (3.7) to obtain a better fit of micromechanical results. The present choice was influenced by the convenient possibility of determining analytically the plastic strain under proportional loading from the unstressed virgin state if the extremal surface is fixed. From (3.6) with fixed k and from (2.16) we obtain the interesting formula

$$\frac{M_{\mathrm{I}}}{\overline{M}} d\bar{\tau} = d\left(\frac{M_{\mathrm{II}}}{\overline{M}}\,\bar{\tau}\right). \tag{3.8}$$

On using (3.6) and the definition of χ in (3.7), the plastic strain under proportional loading is thus given by

$$\boldsymbol{\varepsilon}^{\mathrm{p}} = \mathbf{a}_0\sqrt{2}\int_0^{\bar{\tau}} M_{\mathrm{I}}\, d\bar{\tau} = \mathbf{a}_0 k\sqrt{2}\sin\beta_c^{\max}\int_0^{\chi}\overline{M}\, d\chi\,. \tag{3.9}$$

This motivates the use of $\overline{M}$ expressed in terms of χ. The form $(3.7)_1$ is one of the simplest which ensure $\overline{M}\to\infty$ as $\bar{\tau}$ approaches a fixed k; after integration it yields

$$\boldsymbol{\varepsilon}^{\mathrm{p}} = \mathbf{a}_0\frac{2k\sqrt{2}}{E}\,(2\beta_c^{\max} - \pi + \sin 2\beta_c^{\max})\ln\frac{1}{1-\chi(\beta_0)/\chi(\pi-\beta_c^{\max})} \tag{3.10}$$

with β_0 determined from (3.6) for a fixed extremal surface.

In turn, from (3.9), (3.6) and the definition of χ we obtain

$$\boldsymbol{\varepsilon}^{\mathrm{p}} = M_{\mathrm{II}}\boldsymbol{\sigma}' \qquad \text{if } \overline{M} = \mathrm{const}\,. \tag{3.11}$$

This is precisely the formula of the classical *deformation* theory of plasticity where the proportionality factor between the plastic strain and stress deviators, being a function of $|\boldsymbol{\sigma}'|$, serves as the principal plastic compliance for $\dot{\boldsymbol{\sigma}}'$ orthogonal to $\boldsymbol{\sigma}'$. In view of a fixed relationship between M_{II} and $|\boldsymbol{\sigma}'|$ implied by (2.16) and (2.6), the variant of the deformation theory obtained here for fully active loading at constant $\overline{M}$ is very special and, moreover, inconsistent with the assumption of a fixed extremal surface. The possibility to satisfy Eq. (3.11) *approximately* for the extremal surface subject to a power hardening law will be discussed in Sec. 5.

The assumption (ii) above, and hence the final specification of the incremental plastic constitutive law, cannot be regarded as appropriate for all stress-rates in all states, e.g. in the current state just after partial unloading. Fortunately, to

calculate the material response along some loading path, it usually suffices to know the function $\dot{\boldsymbol{\varepsilon}}^{\mathrm{p}}(\dot{\boldsymbol{\sigma}})$ only in the vicinity of the *actual* stress-rate direction. For a class of non-proportional loading paths, the actual plastic strain-rate and plastic compliances can be calculated from (3.3), or directly from (3.4) and (2.15) or (2.16), respectively, still by using the specifications (i) – (iii) in the following cases:

(A) for every stress-rate in any state $\mathcal{P}_{\mathrm{A}}$ reached from a virgin state $\boldsymbol{\sigma}' = \mathbf{0}$, $\boldsymbol{\alpha} = \mathbf{0}$ along a plastic straining path without unloading (i.e. with $\beta \leq \beta_0$ in the range $\bar{\tau}/k > \sin\beta_c^{\max}$, except in the current state $\mathcal{P}_{\mathrm{A}}$ itself);

(B) along any path starting from a state $\mathcal{P}_{\mathrm{A}}$ and such that $\boldsymbol{\sigma}'$ and $\boldsymbol{\alpha}$ are being contained in a fixed two-dimensional deviatoric subspace and β is preserving its sense, nondecreasing (but possibly discontinuous) in time and satisfying $\beta < \beta_c$;

(C) along any straight path in the deviatoric stress space starting from $\mathcal{P}_{\mathrm{A}}$ and satisfying $\beta < \beta_c$;

(D) along any smooth path of a sufficiently small curvature in the deviatoric stress space, starting from $\mathcal{P}_{\mathrm{A}}$ and satisfying $\beta < \beta_c$.

This can be inferred from the assumptions under which the equations of the computational model have been derived. The common condition in the above list is that no elastic unloading takes place so that the current stress does not leave the vertex on the inner yield surface. This condition could be weakened by allowing for elastic unloading not followed by reloading, and also for certain cases of reloading. The restriction on the path curvature in point (D) is imprecise since it is difficult to specify the circumstances in which the influence of partial unloading on the *actual* tangent compliances along a curved path may still be neglected. A curvature of the order $1/k$ may perhaps be regarded as being "sufficiently small" in this respect.

4. Extension to finite strain

The extension of the constitutive equations from the preceding sections to plastic strain of arbitrary magnitude can be done in the following way, regarded nowadays as standard. With the volume changes assumed to be purely elastic and small, $\boldsymbol{\sigma}$ is replaced by the Kirchhoff stress $\boldsymbol{\tau} = J\boldsymbol{\sigma}$ where J is the current-to-reference volume ratio, while the stress-rate $\dot{\boldsymbol{\sigma}}$ is replaced by $\overset{\nabla}{\boldsymbol{\tau}}$, the Zaremba – Jaumann flux (corotational with the material spin) of $\boldsymbol{\tau}$. An exact elastic constitutive law can be defined as an isotropic linear relationship between the back-rotated Kirchhoff stress and logarithmic elastic strain relative to an unstressed state. Accordingly, the elastic compliances of the linear theory of isotropic elasticity undergo a slight modification, cf. [21]. $\dot{\boldsymbol{\varepsilon}}$ is identified with the Eulerian strain-rate $\mathbf{D}$ while its plastic part $\mathbf{D}^{\mathrm{p}}$ is defined by (3.5) and determined from (3.2) or (3.4) after making the substitutions indicated. A finite strain

problem can be analysed in the usual step-by-step manner if, in every traversed state, $\mathbf{D}$ as an invertible function of $\overset{\nabla}{\boldsymbol{\tau}}$ is specified at least in the vicinity of the actual incremental solution.

Questions resulting from the multiplicative decomposition of the deformation gradient and concerning the effect of plastic rotations on the kinematic hardening law need not be addressed here since they do not affect the proposed modification of a *given* classical plasticity model.

5. Illustrative examples

Figures 4 – 7 illustrate the model behaviour during proportional loading from an unstressed virgin state, by the representative example of uniaxial tension. The tensile stress σ is scaled down by $\sigma_0 = k_0\sqrt{3}$, the initial tensile yield stress in the absence of the yield-vertex modification, i.e. for the classical model. The tensile plastic strain ε^{p} is normalized by the elastic critical strain σ_0/E. Figure 4 shows how the stress varies with the plastic strain for the classical model (the horizontal line) and for $\beta_c^{\max} = 105°$, $120°$, $130°$ and $139.2°$ when the extremal surface is kept fixed. This case corresponds to perfect plasticity within the grains of a polycrystal, where the increase of the macroscopic stress is due to "constraint hardening". The curves can be compared with the results given in [4] for micromechanical models of a polycrystal. The lowest curve in Fig. 4 for $\sin\beta_c^{\max} = \sin 139.2° \approx 1/1.53$ corresponds to an upper bound of the constraint hardening effect (cf. [3, 4]) and, after suitable rescaling, fits approximately the results obtained from the Kröner – Budiansky – Wu self-consistent model. Fitting the results obtained in [4] for Hill's self-consistent model, regarded as more accurate, would require a somewhat smaller value of $\beta_c^{\max}$. Identification of an optimal

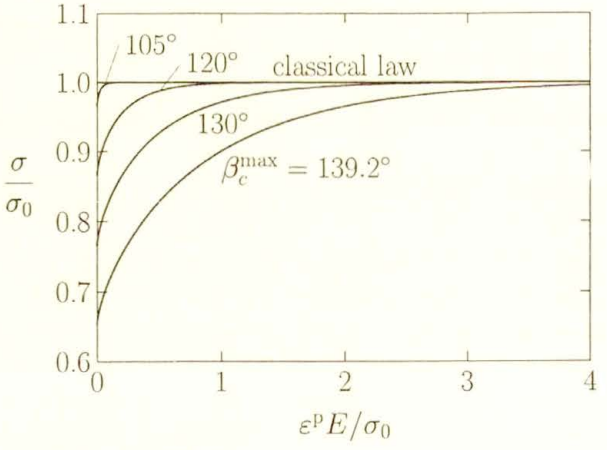

FIG. 4. Non-dimensional stress vs. plastic strain in uniaxial tension for a fixed extremal surface and for different values of $\beta_c^{\max}$.

value of $\beta_c^{\max}$ is not straightforward since the yield-surface corner angle in a phenomenological model should be interpreted as an *effective* angle obtained when an unspecified plastic strain due to some internal mechanisms is neglected. For otherwise, the assumption of the existence of a finite elastic domain at advanced plastic deformation could be questioned; cf. the remark in [4], p. 271.

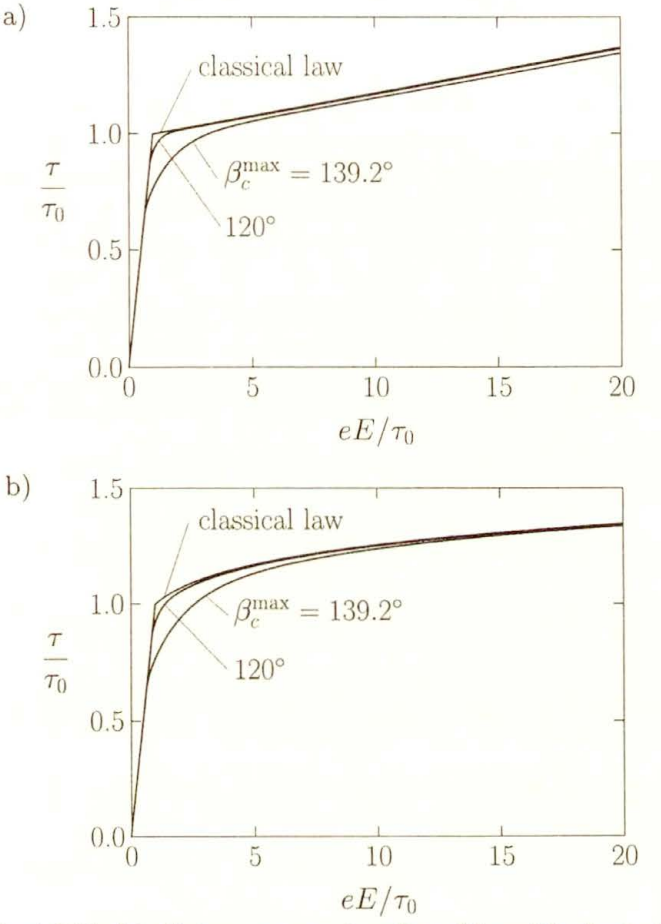

FIG. 5. Uniaxial Kirchhoff stress τ as a function of logarithmic strain e for the extremal surface subject to an isotropic, (a) linear $\tau = k\sqrt{3} = \tau_0 + 0.02Ee^{\mathrm{p}}$, or (b) power hardening law $\tau = \tau_0\,(1 + e^{\mathrm{p}}E/\tau_0)^{0.1}$, for different values of $\beta_c^{\max}$.

The results in Fig. 5 correspond to the extremal surface being not fixed but subject to an isotropic linear or power hardening law. The finite strain version described in Sec. 4 has been employed, with τ_0 as the uniaxial Kirchhoff stress on the initial extremal surface and $\tau = (e - e^{\mathrm{p}})E$. It can be seen that the uniaxial stress-strain curve for the classical law is closely approximated by the curves for the present model when the plastic strain becomes only a few times greater than the elastic strain. However, the difference is no longer fully negligible even

for larger strains, especially for linear hardening with a constant modulus h (equal to $0.02E$ in Fig. 5 a). The reason is that an asymptotic value β_0^∞ of β_0 is now somewhat greater than $(\pi - \beta_c^{\max})$. It can be found from the condition $\mathrm{d}\beta_0/\mathrm{d}e^{\mathrm{p}} = 0$ which leads to the relationship

$$\sin\beta_0^\infty - \frac{2}{3} h M_{\mathrm{I}}(\beta_0^\infty) \sin\beta_c^{\max} = 0\,. \tag{5.1}$$

While the yield-vertex modification of a stress-strain curve for proportional loading at advanced plastic strain may be regarded as insignificant, the corresponding difference in the incremental constitutive law is substantial. This is illustrated in Fig. 6 where plots of the effective tangent shear modulus vs. loading angle after tensile prestrain are presented for different values of $\beta_c^{\max}$. The plots correspond to a fixed extremal surface in the small strain formulation, and the amount of plastic prestrain for each value of $\beta_c^{\max}$ corresponds to the same relative distance to the extremal surface, defined by $(1 - \bar{\tau}/k)/(1 - \sin\beta_c^{\max}) = (1 - 1.3/1.53)/(1 - 1/1.53)$ to allow comparison with the similar Fig. 6 in [4]. The calculated effective tangent shear modulus in the total loading range tends at $\beta_c^{\max} \to \pi/2$ to the elastic shear modulus G, i.e. to the value obtained for the flow theory of plasticity.

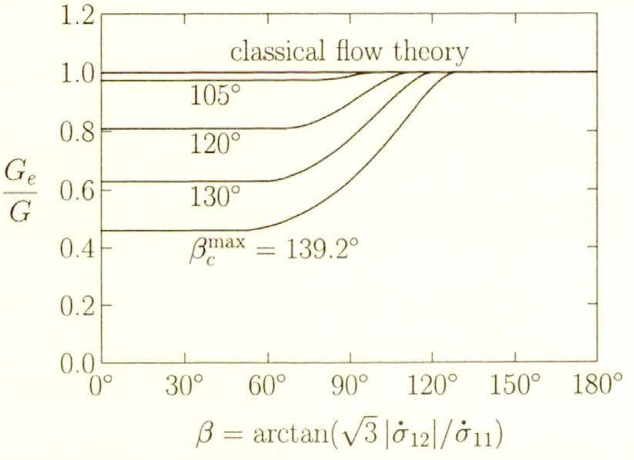

FIG. 6. Effective tangent shear modulus $G_e = \dot{\sigma}_{12}/2\dot{\varepsilon}_{12}$ as a function of the incremental loading angle β after tensile prestrain corresponding to a given relative distance (see the text) to a fixed extremal surface. $G = E/2(1+\nu)$ is the elastic shear modulus with $\nu = 0.3$.

The difference between the incremental characteristics for the present and classical models is also illustrated in Fig. 7. Plots of the principal plastic compliance ratio $M_{\mathrm{II}}/M_{\mathrm{I}}$ vs. strain in uniaxial tension are shown for $\beta_c^{\max} = 120°$ and 135° while for the classical plasticity law the ratio is identically zero. Solid lines correspond to a linear isotropic, broken lines to a power-type isotropic, and

dotted lines to a linear kinematic hardening law for the extremal surface. The material parameters for the isotropic hardening correspond to Figs. 5 a and 5 b, and the kinematic hardening law is specified by $\dot{\boldsymbol{\alpha}} = (2/3)(0.01E)\mathbf{D}^{\mathrm{p}}$. It can be seen that the value of $M_{\mathrm{II}}/M_{\mathrm{I}}$ is only slightly influenced by the type of hardening, and also by the amount of strain beyond a certain initial stage. On the other hand, the ratio depends strongly on the value of $\beta_c^{\max}$. This is, of course, not surprising since this ratio depends only on β_0 as illustrated in Fig. 2. Figure 7 may thus be treated as another illustration of the conclusion that during proportional loading at advanced plastic deformation, when the current hardening modulus is much smaller than E, the value of $\beta_c = \pi - \beta_0$ is close to $\beta_c^{\max}$ and hence almost constant.

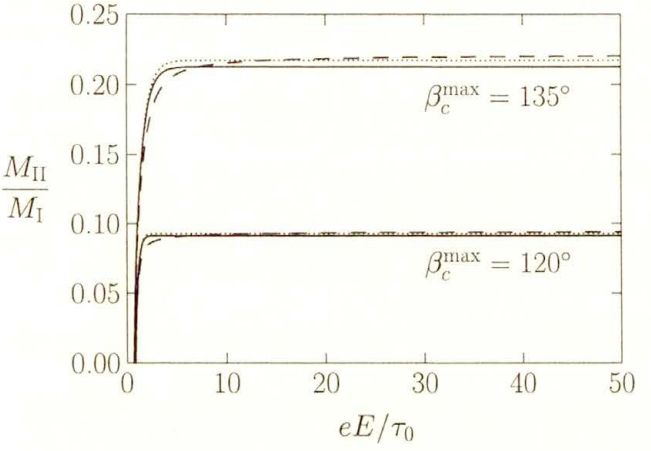

FIG. 7. Variation of principal plastic compliance ratio $M_{\mathrm{II}}/M_{\mathrm{I}}$ with logarithmic strain in uniaxial tension for the extremal surface subject to a linear isotropic ———, power-type isotropic _ _ _ and linear kinematic ..... hardening law for two values of $\beta_c^{\max}$. Isotropic hardening parameters as in Fig. 5, kinematic hardening law $\dot{\boldsymbol{\alpha}} = (2/3)(0.01E)\mathbf{D}^{\mathrm{p}}$.

A stabilized value of the ratio of the principal plastic compliances resembles the well-known property of the deformation theory of plasticity obeying a power hardening law. In the small-strain formulation with the elastic strain neglected, $M_{\mathrm{II}}/M_{\mathrm{I}}$ under proportional loading becomes then equal to the tangent-to-secant modulus ratio, and hence to the constant power exponent. The present model can *approximate* such behaviour provided $\beta_c^{\max}$ is appropriately selected, with the help of the relationship visualized in Fig. 2, to give the required value of the compliance ratio. The power hardening exponent corresponding to $\beta_c^{\max}$ equal to 120° or 135° can be directly read off as a stabilized ordinate in Fig. 7.

It is beyond the scope of this paper to simulate the material response for various paths of non-proportional loading, which is expected to be strongly influenced by the choice of an isotropic/kinematic hardening rule for the extremal

surface. We recall that the proposed yield-vertex modification does not restrict the freedom in selecting such a hardening rule that fits experimental data for a specified material.

6. Concluding remarks

A modification of the family of classical models for plastically deforming metals has been obtained with the help of general conclusions drawn from micromechanical analysis of an elastic-plastic polycrystal. In comparison with the standard equations of the flow theory of plasticity, the proposed model in its simplest computational version involves only one additional material constant which defines the maximal sharpness of the corner at the current loading point on the inner yield surface. A smooth loading surface of the standard form has been used as an outer "extremal" surface [3], not attainable during plastic flow. With the yield-vertex effect included, the high (elastic) stiffness of the classical elastic-plastic model against an abrupt change of the straining direction has been relaxed. This offers a perspective of more adequate modelling of the material behaviour under non-proportional loading, and of arriving at more realistic results in bifurcation and instability studies, still using a typical isotropic/kinematic hardening law for the outer loading surface.

References

1. S.B. BATDORF and B. BUDIANSKY, *A mathematical theory of plasticity based on the concept of slip*, NACA TN, No. 1871, 1949.
2. T.H. LIN, *A proposed theory of plasticity based on slips*, Proc. 2nd U.S. Nat. Congr. Appl. Mech., pp. 461–468, ASME, Ann Arbor 1954.
3. R. HILL, *The essential structure of constitutive laws for metal composites and polycrystals*, J. Mech. Phys. Solids, **15**, 79–95, 1967.
4. J.W. HUTCHINSON, *Elastic-plastic behaviour of polycrystalline metals and composites*, Proc. Roy. Soc. Lond., **A 319**, 247–272, 1970.
5. J. CHRISTOFFERSEN and J.W. HUTCHINSON, *A class of phenomenological corner theories of plasticity*, J. Mech. Phys. Solids, **27**, 465–487, 1979.
6. W.T. KOITER, *Stress-strain relations, uniqueness and variational theorems for elastic-plastic materials with a singular yield surface*, Quart. Appl. Math., **11**, 350–353, 1953.
7. J.L. SANDERS, *Plastic stress-strain relations based on linear loading functions*, Proc. 2nd U.S. Nat. Congr. Appl. Mech., pp. 455–460, ASME, Ann Arbor 1954.
8. B. BUDIANSKY, *A reassessment of deformation theories of plasticity*, ASME J. Appl. Mech., **26**, 259–264, 1959.
9. V.D. KLUSHNIKOV, *On a possible way of constructing the plastic deformation laws* [in Russian], Prikl. Mat. Mekh., **23**, 282–291, 1959.
10. V.D. KLUSHNIKOV, *An analytical theory of plasticity* [in Russian], Izv. AN SSSR Mekhanika, No. 2, 82–87, 1965.
11. M.J. SEWELL, *A plastic flow at a yield vertex*, J. Mech. Phys. Solids, **22**, 469–490, 1974.

12. M. GOTOH, *A class of plastic constitutive equation with vertex effect* – I, II, Int. J. Solids Structures, **21**, 1101–1116, 1117–1129, 1985.

13. Y. TOMITA, A. SHINDO, Y.S. KIM and K. MICHIURA, *Deformation behaviour of elastic-plastic tubes under external pressure and axial load*, Int. J. Mech. Sci., **28**, 263–274, 1986.

14. M. GOYA and K. ITO, *An expression of elastic-plastic constitutive law incorporating vertex formation and kinematic hardening*, ASME J. Appl. Mech., **58**, 617–622, 1991.

15. A. PHILLIPS and R.L. SIERAKOWSKI, *On the concept of the yield surface*, Acta Mech., **1**, 29–35, 1965.

16. Z. MRÓZ, *On the description of anisotropic work-hardening*, J. Mech. Phys. Solids, **15**, 163–175, 1967.

17. Y.F. DAFALIAS and E.P. POPOV, *A model of nonlinearly hardening materials for complex loading*, Acta Mech., **21**, 173–192, 1975.

18. K. HASHIGUCHI, *Constitutive equations of elastoplastic materials with elastic-plastic transition*, ASME J. Appl. Mech., **47**, 266–272, 1980.

19. J. RYCHLEWSKI, *On thermoelastic constants*, Arch. Mech., **36**, 77–95, 1984.

20. H. PETRYK, *On constitutive inequalities and bifurcation in elastic-plastic solids with a yield-surface vertex*, J. Mech. Phys. Solids, **37**, 265–291, 1989.

21. R. HILL, *Constitutive inequalities for isotropic elastic solids under finite strain*, Proc. Roy. Soc. Lond., **A 314**, 457–472, 1970.

POLISH ACADEMY OF SCIENCES
INSTITUTE OF FUNDAMENTAL TECHNOLOGICAL RESEARCH
e-mail: hpetryk@ippt.gov.pl
and
DORTMUND UNIVERSITY
DEPARTMENT OF MECHANICAL ENGINEERING, DORTMUND, GERMANY.

Received March 21, 1997.

Arch. Mech., **49**, 5, pp. 865–876, Warszawa 1997

Symmetrization of systems of conservation equations and the converse to the condition of Friedrichs and Lax

W. LARECKI (WARSZAWA)

THE RESULT OF FRIEDRICHS AND LAX [Proc. Nat. Acad. Sci. U.S.A., **68**, 8, 1686–1688, 1971] concluding that if the system of conservation equations implies the additional conservation equation (balance of entropy) then it can be symmetrized by premultiplication by the Hessian matrix of the entropy, is well known. Basic ingredients of the proof of the converse to this result can be found in the paper by BOILLAT [C.R. Acad. Sci. Paris, **278 A**, 909–914 1974], however this converse has not been explicitly formulated there and, as a consequence, it seems to be overlooked. Therefore, an explicit formulation and the detailed proof of the converse to the condition of Friedrichs and Lax is given in this paper. Due to this result, the restrictions imposed on the system of conservation equations by consistency with the additional conservation equations can be alternatively derived from requirement that it admits Hessian matrix as a symmetrizer while the corresponding entropies can be determined by direct integration of the admissible Hessian symmetrizers. As an illustrative example, the system of conservation equations given in [DOMAŃSKI, JABŁOŃSKI and KOSIŃSKI, Arch. Mech., **48**, 541–550, 1996] is analysed. It is shown that this system can be brought into equivalent symmetric hyperbolic form without appealing to the existence of the additional conservation equation and the whole family of symmetric symmetrizers is determined. Then, the condition that the system admits the additional conservation equation reduces to the requirement that the family of symmetric symmetrizers contains at least one Hessian matrix. This requirement is, in turn, equivalent to the integrability condition for the overdetermined system of second order partial differential equations for the scalar entropy function. Finally, the family of entropies is obtained as a result of integration of this system.

1. Introduction

IN [1], FRIEDRICHS AND LAX have shown that if the system of N conservation equations implies the additional conservation equation (usually called balance of "entropy"), then premultiplication (left multiplication) of this system by Hessian matrix of "entropy" (matrix of second-order partial derivatives) makes it symmetric.

In the paper [2] by DOMAŃSKI, JABŁOŃSKI and KOSIŃSKI, this result has been explicitly quoted as a means for symmetrization of considered particular system of conservation equations, but the employed procedure of symmetrization and interpretation of the results should be rather referred to the *converse* to the result of FRIEDRICHS and LAX [1]. Clearly, in [2], it has been required from the system of conservation equations to be symmetrizable (by premultiplication) by

prescribed Hessian matrix. As a result of this requirement, the algebraic relation between the entries of the prescribed Hessian matrix and the entries of the matrices corresponding to the considered system of conservation equations (written in a matrix form) has been obtained. This relation has been called "symmetrizability condition" for the considered system of conservation equations. Since the system of conservation equations treated in [2] implies the additional conservation (balance of entropy) and prescribed Hessian matrix corresponds precisely to one of the entropies admitted by this system, the "symmetrizability condition", of course, corresponds to "the model compatibility condition which, on the other hand, can be obtained from the second law of thermodynamics", as it has been concluded in [2].

Apparently, the procedure performed in [2] in nothing else but checking that the *converse* to the well known result of FRIEDRICHS and LAX [1] is true for the particular system of conservation equations. Unfortunately, this aspect of the performed calculations has not been noticed in [2].

The converse to the result of FRIEDRICHS and LAX [1], of course, holds for the general case of the system of conservation equations and its proof can be easily deduced from the paper by BOILLAT [3]. Since this result has not been explicitly formulated in [3] as a separate "theorem", contrary to the condition of Friedrichs and Lax, it seems to be overlooked (for example, [2, 6]).

The objective of this note is to formulate explicitly this converse and to demonstrate its complete detailed proof, mostly for pedagogical reasons, as well as to show how this result can be directly applied in practice for derivation of the condition that the system of conservation equations implies the additional conservation equation, and then to determine the "entropies" that can be assigned to this system. It should be emphasised that the crucial points of the reasoning employed in the proof presented here have been found in [3] and, therefore, the converse to the condition of Friedrichs and Lax should be attributed to Boillat. The original method proposed here, consisting in application of this converse for derivation of the restrictions on systems of conservation equations imposed by consistency with the additional conservation equation (balance of "entropy"), can be considered as an alternative to the method of Lagrange–Liu multipliers [5] developed in the framework of extended thermodynamics. In this alternative approach, the restrictions on the system of conservation equations as well as the "entropies" are obtained directly, without use of the auxiliary fields of Lagrange–Liu multipliers.

In Sec. 2, we demonstrate that *if the system of N conservation equations has a symmetrizer which is the Hessian matrix of a certain function of the unknowns then this system of conservation equations implies the additional conservation equation, in which this function of the unknowns is a "density"*. The result of FRIEDRICHS and LAX [1] together with the converse leads to the following necessary and sufficient condition for the system of N conservation equations to be symmetrizable (by premultiplication) by a Hessian matrix: *The system of N con-*

servation equations is symmetrizable (by premultiplication) by a Hessian matrix iff it implies the additional conservation equation.

Therefore, the conditions imposed on the system of N conservation equations by the requirement that it implies the additional conservation equation (for example, thermodynamic restrictions implied by consistency with the balance of entropy) can be obtained by requiring that the system admits symmetric symmetrizer which is a Hessian matrix. The respective procedure can be accomplished in the following five steps: 1) to rewrite the system of conservation equations in a matrix form, 2) to derive the condition on the entries of the respective matrices (necessary and sufficient), that those matrices have common left symmetric symmetrizers, 3) to determine the family of common left symmetric symmetrizers (the entries of such family of matrices are related to the entries of the matrices corresponding to the considered system of conservation equations), 4) to derive the condition on this family of symmetrizers that it contains at least one Hessian matrix (this condition corresponds to the condition that the system of $(1/2)N(N+1)$ second-order partial differential equations for entropy function is integrable), 5) finally, to calculate the entropies admitted by the considered system of $(1/2)N(N+1)$ equations for entropy.

In Sec. 3, the example of application of this complex procedure is presented. In this example, we use the system of conservation equations considered in [2] because of its particular simplicity. Since this system is consistent with the additional conservation equation (balance of entropy) without any restrictions on the functions of dependent variables involved in it, the respective matrices admit common left symmetric symmetrizers without any additional relations between their entries. The family of the respective symmetrizers is derived and the step 2) of the above procedure is not needed in this case. To this end, we note that the equivalence result (existence of entropy and symmetrizability by Hessian matrices) together with the described procedure of application enables one to employ the methods of matrix analysis in studying the properties of systems of conservation equations endowed with entropies.

2. Converse to the condition of Friedrichs and Lax

We consider a quasilinear system of N conservation equations for N unknowns in normal (Cauchy) form

$$\partial_t \mathbf{u} + \partial_i \mathbf{f}^i(\mathbf{u}) = \mathbf{b}(\mathbf{u}), \qquad i = 1,\ 2, ..., m \tag{2.1}$$

with the corresponding matrix form

$$\partial_t \mathbf{u} + \mathbf{A}^i(\mathbf{u})\partial_i \mathbf{u} = \mathbf{b}(\mathbf{u}), \tag{2.2}$$

where

$$
\begin{aligned}
\mathbf{u}^T &= \left[u^1(t,x^i),...,u^N(t,x^i)\right],\\
\mathbf{f}^{iT}(\mathbf{u}) &= \left[f^{i1}(u^K(t,x^i)),...,f^{iN}(u^K(t,x^i)\right],\\
\mathbf{b}^T(\mathbf{u}) &= \left[b^1(u^K(t,x^i)),...,b^N(u^K(t,x^i)\right],\\
\mathbf{A}^i(\mathbf{u}) &= \nabla_{\mathbf{u}}\mathbf{f}^i(\mathbf{u}) = \left[A^{iK}_L(u^M)\right] = \left[\frac{\partial f^{iK}(u^M)}{\partial u^L}\right],\\
i &= 1,\ 2,...,n, \qquad K,L,M = 1,\ 2,...,N,
\end{aligned}
\tag{2.3}
$$

and

$$
\partial_t := \frac{\partial}{\partial t}, \qquad \partial_i := \frac{\partial}{\partial x^i}.
$$

The usual summation convention over repeated upper and lower indices is understood and $(\cdot)^T$ denotes a transpose.

For the system (2.1), (2.2), (2.3), we consider the following additional conservation equation

$$
\partial_t h^0\mathbf{u} + \partial_i h^i\mathbf{u} = \sigma(\mathbf{u}). \tag{2.4}
$$

For the clarity and completeness, we recall the well-known results of FRIEDRICHS and LAX [1]. In [1], FRIEDRICHS and LAX formulated the *statement* which can be expressed in the following way:

The conservation equation (2.4) *"follows from" (is implied by or is a consequence of, in other words) the system of N conservation equations* (2.1) *if and only if*

$$
\frac{\partial h^0(u^M)}{\partial u^J}\frac{\partial f^{iJ}(u^M)}{\partial u^R} = \frac{\partial h^i(u^M)}{\partial u^R}, \qquad i = 1,2,...,m, \tag{2.5}
$$

$$
\frac{\partial h^0(u^M)}{\partial u^J}\, b^J(u^M) = \sigma(u^M), \qquad J,M,R = 1,2,...,n. \tag{2.6}
$$

The term "follows from" (is implied by or is a consequence of, in other words), used in this statement, is understood in a sense that there are N functions $l_J(u^M)$, not all identically zero, such that conservation equation (2.4) is a combination of N equations of (2.1) multiplied by respective $l_J(u^M)$; namely, the equality

$$
\partial_t h^0(u^M) + \partial_i h^i(u^M) - \sigma(u^M) = l_J(u^M)\left[\partial_t u^J + \partial_i f^{iJ}(u^M) - b^J(u^M)\right], \tag{2.7}
$$

holds for all functions $u^M(t,x^i)$ (in the domain of such functions). With this interpretation, the following "proof" justifies this *statement.*

Assume that (2.4) "follows from" (2.1). Then, the following identity is implied by (2.7):

$$\left[\frac{\partial h^0(u^M)}{\partial u^J} - l_J(u^M)\right]\partial_t u^J + \left[\frac{\partial h^i(u^M)}{\partial u^R} - l_J(u^M)\frac{\partial f^{iJ}(u^M)}{\partial u^R}\right]\partial_i u^R + \left[l_J(u^M)b^J(u^M) - \sigma(u^M)\right] \equiv 0 \tag{2.8}$$

which holds for all functions $u^M(t, x^i)$. Since in (2.8) the values of $u^M(t, x^i)$, $\partial_t u^J(t, x^i)$ and $\partial_i u^R(t, x^i)$ can be taken arbitrarily at each point (t, x^i), the terms in square brackets must vanish and, as a consequence, we obtain the following system of identities:

$$l_J(u^M) = \frac{\partial h^0(u^M)}{\partial u^J}, \tag{2.9}$$

$$\frac{\partial h^j(u^M)}{\partial u^R} = l_J(u^M)\frac{\partial f^{iJ}(u^M)}{\partial u^R}, \tag{2.10}$$

$$\sigma(u^M) = l_J(u^M)b^J(u^M). \tag{2.11}$$

Substituting (2.9) into (2.10) and (2.11) we obtain (2.5), (2.6). Conversely, assume that (2.5), (2.6) hold. Multiplying both sides of (2.1) by row vector composed of $\partial h^0(u^M)/\partial u^J$ we obtain the following conservation equation

$$\frac{\partial h^0(u^M)}{\partial u^J}\partial_t u^J + \frac{\partial h^0(u^M)}{\partial u^J}\frac{\partial f^{iJ}(u^M)}{\partial u^R}\partial_i u^R = \frac{\partial h^0(u^M)}{\partial u^J}b^J(u^R) \tag{2.12}$$

which, in view of (2.5), (2.6), corresponds to (2.4).

Therefore, the equality (2.7) is satisfied for

$$l_J(u^M) = \frac{\partial h^0(u^M)}{\partial u^J}.$$

Then, the following *condition* was proved in [1]:

If the system (2.1) *implies the additional conservation equation* (2.4) *then the system* (2.2) *premultiplied (left-multiplied) by the Hessian matrix of* $h^0(\mathbf{u})$ *is symmetric.*

It was also mentioned in [1] that this symmetric system is equivalent to (2.1) if the Hessian matrix of $h^0(\mathbf{u})$ is non-singular, and it is symmetric hyperbolic if $h^0(\mathbf{u})$ is convex (Hessian of $h^0(\mathbf{u})$ is positive definite).

The proof of this *condition* given in [1] is based on differentiation of (2.10) with respect to the components of $\mathbf{u}$, which yields

$$\frac{\partial^2 h^i(u^M)}{\partial u^P \partial u^R} - \frac{\partial h^0(u^M)}{\partial u^J}\frac{\partial^2 f^{iJ}(u^M)}{\partial u^P \partial u^R} = \frac{\partial^2 h^0(u^M)}{\partial u^P \partial u^J}\frac{\partial^2 f^{iJ}(u^M)}{\partial u^R}. \tag{2.13}$$

The left-hand side of (2.13) is symmetric in the indices P, R, so is the right-hand side. It therefore follows from $(2.3)_4$ that Hessian matrix of $h^0(\mathbf{u})$ is the left symmetrizer of the matrices $\mathbf{A}^i(\mathbf{u})$.

The converse to this condition can be formulated as the following implication:

If the system of N conservation equations (2.1) *has a left symmetrizer which is a Hessian matrix of a certain function $h^0(\mathbf{u})$ then the system* (2.1) *implies the additional conservation equation* (2.4) *with $h^i(\mathbf{u})$ and $\sigma(\mathbf{u})$ given by* (2.5), (2.6).

P r o o f. Assume that there exists function $h^0(\mathbf{u})$, such that Hessian matrix of $\mathbf{h}^0(\mathbf{u})$ is the left symmetrizer of the matrices $\mathbf{A}^i(\mathbf{u})$ given by $(2.3)_4$. Then,

$$\frac{\partial^2 h^0(u^M)}{\partial u^P \partial u^Q} \frac{\partial f^{iQ}(u^M)}{\partial u^R} = \frac{\partial^2 h^0(u^M)}{\partial u^R \partial u^S} \frac{\partial f^{iS}(u^M)}{\partial u^P}. \tag{2.14}$$

Let us denote

$$h^i_R(u^M) := \frac{\partial h^0(u^M)}{\partial u^S} \frac{\partial f^{iS}(u^M)}{\partial u^R}. \tag{2.15}$$

For each i, functions $h^i_R(u^M)$ can be interpreted as components of the row vector $\mathbf{h}^{iT}(\mathbf{u})$ which, according to $(2.3)_4$, (2.15), is given by the equation

$$\mathbf{h}^{iT}(\mathbf{u}^M) = \mathbf{l}^T(\mathbf{u})\mathbf{A}^i(\mathbf{u}), \qquad i = 1, 2, ..., n, \tag{2.16}$$

where $\mathbf{l}^T(\mathbf{u}^M)$ is a row vector with components $[\partial h^0(u^M)]/\partial u^S$.

Differentiation of (2.15) with respect to u^Q yields

$$\frac{\partial h^i_R(u^M)}{\partial u^Q} = \frac{\partial^2 h^0(u^M)}{\partial u^Q \partial u^S} \frac{\partial f^{iS}(u^M)}{\partial u^R} + \frac{\partial h^0(u^M)}{\partial u^S} \frac{\partial^2 f^{iS}(u^M)}{\partial u^Q \partial u^R} \tag{2.17}$$

and it follows from (2.14), (2.15), (2.17) that

$$\frac{\partial h^i_R(u^M)}{\partial u^Q} = \frac{\partial h^i_Q(u^M)}{\partial u^R}, \qquad i = 1, 2, ..., m, \tag{2.18}$$

what means that the matrix representing gradient of $\mathbf{h}^i$ (with respect to $\mathbf{u}$) is symmetric.

Equalities (2.18) are necessary and sufficient for the following 1 – forms to be closed

$$\Omega^i = h^i_S \, du^S, \tag{2.19}$$

and, for $\mathbf{u}$ from an open convex domain (without loss of generality, it can be assumed that in (2.1) the domain of $\mathbf{u}$ is an open convex set in R^N), it is exact (see, for example [4]). Hence, there exist functions $h^i(u^M)$ such that

$$\Omega^i = dh^i, \tag{2.20}$$

and therefore

$$h^i_R(u^M) = \frac{\partial h^i(u^M)}{\partial u^R}. \tag{2.21}$$

Substituting (2.21) into (2.15) we obtain (2.5). Then, multiplying both sides of the system (2.1) by the row vector composed of $\partial h^0(u^M)/\partial u^J$ and taking into account (2.5) (implied by (2.21), (2.15)), we finally obtain the following conservation equation

$$\partial_t h^0(\mathbf{u}) + \partial_i h^i(\mathbf{u}) = \frac{\partial h^0(u^M)}{\partial u^J} b^J(u^M). \tag{2.22}$$

Hence, the system (2.1) implies the additional conservation equation with the right-hand side term

$$\sigma(u^M) = \frac{\partial h^0(u^M)}{\partial u^J} b^J(u^M).$$

The following *observation* given in [3] is a direct consequence of the *condition* of Friedrichs and Lax and its converse:

The system (2.1), (2.2) *of* **N** *conservation equations implies the additional conservation equation* (2.4) *(with* $h^i(\mathbf{u})$ *and* $\sigma(\mathbf{u})$ *given by* (2.5), (2.6), *respectively) iff there exists a function* $h^0(\mathbf{u})$ *such that its Hessian matrix is the common left symmetrizer of the matrices* $(2.3)_4$.

The necessary and sufficient condition corresponding to this *observation* but expressed in the framework of geometrical (coordinate-free) description of the systems of conservation equations (affine transformations of independent variables and dependent variables interpreted as local coordinate system on the manifold) is given by PIEKARSKI [6].

3. Example of application of the converse to the condition of Friedrichs and Lax

In the Introduction, we have briefly described the details of the general procedure of determination of the conditions that the system of conservation equations is consistent with the additional conservation equation, based on the consequences of the converse to the result of Friedrichs and Lax. In order to illustrate this procedure, we have chosen here, as an example, the system of conservation equations from [2] because of its extreme structural simplicity and because, in [2], the respective calculations related to verification of the converse to the result of Friedrichs and Lax are given in explicit form. Moreover, this system of conservation equations is consistent with the balance of entropy and therefore it admits symmetric symmetrizers. Hence, the procedure considerably simplifies due to those facts and reduces to determination of the family of symmetric left

symmetrizers of the system, to exploitation of the condition that this family contains Hessian matrices and, finally, to integration of the respective system of second-order partial differential equations in order to obtain the entropies.

3.1. System of conservation equations considered in [2]

In [2], the following particular case of $N = 5$ conservation equations (2.2) in $i = 3$ spatial dimensions has been considered

$$\mathbf{u}^T(t,x^i) = \left[e(t,x^i), q^1(t,x^i), q^2(t,x^i), q^3(t,x^i), \beta(t,x^i)\right], \tag{3.1}$$

$$\mathbf{A}^1(\mathbf{u}) = \begin{bmatrix} \alpha'(e)q^1 & \alpha(e) & 0 & 0 & 0 \\ f_1'(e) & 0 & 0 & 0 & 0 \\ 0 & 0 & 0 & 0 & 0 \\ 0 & 0 & 0 & 0 & 0 \\ 0 & 0 & 0 & 0 & 0 \end{bmatrix},$$

$$\mathbf{A}^2(\mathbf{u}) = \begin{bmatrix} \alpha'(e)q^2 & 0 & \alpha(e) & 0 & 0 \\ 0 & 0 & 0 & 0 & 0 \\ f_1'(e) & 0 & 0 & 0 & 0 \\ 0 & 0 & 0 & 0 & 0 \\ 0 & 0 & 0 & 0 & 0 \end{bmatrix}, \tag{3.2}$$

$$\mathbf{A}^3(\mathbf{u}) = \begin{bmatrix} \alpha'(e)q^3 & 0 & 0 & \alpha(e) & 0 \\ 0 & 0 & 0 & 0 & 0 \\ 0 & 0 & 0 & 0 & 0 \\ f_1'(e) & 0 & 0 & 0 & 0 \\ 0 & 0 & 0 & 0 & 0 \end{bmatrix},$$

$$\alpha'(e) = \frac{d\alpha(e)}{de}, \qquad f_1'(e) = \frac{df_1(e)}{de},$$

$$\mathbf{b}^T(\mathbf{u}) = \left[\varrho r,\ f_2'(\beta)q^1,\ f_2'(\beta)q^2,\ f_2'(\beta)q^3,\ f_1(e) + f_2(\beta)\right]. \tag{3.3}$$

The system of conservation equations (2.2), (3.1), (3.2), (3.3) corresponds to the phenomenological model of a rigid conductor of heat with internal state variable β (called "semi-empirical temperature"). In this model, e is the internal energy density, q_i $(i = 1,2,3)$ are the components of gradient of $(-\beta)$, ϱr is the heat source density and $\alpha(e)$, $f_1(e)$ are constitutive functions.

In [2], the condition

$$\mathbf{H}(\mathbf{u})\mathbf{A}^i(\mathbf{u}) = \left[\mathbf{H}(\mathbf{u})\mathbf{A}^i(\mathbf{u})\right]^T, \qquad i = 1,2,...,n, \tag{3.4}$$

has been imposed on the matrices (3.2) for *prescribed* postulated matrix $\mathbf{H}(\mathbf{u})$

$$\mathbf{H}(\mathbf{u}) = \operatorname{diag}\left[\eta_e''(e),\ c_1,\ c_1,\ c_1,\ c_2\right], \tag{3.5}$$
$$\eta_e''(e) = \frac{d^2\eta_e(e)}{de^2}, \qquad c_1, c_2 - \text{const},$$

which, in fact, is a *Hessian matrix* of the following function h^0 of the arguments e, q^i, β,

$$h^0(\mathbf{u}) = h^0(e, q^i, \beta) = \eta_e(e) + \frac{1}{2}c_1 q_i q^i + \frac{1}{2}c_2\beta^2. \tag{3.6}$$

As a consequence of this condition, the relation between $\alpha(e)$, $f_1(e)$ and $\eta_e(e)$ has been obtained

$$c_1 f_1'(e) = \alpha(e)\eta_e''(e), \tag{3.7}$$

and called "*symmetrizability condition*" for the system (2.2), (3.1), (3.2), (3.3).

In view of the *observation* given in Sec. 2, the "symmetrizability condition" (3.7) is nothing else but the condition that the system (2.1), (3.1), (3.2), (3.3) implies the balance of entropy (2.4) for the entropy (3.6).

In the following, we show how the condition (3.7) and the family of entropies containing, as a special case, the function (3.6) can be obtained from the requirement that the family of common symmetric left symmetrizers of the matrices (3.2) admits Hessian matrices, in other words, by selecting Hessians from this family.

3.2. Family of the symmetric left symmetrizers of the matrices (3.2)

The term "symmetrizability condition" used in [2] to denote the condition (3.7) (which, in fact, is the condition of consistency with the entropy balance (2.4) for entropy (3.6)) seems to be particularly inadequate in view of the fact that the matrices (3.2) have a family of common left symmetric symmetrizers (for arbitrary $\alpha(e)$, $f_1(e)$)

$$\mathbf{S}(\mathbf{u}) = \operatorname{diag}\left[\chi,\ \chi\frac{\alpha(e)}{f_1'(e)},\ \chi\frac{\alpha(e)}{f_1'(e)},\ \chi\frac{\alpha(e)}{f_1'(e)},\ \lambda\right] \tag{3.8}$$

parametrized by two arbitrary functions $\chi(e, q^i, \beta)$, $\lambda(e, q^i, \beta)$.

To see this, one can simply verify by inspection that

$$\mathbf{S}(\mathbf{u})\mathbf{A}^i(\mathbf{u}) = \left[\mathbf{S}(\mathbf{u})\mathbf{A}^i(\mathbf{u})\right]^T, \qquad i = 1, 2, 3, \tag{3.9}$$

holds for $\mathbf{A}^i(\mathbf{u})$ given by (3.2) and $\mathbf{S}(\mathbf{u})$ given by (3.8). The family of matrices (3.8) represents all symmetric solutions $\mathbf{S}(\mathbf{u})$ ($\mathbf{S}(\mathbf{u}) = \mathbf{S}^T(\mathbf{u})$) of the system of three matrix equations (3.9) with the matrices $\mathbf{A}^i(\mathbf{u})$ given by (3.2).

The fact that the matrices (3.2) have common symmetric left symmetrizers and the family of those symmetrizers takes the form (3.8), is a consequence of a very specific structure of the set of matrices (3.2); namely, except the first entry on the main diagonal, they can be obtained one from the other simply by permuting the respective rows and columns (similarity transformations by the respective permutation matrices).

Thus, the system (2.2), (3.1), (3.2), (3.3) considered in [2] can be symmetrized without appealing to the fact that it admits the additional conservation equation and, as it follows from (3.8), it admits a more general class of symmetrizers than that obtained in [2]. By choosing $\chi(e, q^i, \beta) > 0$ and $\lambda(e, q^i, \beta) > 0$ for all e, q^i, β (from the respective domain), positive definite symmetrizers can be obtained from the family (3.8) provided that either $\alpha(e) > 0$ and $f_1'(e) > 0$ or $\alpha(e) < 0$ and $f_1'(e) < 0$. Hence, the only conditions on $\alpha(e)$ and $f_1(e)$ that ensure symmetric hyperbolicity of symmetric systems obtained by premultiplication of (2.2), (3.2) by $\mathbf{S}(\mathbf{u})$ from (3.1) with $\chi > 0$, $\lambda > 0$ is either $\alpha(e) < 0$, $f_1'(e) < 0$ or $\alpha(e) > 0$, $f_1'(e) > 0$.

3.3. Condition of consistency with balance of entropy and the family of entropies

The condition that the system (2.2), (3.1), (3.2), (3.3) is symmetrizable by Hessian matrix of a certain entropy function $h^0(e, q^i, \beta)$ is equivalent to the condition that at least one of the matrices $\mathbf{S}(\mathbf{u})$ of the family (3.8) is the Hessian of $h^0(e, q^i, \beta)$. This condition is, therefore, the integrability condition of the following system of 15 second-order partial differential equations for $h^0(e, q^i, \beta)$.

$$
\begin{aligned}
&\frac{\partial^2 h^0}{\partial e^2} = \chi(e, q^i, \beta), \\
&\frac{\partial^2 h^0}{\partial e \partial q^i} = 0, \qquad i = 1, 2, 3, \\
&\frac{\partial^2 h^0}{\partial e \partial \beta} = 0, \\
&\frac{\partial^2 h^0}{\partial (q^i)^2} = \chi(e, q^i, \beta) \frac{\alpha(e)}{f_1'(e)}, \qquad i = 1, 2, 3, \\
&\frac{\partial^2 h^0}{\partial q^i \partial q^j} = 0, \qquad i, j = 1, 2, 3, \quad i \neq j, \\
&\frac{\partial^2 h^0}{\partial q^i \partial \beta} = 0, \qquad i = 1, 2, 3, \\
&\frac{\partial^2 h^0}{\partial \beta^2} = \lambda(e, q^i, \beta).
\end{aligned}
\tag{3.10}
$$

It can be easily verified that the system (3.10) is integrable iff

$$
\begin{aligned}
\chi(e, q^i, \beta) &= \overline{\chi}(e), \\
\lambda(e, q^i, \beta) &= \overline{\lambda}(e), \\
\overline{\chi}(e)\frac{\alpha(e)}{f_1'(e)} &= c, \qquad c = \text{const.}
\end{aligned}
\tag{3.11}
$$

With the conditions (3.11), the system (3.10) can be integrated and its solutions (entropies) take the following form:

$$
h^0(e, q^i, \beta) = h_e^0(e) + \frac{1}{2} c q_i q^i + h_\beta^0(\beta),
\tag{3.12}
$$

where

$$
\begin{aligned}
\overline{\chi}(e) &= \frac{d^2 h_e^0(e)}{de^2} = h_e^{0\prime\prime}(e) = c\frac{f_1'(e)}{\alpha(e)}, \\
\overline{\lambda}(e) &= \frac{d^2 h_\beta^0(e)}{d\beta^2} = h_\beta^{0\prime\prime}(e),
\end{aligned}
\tag{3.13}
$$

and $h_e^0(e)$, $h_\beta^0(\beta)$ are arbitrary $C^2(R)$ functions, and c is an arbitrary real constant. Identifying $h_e^0(e)$ with $\eta_e(e)$ and c with c_1 and taking into account $(3.13)_1$, we recognize the condition (3.7) in integrability conditions $(3.11)_{1,3}$ and notice that the function (3.6) corresponding to prescribed symmetrizer (3.5) is a particular entropy (3.12) corresponding to $h_\beta^0(\beta) = (1/2)c_2\beta^2$.

It follows from Sec. 2 of [2] that the original system of field equations corresponding to the considered model of a rigid conductor of heat is the system of two partial differential equations of the first order with respect to the temperature Θ, and of the second order with respect to β, and that the second law of thermodynamics (entropy inequality) implies the entropy associated to this system of the form [2. Eq. (2.5)]

$$
\eta^\star(\Theta, \nabla\beta) = \eta_e^\star(\Theta) - \frac{1}{2} c|\nabla\beta|^2, \qquad c - \text{const.}
\tag{3.14}
$$

It is assumed in [2] that internal energy e is the inevitable function of Θ, so the original system of field equations can be equivalently expressed as the system of two partial differential equations for e and β (first order with respect to e and second order with respect to β), and, according to (3.14), the corresponding entropy must be of the form

$$
\eta(e, \nabla\beta) = \eta_e(e) - \frac{1}{2} c|\nabla\beta|^2.
\tag{3.15}
$$

The system of five conservation equations (2.2), (3.1), (3.2), (3.3) has been obtained in [2] from the original system of two field equations expressed in terms

of e, β, supplemented by the additional three equations obtained through spatial differentiation of one suitably chosen member of this original system. For such system of five equations, the variable $\mathbf{q}$ has been introduced through the substitution

$$\mathbf{q} = -\nabla\beta. \tag{3.16}$$

With the substitution (3.16), the entropy (3.15) corresponding to the original system of field equations expressed in terms of e, β (implied by the entropy inequality) takes the form

$$\eta(e, \mathbf{q}) = \eta_e(e) - \frac{1}{2}c|\mathbf{q}|^2, \tag{3.17}$$

while the system (2.2), (3.1), (3.2), (3.3) admits the family of entropies (3.12) implied by the balance of entropy (entropy inequality replaced by the corresponding balance law). The entropy (3.17) is a particular member of the family (3.12) corresponding to $h^0_\beta(\beta) \equiv 0$.

Hence, the entropy (3.17) obtained from thermodynamic restrictions imposed on the original second order system of field equations cannot be employed for symmetrization of the corresponding first order system of conservation equations (2.2), (3.1), (3.2), (3.3) since, when treated as a function of e, q^i, β, it will lead to the singular Hessian matrix.

References

1. K.O. FRIEDRICHS and P.D. LAX, *Systems of conservation equations with a convex extension*, Proc. Nat. Acad. Sci. U.S.A., **68**, 8, 1686–1688, 1971.
2. W. DOMAŃSKI, T.F. JABŁOŃSKI and W. KOSIŃSKI, *Symmetrization of heat conduction model for a rigid medium*, Arch. Mech., **48**, 3, 541–550, 1996.
3. G. BOILLAT, *Sur l'extence et la recherche d'equations de conservation supplementaire pour les systemes hyperboliques*, C.R. Acad. Sci. Paris, **278 A**, 909–914, 1974.
4. W. RUDIN, *Principles of mathematical analysis*, McGrow-Hill, Inc., 1964.
5. I-S. LIU, *Method of Lagrange multipliers for exploitation of the entropy principle*, Arch. Rat. Mech. Anal., **46**, 131–142, 1972.
6. S. PIEKARSKI, *On the uniqueness of symmetric algebraic consequences implied by a system of conservation laws consistent with the additional conservation equation*, Continuum Mech. Thermodyn., **6**, 21–29, 1994.

POLISH ACADEMY OF SCIENCES
INSTITUTE OF FUNDAMENTAL TECHNOLOGICAL RESEARCH
e-mail: wlarecki@ippt.gov.pl

Received January 14, 1997; new version May 9, 1997.

Arch. Mech., 49, 5, pp. 877–892, Warszawa 1997

Asymptotic analysis of propagation of a signal with finite rise time in a dispersive, lossy medium

A. CIARKOWSKI (WARSZAWA)

PROPAGATION of an electromagnetic high frequency modulated signal with a finite rise time through a dispersive medium described by the Lorentz model is considered. Asymptotic approximations, based on uniform asymptotic methods, are found for the Sommerfeld and Brillouin precursors, and for the steady state contribution to the propagated field.

1. Introduction

THIS PAPER is concerned with the analysis of propagation of a plane electromagnetic wave in a linear dispersive medium with absorption. The medium occupying the half-space $z > 0$ is described by the Lorentz (single resonance) model, otherwise it is homogeneous and isotropic. The wave propagating in the z direction has a finite rise time on the medium interface $z = 0$. Fundamental works on an electromagnetic signal evolution as it propagates through a dispersive medium are due to SOMMERFELD [1] and BRILLOUIN [2, 3]. On the grounds of asymptotic considerations, the authors showed that the main change in the form of an electromagnetic signal propagating in a dispersive medium takes place at the initial stage of propagation, at higher penetration depths the pulse form being almost unchanged. They revealed that two different precursors contribute to the signal. The precursors took their names from the names of the aforementioned authors. Those early results are not, however, fully satisfactory. They were obtained with classical (non-uniform) asymptotics and as such, they break down at some space-time points in the field.

Recently, significant research in this area has been done by OUGHSTUN and SHERMAN, see [4–10], based on the use of modern (uniform) asymptotic techniques. In those works the classical results have been reexamined and enriched by removing the obstacles characteristic of non-uniform asymptotic methods, and by providing deeper insight into the dynamics of propagation of waves of various forms. The works by Oughstun and Sherman gave motivation for this paper which depends strongly on basic results obtained in those works.

In the analysis of a signal evolution in dispersive media, asymptotic techniques are particularly appealing for their ability to generate results readily interpreted in physical terms. It is worth mentioning, however, that alternative approach may here be used. It consists in the examination of interaction of various spectral components of the incident signal with the medium, and then summing up

the results. Such an approach was successfully used by BLASHAK and FRANZEN in [12]. The authors studied pulse propagation in dispersive media described by both the Lorentz and Debye models. By assuming oblique incidence of the incoming signal on the media interface they were able, among others, to determine propagation directions of both precursors.

In this paper we examine, using uniform asymptotic apparatus, the propagation of an electromagnetic signal with finite rise time in a dispersive lossy medium described by the Lorentz model. The signal is zero for $t < 0$ and is hyperbolic tangent modulated for $t \geq 0$. Here and throughout t stands for time. In [8] the hyperbolic tangent was used as the signal envelope for time ranging from minus to plus infinity, i.e. the signal was switched on at $t \to -\infty$. As a consequence, the wave studied here differs in form from that used in [8] and is more realistic as a model for possible applications.

The problem studied here is of much interest from both the applications and scientific point of view. The renewed interest in dispersion phenomena was recently stimulated by investigation concerning interaction of electromagnetic fields with organ tissue. Dispersion is also important in many instances of propagation of electromagnetic high-frequency fields through dielectric media, since all dielectrics are less or more dispersive. On the other hand, thorough investigation of the problem on asymptotic grounds requires application of modern asymptotic techniques, which can be employed to evaluate contour integrals with such special cases as coalescent saddle points, saddle points tending to infinity or interacting saddle points with poles in the integrands.

2. Plane wave description in the dispersive medium

Consider the problem of an electromagnetic plane wave propagation in a linear, homogeneous and isotropic medium whose dispersive properties are described by the Lorentz model of resonance polarization. The complex index of refraction in the medium is given by the following, frequency-dependent function

$$n(\omega) = \left(1 - \frac{b^2}{\omega^2 - \omega_0^2 + 2i\delta\omega}\right)^{1/2}, \tag{2.1}$$

where $b^2 = 4\pi Ne^2/m$, N, e and M standing, respectively, for the number of electrons per unit volume, electron charge and its mass, δ is a damping constant and ω_0 is a characteristic frequency. It is assumed that the medium occupies the half-space $z \geq 0$ and that the wave propagates perpendicularly to the plane $z = 0$ in the direction of increasing z. Arbitrary component of the wave itself or of a corresponding Hertz vector can be represented in the medium by the scalar function

$$A(z,t) = \frac{1}{2\pi} \int_C \tilde{f}(\omega) \exp\left[\frac{z}{c}\phi(\omega,\theta)\right] d\omega. \tag{2.2}$$

Here, the complex phase function $\phi(\omega, \theta)$ is given by

$$\phi(\omega, \theta) = i\frac{c}{z}\left[\tilde{k}(\omega)z - \omega t\right] = i\omega[n(\omega) - \theta], \tag{2.3}$$

where

$$\theta = \frac{ct}{z} \tag{2.4}$$

is a dimensionless parameter that characterizes a space-time point (z, t) in the field. The function $\tilde{f}(\omega)$ is a temporal Fourier spectrum of the initial pulse $f(t) = A(0, t)$ at the plane $z = 0$. The contour C is the line $\omega = \omega' + ia$, a being a constant greater than the abscissa of absolute convergence ([13]) for $f(t)$ and ω' ranges from negative to positive infinity.

If the incident signal is a sine wave of fixed real frequency ω_c with its envelope described by a real function $u(t)$ that vanishes for $t < 0$, i.e.

$$f(t) = \begin{cases} 0 & t < 0, \\ u(t)\sin(\omega_c t) & t \geq 0, \end{cases} \tag{2.5}$$

then (2.2) can be represented in the alternative form

$$A(z, t) = \frac{1}{2\pi}\operatorname{Re}\left\{ i\int_{ia-\infty}^{ia+\infty} \tilde{u}(\omega - \omega_c)\exp\left[\frac{z}{c}\phi(\omega, \theta)\right] d\omega \right\}, \tag{2.6}$$

where $\tilde{u}(\omega)$ is the Laplace transform of $u(t)$.

It can be proved that if $A(0, t)$ is zero for $t < 0$ and if the model of the material dispersion is casual, then the field $A(z, t)$ vanishes for all $\theta = ct/z < 1$, with $z \geq 0$. Therefore, with these conditions fulfilled one can restrict the study to the case $\theta \geq 1$.

In this paper we specify the envelope of the incident pulse to be a product of a unit step function and a hyperbolic tangent function, i.e.

$$u_\beta(t) = \begin{cases} 0 & t < 0, \\ \tanh \beta t & t \geq 0, \end{cases} \tag{2.7}$$

where the parameter $\beta \geq 0$ determines the rapidity of the pulse growth.

In order to find its Laplace transform we take advantage of ([16])

$$\int_0^\infty \frac{e^{-px}}{1 + e^{-qx}} dx = \frac{1}{q}\mathcal{B}\left(\frac{p}{q}\right), \qquad \operatorname{Re} p > 0, \quad q > 0, \tag{2.8}$$

where $\mathcal{B}(\cdot)$ is the beta function. The latter function is defined by the psi function as

$$\mathcal{B}(x) = \frac{1}{2}\left[\psi\left(\frac{x+1}{2}\right) - \psi\left(\frac{x}{2}\right)\right] \tag{2.9}$$

and alternatively can be expressed in terms of the series

$$\mathcal{B}(x) = \sum_{k=0}^{\infty} \frac{(-1)^k}{x+k}. \tag{2.10}$$

It follows that the Laplace transform of $u(t)$ is

$$\tilde{u}_\beta(\omega) = \frac{1}{\beta}\mathcal{B}\left(-\frac{i\omega}{2\beta}\right) - \frac{i}{\omega}, \qquad \operatorname{Im}\omega > 0, \quad \beta > 0, \tag{2.11}$$

or, by (2.10),

$$\tilde{u}_\beta(\omega) = \frac{i}{\omega} - 2i\left(\frac{1}{\omega + 2i\beta} - \frac{1}{\omega + 4i\beta} + \ldots\right). \tag{2.12}$$

One can see from this formula that in the limit as $\beta \to \infty$ the function tends to i/ω, which is the Laplace transform of the Heaviside unit step function, corresponding to the pulse with zero rise time.

With (2.11) used in (2.6) $A(z,t)$ specifies to

$$A(z,t) = \frac{1}{2\pi}\operatorname{Re}\left\{i\int_{ia-\infty}^{ia+\infty}\left[\frac{1}{\beta}\mathcal{B}\left(-\frac{i(\omega-\omega_c)}{2\beta}\right) - \frac{i}{\omega-\omega_c}\right]e^{\frac{z}{c}\phi(\omega,\theta)}\,d\omega\right\}. \tag{2.13}$$

This integral formula describes the dynamics of propagation of the initial signal with envelope given by (2.7), oscillating with angular frequency ω_c.

3. Asymptotic analysis

As seen from (2.13), construction of an asymptotic approximation to $A(z,t)$ in the mature dispersion regime, i.e. as $z \to \infty$, is closely related to asymptotic evaluation of the integral describing the field. In general, asymptotic behavior of an integral depends strongly on analytic properties of its integrand [14]. Therefore our first step is to establish all the critical points of the integral in (2.13) in the complex ω plane which contribute to the asymptotic expansion of $A(z,t)$. The critical points associated with the phase function $\phi(\omega,\theta)$ are the saddle points. The first derivative (and possibly higher derivatives) of the phase function with respect to the variable of integration vanishes at those points. In the present case

the phase $\phi(\omega,\theta)$ is an analytic function in the complex ω plane except along the branch cuts $\omega'_-\omega_-$ and $\omega_+\omega'_+$, where

$$\begin{aligned} \omega'_\pm &= \pm(\omega_1^2-\delta^2)^{1/2}-i\delta\,, \\ \omega_\pm &= \pm(\omega_0^2-\delta^2)^{1/2}-i\delta \end{aligned} \tag{3.1}$$

are the branch points of $n(\omega)$ and $\omega_1^2=\omega_0^2+b^2$. The requirement $\phi'_\omega(\omega,\theta)=0$ leads to the equation

$$n(\omega)+\omega n'(\omega)-\theta=0, \tag{3.2}$$

or

$$\left[\omega^2-\omega_1^2+2id\omega+\frac{b^2\omega(\omega+i\delta)}{\omega^2-\omega_0^2+2id\omega}\right]^2 = \theta^2(\omega^2-\omega_1^2+2id\omega)(\omega^2-\omega_0^2+2id\omega). \tag{3.3}$$

This equation determines exact locations of the relevant saddle-points. It does not seem possible to solve (3.3) exactly. However, from numeric investigation of $\phi(\omega,\theta)$ it follows that there are two kinds of saddle-points: the distant and the near saddle-points. Each kind contains at most two points. The distant saddle-points, to be denoted by $SP_D^\pm$, are located symmetrically about the imaginary axis in the lower ω half-plane. As θ varies from 1 to ∞ they move in the region $|\omega|>\omega_1$, and take the limiting values $\pm\infty-2i\delta$ for $\theta=1$ and $\omega'_\pm$ for $\theta\to\infty$. The near saddle-points, denoted by $SP_N^\pm$, vary in the region $\omega<|\omega_0|$. As θ increases from 1 to θ_1, they approach each other along the imaginary ω-axis and meet at $\theta=\theta_1$ to produce one saddle-point of the second order. Next, as θ varies from θ_1 to ∞, there are two first-order saddle points which detach from the imaginary axis and tend symmetrically about this axis to $\omega=\omega_\pm$ (see Fig. 1).

Equation (3.3) was being solved approximately to find analytic description of the location of the saddle-points. Apparently the best approximation obtained so far is due to OUGHSTUN and SHERMAN (see [4]). According to their results, the distant saddle-point locations are given by

$$\omega_{SP_D^\pm}\cong\pm\xi(\theta)-i\delta[1+\eta(\theta)], \tag{3.4}$$

where

$$\begin{aligned} \xi(\theta) &= \left(\omega_0^2-\delta^2+\frac{b^2\theta^2}{\theta^2-1}\right)^{1/2}, \\ \eta(\theta) &= \frac{\delta^2/27+b^2/(\theta^2-1)}{\xi^2(\theta)}. \end{aligned} \tag{3.5}$$

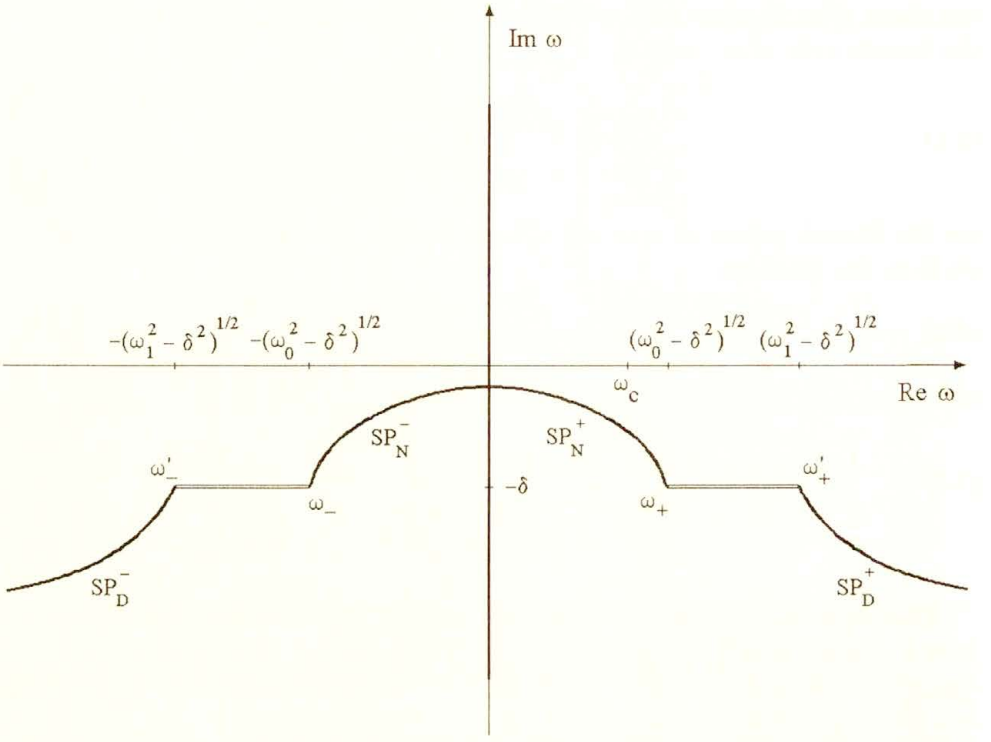

FIG. 1. Trajectories followed by the saddle-points $SP_D^{\pm}$ and $SP_N^{\pm}$ in the complex ω-plane as θ varies from 1 to ∞.

The locations of near saddle-points are described by

$$\omega_{SP_N^{\pm}} \cong \begin{cases} i\left[\pm|\psi(\theta)| - \dfrac{2}{3}\delta\zeta(\theta)\right], & 1 \le \theta < \theta_1\,, \\ -i\dfrac{2\delta}{3\alpha}\,, & \theta = \theta_1\,, \\ \pm\psi(\theta) - i\dfrac{2}{3}\delta\zeta(\theta), & \theta > \theta_1\,, \end{cases} \tag{3.6}$$

where

$$\psi(\theta) = \left[\frac{\omega_0^2(\theta^2-\theta_0^2)}{\theta^2-\theta_0^2+3\alpha b^2/\omega_0^2} - \delta^2\left(\frac{\theta^2-\theta_0^2+2b^2/\omega_0^2}{\theta^2-\theta_0^2+3\alpha b^2/\omega_0^2}\right)^2\right]^{1/2},$$

$$\zeta(\theta) = \frac{3(\theta^2-\theta_0^2+2b^2/\omega_0^2)}{2(\theta^2-\theta_0^2+3\alpha b^2/\omega_0^2)}, \tag{3.7}$$

$$\alpha = 1 - \frac{\delta^2}{3\omega_0^2\omega_1^2}(4\omega_1^2+b^2).$$

The special values of θ are

$$\theta_0 = n(0) = (1 + b^2/\omega_0^2)^{1/2}, \tag{3.8}$$

$$\theta_1 \cong \theta_0 + \frac{2\delta^2 b^2}{\theta_0 \omega_0^2 (3\alpha\omega_0^2 - 4\delta^2)}.$$

As seen from (2.12), the amplitude factor under integral sign in (2.13) is a meromorphic function with infinite number of simple poles at

$$\omega = -i2k\beta + \omega_c, \qquad k = 0, 1, 2, \ldots. \tag{3.9}$$

Adjacent poles are equally separated by the quantity $i2\beta$. If $\beta \to \infty$, only the pole at $\omega = \omega_c$ is of importance.

Having established the critical points of the integral in (2.6), one can set about the asymptotic evaluation of $A(z,t)$. The first step is to change the original contour of integration to a new one, to be denoted by $P(\theta)$, which is chosen such that it passes through the saddle points along a path consisting of paths of descent between adjacent saddle points (see Fig. 2 a, b). It was shown in [4] that such a change is possible (in the case of $1 \leq \theta < \theta_1$ the lower saddle point is not included because of the branch cut $\omega_+\omega_+'$ that makes the contour deformation to the contour through that point forbidden). By using this procedure, together with the Cauchy theorem, it follows that $A(z,t)$ can be represented as

$$A(z,t) = I(z,\theta) - \operatorname{Re}\left[2i\pi\Lambda(\theta)\right], \tag{3.10}$$

where

$$\Lambda(\theta) = \sum_p \operatorname*{Res}_{\omega=\omega_p} \left\{ \frac{i}{2\pi} \tilde{u}_\beta(\omega - \omega_c) e^{\frac{z}{c}\phi(\omega,\theta)} \right\} \tag{3.11}$$

is the sum of the residues at the poles that were intercepted in the course of contour deformation, and

$$I(z,\theta) = \frac{1}{2\pi} \operatorname{Re}\left\{ i \int_{P(\theta)} \tilde{u}_\beta(\omega - \omega_c) \exp\left[\frac{z}{c}\phi(\omega,\theta)\right] d\omega \right\}. \tag{3.12}$$

The problem thus reduces to the asymptotic evaluation of the integral $I(z,\theta)$ as z tends to infinity.

Results obtained with classical asymptotic methods, often referred to as non-uniform, fail for some special configurations of the critical points in the complex ω-plane (comp. [5]). In the present context these configurations are: (i) the pair of the distant saddle points tend to infinity, (ii) the near simple saddle points coalesce into one saddle point of the second order, and, (iii) the contour $P(\theta)$ crosses a pole of $\tilde{u}_\beta(\omega - \omega_c)$ as θ evolves. The first and the second case occur when θ is close, respectively, to 1 and to $\theta \cong \theta_1$. In order to obtain asymptotic representation of $A(z,t)$ which remains valid for all $\theta \geq 1$ including all three cases, uniform asymptotic techniques will here be used.

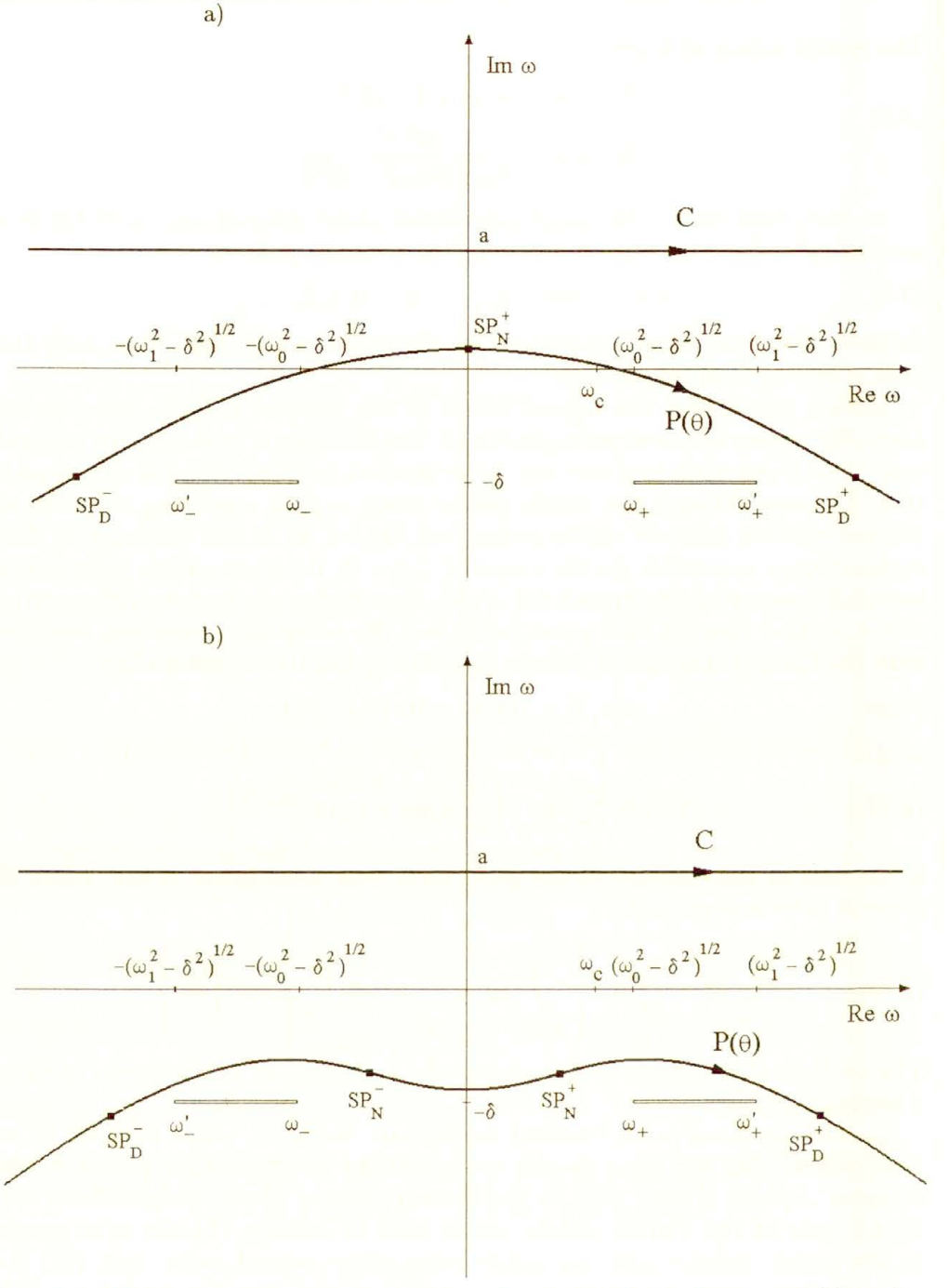

FIG. 2. a. The original contour of integration C and the deformed contour $P(\theta)$ in the case of $1 < \theta \leq \theta_1$. b. The original contour of integration C and the deformed contour $P(\theta)$ in the case of $\theta > \theta_1$.

3.1. Asymptotic representation of the Sommerfeld precursor

First, consider the contribution to the asymptotic expansion of $A(z,t)$ which is due to the pair of the distant saddle points $SP_D^{\pm}$. These points are dominant([1]) over the near saddle points in the interval $1 \leq \theta < \theta_{SB} < \theta_1$, where θ_{SB} is given by (see [4])

$$\theta_{SB} \cong \theta_0 - \frac{4\delta^2 b^2}{3\theta_0 \omega_0^4} - \left[\frac{27\delta^2 b^2(\theta_0-1)^2}{4\theta_0\omega^4}\right]^{1/3} \times \left(\left\{\left[1+\frac{\delta^2 b^2}{27\theta_0(\theta_0-1)\omega_0^4}\right]^{1/2}+1\right\}^{1/3} - \left\{\left[1+\frac{\delta^2 b^2}{27\theta_0(\theta_0-1)\omega_0^4}\right]^{1/2}-1\right\}^{1/3}\right). \tag{3.13}$$

For θ close to 1 the distant saddle points tend symmetrically about the imaginary axis to $\pm\infty$ and transform in the limit as $\theta = 1$ into a saddle point of infinite order. Classical asymptotic methods fail to describe such a situation; instead, a uniform asymptotic approach is here required. Procedure appropriate for this case was proposed by BLEISTEIN and HANDELSMAN [14]. It was adapted by OUGHSTUN and SHERMAN to integrals of the form of (3.12) to yield [5]

$$\begin{aligned} A_S(z,t) \sim \frac{\xi(\theta)}{2b}&\left\{\theta - 1 + \frac{b^2/2}{\xi^2(\theta)+\delta^2[1-\eta(\theta)]^2}\right\}^{1/2} \\ &\times \exp\left(-\delta\frac{z}{c}\left\{[1+\eta(\theta)](\theta-1)+\frac{(1/2)b^2[1-\eta(\theta)]}{\xi^2(\theta)+\delta^2[1-\eta(\theta)]^2}\right\}\right) \\ &\times \operatorname{Re}\left\{\exp\left(-i\frac{\pi}{2}\nu\right)\left[(\tilde{u}(\omega_{SP_D^+}-\omega_c)\{\xi(\theta)+(3/2)\delta i[1-\eta(\theta)]\}\right.\right. \\ &\quad + (-1)^{1+\nu}\tilde{u}(\omega_{SP_D^-}-\omega_c)\{\xi(\theta)-(3/2)\delta i[1-\eta(\theta)]\}) \\ &\quad \times J_\nu\left(\frac{z}{c}\xi(\theta)\left\{\theta-1+\frac{b^2/2}{\xi^2(\theta)+\delta^2[1-\eta(\theta)]^2}\right\}\right) \\ &\quad + \exp\left(-i\frac{\pi}{2}\right)\left(\tilde{u}(\omega_{SP_D^+}-\omega_c)\{\xi(\theta)+(3/2)\delta i[1-\eta(\theta)]\}\right. \\ &\quad\quad \left.\left.\left. - (-1)^{1+\nu}\tilde{u}(\omega_{SP_D^-}-\omega_c)\{\xi(\theta)-(3/2)\delta i[1-\eta(\theta)]\}\right) \right.\right. \\ &\quad\quad \left.\left. \times J_{\nu+1}\left(\frac{z}{c}\xi(\theta)\left\{\theta-1+\frac{b^2/2}{\xi^2(\theta)+\delta^2[1-\eta(\theta)]^2}\right\}\right)\right]\right\} \end{aligned} \tag{3.14}$$

([1]) A critical point is dominant over other critical points if $\operatorname{Re}[\phi(\omega,\theta)]$ at this point attains its maximum value, thus making the point least attenuated.

as $z \to \infty$, where J_ν is a Bessel function of the first kind. The parameter ν determines the behavior of the amplitude function at infinity ($\tilde{u}$ behaves like $\omega^{-(1+\nu)}$ as $|\omega| \to \infty$).

In the Bleistein and Handelsman method it is assumed that the amplitude factor in the integrand has a convergent Laurent series expansion in some neighborhood of infinity. In the case considered here this condition is not satisfied as the function $\tilde{u}(\omega - \omega_c)$ has poles along the line $\omega = -i2k\beta + \omega_c$. Those poles, however, do not affect the procedure of asymptotic expansion construction. It is so because the amplitude function is regular in the region which is the intersection of the region $|\omega| > R$ for some positive R, and a domain where all deformed integration contours appear. Apart from the line where $\tilde{u}(\omega - \omega_c)$ has pole singularities, this function behaves like

$$\tilde{u}(\omega - \omega_c) \sim -\frac{\beta}{\omega^2} + O(\omega^{-3}), \tag{3.15}$$

so that $\nu = 1$. As a result, the asymptotic expansion of $A_S(z,t)$, as $z \to \infty$, for the signal envelope given by (2.7), becomes

$$\begin{aligned} A_S(z,t) \sim \frac{\xi(\theta)}{2b} &\left\{\theta - 1 + \frac{b^2/2}{\xi^2(\theta) + \delta^2[1-\eta(\theta)]^2}\right\}^{1/2} \\ &\times \exp\left(-\delta\frac{z}{c}\left\{[1+\eta(\theta)](\theta-1) + \frac{(1/2)b^2[1-\eta(\theta)]}{\xi^2(\theta) + \delta^2[1-\eta(\theta)]^2}\right\}\right) \\ &\times \operatorname{Im}\Big[(\tilde{u}_\beta(\omega_{SP_D^+} - \omega_c)\{\xi(\theta) + (3/2)\delta i[1-\eta(\theta)]\} \\ &\quad + \tilde{u}_\beta(\omega_{SP_D^-} - \omega_c)\{\xi(\theta) - (3/2)\delta i[1-\eta(\theta)]\}) \\ &\quad \times J_1\left(\frac{z}{c}\xi(\theta)\left\{\theta - 1 + \frac{b^2/2}{\xi^2(\theta) + \delta^2[1-\eta(\theta)]^2}\right\}\right) \\ &\quad -i\Big(\tilde{u}_\beta(\omega_{SP_D^+} - \omega_c)\{\xi(\theta) + (3/2)\delta i[1-\eta(\theta)]\} \\ &\quad - \tilde{u}_\beta(\omega_{SP_D^-} - \omega_c)\{\xi(\theta) - (3/2)\delta i[1-\eta(\theta)]\}\Big) \\ &\quad \times J_2\left(\frac{z}{c}\xi(\theta)\left\{\theta - 1 + \frac{b^2/2}{\xi^2(\theta) + \delta^2[1-\eta(\theta)]^2}\right\}\right)\Big], \end{aligned} \tag{3.16}$$

where

$$\begin{aligned} &\tilde{u}_\beta(\omega_{SP_D^\pm} - \omega_c) \\ &\quad \cong \frac{1}{\beta}\mathcal{B}\left(\frac{\pm\xi(\theta) - \omega_c - \delta i[1+\eta(\theta)]}{2i\beta}\right) - \frac{i}{\pm\xi(\theta) - \omega_c - \delta i[1+\eta(\theta)]}. \end{aligned} \tag{3.17}$$

This expansion is uniform with respect to $\theta \geq 1$. It represents the Sommerfeld precursor, for it is related to the pair of distant saddle points which are dominant for small θ, and hence for small t.

3.2. Asymptotic representation of the Brillouin precursor

We now consider the contribution to the asymptotic expansion of $A(z,t)$ due to the near saddle points $SP_N^{\pm}$. Their contribution is descriptive of the Brillouin precursor and dominates over the Sommerfeld precursor as $\theta > \theta_{SB}$. If θ approaches θ_1 then the near saddle points coalesce and produce one saddle point of the second order. Since classical asymptotic methods fail to describe the field $A(z,t)$ in this case, a uniform approach should then be used. Such an approach was first proposed by CHESTER, FRIEDMAN and URSELL [17]. It is also derivable by using BLEISTEIN and HANDELSMAN theory [14], and was adapted by OUGHSTUN and SHERMAN [5] to integrals of the form of (3.12). Here, we employ the latter result.

Since there are two different descriptions of the locations of the near saddle points, depending on whether $1 \leq \theta < \theta_1$ or $\theta > \theta_1$, (comp. (3.6)), the asymptotic procedure is to be carried out for each of these cases separately. First, consider the case $1 \leq \theta < \theta_1$. Using the Oughstun and Sherman result one obtains

$$
\begin{aligned}
(3.18)\qquad A_B(z,t) \sim \exp\left[\frac{z}{c}a_0(\theta)\right] \Bigg(& \frac{1}{2}\left(\frac{c}{z}\right)^{1/3} \operatorname{Re}\{i[\tilde{u}_\beta(\omega_{SP_1}-\omega_c)|h_1(\theta)| \\
& + \tilde{u}_\beta(\omega_{SP_2}-\omega_c)|h_2(\theta)|]\}\operatorname{Ai}\left[|\alpha_1(\theta)|\left(\frac{z}{c}\right)^{2/3}\right] \\
& - \frac{1}{2|\alpha_1(\theta)|^{1/2}}\left(\frac{c}{z}\right)^{2/3} \operatorname{Re}\{i[\tilde{u}_\beta(\omega_{SP_1}-\omega_c)|h_1(\theta)| \\
& - \tilde{u}_\beta(\omega_{SP_2}-\omega_c)|h_2(\theta)|]\}\operatorname{Ai}^{(1)}\left[|\alpha_1(\theta)|\left(\frac{z}{c}\right)^{2/3}\right]\Bigg)
\end{aligned}
$$

as $z \to \infty$, where

$$
\begin{aligned}
\alpha_0(\theta) \cong -\delta\Bigg(\frac{2}{3}\zeta(\theta)(\theta-\theta_0) + \frac{b^2}{\theta_0\omega_0^4}\Bigg\{ & |\psi(\theta)|^2[\alpha\zeta(\theta)-1] \\
& - \frac{4}{9}\delta^2\zeta^2(\theta)\left[\frac{1}{3}\alpha\zeta(\theta)-1\right]\Bigg\}\Bigg),
\end{aligned}
$$

$$
\begin{aligned}
(3.19)\qquad \alpha_1 \cong |\psi(\theta)|\Bigg(\frac{3}{2}\Bigg\{ & \theta-\theta_0+\frac{b^2}{\theta_0\omega_0^4} \\
& \times\left[\frac{3}{4}\alpha|\psi(\theta)|^2+\alpha\delta^2\zeta^2(\theta)-2\delta^2\zeta(\theta)\right]\Bigg\}\Bigg)^{2/3},
\end{aligned}
$$

$$
\begin{aligned}
h_{1,2}(\theta) \cong \Bigg(\Bigg\{\frac{2\theta_0\omega^4}{3\alpha b^2|\psi(\theta)| \pm 2\delta[1-\alpha\zeta(\theta)]}\Bigg\}^3 & |\psi(\theta)|\Bigg\{\frac{3}{2}(\theta-\theta_0) \\
& + \frac{b^2}{\theta_0\omega_0^4}\left[\frac{3}{4}\alpha|\psi(\theta)|^2+\alpha\delta^2\zeta^2(\theta)-2\delta^2\zeta(\theta)\right]\Bigg\}\Bigg)^{1/6}
\end{aligned}
$$

and Ai is the Airy function. The plus sign in $(3.19)_3$ corresponds to the index 1 and the minus sign corresponds to the index 2. The functions $\tilde{u}_\beta(\omega_{SP_N^\pm} - \omega_c)$ are given by

$$(3.20)\qquad \tilde{u}_\beta(\omega_{SP_{1,2}} - \omega_c) \cong \frac{1}{\beta}\mathcal{B}\left(\frac{\pm|\psi(\theta)| - \frac{2}{3}\delta\zeta(\theta) + i\omega_c}{2\beta}\right) - \frac{1}{\pm|\psi(\theta)| - \frac{2}{3}\delta\zeta(\theta) + i\omega_c}.$$

Since the argument of the Airy function and its derivative is real and nonnegative for $\theta \leq \theta_1$, the Brillouin precursor is described by nonoscillating function in this domain.

In the case of $\theta > \theta_1$ the asymptotic description of the Brillouin precursor takes on the form

$$(3.21)\qquad A_B(z,t) \sim \exp\left[\frac{z}{c}a_0(\theta)\right]\left(\frac{1}{2}\left(\frac{c}{z}\right)^{1/3}\mathrm{Re}\,\{i[\tilde{u}_\beta(\omega_{SP_N^+} - \omega_c)|h^+(\theta)| + \tilde{u}_\beta(\omega_{SP_N^-} - \omega_c)|h^-(\theta)|]\}\mathrm{Ai}\left[-|\alpha_1(\theta)|\left(\frac{z}{c}\right)^{2/3}\right] + \frac{1}{2|\alpha_1(\theta)|^{1/2}}\left(\frac{c}{z}\right)^{2/3}\mathrm{Re}\,[\tilde{u}_\beta(\omega_{SP_N^+} - \omega_c)|h^+(\theta)| - \tilde{u}_\beta(\omega_{SP_N^-} - \omega_c)|h^-(\theta)|]\mathrm{Ai}^{(1)}\left[-|\alpha_1(\theta)|\left(\frac{z}{c}\right)^{2/3}\right]\right)$$

as $z \to \infty$, where

$$\alpha_0(\theta) \cong -\delta\left(\frac{2}{3}\zeta(\theta)(\theta_0) + \frac{b^2}{\theta_0\omega_0^4}\left\{[1 - \alpha\zeta(\theta)]\psi^2(\theta) + \frac{4}{9}\delta^2\zeta^2(\theta)\left[\frac{1}{3}\alpha\zeta(\theta) - 1\right]\right\}\right),$$

$$(3.22)\qquad \alpha_1^{1/2} \cong \left[-\frac{2}{3}i\psi(\theta)\left(\theta - \theta_0 - \frac{b^2}{2\theta_0\omega_0^4} \times \left\{\frac{4}{3}\delta^2\zeta(\theta)[2 - \alpha\zeta(\theta)] + \alpha\psi^2(\theta)\right\}\right)\right]^{1/3},$$

$$h^\pm(\theta) \cong \left[\left[i\frac{2\theta_0\omega^4}{3\alpha b^2\psi(\theta)}\right]^3\left[-\frac{3}{2}i\psi(\theta)\right]\left(\theta - \theta_0 - \frac{b^2}{2\theta_0\omega_0^4} \times \left\{\frac{4}{3}\delta^2\zeta(\theta)[2 - \alpha\zeta(\theta)] + \alpha\psi^2(\theta)\right\}\right)\right]^{1/6}.$$

Here,

$$\tilde{u}_\beta(\omega_{SP_N^\pm} - \omega_c) \cong \frac{1}{\beta}\mathcal{B}\left(\frac{\mp i\psi(\theta) - \frac{2}{3}\delta\zeta(\theta) + i\omega_c}{2\beta}\right) - \frac{1}{\mp i\psi(\theta) - \frac{2}{3}\delta\zeta(\theta) + i\omega_c}. \tag{3.23}$$

Since the argument of the Airy function and its derivative is real and nonpositive for $\theta \geq \theta_1$, the Brillouin precursor is oscillating in this domain.

It can be shown that the formulas (3.18) and (3.21) represent a continuous function of θ. Moreover, these formulas provide a smooth transition in algebraic order of z, as the argument of the Airy function and its derivative tends to zero. Indeed, the algebraic order of $z^{-1/3}\mathrm{Ai}[-|\alpha_1(\theta)|(z/c)^{2/3}]$ and $z^{-2/3}\mathrm{Ai}^{(1)}[-|\alpha_1(\theta)| \cdot (z/c)^{2/3}]$ is $z^{-1/2}$, while the order of both $\mathrm{Ai}(0)$ and $\mathrm{Ai}^{(1)}(0)$ is $0(1)$. Hence, the resultant field is of the order of $z^{-1/2}$ when the near saddle points are separated, and of the order of $z^{-1/3}$ if they coalesce into one saddle point of the second order. This agrees with known results obtainable with non-uniform asymptotic approach.

The Brillouin precursor is insignificant for θ close to 1, but becomes of importance at $\theta > \theta_{SB}$, when it begins to dominate over the Sommerfeld precursor. In particular, at $\theta = \theta_0$ it suffers no exponential attenuation.

3.3. Interaction of pole singularity with the saddle point

As θ increases from 1 to ∞, singular points associated with the spectral function $\tilde{u}_\beta(\omega_{SP_N^\pm} - \omega_c)$ are intercepted while the contour $P(\theta)$ evolves and their contribution is represented by the function $\Lambda(\theta)$, as defined by (3.11). This contribution introduces a clearly discontinuous term on the rhs of (3.10), while the lhs is a continuous function of θ. Thus the problem at hand is to find asymptotic evaluation of $I(z,\theta)$ such, that the rhs of (3.10) is also continuous and equal asymptotically to $A(z,t)$.

A suitable tool, appropriate for this task, is that proposed by Bleistein and Handelsman. Their method allows for asymptotic evaluation of a contour integral with simple saddle point coalescing on an algebraic singularity of the integrand, [14]. In case the singularity is a simple pole, their procedure is equivalent to the VAN DER WAERDEN method, [18]. General results for this case have been adopted to integrals considered here by OUGHSTUN and SHERMAN [5] and will be employed in this paper.

Here, it is assumed that β is large enough so that only one pole, equal to $\omega = \omega_c$, is crossed by the contour $P(\theta)$. Additionally, the carrier frequency ω_c is assumed to lie above the dielectric absorption band, i.e. $\omega_c > (\omega_1^2 - \delta^2)^{1/2}$, but otherwise is finite. Under these assumptions the pole at $\omega = \omega_c$ interacts with the distant saddle point SP_D^+. According to the results obtained in [5],

the asymptotic approximation to $A(z,t)$ depends on the value of $\Delta(\theta)$, which is defined as

$$\Delta(\theta) = \left[\phi(\omega_{SP_D^+}, \theta) - \phi(\omega_c, \theta)\right]^{1/2}. \tag{3.24}$$

As θ increases from 1 to ∞, the saddle point SP_D^+ moves leftwards in the complex θ plane, and the path $P(\theta)$ through that point crosses the pole at $\theta = \theta_s$. With the help of the Bleistein and Handelsman method and its Oughstun and Sherman adaptation, the following asymptotic contribution to $A(z,t)$ is obtained. If $1 \leq \theta < \theta_s$, then the distance between the origin and the intersection of $P(\theta)$ with the real ω axis is larger than the distance between the origin and the pole, $\mathrm{Im}[\Delta(\theta)] > 0$, and

$$A_c(z,t) \sim \frac{1}{2\pi}\left\{-i\pi \operatorname{erfc}\left[-i\Delta(\theta)\left(\frac{z}{c}\right)^{1/2}\right]\exp\left[\frac{z}{c}\phi(\omega_p,\theta)\right] + \frac{1}{\Delta(\theta)}\left(\frac{\pi c}{z}\right)^{1/2}\exp\left[\frac{z}{c}\phi(\omega_{SP_D^+},\theta)\right]\right\} \tag{3.25}$$

as $z \to \infty$. If $\theta = \theta_s$, i.e. the path $P(\theta)$ crosses the simple pole singularity at $\omega = \omega_c$, then $\mathrm{Im}[\Delta(\theta)] = 0$, $\Delta(\theta) \neq 0$, and

$$A_c(z,t) \sim \frac{1}{2\pi}\left\{-i\pi \operatorname{erfc}\left[-i\Delta(\theta)\left(\frac{z}{c}\right)^{1/2}\right]\exp\left[\frac{z}{c}\phi(\omega_p,\theta_s)\right] + \frac{1}{\Delta(\theta_s)}\left(\frac{\pi c}{z}\right)^{1/2}\exp\left[\frac{z}{c}\phi(\omega_{SP_D^+},\theta_s)\right]\right\} + \mathrm{Re}\left\{i\exp\left[\frac{z}{c}\phi(\omega_p,\theta_s)\right]\right\} \tag{3.26}$$

as $z \to \infty$. In the remaining case, i.e. when $\theta > \theta_s$, or equivalently, when the distance between the origin and the intersection of $P(\theta)$ with the real ω axis is smaller than the distance between the origin and the pole, one has $\mathrm{Im}[\Delta(\theta)] < 0$, and

$$A_c(z,t) \sim \frac{1}{2\pi}\left\{i\pi \operatorname{erfc}\left[i\Delta(\theta)\left(\frac{z}{c}\right)^{1/2}\right]\exp\left[\frac{z}{c}\phi(\omega_p,\theta)\right] + \frac{1}{\Delta(\theta)}\left(\frac{\pi c}{z}\right)^{1/2}\exp\left[\frac{z}{c}\phi(\omega_{SP_D^+},\theta)\right]\right\} + \mathrm{Re}\left\{i\exp\left[\frac{z}{c}\phi(\omega_p,\theta)\right]\right\} \tag{3.27}$$

as $z \to \infty$.

Here,

$$\operatorname{erfc}(\xi) = \frac{2}{\pi^{1/2}}\int_{\xi}^{\infty}\exp(-y^2)\,dy. \tag{3.28}$$

In (3.25) through (3.27) we have taken advantage of

$$\lim_{\omega\to\omega_c}[(\omega-\omega_c)\tilde{u}(\omega-\omega_c)]=i, \tag{3.29}$$

and of (3.12). The asymptotic expansion of $A_c(z,t)$, as given by (3.25)–(3.27), is a continuous function of θ, and hence yields a uniform asymptotic contribution to $A(z,t)$. As noted in [5], if the absolute value of the argument in erfc function is large enough, then this function can be replaced in (3.25)–(3.27) by its asymptotic representation, thus leading to the non-uniform asymptotic approximation to $A_c(z,t)$. It then follows that for the pole and the distant saddle point bounded away and z large, (3.25) introduces asymptotically no modification to the field; it is important only in the case of moderate values of the erfc argument. On the other hand, if the absolute value of this argument in (3.27) is large, $A_c(z,t)$ contribution to the field is, as expected, due to the residue of $\tilde{u}(\omega-\omega_c)$ at $\omega=\omega_c$. Note, that $A_c(z,t)$ is independent of β, and is the same as in the case of unit step envelope function [5].

To collect the results of the previous sections we note that contributions stemming from various critical points of an integral appear in the asymptotic expansion of the integral in the form of uncoupled components (comp. [14, 5, 19]). Accordingly, the asymptotic approximation to $A(z,t)$ is the sum consisting of the Sommerfeld and the Brillouin precursors, and the steady state contribution due to the pole singularity, i.e.

$$A(z,t)\sim A_S(z,t)+A_B(z,t)+A_c(z,t) \tag{3.30}$$

as $z\to\infty$.

4. Conclusion

The propagation of an electromagnetic signal in a dispersive medium described by the Lorentz model has been considered. The initial signal was chosen to be a sine wave of high real frequency modulated with the envelope described by the product of hyperbolic tangent and unit step function. A uniform asymptotic expansion of the propagating pulse in the medium in the mature regime was obtained with the help of modern asymptotic techniques.

Although the asymptotic representation for the field $A(z,t)$ was obtained under the restriction that the carrier frequency lies above the medium absorption band, a similar reasoning can be applied if this frequency occurs below that band.

References

1. A. SOMMERFELD, *Über die Fortpflanzung des Lichtes in disperdierenden Medien*, Ann. Phys. (Lepzig), **44**, 177–202, 1914.
2. L. BRILLOUIN, *Über die Fortpflanzung des Lichtes in disperdierenden Medien*, Ann. Phys. (Lepzig), **44**, 203–240, 1914.

3. L. BRILLOUIN, *Wave propagation and group velocity*, Academic, New York 1960.
4. K.E. OUGHSTUN and G.C. SHERMAN, *Propagation of electromagnetic pulses in a linear dispersive medium with absorption (the Lorentz medium)*, J. Opt. Soc. Am., **B 5**, 817–849, 1988.
5. K.E. OUGHSTUN and G.C. SHERMAN, *Uniform asymptotic description of electromagnetic pulse propagation in a linear dispersive medium with absorption (the Lorentz medium)*, J. Opt. Soc. Am., **A 6**, 1394–1420, 1989.
6. K.E. OUGHSTUN and G.C. SHERMAN, *Uniform asymptotic description of ultrashort rectangular optical pulse propagation in a linear, causally dispersive medium*, Phys. Rev., **A 41**, 6090–6113, 1990.
7. K.E. OUGHSTUN, *Pulse propagation in a linear, casusally dispersive medium*, Proc. IEEE, **79**, 1379–1390, 1991.
8. K.E. OUGHSTUN, *Noninstantaneous, finite rise-time effects on the precursor field formation in linear dispersive pulse propagation*, J. Opt. Soc. Am., **A 12**, 1715–1729, 1995.
9. P. WYNS, D.P. FOTY and K.E. OUGHSTUN, *Numerical analysis of the precursor fields in linear dispersive pulse propagation*, J. Opt. Soc. Am., **A 6**, 1394–1420, 1989.
10. K.E. OUGHSTUN, P. WYNS and D.P. FOTY, *Numerical determination of the signal velocity in dispersive pulse propagation*, J. Opt. Soc. Am., **A 6**, 1430–1440, 1989.
11. G.C. SHERMAN and K.E. OUGHSTUN, *Energy-velocity description of pulse propagation in absorbing, dispersive dielectrics*, J. Opt. Soc. Am., **B 12**, 229–247, 1995.
12. J.G. BLASCHAK and J. FRANZEN, *Precursor propagation in dispersive media from short rise-time pulses at oblique incidence*, J. Opt. Soc. Am., **A 12**, 1501–1512, 1995.
13. J.A. STRATTON, *Electromagnetic theory*, Mc Graw Hill, New York, pp. 333–340, 1941.
14. N. BLEISTEIN and R.A. HANDELSMAN, *Asymptotic expansions of integrals*, Holt, Rinehart and Winston, Ch. 9, 1975.
15. K.E. OUGHSTUN, *Propagation of optical pulses in dispersive media*, Ph.D. dissertation, University of Rochester, Rochester, N.Y. 1978.
16. I.M. RIZHIK and I.S. GRADSHTEIN, *Tables of integrals, sums, series and products* [in Russian], Fizmatgiz, Moscow, Ch. 6, 1962.
17. C. CHESTER, B. FRIEDMAN and F. URSELL, *An extension of the method of steepest descents*, Proc. Cambridge Philos. Soc., **53**, 599–611, 1957.
18. B. VAN DER WAERDEN, *On the method of saddle points*, Appl. Sci. Res., no. B 2, 33–45, 1952.
19. A. CIARKOWSKI, *Uniform asymptotic expansion of an integral with a saddle point, a pole and a branch point*, Proc. R. Soc. Lond., **A 426**, 273–286, 1989.

POLISH ACADEMY OF SCIENCES
INSTITUTE OF FUNDAMENTAL TECHNOLOGICAL RESEARCH
e-mail: aciark@ippt.gov.pl

Received December 23, 1996; new version June 6, 1997.

Arch. Mech., 49, 5, pp. 893–917, Warszawa 1997

On the description of the consolidation phenomenon by means of a two-component continuum

W. KEMPA (ESSEN)

THE PURPOSE of the present paper is the consistent formulation of the initial-boundary value problem for the consolidation phenomenon within the frame of a new two-component continuum model. The new class of models of two-component continua characterized by the balance equation for porosity is presented. The initial-boundary value problem with regard to the physical features of the consolidation is formulated. Some additional constitutive relations for the boundary quantities are proposed. Bearing in mind these constitutive relations, an example of a one-dimensional structure is calculated. The results of the numerical simulation are the basis for the parameter study of some constants of the model.

1. Introduction

THE HISTORY of development of the mathematical description of the consolidation phenomenon goes back to the twenties of this century. At this time *von Terzaghi* has derived the consolidation equation under strongly simplifying assumptions and presented it in his work [1]. The most important assumption was that the influence of the inertia forces has been neglected in his investigations. The consequences of this assumption are that the disturbance propagates in the domain with infinite speed what does not agree with the reality. This equation is the basis of consolidation calculation within the scope of soil mechanics up to the present time.

The development of the mixture theories and, especially, of the porous media theories based on the principles of the continuum mechanics has allowed to describe this phenomenon on the macroscopical level in mathematically exact and physically more accurate way.

The most of the existing macroscopic models of this sort are based on the model of multicomponent continuum with the so-called incompressible components that have been introduced by BOWEN [2]. From the point of view of continuum mechanics these models differ from each other only in the choice of constitutive relations. However, the model of BOWEN and its different modifications cause serious mathematical problems, particularly in their numerical treatment because the number of the governing equations and the number of the unknown fields are not equal.

One of the consequences of this fact is that the consistent formulation of the boundary value problem for most models of this type is not possible. The existing numerical calculations could be obtained only with additional conditions on the boundary. These conditions are justified neither from the mathematical nor from the physical point of view. HUTTER, JÖHNK and SVENDSEN show in their work [3] an example of such a model yielding results only in one of the limit cases namely only then if solely one of the constituting components exists! We shall not discuss the problems connected with the construction of the class of Bowen-like models, nevertheless it can be easily proved that most of these models are mathematically not consistent.

Moreover, there exist also models proposed in the works [4, 5, 6 and 7] based on the concept of the so-called equilibrated forces. The system of the governing equations in such models is closed with an additional equation which is motivated by the information won from the microscopic level of observation. However, the identification of the microscopic quantities is not obvious and it causes some problems.

A detailed overview of the existing porous media models and the discussion of some new tendencies in the theories of porous media can be found in the paper by DE BOER [8].

The class of models which is the basis for the formulation of the initial-boundary value problem and for the numerical calculation in this work is the new one. It has been developed by WILMAŃSKI and presented first in the paper [9].

The system of governing equations of this model includes the balance equation for porosity. This equation allows the macroscopical description of the properties of the semimicroscopical level of observation. Due to the fact that the porosity is a scalar variable, only one of the properties of the semimicroscopic domain, namely the volume contribution of the pores, can be reflected on the macroscopic level in this way. The physical motivation for this equation and its derivation can be taken from the work [10] of WILMAŃSKI.

The aim of this work is the formulation of the initial-boundary value problem for the consolidation phenomenon and the numerical parameter study of some model constants appearing in the class of models presented in the paper [9]. In the second section, a simplified model constituting the basis for our calculation is described. Then, we go over to the main part of this paper. We formulate the initial-boundary value problem for the simplified model in a consistent way. The fourth section is devoted to the description of the methods enabling the calculation of a simple one-dimensional example. Finally, the work is closed with the discussion of the numerical results and completed with the concluding remarks.

2. Basic concepts

The thermodynamical behaviour of a two-component continuum constituting of materially homogeneous components, a solid and a fluid one, can be described

generally in a similar way as the behaviour of a mixture of two immiscible fluids, by using the spatial description for the fluid and the material description for the solid through the following set of unknown fields

$$\{\varrho_t^F, \mathbf{v}_F\} \times \{\varrho^S, \boldsymbol{\chi}_S, n\} \,. \tag{2.1}$$

The only difference between a two-component porous medium and a mixture of two immiscible fluids is the occurence of the variable n standing for the porosity which apears in the set (2.1). The quantities ϱ_t^F and ϱ^S describe the macroscopical partial mass densities of the fluid (current) and of the solid (initial), respectively. The motion of the solid component is described by the function $\boldsymbol{\chi}_S$ and the kinematics of the fluid is defined by the *Eulerian* description by the velocity field $\mathbf{v}_F$.

In order to avoid the difficulties in the formulation of the boundary value problem we choose after WILMAŃSKI [11] the *Lagrangean* uniform description for both components. In such a case we have for a homogeneous solid without mass exchange between components

$$\varrho^S = \text{const} \,. \tag{2.2}$$

Then, the kinematic behaviour of the fluid is determined by the so-called *Lagrangean* fluid velocity $\mathbf{X}'_F$, which has been derived in [11].

The set (2.1) of the unknown fields takes now the form

$$f := \{\varrho^F, \mathbf{X}'_F, \boldsymbol{\chi}_S, n\} \,, \tag{2.3}$$

where ϱ^F is the mass density of the fluid referred to the reference configuration of the solid.

Due to the *Lagrangean* uniform description for both components, the functions of the set f have the same domain, i.e. they are functions of the material points X of the skeleton and of the time t.

The material points X of the skeleton belong to the domain $\mathcal{B}(X \in \mathcal{B})$ of the three-dimensional differentiable manifold. In this work we identify the domain $\mathcal{B}$ with a chosen configuration of the skeleton with the positions $\mathbf{X}$ of the material points X at the instant of time $t \equiv t_0$. Then, the current position of a material point X of the solid is defined in the following way

$$\mathbf{x} = \boldsymbol{\chi}_S(\mathbf{X}, t), \qquad \mathbf{x} \in \mathcal{B}_t \,, \qquad \mathcal{B}_t := \boldsymbol{\chi}_S(\mathcal{B}, t) \subset \mathbf{R}^3, \quad t \in \mathcal{T} \subset \mathbf{R}^1, \tag{2.4}$$

where $\mathcal{B}_t$ is the actual configuration.

If the set f of mappings is the solution of an appriopriate initial-boundary value problem for the set of field equations then isothermal processes taking place in the above continuum can be defined in the following way

$$\bigwedge_{\mathbf{x}\in\mathcal{B},\, t\in\mathcal{T}} : (\mathbf{X}, t) \mapsto (\varrho^F, \mathbf{X}'_F, \mathbf{x}, n) \in \mathcal{V}^8, \tag{2.5}$$

where $\mathcal{V}^8$ is the eight-dimensional vector space of the values of the fields.

The fields (2.3) should be determined through the system of partial differential equations following from the balance equations. In the case of the linear model, considered in this work, we do not have to distinguish between the material (*Lagrangean*) and *Eulerian* description of motion [11]. We can also use the displacement vector $\mathbf{u}_S$ instead of the function of motion $\boldsymbol{\chi}_S$. Consequently, the set of unknown fields for such a case can be chosen in the following manner

$$F := \left\{ \varrho_t^F, n^{\triangle}, \mathbf{v}_F, \mathbf{u}_S \right\}, \qquad n^{\triangle} := n - n_0 , \tag{2.6}$$

where n_0 is the constant equilibrium value of the porosity.

The corresponding field equations follow from the balance laws. For the elastic skeleton and the ideal fluid, they have the form

$$\begin{aligned}
&\frac{\partial \varrho_t^F}{\partial t} + \operatorname{div}(\varrho_t^F \mathbf{v}_F) = 0, \\
&\frac{\partial n^{\triangle}}{\partial t} + \gamma_0 \operatorname{div} \mathbf{v}_F = -\frac{n^{\triangle}}{\tau}, \\
&\varrho^S \frac{\partial^2 \mathbf{u}_S}{\partial t^2} - \operatorname{div} \mathbf{T}_S - \bar{\pi}\mathbf{w} - \varrho^S \mathbf{b}_S = \mathbf{0}, \\
&\varrho_t^F \frac{\partial \mathbf{v}_F}{\partial t} + \varrho_t^F \operatorname{grad} \mathbf{v}_F \mathbf{v}_F - \operatorname{div} \mathbf{T}_F + \bar{\pi}\mathbf{w} - \varrho_t^F \mathbf{b}_F = \mathbf{0}, \quad \mathbf{w} := \mathbf{v}_F - \frac{\partial \mathbf{u}_S}{\partial t},
\end{aligned} \tag{2.7}$$

where the partial stress tensors $\mathbf{T}_S$ and $\mathbf{T}_F$ satisfy the following constitutive relations

$$\begin{aligned}
&\mathbf{T}_S = \mathbf{T}_S^{\mathrm{cl}} + p^{\mathrm{int}}\mathbf{I}, \qquad \mathbf{T}_S^{cl} = \lambda^S (\mathbf{E}_S \cdot \mathbf{I})\mathbf{I} + 2\mu^S \mathbf{E}_S , \\
&\mathbf{T}_F = -p_{c1}^F \mathbf{I} - p^{\mathrm{int}}\mathbf{I}, \quad p_{c1}^F := p_0^F + \frac{1}{\kappa^F} \ln\left(\frac{\varrho_t^F}{\varrho_{t0}^F}\right), \qquad p^{\mathrm{int}} := \gamma_0 \frac{\varrho_t^F}{\tau \mathcal{N}} n^{\triangle} .
\end{aligned} \tag{2.8}$$

The above relations contain the following material constants depending on the equilibrium porosity n_0

$$\mathcal{C} := \{\lambda^S, \mu^S, \kappa^F, \bar{\pi}, \mathcal{N}, \tau, \gamma_0\} . \tag{2.9}$$

As shown in the earlier papers on the subject (e.g. [9, 12]), they can be found for many materials by means of dynamical experiments.

Otherwise, the tensor $\mathbf{E}_S$ in (2.8) denotes the *Green–St. Venant* deformation tensor for small deformations

$$\mathbf{E}_S \approx \frac{1}{2}\left[\operatorname{grad} \mathbf{u}_S + (\operatorname{grad} \mathbf{u}_S)^T\right] \tag{2.10}$$

and ϱ_{t0}^F denotes the reference value of the fluid mass density corresponding to the pressure p_0^F.

3. The consistent formulation of the initial-boundary value problem for consolidation

The consolidation phenomenon as a special kind of physical processes is already well known. During such processes, which take place in multicomponent continua, one or more components flow out of the domain of the multicomponent continuum due to the action of the external load. Consequently, the concept of free surface must be accounted for by the calculation of the consolidation phenomena. In contrast to the one-component materials, in which the free surface problems appear only then if wave propagation, phase changes, plastic deformation and some other problems of the change of material structure are being treated, the free surface in the multicomponent continua appears already if the free boundary is permeable.

If we assume that the boundary surface is material with respect to the solid boundary $\partial\mathcal{B}$, i.e. we identify the boundary of the treated continuum with the boundary of the skeleton then it is singular as well as non-material for the outflowing component. This fact is then reflected in the relation

$$\mathbf{c} \equiv \mathbf{v}_S|_{\partial\mathcal{B}}\,, \tag{3.1}$$

where $\mathbf{c}$ is the velocity of the free boundary.

Further, we shall assume that the boundary surface is ideal, i.e. it does not possess any intrinsic structure. We denote such a boundary surface as S.

In order to describe this surface we have to formulate the balance equations on the ideal surface S. We do not need to derive these conditions because their derivation is standard and it has been found by WILMAŃSKI in his work [11]. If we write the governing equations (2.7) in the integral form and extend them to hold in the limit on the singular surfaces then we obtain the following local dynamic compatibility conditions:

- for the solid component

$$[\mathbf{T}_S]\,\mathbf{n} = \mathbf{0}, \tag{3.2}$$

- for the fluid component

$$[\varrho_t^F(\mathbf{v}_F - \mathbf{v}_S)]\cdot\mathbf{n} = 0, \tag{3.3}$$

$$[\mathbf{T}_F]\,\mathbf{n} = [\varrho_t^F(\mathbf{v}_F - \mathbf{v}_S)\cdot\mathbf{n}\,\mathbf{v}_F]\,, \tag{3.4}$$

- for the porosity

$$[N_0(\mathbf{v}_F - \mathbf{v}_S)]\cdot\mathbf{n} = 0, \tag{3.5}$$

where N_0 is a constant and the square brackets denote the difference of the limit values between the positive and the negative sides of the surface S, i.e.

$$[...] := (...)^+ - (...)^- \tag{3.6}$$

and the internal side of the boundary has been chosen as the negative one. It is convenient to introduce the following definition

$$m^F := \varrho_t^F (\mathbf{v}_F - \mathbf{v}_S) \cdot \mathbf{n}. \tag{3.7}$$

The relation (3.7) represents namely the mass flux of the fluid component through the boundary surface S per time unit and area unit. The physical meaning of the flow continuity through the non-material surface for the fluid is that the fluid component does not stick to this surface.

In contrast to the relation (3.4), the relation (3.2) is identical with the classical *Poisson* condition. The relation (3.4) shows that the contact force in the fluid is not continuous. We will see in the sequel that this fact has a great influence on the formulation of the boundary value problem because such an inhomogeneous dynamic compatibility condition indicates the existence of the free surface. The compatibility condition (3.5) for the porosity does not influence the formulation of the boundary value problem in the simplified case considered in this work. Therefore we skip it in our consideration. Finally it should be mentioned that the mass conservation law for the skeleton does not appear as a dynamic compatibility condition because it is identically fulfilled.

We can now pass over to the formulation of the boundary value problem. Since we have to formulate the boundary quantity neither for the mass conservation law $(2.7)_1$ nor for the equation for porosity $(2.7)_2$, the mathematical structure of the governing equations (2.7) requires only the formulation of two vector quantities on the boundary. We can see that in the case of the chosen simplified model, the balance equation for porosity transforms to the evolution equation $(2.7)_2$.

For this reason, we shall treat in the sequel only both the balance equations of momentum. First, we integrate the relations $(2.7)_3$ and $(2.7)_4$ over the domain $\mathcal{B}$ and obtain, after using the compatibility conditions (3.2), (3.4) and the definition (3.7),

$$\begin{aligned}
&\int_{\mathcal{B}} \left(\varrho^S \frac{\partial^2 \mathbf{u}_S}{\partial t^2} - \bar{\pi}\mathbf{w} - \varrho^S \mathbf{b}_S \right) dv = \int_{\partial\mathcal{B}} \mathbf{t}_S^+ \, da \,, \\
&\int_{\mathcal{B}} \left(\varrho_t^F \frac{\partial \mathbf{v}_F}{\partial t} + \varrho_t^F \operatorname{grad} \mathbf{v}_F \mathbf{v}_F + \bar{\pi}\mathbf{w} - \varrho_t^F \mathbf{b}_F \right) dv \\
&\qquad = \int_{\partial\mathcal{B}} \left[\mathbf{t}_F^+ - m^{F+} \left(\mathbf{v}_F^+ - \mathbf{v}_F^- \right) \cdot \mathbf{n}\, \mathbf{n} \right] da \,.
\end{aligned} \tag{3.8}$$

In this transformation we have employed the following relation

$$\mathbf{v}_F^+ - \mathbf{v}_F^- = \left(\mathbf{v}_F^+ \cdot \mathbf{n} - \mathbf{v}_F^- \cdot \mathbf{n}\right)\mathbf{n} \tag{3.9}$$

resulting from the fact that the partial fluid stress tensor contains only the spherical part.

The analysis of the relations (3.8) leads to the conclusion that due to the outflow of the fluid component, two vector and two scalar boundary quantities for two-component continua described by similar equations as the relations (2.7) must be specified on the boundary. These are in our case

$$\mathcal{R} := \left\{\mathbf{t}_S^+, \mathbf{t}_F^+, m^{F^+}, \mathbf{v}_F^+ \cdot \mathbf{n}\right\}. \tag{3.10}$$

It should also be mentioned that the treatment of one-component continua does not require the formulation of an additional scalar quantity until we have to solve a problem with the non-material surface such as, for instance, the wave propagation problems. This fact has been illustrated in the paper [13] in the discussion of an example of propagation of surface waves.

Next, we formulate the set of boundary quantities (3.10) in accordance with the physics of the consolidation phenomenon. Before we do so, the class of boundaries which can appear in the consolidation problem must be defined.

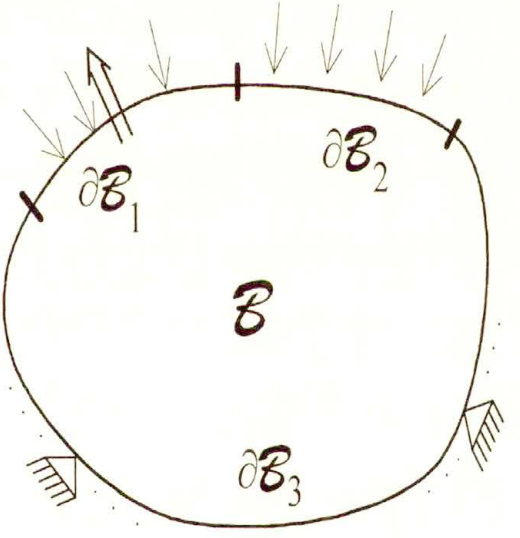

FIG. 1. The class of boundaries by consolidation – a possibility.

In Fig. 1 we show schematically these possible classes of boundary conditions on the boundary $\partial\mathcal{B}$ $(= \partial\mathcal{B}_1 + \partial\mathcal{B}_2 + \partial\mathcal{B}_3)$ of the body $\mathcal{B}$. Namely

- $\partial\mathcal{B}_1$ – loaded and permeable free boundary,

- $\partial\mathcal{B}_2$ – loaded and impermeable boundary,
- $\partial\mathcal{B}_3$ – impermeable fixed boundary.

By the definition of the boundary quantities the physical features of consolidation must be taken into consideration. As we have already mentioned, the consolidation process will be characterized through the outflow of one or more fluid components outside from the domain of the multicomponent continuum due to the action of the external load. One of the consequences of the outflow process is the existence of the free surface, whose description, as we have shown already, requires an additional scalar quantity prescribed on the boundary. Moreover, the acting external load cannot be *a priori* divided into separate parts acting on the fluid and on the solid, respectively, because it does not happen in the reality.

According to this, we add up the partial loads $\mathbf{t}_S^+$ and $\mathbf{t}_F^+$ in the following constitutive way

$$\mathbf{t}^{\text{ext}} = \mathbf{t}_S^+ + \mathbf{t}_F^+ , \tag{3.11}$$

where the index "ext" indicates the whole external acting load. If we make the above assumption we cannot use the set (3.10) in the formulation of the boundary value problem because we are missing one vector quantity. However, this additional vector quantity can be defined on the boundary in accordance with the physical features of the consolidation phenomenon.

The outflow of the fluid component through the boundary of the domain of the multicomponent continuum means that the velocity difference $\mathbf{w}$ on the boundary is not equal to zero. So we choose this vector quantity as the missing second vector boundary relation. It can be also written in the form

$$\mathbf{w}^+ = w^+\mathbf{n} + \mathbf{w}_\perp^+ , \tag{3.12}$$

where $\mathbf{w}_\perp$ has the meaning of the velocity difference, perpedicular to the unit outward normal vector $\mathbf{n}$. For all components of the vector $\mathbf{w}^+$ we must propose constitutive relations. Before we pass over to the formulation of the boundary quantities, we want to replace the scalar quantity $(\mathbf{v}_F^+ \cdot \mathbf{n})$ by $\varrho_t^{F^+}$ by means of the definition (3.7) in the following way

$$\left(\mathbf{v}_F^+ - \mathbf{v}_F^-\right) \cdot \mathbf{n} = m^{F^+} \left(\frac{1}{\varrho_t^{F+}} - \frac{1}{\varrho_t^{F-}}\right). \tag{3.13}$$

With (3.13) the right-hand side of the relation $(3.8)_2$ transforms to

$$\int_{\mathcal{B}} (...)\, dv = \int_{\partial\mathcal{B}} \left[\mathbf{t}_F^+ - \left(m^{F^+}\right)^2 \left(\frac{1}{\varrho_t^{F+}} - \frac{1}{\varrho_t^{F-}}\right)\mathbf{n}\right] da. \tag{3.14}$$

It has been shown in the paper [13] that the second term of the surface integral can be neglected in consolidation problems because the value of the

acting force normal to the boundary is much greater than the value of the second term, the so-called flow force. However, this force must be taken into account in cases characterized through the rapid outflow processes such as combustion. This problem is nonlinear, even if the operator is linear because the nonlinearity results from the nonlinear boundary condition.

The above considerations show that the set (3.10) must be replaced by the following one

$$\mathcal{R}' := \left\{ \mathbf{t}^{\text{ext}}, \mathbf{w}^{+}, m^{F^{+}}, \varrho_t^{F^{+}} \right\}. \tag{3.15}$$

For the last three quantities the constitutive realtions must be formulated. We begin with the vector quantity $\mathbf{w}^{+}$. We assume after WILMAŃSKI ([11]) that the outflowing fluid cannot slip along the boundary. Therefore, we obtain for both components which are perpedicular to the normal vector

$$\mathbf{w}_{\perp}^{+} \equiv \mathbf{0}. \tag{3.16}$$

In the case of an ideal fluid, this result can be obtained indepedently as a mathematical consequence of the material properties.

The component in the direction of the normal unit vector can be directly formulated from the relation (3.7) using the definition $(2.7)_5$

$$w^{+} = \frac{m^{F^{+}}}{\varrho_t^{F^{+}}}. \tag{3.17}$$

We see, that the normal component of one of the two vector boundary quantities is determined by the remaining scalar boundary quantities. One can also observe that the vector boundary quantity (3.12) is an inhomogeneous one. This is an additional characteristic property of the multicomponent continua. For the mass flux of the fluid component we assume the following constitutive relation

$$m^{F^{+}} = \beta \left(p^{F^{-}} \Big|_{\partial \mathcal{B}} - n^{-}|_{\partial \mathcal{B}}\, p^{A} \right). \tag{3.18}$$

A similar relation has been proposed for the consolidation phenomenon by RUNESSON in his Ph.D. Thesis [14]. However, relations of this form are also well known in other fields of physics (e.g. heat transfer through thin walls). Some indications of the difficulties connected with the formulation of the boundary value problem can be also found in the papers [20 – 23].

We see, that the mass flux of the fluid is determined by the partial pressure of the fluid and by one more external quantity, namely the atmospheric pressure p^{A}, weighted, according to *Dalton*'s law, with the porosity. The coefficient β describes the physical properties of the boundary and has, due to this interpretation, the meaning of surface permeability. We shall show in the parameter study in the Sec. 5, how great is the influence of the value of this coefficient on the value of the

mass transport through the boundary. For the purpose of this work we assume that the properties of the boundary are independent of the time and piecewise homogeneous. We obtain then

$$\frac{\partial \beta}{\partial t} \equiv 0, \qquad \frac{\partial \beta}{\partial \mathbf{x}} \equiv \mathbf{0} \;\Rightarrow\; \beta = \text{const}. \tag{3.19}$$

We shall assume for the second scalar boundary quantity that the fluid mass density on the exterior of the boundary is constant, i.e.

$$\varrho_t^{F^+} = \text{const}. \tag{3.20}$$

We see that the relations (3.11) ÷ (3.12), (3.16) ÷ (3.18) and (3.20) determine the quantities included in the set $\mathcal{R}'$. Summarizing the above analysis we obtain the following relations for the whole boundary (see Fig. 1):

- loaded and permeable free boundary

$$\bigwedge_{\mathbf{x}\in\partial\mathcal{B}_1} \begin{cases} \mathbf{t}^{\text{ext}} \neq \mathbf{0}, \\ \mathbf{w}^+ = \dfrac{m^{F^+}}{\varrho_t^{F^+}}\mathbf{n}, \\ m^{F^+} = \beta\left(p^{F^-} - n^- p^A\right), \\ \varrho_t^{F^+} = \text{const}, \end{cases} \tag{3.21}$$

- loaded and impermeable boundary

$$\bigwedge_{\mathbf{x}\in\partial\mathcal{B}_2} \begin{cases} \mathbf{t}^{\text{ext}} \neq \mathbf{0}, \\ \mathbf{w}^+ = \dfrac{m^{F^+}}{\varrho_t^{F^+}}\mathbf{n}, \\ m^{F^+} = 0, \\ \varrho_t^{F^+} = \text{const}, \end{cases} \tag{3.22}$$

- impermeable fixed boundary

$$\bigwedge_{\mathbf{x}\in\partial\mathcal{B}_3} \begin{cases} \mathbf{v}_F^+ = \mathbf{0}, \\ \mathbf{w}^+ = \mathbf{0}, \end{cases} \tag{3.23}$$

where the boundary quantities can take the forms defined above.

Let us mention that the conditions (3.21) and (3.22) are the so-called mixed or *Robbin*'s boundary conditions and the conditions (3.23) are the well known essential or *Dirichlet*'s boundary conditions. In the case of a fixed boundary we can accept another possible definition of the boundary quantities since we need only two from the three existing kinematic quantities.

Due to the choice of the second vector quantity, namely the velocity difference $\mathbf{w}$, the system of the governing equations (2.7) must be transformed in a suitable way because the velocity difference $\mathbf{w}$ does not belong to the set (2.6) of the unknown fields. There are two ways of transforming the governing equations. The first one is the extension of the set of fields and of the equations through the relation $(2.7)_5$. The second one is the variable transformation

$$\left\{\varrho_t^F, n^{\triangle}, \mathbf{v}_F, \mathbf{u}_S\right\} \to \left\{\varrho_t^F, n^{\triangle}, \mathbf{v}_F, \mathbf{w}\right\}. \tag{3.24}$$

We have decided to go the first way because it is technically easier to handle. Let us notice that the boundary value problem for the additional equation does not need to be formulated since the relation $(2.7)_5$ belongs to the class of the evolution equations. The set of the unknown fields (2.6) takes now the form

$$F' := \left\{\varrho_t^F, n^{\triangle}, \mathbf{v}_F, \mathbf{u}_S, \mathbf{w}\right\}. \tag{3.25}$$

Finally, we formulate the initial value problem for the above set of unknown fields. We choose

$$\bigwedge_{\mathbf{x}\in\mathcal{B}} \begin{cases} \varrho_t^F(\mathbf{x},t)|_{t=0} = \varrho_0^F(\mathbf{x}), \\ n^{\triangle}(\mathbf{x},t)\big|_{t=0} = 0, \\ \mathbf{u}_S(\mathbf{x},t)|_{t=0} = \mathbf{0}, \\ \mathbf{v}_F(\mathbf{x},t)|_{t=0} = \mathbf{0}, \\ \mathbf{w}(\mathbf{x},t)|_{t=0} = \mathbf{0}, \end{cases} \tag{3.26}$$

where the function $\varrho_0^F(\mathbf{x})$ is the one-dimensional static solution of the balance law of momentum for fluid. If we introduce the coordinates shown in the Fig. 2 a, we obtain then the following distribution of the initial fluid mass density

$$\varrho_0^F \equiv \varrho^F(z, t=0) \cong \varrho_{t0}^F\left[1 + \kappa^F \varrho_{t0}^F g(h-z)\right] \tag{3.27}$$

with g as the value of the gravity acceleration.

With the last assertion we have closed the formulation of the initial-boundary value problem and now we pass over to the treatment of the numerical example.

4. Numerical simulation

In the present section we proceed to construct the weak formulation with respect to the already mentioned physical features of the consolidation.

The numerical simulation will be carried by the finite element method. We shall treat a simple one-dimensional example shown below in the Fig. 2 a. In this case the set (3.25) of unknown fields takes the following form

$$F^1 := \left\{\varrho_t^F, n^{\triangle}, u^S, v^F, w\right\}. \tag{4.1}$$

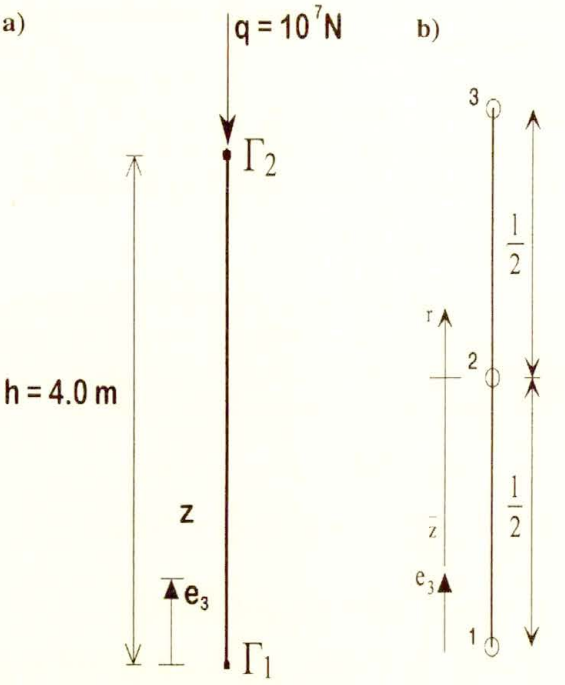

FIG. 2. a. The one-dimensional domain. b. Three-nodal continuum element.

For the purpose of the space discretization we use the finite element method and proceed in the following way. We identify a finite number G of points in the whole one-dimensional domain D, shown in the Fig. 2 a, and these shall be called nodal points. The whole domain will be divided in the standard way into E subdomains (finite elements) connected at nodes on their boundaries. The functions which form the set F^1 will be approximated locally over each finite element by continuous functions, the so-called trial functions, which are uniquely defined in terms of the values of the functions (or also their derivatives) at the nodal points belonging to each element. Furthermore, we make use of isoparametric elements by which the approximation of the element coordinates and of the functions appears by applying the same interpolation functions.

In accordance with the chosen one-dimensional domain, we use for the discretization three-nodal elements (see Fig. 2 b) with the well known quadratic linearly independent trial functions

$$\begin{aligned} \varphi_1 &= \frac{1}{2}(1-r) - \frac{1}{2}(1-r^2), \\ \varphi_2 &= 1 - r^2, \\ \varphi_3 &= \frac{1}{2}(1+r) - \frac{1}{2}(1-r^2), \end{aligned} \tag{4.2}$$

where the relation $r \equiv (2/1)\bar{z} - 1$ to calculate the natural coordinates holds true. We construct then the approximating functions $\check{\xi}$ for all unknown fields in the following manner

$$\check{\xi} = \sum_{j=1}^{3} \check{\xi}_j \varphi_j \,, \qquad \check{\xi} \equiv \left\{ \check{\varrho}_t^F, \check{n}^{\triangle}, \check{u}^S, \check{v}^F, \check{w} \right\}. \tag{4.3}$$

The most important property of the above relations is the fact that they fulfil each boundary condition for the chosen finite element because the trial function takes the value one on the node it is defined for, and vanishes identically on the other nodes of the element.

It is clear that the approximating functions do not fulfil exactly the set of the governing equations. If we insert the relations (4.3) into the governing equations they shall not be satisfied. There remains the error ε which is also called the residuum. In order to minimize the residuum ε, the undetermined parameters $\check{\xi}_j$ must be properly chosen. Let us mention that the above form (4.3) of the approximating functions is the conventional one in which the parameters $\check{\xi}_j$ depend on time and the trial functions (4.2) are functions of the space variable.

For the optimization of the approximating functions (4.3) the *Galerkin* method has been chosen. In the same way as by the application of other weighted residual methods, the arising errors will be projected one after another on the test functions, which are in the case of the *Galerkin* method the same as the trial functions φ_j. We obtain then for each equation an orthogonality condition of the form

$$\bigwedge_{i=\{1,2,3\}} (\varepsilon, \varphi_i) \equiv \int_{\mathcal{B}} \varepsilon \varphi_i \, dv = 0. \tag{4.4}$$

Using this procedure, the errors ε_j will be minimized in the averaging sense because the limited number of the trial functions spans only a finite-dimensional subspace of the space of exact solutions.

The use of the *Galerkin* method does not allow to define the essential boundary conditions. Therefore, we define in the sequel the coefficients which have the sense of the arbitrary increments of the prescribed kinematic boundary quantities. These arbitrary increments vanish identically for the prescribed value of the corresponding quantity and are undetermined if the quantity is unknown. Due to the relation (3.23), such arbitrary increments must be defined in our one-dimensional case for v^F and for w.

If we now apply the orthogonality conditions (4.4) to each of the governing equations (2.7) using the definition of the scalar product, we obtain in the

one-dimensional case the following equations:

$$
\bigwedge_{i:\ i=1,2,3}
\begin{cases}
\displaystyle\int_{-1}^{1}\left\{\frac{\partial\check{\varrho}_t^F}{\partial t}+\frac{\partial\check{\varrho}_t^F}{\partial z}\check{v}^F+\check{\varrho}_t^F\frac{\partial\check{v}^F}{\partial z}\right\}\varphi_i\,dr=0,\\
\displaystyle\int_{-1}^{1}\left\{\frac{\partial\check{n}^{\triangle}}{\partial t}+\gamma_0\frac{\partial\check{v}^F}{\partial z}+\frac{\check{n}^{\triangle}}{\tau}\right\}\varphi_i\,dr=0,\\
\displaystyle\int_{-1}^{1}\left\{\varrho^S\frac{\partial\check{v}^F}{\partial t}-\varrho^S\frac{\partial\check{w}}{\partial t}-\frac{\partial\check{\sigma}^S}{\partial z}-\bar{\pi}\check{w}+\varrho^S g\right\}\varphi_i\,dr=0,\\
\displaystyle\int_{-1}^{1}\left\{\check{\varrho}_t^F\frac{\partial\check{v}^F}{\partial t}+\check{\varrho}_t^F\frac{\partial\check{v}^F}{\partial z}\check{v}^F-\frac{\partial\check{\sigma}^F}{\partial z}+\bar{\pi}\check{w}\right\}\check{v}_i^{F^\delta}\varphi_i=0,\\
\displaystyle\int_{-1}^{1}\left\{\frac{\partial\check{u}^S}{\partial t}-\check{v}^F+\check{w}\right\}\check{w}_i^\delta\varphi_i\,dr=0,
\end{cases}
\tag{4.5}
$$

where $\check{v}_i^{F^\delta}$ and $\check{w}_i^\delta$ are the arbitrary increments described above, and the following definitions have been used

$$
\begin{aligned}
\check{\sigma}^S &:= (\lambda^S+2\mu^S)\frac{\partial\check{u}^S}{\partial z}+\frac{\gamma_0}{\mathcal{N}\tau}\check{\varrho}_t^F\check{n}^{\triangle},\\
\check{\sigma}^F &:= -\left(p_0^F+\frac{1}{\kappa^F}\ln\left(\frac{\check{\varrho}_t^F}{\varrho_{t0}^F}\right)+\frac{\gamma_0}{\mathcal{N}\tau}\check{\varrho}_t^F\check{n}^{\triangle}\right).
\end{aligned}
\tag{4.6}
$$

Let us mention that, due to prescribed distribution of the initial partial fluid mass density (see (3.27)), the influence of the gravity force on the fluid component has already been accounted for. In such a case the gravity force does not appear in the relation $(4.5)_4$.

If we prescribe the natural boundary condition on the boundary Γ_1 (see Fig. 2 a) and neglect (as mentioned in the Sec. 3) the nonlinear boundary contributions, then, bearing in mind the structure of the unspecified boundary quantities, the dynamic compatibility conditions (3.2)÷(3.4) and the definition (3.7), we obtain from the equation $(4.5)_4$

$$
\int_{-1}^{1}\left\{\left[\check{\varrho}_t^F\frac{\partial\check{v}^F}{\partial t}+\check{\varrho}_t^F\frac{\partial\check{v}^F}{\partial z}\check{v}^F+\bar{\pi}\check{w}\right]\check{v}^{F^\delta}+\check{\sigma}^F\frac{\partial\check{v}^{F^\delta}}{\partial z}+\frac{\partial(\check{\sigma}^S\check{v}^{F^\delta})}{\partial z}\right\}dr
= t^{\mathrm{ext}}\check{v}^{F^\delta}\Big|_{\Gamma=\Gamma_1+\Gamma_2},
\tag{4.7}
$$

where the relations $t^{\mathrm{ext}}\big|_{\Gamma_1}=-q$ for the top element and $\check{v}_1^{F^\delta}\big|_{\Gamma_2}\equiv 0$ for the

bottom element hold. To simplify the notation the following definition

$$\check{v}^{F^\delta} := \sum_{i=1}^{3} \check{v}_i^{F^\delta} \varphi_i \tag{4.8}$$

has been introduced.

Replacing Eq. $(4.5)_4$ by the relation (4.7) and integrating the system of Eqs. (4.5) over the treated one-dimensional domain we obtain a nonlinear system of algebraic equations which can be written in the following matrix form

$$\mathsf{D}\,\dot{\mathsf{u}} + \mathsf{K}\,\mathsf{u} = \mathsf{R}\,, \tag{4.9}$$

where D is the so-called damping matrix, K the so-called stiffness matrix, u and $\dot{\mathsf{u}}$ denote the process vector and its time derivative, respectively, and R denotes the load vector. We skip here the presentation of their explicit form. The solution of the system of nonlinear equations can be obtained by means of the *Newton – Raphson* method and the time integration by means of the *Newmark* method. Since the *Newmark* method is an implicit one, the relation (4.9) will be solved for the time $t + \triangle t$. The matrix equation (4.9) takes then the form

$$^{t+\triangle t}\mathsf{D}\,^{t+\triangle t}\dot{\mathsf{u}} + {}^{t+\triangle t}\mathsf{K}\,^{t+\triangle t}\mathsf{u} = {}^{t+\triangle t}\mathsf{R}\,. \tag{4.10}$$

The linearization of the above relation by means of the *Newton – Raphson* method leads to

$$^{t+\triangle t}_{(\iota-1)}\mathsf{D}\,^{t+\triangle t}_{(\iota)} \triangle \dot{\mathsf{u}} + {}^{t+\triangle t}_{(\iota-1)}\mathsf{K}\,^{t+\triangle t}_{(\iota)} \triangle \mathsf{u} = {}^{t+\triangle t}\mathsf{R} - {}^{t+\triangle t}_{(\iota-1)}\mathsf{F}\,, \tag{4.11}$$

where the index ι denotes the number of the iteration step, ${}^{t+\triangle t}_{(\iota-1)}\mathsf{F}$ is the internal force vector corresponding to the stresses, and $\triangle \mathsf{u}$ and $\triangle \dot{\mathsf{u}}$ denote the increments of the process vector and of its time derivative, respectively.

For the approximation of the increment of the time derivative of the process vector, the following linearized *Newmark* ansatz will be used

$$^{t+\triangle t} \triangle \dot{\mathsf{u}} = \frac{\delta}{\alpha \triangle t}\, {}^{t+\triangle t} \triangle \mathsf{u}\,. \tag{4.12}$$

Substitution of the above relation into Eq. (4.11) yields

$$^{t+\triangle t}_{(\iota-1)}\hat{\mathsf{K}}\,^{t+\triangle t}_{(\iota)} \triangle \mathsf{u} = {}^{t+\triangle t}\mathsf{R} - {}^{t+\triangle t}_{(\iota-1)}\mathsf{F}\,, \tag{4.13}$$

with the following definition of the so-called effective stiffness matrix

$$^{t+\triangle t}_{(\iota-1)}\hat{\mathsf{K}} := \frac{\delta}{\alpha \triangle t}\, {}^{t+\triangle t}_{(\iota-1)}\mathsf{D} + {}^{t+\triangle t}_{(\iota-1)}\mathsf{K}\,. \tag{4.14}$$

Furthermore, we choose for the constants α and δ the values 0.25 and 0.50, respectively. In this case the *Newmark* method is identical with the constant average acceleration method.

With the solution of Eq. (4.13) the process vector at the time $t + \triangle t$ and for the iteration step ι can be determined from the relation

$$(4.15) \qquad {}^{t+\triangle t}_{(\iota)}\mathsf{u} = {}^{t+\triangle}_{(\iota-1)}\mathsf{u} + {}^{t+\triangle t}_{(\iota)}\triangle\,\mathsf{u}\,.$$

If a chosen breaking off criterion is fulfilled, the value ${}^{t+\triangle t}_{(\iota)}\mathsf{u}$ is simultaneously the initial value of the process vector for the next time step.

5. Parameter study and concluding remarks

The purpose of this section is to study the constants of the chosen simplified model. We present here the qualitative comparison of the results obtained in this work with the classical results of the consolidation theory as well as we study the influence of variation the material constants on the quantitative results. The values of the following constants: λ^S, μ^S, $\mathcal{N}$ and τ have been taken from the work [15] of WILMAŃSKI. He has determined of values for these constants by means of the wave analysis using the experimental data quoted in the book [16] of BOURBIE, COUSSY and ZINSZNER. For the Massillon sandstone with empty pores and the porosity $n_0 = 0.23$ he obtained the following values:

$$(5.1) \qquad \begin{aligned} \lambda^S &= 10.766 \times 10^7\,\mathrm{Pa}\,,\\ \mu^S &= 6.144 \times 10^7\,\mathrm{Pa}\,,\\ \mathcal{N} &= 1.986 \times 10^{-2}\,\mathrm{sm}^{-2}\,,\\ \tau &= 3.699 \times 10^{-6}\,\mathrm{s}\,. \end{aligned}$$

The remaining quantities of the set (2.9) of the model constants are κ^F, $\bar{\pi}$, γ_0 and the additional constant β.

Let us treat a two-component material constituted by the solid component whose properties are described by the constants (5.1) and which is fully saturated with water. Simultaneously, we assume the effective compressibility of water

$$(5.2) \qquad \kappa^F = 0.452 \times 10^{-9}\,\mathrm{Pa}^{-1}\,.$$

The permeability coefficient $\bar{\pi}$ has been investigating of CHAMSAZ in his dissertation [17] and it takes the value $2.602 \times 10^{-9}\,\mathrm{Pa\,m^{-2}s}$ for the Massillon sandstone. For this order of magnitude of $\bar{\pi}$ CHAMSAZ obtains the value $w \simeq 0.14\,\mathrm{mh}^{-1}$ for the velocity difference which is a realistic one in the consolidation processes. Using the above value $\bar{\pi}$, the order of magnitude of the surface permeability β has been investigated in the paper [13]. It has been shown that

we can assume its value to be $\approx 1.0 \times 10^{-8}\,\mathrm{sm}^{-1}$. Both coefficients $\bar{\pi}$ and β will be varied in the following parameter study.

Finally let us assume for the last constant

$$\gamma_0 \equiv n_0 = 0.23\,. \tag{5.3}$$

This assumption can be motivated by the analysis of the limits of the present model. We shall skip these considerations in this paper. We assume the remaining constants to be

$$\begin{aligned} \varrho^S &= 1000.0\,\mathrm{kgm}^{-3}, \\ \varrho^F_{t0} &= 230.0\,\mathrm{kgm}^{-3}, \\ g &= 10.0\,\mathrm{ms}^{-2}, \\ p^A &= 100\,000.0\,\mathrm{N} \end{aligned} \tag{5.4}$$

and define the integration constant as follows

$$p^F_0 := n_0 p^A = 23\,000.0\ \mathrm{N}\,. \tag{5.5}$$

The above values of constants reflect the order of magnitude of the real constants which should be obtained by the proper averaging procedure. Such procedures are being presently investigated([1]). We shall not discuss this very important problem here.

As we have already mentioned, the character of the numerical simulation will be characterized by the parameter study. The parameters which have been chosen to be variable are:

- the number of elements: 10 or 30,
- the value of the permeability coefficient $\bar{\pi} = 2.602{\times}10^{8} \div 2.602{\times}10^{10}\ \mathrm{Pa\,m^{-2}s}$,
- the value of the surface permeability $\beta = 10^{-6} \div 10^{-11}\ \mathrm{kg^{-1}m^{2}s}$.

For the numerical simulation we have developed the finite element program LFEP which has been written using the macro-language of the program system MAPLE V2. Although the capacity of this program is limited, it is large enough for our purposes.

We begin with the variation of the permeability coefficient $\bar{\pi}$. Figure 3 shows how the permeability coefficient influences the growth and the relaxation of the partial fluid pressure. Due to the well known fact that the whole load will be carried at the beginning of the consolidation process only through the fluid component, the partial pressure p^F increases quickly and then in the second step relaxes from the fluid component to the solid one. This fact shall be illustrated later. The speed of this process depends also on the value of the source of momentum $\bar{\mathbf{p}}$ which is proportional to the difference velocity $\mathbf{w}$ through the coefficient $\bar{\pi}$.

([1]) One of such procedures can be found for example by SHAFIRO and KACHANOV [18].

The Fig. 3 shows the relaxation behaviour of the partial fluid pressure for three different values of $\bar{\pi}$ for a chosen depth and for a chosen value of β. It is easy to see the characteristic excess of the partial pressure of the fluid component which has also been observed in experiments, and which is called the *Mandel – Cryer* effect. The different maximum values can be attributed to the inertia effects which have been neglected in the classical consolidation theory.

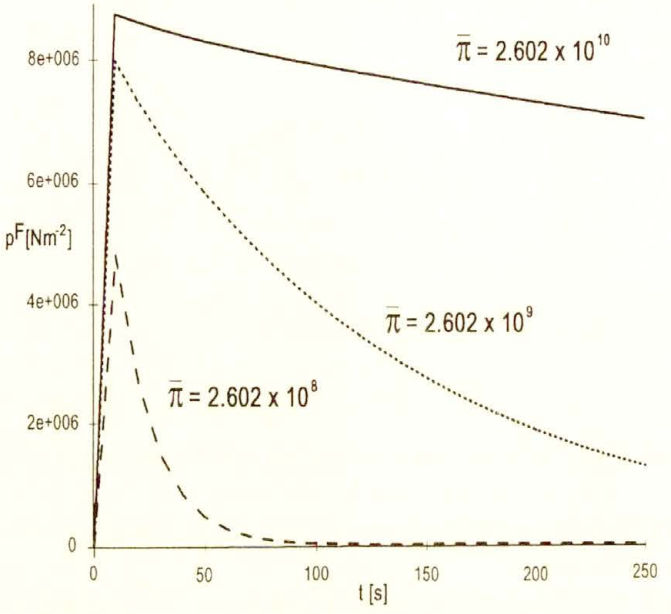

FIG. 3. Partial fluid pressure p^F vs. time: 10 elements, $\beta = 10^{-6}$, $z = 1.80\,\mathrm{m}$.

In the next figure it is shown how the value of the permeability coefficient influences the values of the partial fluid pressure as a function of the depth of the chosen structure.

Let us remind that the variable z is measured from the bottom of the structure, i.e., for instance, the point $z = 4.0\,\mathrm{m}$ in Fig. 4 corresponds to the loaded boundary.

We see that for the chosen time step $t = 100\,\mathrm{s}$ the highest value of the pressure p^F appears at the bottom of the structure for the smallest coefficient $\bar{\pi}$, i.e. then, if the permeability is high. In such a case the friction force acting as the source of momentum between the components is the lowest one, and the external load will be quickly distributed through the whole structure down to its bottom.

Figure 5 illustrates the relaxation behaviour of the partial fluid pressure p^F as a function of depth and chosen time steps for the fixed values of $\bar{\pi} = 2.602 \times 10^9$ and $\beta = 10^{-6}$. As we can see, the partial fluid pressure decreases for increasing time. This relaxation behaviour has been also observed in the Fig. 3. We return to this property in the sequel, where it shall be shown how the acting external load relaxes from the fluid to the solid component.

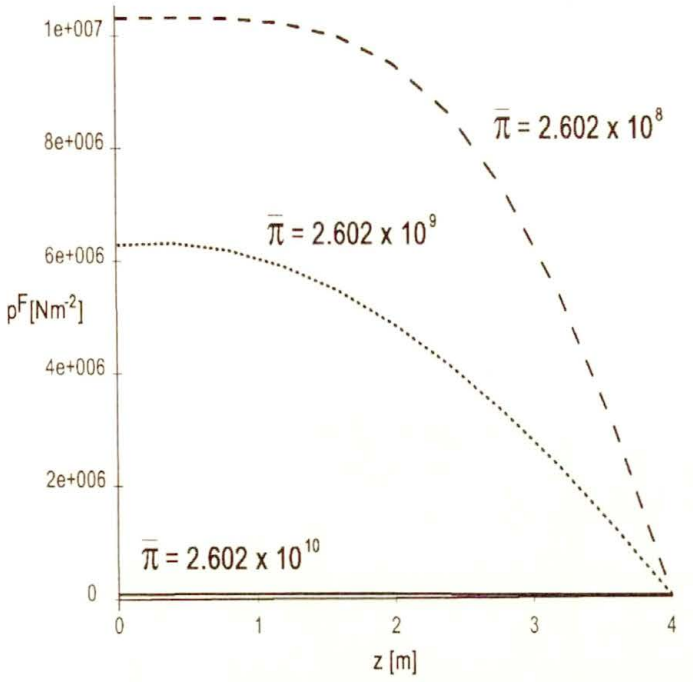

FIG. 4. Partial fluid pressure p^F vs. depth; 10 elements, $\beta = 10^{-6}$, $t = 100\,\mathrm{s}$.

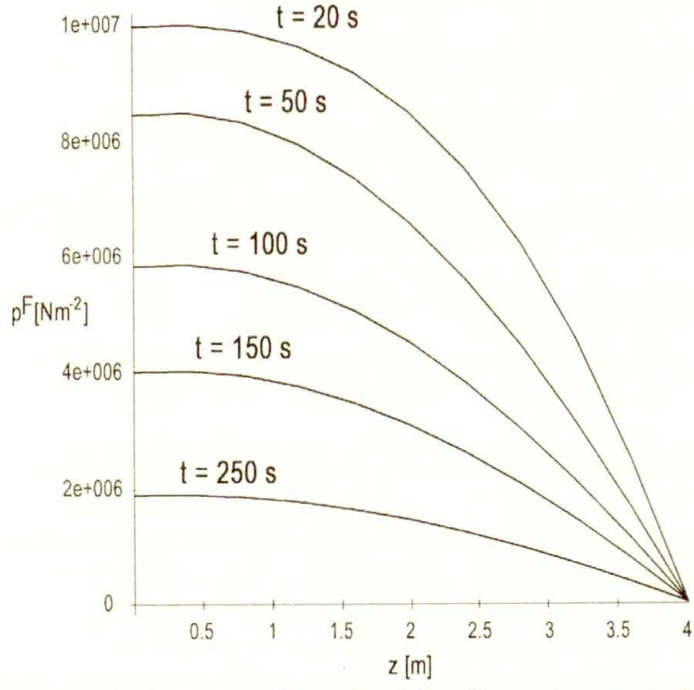

FIG. 5. Partial fluid pressure p^F vs. depth for chosen time steps; 10 elements, $\bar{\pi} = 2.602 \times 10^9$, $\beta = 10^{-6}$.

In the Fig. 6 we can observe a similar behaviour as that in the Fig. 3, however, for another parameter of the function, namely the depth. The surface permeability has been chosen to be $\beta = 10^{-6}$. We see that for the bottom of the structure ($z = 0.00$ m) the partial fluid pressure reaches its maximum. The same value of the pressure can be taken from the figures for t equal 20 s. Due to the velocity of the propagating waves, the exact course of the function $p^F(t)$ can be reached only for very small time steps. This unfortunately exceeds the capacity of our program.

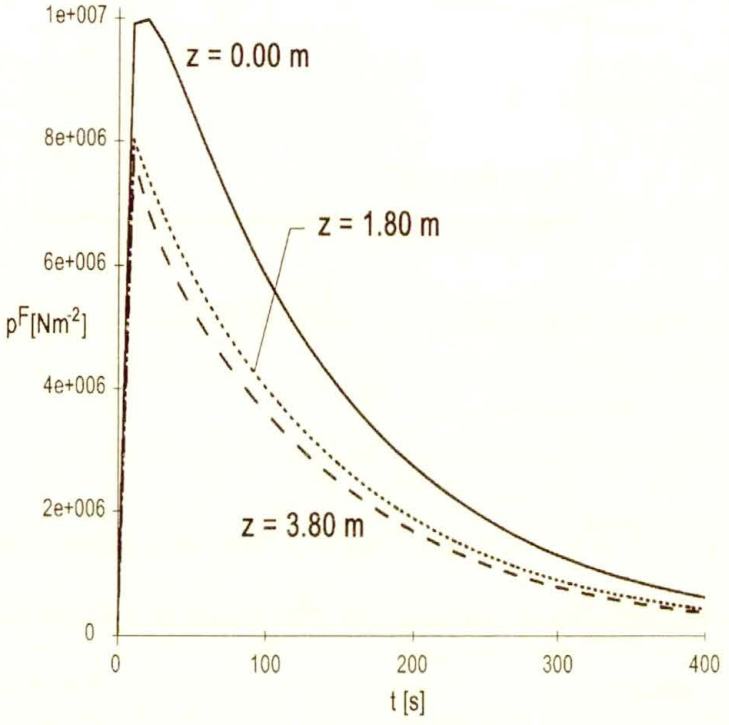

FIG. 6. Partial fluid pressure p^F vs. time for chosen depths; 10 elements, $\bar{\pi} = 2.602 \times 10^9$, $\beta = 10^{-6}$.

Figure 7 illustrates the relaxation behaviour discussed above for different values of the permeability $\bar{\pi}$. The value of the fluid pressure increases and reaches ist maximum after a short time. We have explained this behaviour by the analysis of Fig. 3. It is clear that at the beginning of the consolidation process nearly the whole external load shall be carried through the fluid component. In contrast to the classical simple theory of *von Terzaghi*, a part of the load is also carried through the solid component. As we have already mentioned, the difference in the results between these models is caused by the fact that *von Terzaghi* has neglected the acceleration terms, i.e. the influence of the inertial forces in his model. Nevertheless, the courses of the figure coincide very well with the results

obtained in experiments, where the fluid pressure relaxes to its initial value and finally, at the end of the consolidation process the solid component carries the whole external load.

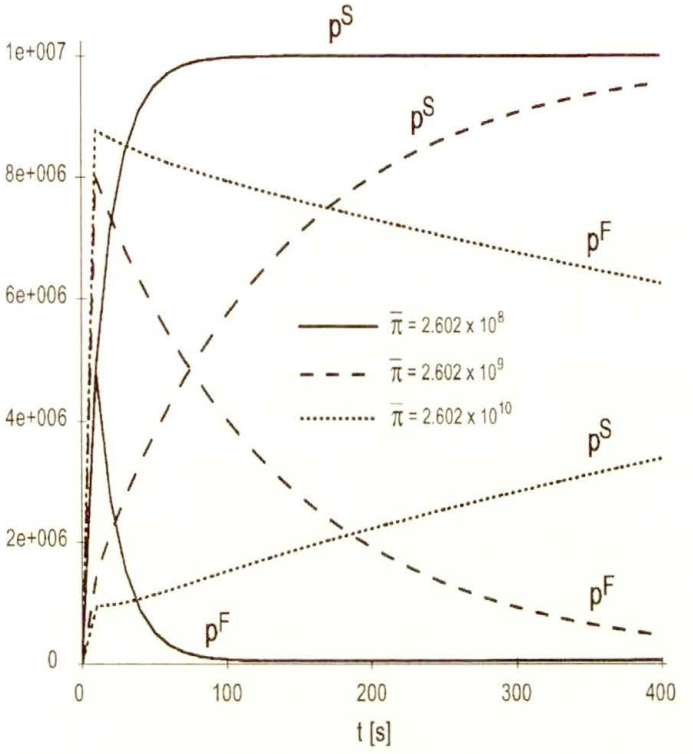

FIG. 7. Time relaxation between the fluid and the solid pressure for $z = 1.80\,\mathrm{m}$; 10 elements, $\bar{\pi} = 2.602 \times 10^9$, $\beta = 10^{-6}$.

In the next figure we present the courses of the functions of the hydraulic gradient $i \equiv \partial p^F / \partial z$ for the chosen points of the structure having in this case the depth of $h = 12\,\mathrm{m}$. The graphs of the Fig. 8 correspond qualitatively to the curves appearing in the literature [17, 19] in the range of short times. Neither the quantitative comparison nor the asymptotic behaviour for large time could be carried through, due to the limited efficiency of the present numerical code. It should be also borne in mind that the classical curves for the hydraulic gradient have been obtained for the semi-infinite medium and not for the layer of the finite thickness which is the subject of this work. It means that we can expect considerable deviations in the boundary regions. These deviations are also due to the novel formulation of the inhomogeneous outflow condition. For this reason we present in Fig. 8 the results for the middle region of the layer. This point shall be discussed again in the forthcoming paper on the two-dimensional consolidation problem.

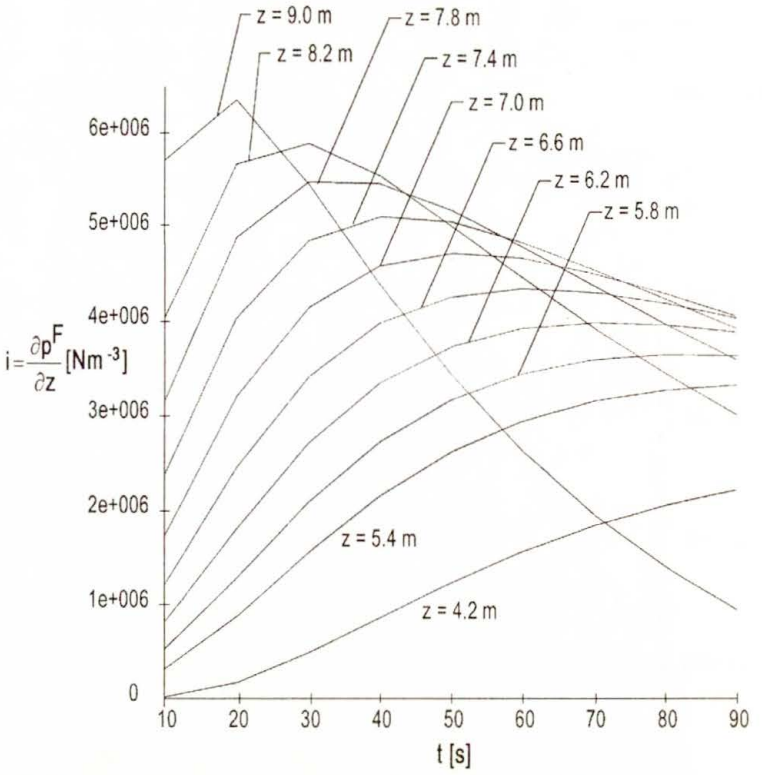

FIG. 8. Hydraulic gradient vs. time for chosen depths; 30 elements, $\bar{\pi} = 2.602 \times 10^9$, $\beta = 10^{-6}$.

We pass over to the last two figures. The former shows the courses of the time-dependent outflow of the fluid component through the free boundary as the function of the surface permeability β. It is clear that for low values of this coefficient, the mass transport of the fluid through the boundary is very low. This fact confirms the physical meaning of the coefficient β as the surface permeability. It has been anticipated earlier in this work. We can also see that for the range $10^{-6} \div 10^{-8}$ of the values of the surface permeability the courses of the function $m^F(t)$ are approximately the same. It seems that these values determine a kind of the asymptote for the magnitude of the surface permeability, of the treated simplified model. Moreover, we see in this figure, due to the relation (5.18), the same effect of the excess of the $m^F(t)$-function which we have observed in the Fig. 3 for the partial fluid pressure.

The latter figure shows the time-depedence of the solid displacement for two chosen points of the structure presented in the Fig. 2 a. Both courses of these functions reproduce the assumption of the linear behaviour of the solid component. In other words, in the case of $z = 3.80$ m the maximum strain amounts approximately to four per cent, what should be expected in the linear case.

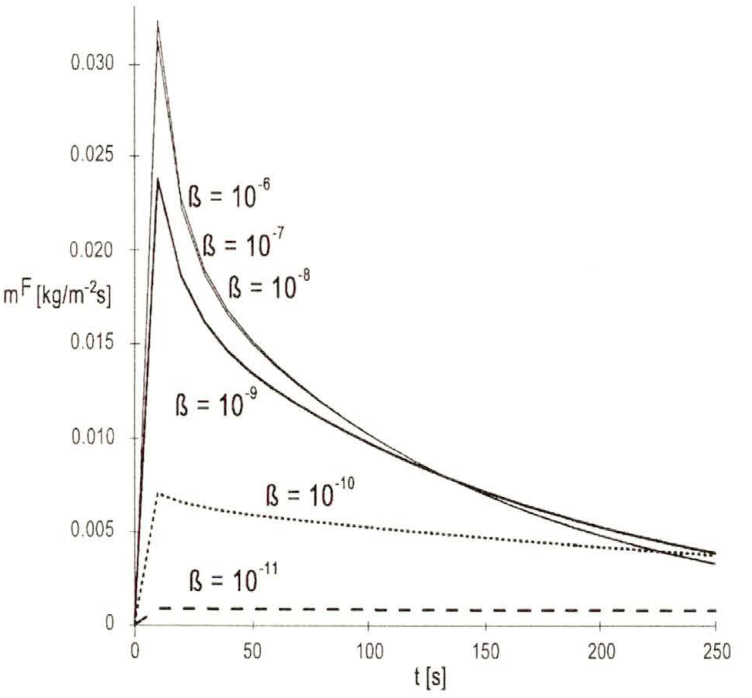

FIG. 9. Mass transport m^F of the fluid through the boundary vs. time; 10 elements, $\bar{\pi} = 2.602 \times 10^9$.

The numerical results presented in this section show that the new class of models developed by WILMAŃSKI, in particular the chosen simplified model described in Sec. 2, agree not only with the well known results obtained by application of the classical model of *von Terzaghi* but also with the phenomena observed in experiments. By means of this model one can simulate the phenomena taking place in the two-component continua. However, we have only focused on the qualitative comparison of the results. The adaptation of the constants of this model as well as their calculation from the point of view of their effective values was not the topic of this paper. Nevertheless the presented results make it clear that it is worthwhile to develop an efficient finite element program to calculate two-dimensional structures with nonlinearities. This is the subject of the current research.

Another important issue of this work was the consistent formulation of the initial-boundary value problem for the consolidation phenomenon. The most important part of this topic was the analysis of the boundary value problem on the free boundary and the formulation of the inhomogeneous boundary condition on it, as well as the formulation of additional boundary quantities for the free surface. We shall present an overview of the existing and possible types of boundaries in two-component continua in a forthcoming paper.

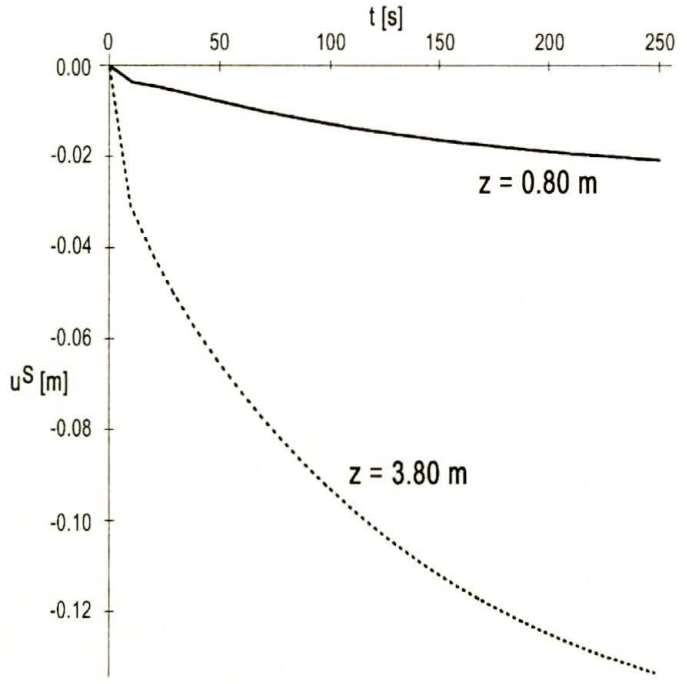

FIG. 10. Displacement u^s vs. time for two chosen points; 10 elements, $\beta = 10^{-6}$, $\bar{\pi} = 2.602 \times 10^9$.

Acknowledgment

This paper could not have been written without the help and advice given me in many discussions by my teacher professor K. WILMAŃSKI.

A part of this research has been supported by the grant of the Deutsche Forschungsgemeinschaft to the Institute of Mechanics, University of Essen, Germany.

References

1. K. v. TERZAGHI, *Die Berechnung der Durchlässigkeit des Tones aus dem Verlauf der hydrodynamischen Spannungserscheinungen*, Akademie der Wissenschaften in Wien, Sitzungsberichte der math.-naturw. Kl., Abt. IIa, **132**, 3/4, 125–138, 1923.
2. R.M. BOWEN, *Incompressible porous media models by use of the theory of mixtures*, Int. J. Engng. Sci., **18**, 1129–1148, 1980.
3. K. HUTTER, K. JÖHNK and B. SVENDSEN, *On interfacial transition conditions in two-phase gravity flow*, ZAMP, **45**, 1994.
4. M.A. GOODMAN and S.C. COWIN, *A continuum theory for granular materials*, Arch. Rat. Mech. Anal., **44**, 249–266, 1972.

5. S.L. PASSMAN, *Mixtures of granular materials*, Int. J. Engng. Sci., **15**, 117–129, 1977.
6. S.L. PASSMAN, I.W. NUNZIATO and E.K. WALSH, *A theory of multiphase mixtures*, [in:] Rational Thermodynamics, C. TRUESDELL [Ed.], Second Edition, 286–325, Springer-Verlag, N.Y. 1984.
7. M.R. BAER and I.W. NUNZIATO, *A two-phase mixture theory for the deflagration-to-detonation transition (DDT) in reactive granular materials*, Int. J. Multiphase Flow, **12**, 861–889, 1986.
8. R. DE BOER, *Highlights in the historical development of the porous media theory*, Appl. Mech. Rev., **49**, 4, 201–262, 1996.
9. K. WILMAŃSKI, *On weak discontinuity waves in porous materials*, [in:] Interactions of Mechanics and Mathematics, J.F. RODRIGUEZ [Ed.], STAMM 94, Longman Scientific & Technical, Essex 1995.
10. K. WILMAŃSKI, *The thermodynamical model of the compressible porous material with the balance equation for porosity*, J. Non-Equilibrium Thermodyn., [to appear 1996].
11. K. WILMAŃSKI, *Lagrangean model of two-phase porous material*, J. Non-Equilibrium Thermodyn., **20**, 1, 50–78, 1995.
12. K. WILMAŃSKI, *Porous media at finite strains. The new model with the balance equation for porosity*, Arch. Mech., **48**, 4, 591–628, 1996.
13. W. KEMPA, *Das Grenzwertproblem bei Konsolidation – eine konsistente Konstruktion der schwachen Formulierung*, MECH-Report 95/13, Universität-GH Essen, Essen 1995.
14. K. RUNESSON, *On non-linear consolidation of soft clay*, Ph.D. Thesis, Dept. of Struct. Mech., Chalmers Univ. of Technology, Göteborg 1978.
15. K. WILMAŃSKI, *Acceleration waves in two-component porous media. Part II. Supplementary remarks on the model and the evolution of amplitudes*, MECH-Bericht 95/2, Universität-GH Essen, Essen 1995.
16. T. BOURBIE, O. COUSSY and B. ZINSZNER, *Acoustics of porous media*, Editions Technip, Paris 1987.
17. B. CHAMSAZ, *Einige quasistatische Probleme ebener Verzerrungen bei kompressiblen porösen Körpern*, Diplomarbeit 95/3, Institut für Mechanik, Fachbereich Bauwesen, Universität-GH Essen, Essen 1995.
18. B. SHAFIRO and M. KACHANOV, *Materials with fluid-filled pores of various shapes: Effective elastic properties and fluid pressure polarization*, Int. J. Solids & Struct., [in press].
19. J.K. MITCHELL, *Fundamentals of soil behavior*, John Wiley & Sons, Inc., University of California, Berkeley 1976.
20. M. CIESZKO and J. KUBIK, *On the compatibility conditions in the fluid-fluid saturated porous solid contact problems*, Arch. Mech., **45**, 1, 77–91, 1993.
21. T. LEVY and E. SANCHEZ-PALENCIA, *On boundary conditions for fluid flow in porous media*, Int. J. Engng. Sci., **13**, 923–940, 1975.
22. K. VAFAI and C.L. TIEN, *Boundary and inertia effects on flow and heat transfer in porous media*, Int. J. Heat Maff Transfer, **24**, 195–203, 1981.
23. K.R. RAJAGOPAL, A.S. WINEMAN and M. GANDHI, *On boundary conditions for a certain class of problems in mixture theory*, Int. J. Engng. Sci., **24**, 1453–1463, 1986.

UNIVERSITY OF ESSEN
INSTITUTE OF MECHANICS, ESSEN, GERMANY.
e-mail: wkempa@mechanik.bauwesen.uni-essen.de

Received December 11, 1996; new version June 25, 1997.

Arch. Mech., 49, 5, pp. 919–962, Warszawa 1997

Large scale motion and temperature distributions in land-based ice shields; the Greenland Ice Sheet in response to various climatic scenarios

R. CALOV and K. HUTTER (DARMSTADT)

Dedicated to Prof. Franz Ziegler on the occasion of his 60-th birthday

A REVIEW IS GIVEN of the theory of cold ice sheets in the so-called shallow ice approximation, and a literature survey is performed of its application in ice sheet modelling of the large ice shields, such as Greenland, Antarctica and other, historical, ice sheets. As model applications, steady state and time-dependent computations are performed for the Greenland Ice Sheet using an ice sheet model on the basis of the 3-D shallow ice equations of a viscous, heat-conducting incompressible fluid. The interaction with the solid earth is through a heat-conducting homogeneous isotropic rigid solid subjected to geothermal heat. The climate driving is effected through a prescribed atmospheric surface temperature and accumulation rate function. Computations are performed for the ice-thickness distribution to steady driving conditions when external and internal parameters are varied. It is shown that the sliding coefficient and the amplitude of the annual temperature variation are particularly critical. Finally, the evolution of the basal temperature distribution at Dye 3, Summit and Camp Century through idealized scenarios of the ice age(s) is computed; these computations show that the basal temperature regime depends critically on the thermal inertia of the bedrock and the magnitude of the ice fluidity. Our computations with various climate state scenarios demonstrate how well the model reproduces the measured flow data in Greenland and indicates how it must be extended to accomodate the polythermal structure of the ice and to include longitudinal stretching effects.

1. Introduction

FIRST AD-HOC DESCRIPTIONS of the distributions of velocity, temperature and evolution of the geometry of ice sheets are largely due to NYE [138-151, 153], GLEN [48, 65], LLIBOUTRY [107–116], WEERTMAN [178–187] and others; however, while these works contain the essential ingredients of the theoretical formulation and systematic development of a mathematical boundary value problem, rational deduction of the latter had to await the works of FOWLER [37–40, 41–46], HUTTER [66–72, 78, 79, 61–63] and MORLAND [131–137].

Computational results are presented here on the flow, temperature and geometry of the Greenland Ice Sheet in response to various climate scenarios using an ice sheet model that is based on the Shallow Ice Approximation [25, 26]. The growth and retreat of inland ice masses is governed by the snowfall onto the surface, the melting and calving of the ice close to and at the outer ice boundaries. Owing to its own weight, the ice deforms with velocities of typically $100\,\mathrm{m\,a^{-1}}$ causing a transport of ice towards the ice sheet boundaries where the ice melts and calves. This process, in turn, is influenced by the temperature distribution within the ice, implying a delicate balance between the thermal and mechanical regimes that are established by the climate input and the geothermal conditions of the substrate. The thermomechanically coupled ice dynamics together with the mass flux due to snowfall and mass loss in the vicinity of ice boundaries determine the thickness distribution of a particular ice sheet.

The deformation of an ice sheet and the variation of its temperature distribution depends to a large extent on its thermomechanical constitutive modelling. Here, we treat ice as a rheologically nonlinear, thermally coupled, viscous fluid, i.e., we assume its fluidity (inverse viscosity) to be temperature-dependent, the latter according to a power law with exponent $n = 3$, the former essentially following an Arrhenius-type relationship. When the temperature reaches the melting point, it is held at pressure melting without accounting energetically for the water production. This body is subject to driving mechanisms from the outside world that are imposed on the ice sheet via its surrounding boundaries. At its bottom we account for the presence of a heat-conducting rigid solid of 4 km thickness. At the free surface, the climate input is effected by the prescription of the mean annual atmospheric temperature and accumulation rate fuctions; the latter expresses the rate of mass added and subtracted according to the amount of snowfall and melting of surface ice, respectively. At the base, a relatively complex viscous-type sliding law is implemented and a thermodynamic jump condition of heat flow provides the connection with the heat-conducting lithosphere. As for the former, the no-slip condition applies where the basal ice is below the pressure melting point, but a power law relationship between shear traction and sliding velocity is imposed when the basal ice is at the pressure melting point. At the lower boundary of the rigid substrate the geothermal heat flow is prescribed.

By using standard climate driving functions (constant climate and idealized interglacial variations) for the surface temperature and mass balance, we study the reaction of the Greenland Ice Sheet to (i) variations in the parameterization of the driving functions, (ii) the viscous-type basal sliding law, (iii) the apparent viscosity (fluidity) of the ice and (iv) the role played by the thermal inertia of the rock bed. In particular it is shown that the amplitude of the annual variation of the surface temperature and the drag coefficient of the basal sliding law are critical for climate stability of large ice sheets.

Furthermore, using several reasonable climate scenarios for the past, and numerical values for the material and climate parameters appropriate for Green-

land, it is shown that, while the temperate patches at the base always existed, the locations of Dye 3, Camp Century and Summit were always cold.

2. The model

A review is presented of the governing equations of ice sheet dynamics: how they emerge from first principles of continuum thermodynamics, how the equations have been simplified by an asymptotic analysis that is based on a shallowness assumption, and what mathematical-numerical difficulties arise in using this shallow ice approximation (SIA). The intention is to present to the reader an up-to-date state-of-the-art which is fairly complete; as far as the current literature goes, we cannot claim, however, that the cited literature is exhaustive.

2.1. Field equations

The ice in large ice masses (Fig. 1) is generally polythermal, i.e., the ice mass consists of disjoint regions in which the ice is either cold (i.e., its temperature is below the melting point) or temperate (i.e., it is at the pressure melting point), but except for a few very recent cases [5, 7, 45, 68, 74, 75, 76, 47, 49–56], theoretical formulations are restricted to *cold ice*. For such a case the continuum mechanical postulate "ice is an incompressible heat-conducting nonlinear viscous

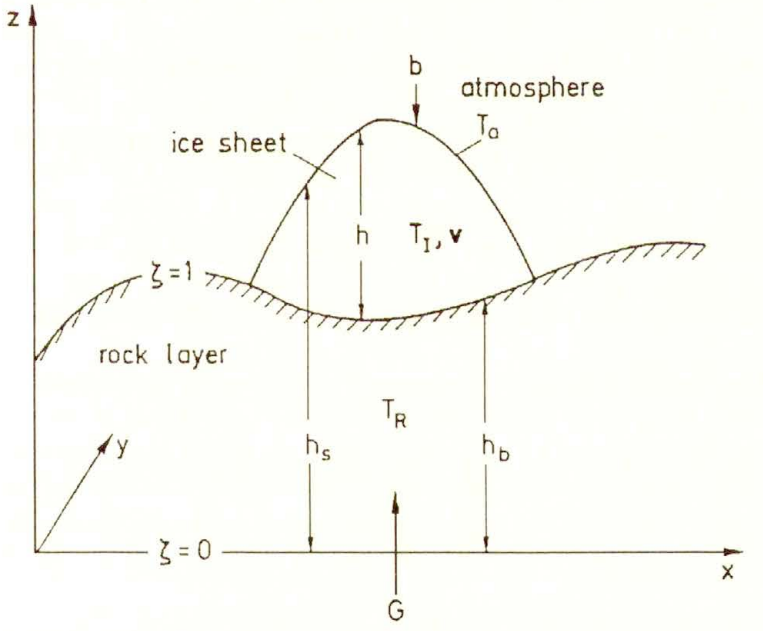

FIG. 1. Model variables with the coordinate system for the ice sheet and the lithosphere layer.

fluid" yields the following balance laws of mass, momentum and energy as well as constitutive relations:

$$
\begin{aligned}
\operatorname{div}\mathbf{v} &= 0,\\
\varrho\dot{\mathbf{v}} &= -\operatorname{grad} p + \operatorname{div}\boldsymbol{\sigma} + \varrho\mathbf{g},\\
\varrho\dot{\varepsilon} &= -\operatorname{div}\mathbf{q} + \operatorname{tr}(\boldsymbol{\sigma}'\mathbf{D}),\\
\varepsilon &= \int_0^T C_p(\bar{T})d\bar{T} + \varepsilon_0,\\
\mathbf{q} &= -\chi(T)\operatorname{grad} T,\\
\mathbf{D} &= \operatorname{sym}(\operatorname{grad}\mathbf{v}) = EA(T')f(I\!I_{\sigma'})\boldsymbol{\sigma}',
\end{aligned}
\tag{2.1}
$$

in which $\mathbf{v}$, ϱ, p, σ', $\mathbf{g}$, ε, $\mathbf{q}$, c_p, χ_I are, respectively, the velocity vector, ice density, pressure, Cauchy stress deviator (i.e., $\operatorname{tr}(\sigma') = 0$, where $\operatorname{tr}(\cdot)$ is the trace operator), specific gravity, internal energy, heat flux vector, specific heat (at constant pressure) and heat conductivity. Furthermore,

$$
T' = T + ap, \qquad A(T') = A_0 \exp\left(-\frac{Q}{R(T_0 + T')}\right), \qquad I\!I_\sigma = \frac{1}{2}\operatorname{tr}(\boldsymbol{\sigma}'^2),
\tag{2.2}
$$

where T' is the homologous temperature, a the Clausius–Clapeyron constant, A a temperature-dependent rate factor, $f(I\!I_{\sigma'})$ the fluidity with $n = 3$ and E a so-called enhancement factor. The power law fluidity has been introduced into glaciology by NYE [141] and GLEN [48] but should be replaced by a finite viscosity law because of its singular behaviour at small stretchings (HUTTER [71] and MORLAND [134]) when $n > 1$. For its experimental justification, see [8, 24, 29, 33, 34, 106, 168]. The enhancement factor E accounts for the apparent different flow properties of Holocene and Pleistocene ice [28, 29, 31]. Up to today $E = E(\mathfrak{A})$ is assumed to be a function of age with values $E = 1$, for Holocene, and $E = 3$, for Pleistocene ice, and $\mathfrak{A}$ satisfies the differential equation([1]) $\dot{\mathfrak{A}} = 1$. A_0 is a constant, Q the activation energy of ice, R the gas constant and $T_0 = 273.15\,\mathrm{K}$ the melting temperature at normal pressure (10^5 Pa). Numerical values are given in Table 1.

The above model (2.1), (2.2) is standard except for the occurrence of E. From a thermodynamic point of view, this variable has the meaning of an internal variable and was first introduced into a theoretical model by HUTTER and VULLIET [77]. Glaciologists are generally unaware of this and use it as a fudge factor. More important than this is the fact that the above fluid model is necessarily isotropic and thus cannot describe stress-induced anisotropies evident in specimens from boreholes [27, 49, 117, 130, 174, 175].

([1]) An initial distribution of $\mathfrak{A}$ and the values of $\mathfrak{A}$ of any ice particle at the time when it is formed must be prescribed. Since ice is accumulated at the free surface, this essentially amounts to prescribing $\mathfrak{A}(t_0)$, $t_0 < t$ on those parts of the free surface where snow is accumulating.

Table 1. Physical constants used in ice sheet models.

Earth's acceleration g		$9.81\ \mathrm{m\,s^{-2}}$
Density	Ice ϱ	$0.9 \cdot 10^3\ \mathrm{kg\,m^{-1}}$
Heat conduction	Ice χ	$2.1\ \mathrm{W\,m^{-1}K^{-1}}$
	Rock χ_R	$3\ \ \mathrm{W\,m^{-1}K^{-1}}$
Thermal diffusivity	Ice κ	$1.15 \cdot 10^{-6}\ \mathrm{m^2 s^{-1}}$
	Rock κ_R	$1.5 \cdot 10^{-6}\ \mathrm{m^2 s^{-1}}$
Specific heat of ice C_v		$2009\ \mathrm{J\,kg^{-1}K^{-1}}$
Clausius–Clapeyron constant a		$7.42 \cdot 10^{-5}\ \mathrm{K(kPa)^{-1}}$
Latent heat of fusion for ice L_s		$335 \cdot 10^3\ \mathrm{J\,kg^{-1}}$
Geothermal heat flow G		$42 \cdot 10^{-3}\ \mathrm{Wm^{-2}}$
Power law exponent n		3
Gas constant R		$8.314\ \mathrm{J\,mol^{-1}\,K^{-1}}$
Rate factor A_0	$T' \geq -10°\mathrm{C}$	$6.3 \times 10^{10}\ \mathrm{a^{-1}\,Pa^{-3}}$
	$T' < -10°\mathrm{C}$	$1.3 \times 10^{-5}\ \mathrm{a^{-1}\,Pa^{-3}}$
Activation energy Q	$T' \geq -10°\mathrm{C}$	$139\ \mathrm{kJ\,mol^{-1}}$
	$T' < -10°\mathrm{C}$	$60\ \mathrm{kJ\,mol^{-1}}$

This thermomechanical model for the ice is coupled to the heat conduction equation of a rigid substratum

$$\varrho c_R \dot{T}_R = \mathrm{div}(\chi_R \mathrm{grad} T_R) = \chi_R \triangle T_R \tag{2.3}$$

(R for rock), the evolution equations for the ice thickness $h = h_s - h_b$,

$$\frac{\partial h}{\partial t} + \nabla_H \cdot \mathbf{V}_H = b_s + b_b\,, \qquad \mathbf{V}_H = \int_{h_b}^{h_s} \mathbf{v}_H\, dz \tag{2.4}$$

as well as bed sinking

$$\frac{\partial h_b}{\partial t} = -\frac{1}{\tau_l}\left(h_b - h_0 + \frac{\varrho}{\varrho_a} h\right). \tag{2.5}$$

In (2.3) T_R and χ_R are the temperature and heat conductivity of the rock; radio-active heating of the rock is ignored, so as are the contributions due to internal stresses and dissipation. In this sense, the substratum is rigid; however, motions due to bedrock sinking are incorporated in the convective terms (contained in $\dot{T}_R$) and described by (2.5). In Eq. (2.4) $\mathbf{v}_H$ and $\mathbf{V}_H$ are the horizontal velocity components of the ice and its horizontally integrated flux, respectively, and $\nabla_H = (\partial x, \partial y)$. Furthermore, b_s and b_b are the accumulation/ablation and basal melting rate functions, respectively; since basal melting is small, b_b is often

ignored. Formally, (2.4) is a vertically integrated mass balance. Finally, (2.5) is a relaxation-type relationship for the vertical position of the basal boundary of the ice; it models the bed adjustment with the relaxation time $\tau_l \approx 3 \div 5 \times 10^3$ a; h_0 is the relaxed, undisturbed bed topography and ϱ_a the density of the asthenosphere.

Other models of bedrock sinking have also been used, e.g. a diffusion equation

$$\frac{\partial h_b}{\partial t} = D_a \triangle_H (h_b - h_0 + w_a)\,, \tag{2.6}$$

where $D_a = 0.5 \times 10^8$ m^{2}a^{-1} is the asthenosphere diffusivity, $\triangle_H$ the two-dimensional Laplacian and w_a the deflection of the constant thickness lithosphere for which the plate equation

$$D \triangle\triangle\, w_a = q - \varrho_m w_a,$$
$$q = \begin{cases} \varrho g h, & \text{if} \quad \dfrac{\varrho}{\varrho_R} + h_{sl} \leq h, \\ \varrho_R g (h_{sl} - h), & \text{if} \quad -\dfrac{\varrho}{\varrho_R} + h_{sl} > h \end{cases} \tag{2.7}$$

is solved, where D is the bending rigidity of the lithosphere (10^{25} N m), ϱ_R the density of the mantle (3300 kg m^{-3}) and $h_{sl} =$ is a constant, see [82, 176]. Models which treat the lithosphere as thermoviscoelastic and the asthenosphere as nonlinearly viscous have also been proposed, TURCOTTE and SCHUBERT [176], but so far not implemented in ice sheet models.

If in the solution of the above equations the ice temperature at any point should reach values above the melting point, it is set back to $T = T_M$, and the energy equation is disregarded in these points. Regions where $T = T_M$ are defined as temperate. Thus the thermal processes are not accounted for in these regions, by e.g. calculating the production of water via dissipation and latent heat of fusion, what makes the model approximate.

2.2. Boundary conditions

Boundary conditions that close the equations to a complete boundary value problem must be formulated at the free surface, the ice-bedrock interface, the lower boundary of the rock bed and the ice margins.

At the free surface $z = h_s(x, y, t)$, we assume stress-free conditions and prescribe the surface temperature and the accumulation ablation rate function,

$$T = T_s(x, y, t), \qquad b_s = b_s(x, y, t), \tag{2.8}$$

where examples for this climate driving are given in [25, 26, 36, 59, 154, 155, 162].

At the *ice-bedrock interface* $z = h_b(x, y, t)$ continuity of temperature and the energy jump conditions must be fulfilled. This implies

$$\chi \frac{\partial T}{\partial n} = \chi_R \frac{\partial T_R}{\partial n}, \qquad T = T_R \tag{2.9}$$

when the base is cold, and

$$b_b = \frac{1}{\varrho_w L_s} \left(\chi \frac{\partial T}{\partial n} - \chi_R \frac{\partial T_R}{\partial n} + \tau^* v_{||} \right), \qquad T = T_R = T_M, \tag{2.10}$$

when it is temperate. In the above, $\mathbf{n}(n)$ indicates the unit vector (direction) normal to and directed into the ground, L_s the latent heat of fusion, $\boldsymbol{\tau}^* \cdot \mathbf{v}_{||}$ the frictional heat due to sliding of the ice sole over the bedrock and $\boldsymbol{\tau}^* = (\boldsymbol{\sigma} - p^* \mathbf{1})\mathbf{n}$ denoting the tangential tractions and $v_{||}$ the jump in tangential velocity. In general, the lithosphere velocity is ignored, so $\mathbf{v}_{||} = -(\mathbf{v} - (\mathbf{v} \cdot \mathbf{n}))\mathbf{n}|_{\text{Ice}}$. Common sliding laws are

$$v_{||} = \begin{cases} \mathcal{C}(|\boldsymbol{\tau}^*|, p^*)\boldsymbol{\tau}^* = c|\boldsymbol{\tau}^*|^{m-1}, p^{*-l}\boldsymbol{\tau}^*, & \text{if} \quad T = T_M, \\ 0, & \text{if} \quad T < T_M, \end{cases} \tag{2.11}$$

according to [112, 137, 178, 182, 183, 185, 187] and with appropriate choices for c, m and l, see [25, 26].

At the *lower boundary of the rock* $z = h_b(x, y)$, we simply prescribe the thermal Neumann condition

$$\chi_R \frac{\partial T_R}{\partial z} = -G, \tag{2.12}$$

where G (≈ 42 mW m^{-2}) (see, however, also [55, 83, 177]) is the geothermal heat flow.

As long as the *ice margin* stays on the continent, we let it freely evolve, either advancing or retreating, depending on whether there is net mass addition or subtraction. When the ice margin reaches the ocean then all mass flowing through that margin position is treated as calving and is lost to the ice sheet. This mechanism is interrupted only when the ice is retreating again at sheet positions distant from the ocean. This is a simplified marginal condition as the formation of ice shelves is ignored. It could be incorporated, see e.g. [9, 58, 60, 83, 84, 85], [121 – 124], if an ice shelf model is adjoined.

2.3. Shallow ice approximation

Ice sheets are long and wide but generally shallow. This suggests to introduce a scaling of the equations of the preceding section such that the aspect ratio $\varepsilon = [H]/[L] \ll 1$, in which $[H]$ and $[L]$ are a typical depth and horizontal distance, explicitly enters the equations, and perturbation methods in the small parameter ε can be used. The lowest order equations of this scheme have been coined the shallow ice approximation [71].

2.3.1. Introduction of scales. In the Cartesian coodinate system x, y (horizontal), z (vertical) we now choose the following scalings:

$$
\begin{aligned}
\{x, y, z, t\} &= \left\{[L]x^*, [L]y^*, [H]z^*, \frac{[L]}{[H]}t^*\right\}, \\
\{u, v, w, b_s, b_b\} &= \{[U]u^*, [U]v^*, [W]w^*, [W]b_s^*, [W]b_b^*\}, \\
\{p, \sigma_x', \sigma_y', \sigma_z', \tau_{xy}, \tau_{xz}, \tau_{xz}\} & \\
&= [\varrho g H]\{p^*, \varepsilon^2\sigma_x^{*\prime}, \varepsilon^2\sigma_y^{*'}, \varepsilon^2\sigma_z^{*\prime}, \varepsilon^2\tau_{xy}^*, \varepsilon\tau_{xz^*}, \varepsilon\tau_{xz}^*\}, \\
T &= T_0 + [\Delta T]T^*, \\
A(T')f(I\!I_{\sigma'}) &= \frac{[D]}{[\sigma]}A^*(T^{*\prime})f^*(I\!I_{\sigma'}^*),
\end{aligned}
\tag{2.13}
$$

where $[L]$, $[H]$, $[U]$, $[W]$, $[\Delta T]$, $[D]$, $[\sigma]$ are length and velocity scales and scales for the temperature range, stretching and typical material stresses. The quantities in brackets are typical values of the variables arising in ice sheets and those with an asterisk are dimensionless and necessarily varying in the range $\mathcal{O}((-1, 1))$, if the bracketed terms are appropriately selected; for typical values see Table 2. The principal assumption of the shallow ice approximation is that

$$
[H]/[L] = [W]/[U] = \epsilon \ll 1\,, \tag{2.14}
$$

anticipated in (2.13) in which several terms are weighted with ϵ and ϵ^2, respectively. This delicate balance introduced here by hindsight, is not obvious and constitutes the essential step towards a formal perturbation procedure obtained independently by HUTTER [67–72] and MORLAND [133, 134].

Table 2. Typical scales of ice sheets.

$[L] = 10^5 - 10^6$ m,	$[\sigma] \approx 10^5$ Pa,
$[H] = 10^2 - 10^3$ m,	$[\varrho] \approx 10$ kg m^{-3},
$[U] = 10 - 10^3$ m a^{-1}	$[g] \approx 10$ m s^{-2},
$[W] = 1 - 10$ m a^{-1}	$[\chi/(\varrho c)] \approx 11.15 \cdot 10^{-6}$ m^2 s^{-1}
$[D] = 1$ a	

With (2.13) and (2.14) the balance laws of mass, momentum and energy and the constitutive relations of stress take the forms

$$
\begin{aligned}
&\frac{\partial u^*}{\partial x^*} + \frac{\partial v^*}{\partial y^*} + \frac{\partial w^*}{\partial z^*} = 0, \\
&\frac{\mathcal{F}}{\epsilon}\frac{\partial u^*}{\partial t^*} = -\frac{\partial p^*}{\partial x^*} + \epsilon^2\frac{\partial \sigma_x^{*\prime}}{\partial x^*} + \epsilon^2\frac{\partial \tau_{xy}^*}{\partial y^*} + \frac{\partial \tau_{xz}^*}{\partial z^*}\,, \\
&\frac{\mathcal{F}}{\epsilon}\frac{\partial v^*}{\partial t^*} = \epsilon^2\frac{\partial \tau_{xy}^*}{\partial x^*} - \frac{\partial p^*}{\partial y^*} + \epsilon^2\frac{\partial \sigma_y^{*\prime}}{\partial y^*} + \frac{\partial \tau_{yz}^*}{\partial z^*},
\end{aligned}
\tag{2.15}
$$

$$
\begin{aligned}
(2.15)\ [\text{cont.}]\quad & \mathcal{F}\epsilon\frac{\partial w^*}{\partial t^*} = \epsilon^2\left\{\frac{\partial \tau^*_{xz}}{\partial x^*} + \frac{\partial \tau^*_{yz}}{\partial y^*}\right\} - \frac{\partial p^*}{\partial z^*} + \epsilon^2\frac{\partial \sigma^{*\prime}_z}{\partial z^*} - 1,\\
& \frac{dT^*}{dt^*} = \mathcal{D}\left\{\epsilon^2\boldsymbol{\nabla}^*_H\cdot(\chi^*_I\boldsymbol{\nabla}^*_H T^*) + \frac{\partial}{\partial z^*}\left(\chi_*\frac{\partial T^*}{\partial z^*}\right)\right\} + \mathcal{E}2A^*(T^*)f^*(\cdot)\mathit{I\!I}^*_{\sigma'},\\
& \frac{\partial u^*}{\partial z^*} + \epsilon^2\frac{\partial w^*}{\partial x^*} = 2\mathcal{G}A^*(T^*)f^*(\mathit{I\!I}_{\sigma'})\tau^*_{xz},\\
& \frac{\partial v^*}{\partial z^*} + \epsilon^2\frac{\partial w^*}{\partial y^*} = 2\mathcal{G}A^*(T^*)f^*(\mathit{I\!I}_{\sigma'})\tau^*_{yz},
\end{aligned}
$$

as well as

$$
\begin{aligned}
(2.16)\quad & \frac{\partial u^*}{\partial x^*} = \mathcal{G}A^*(T^*)f^*(\mathit{I\!I}_{\sigma'})\sigma^{*\prime}_x,\\
& \frac{\partial v^*}{\partial y^*} = \mathcal{G}A^*(T^*)f^*(\mathit{I\!I}_{\sigma'})\sigma^{*\prime}_y,\\
& \frac{\partial w^*}{\partial z^*} = \mathcal{G}A^*(T^*)f^*(\mathit{I\!I}_{\sigma'})\sigma^{*\prime}_z,\\
& \frac{\partial u^*}{\partial y^*} + \frac{\partial v^*}{\partial x^*} = 2\mathcal{G}A^*(T^*)f^*(\mathit{I\!I}_{\sigma'})\tau^*_{xy}
\end{aligned}
$$

in which

$$
\begin{aligned}
\mathit{I\!I}_{\sigma'} &= [\varrho g H]\epsilon^2\left\{{\tau^*_{xz}}^2 + {\tau^*_{yz}}^2 + \epsilon^2\left[\frac{1}{2}\left(\sigma^{*\prime 2}_x + \sigma^{*\prime 2}_y + \sigma^{*\prime 2}_z\right) + {\tau^*_{xy}}^2\right]\right\}\\
&= [\varrho g H]\epsilon^2\mathit{I\!I}^*,
\end{aligned}
$$

$$
\begin{aligned}
(2.17)\quad & \mathcal{F} = \frac{[U^2]}{g[L]}, \quad \mathcal{G} = \frac{\epsilon^2}{\mathcal{S}_\Sigma\mathcal{D}_\Delta}, \quad \mathcal{S}_\Sigma = \frac{[\sigma]}{\varrho g H}, \quad \mathcal{D}_\Delta = \frac{[W]/[H]}{[D]},\\
& \mathcal{D} = \frac{[\chi_I]}{\varrho c_p}\frac{1}{WH}, \quad \mathcal{E} = \frac{\mathcal{A}}{\mathcal{S}_\Sigma\mathcal{D}_\Delta}, \quad \mathcal{A} = \frac{g[H]}{c_p[\Delta T]}.
\end{aligned}
$$

$\mathcal{F}$ is the Froude number, $\mathcal{S}_\Sigma$ the ratio of deviatoric stress to overburden pressure, $\mathcal{D}_\Delta$ a ratio of mean vertical stretching normalising strain-rate magnitude and $\mathcal{A}$ the energy ratio of gravitational energy to internal thermal energy. $\mathcal{G}$ has the meaning of a dimensionless shear viscosity, while $\mathcal{E}$ measures energy dissipation. Moreover, for Glen's power law, when $(2.2)_2$ is used,

$$
\begin{aligned}
(2.18)\quad & A^* = \exp\left\{-\frac{Q}{RT_0}\frac{1}{1+\dfrac{[\Delta T]}{T_0}T^*}\right\},\\
& f^* = \mathcal{S}\mathit{I\!I}^{*(n-1)/2}, \qquad \mathcal{S} := \frac{[\sigma](\epsilon[\varrho g H])^{n-1}}{A_0}.
\end{aligned}
$$

We also have separated the constitutive relations (2.16) from the remaining equations (2.15) because in the lowest order approximation they will not be needed. Similarly, equations (2.3) – (2.12) would also have to be nondimensionalized; however, to motivate the shallow ice approximation, they are not needed.

2.3.2. The limiting theory. Using the scales collected in Table 2 and the definitions (2.17), (2.18) it is seen that $\varepsilon = \mathcal{O}(10^{-2} \div 10^{-3})$, $\mathcal{F} = \mathcal{O}(10^{-8})$ while $\mathcal{G}$, $\mathcal{D}$ and $\mathcal{E}$ are between $\mathcal{O}(1)$ and $\mathcal{O}(10^{-2})$. Thus $\mathcal{F}$ is much smaller than any one of the other dimensionless parameters arising in (2.15) and (2.16), suggesting the Stokes flow limit $\mathcal{F} \to 0$, $\mathcal{F}/\varepsilon \to 0$. The so emerging equations could now be solved by a perturbation expansion $\Phi^* = \sum_{\nu=0}^{\infty} \varepsilon^\nu \Phi_\nu$ for all independent fields $\Phi^* = \{u^*, v^*, w^*, p^*, \sigma_x^*, \sigma_y^*, \sigma_z^*, \tau_{xz}^*, \tau_{yz}^*, \tau_{xy}^*, T^*\}$; however, the shallow ice approximation restricts consideration to the lowest order terms ($\nu = 0$), corresponding to the simultaneous limits

$$\mathcal{F} \to 0, \qquad \mathcal{F}/\varepsilon \to 0, \qquad \varepsilon \to 0. \tag{2.19}$$

Returning back to the dimensional notation, equations (2.15) then reduce to

$$\begin{aligned}
\nabla_H \cdot \mathbf{v}_H + \frac{\partial w}{\partial z} &= 0, \\
-\frac{\partial p}{\partial x} + \frac{\partial \tau_{xz}}{\partial z} &= 0, \\
-\frac{\partial p}{\partial y} + \frac{\partial \tau_{yz}}{\partial z} &= 0, \\
-\frac{\partial p}{\partial z} &= \varrho g, \\
\frac{dT}{dt} = \frac{\partial}{\partial z}\left(\kappa \frac{\partial T}{\partial z}\right) &+ 2EA(T')f(\tau^2)\tau^2, \\
\frac{\partial \mathbf{v}_H}{\partial z} &= 2EA(T')f(\tau^2)\boldsymbol{\tau}
\end{aligned} \tag{2.20}$$

in which $\mathbf{v}_H = (u, v)$, $\nabla_H = (\partial x \partial y)$ and $\boldsymbol{\tau} = (\tau_{xz}, \tau_{yz})$. These are seven equations for the seven unknowns $\mathbf{v}_H$, w, p, $\boldsymbol{\tau}$ and T. They comprise the field equations of the shallow ice approximation.

It turns out that a similar scale analysis for the heat equation in the rock yields

$$\dot{T}_R = \frac{\partial}{\partial z}\left(\kappa_R \frac{\partial T_R}{\partial z}\right), \tag{2.21}$$

while the evolution equations for the free surface (2.4) and the bed (2.5) remain unchanged. Alternatively, the reduced boundary conditions become:

- at the free surface $z = h_s(x, y, t)$

$$p = 0, \qquad \tau_{xz} = \tau_{yz} = 0, \qquad T_s = T_s(x, y, t), \qquad b_s = b_s(x, y, t); \tag{2.22}$$

- at the ice bedrock interface $z = h_b(x, y, t)$

$$\left.\begin{aligned} \chi\frac{\partial T}{\partial z} &= \chi_R\frac{\partial T_R}{\partial z}, \quad T = T_R\,, \\ \mathbf{v}_H &= 0 \end{aligned}\right\} \text{cold ice,}$$

$$\left.\begin{aligned} b_b &= \frac{1}{\varrho_w L_s}\left(\chi\frac{\partial T}{\partial z} - \chi_R\frac{\partial T_R}{\partial z} + \tau^* v_{||}\right), \quad T = T_R = T_M, \\ \mathbf{v}_H &= c|\boldsymbol{\tau}|^{m-1}p^{-l}\boldsymbol{\tau}, \end{aligned}\right\} \text{temperate ice;}$$

(2.23)

- at the lower boundary of the rock: $z = 0$

$$\chi_R\frac{\partial T_R}{\partial z} = -G. \tag{2.24}$$

The distinctive features of the shallow ice approximation are the following three points (i)–(iii):

(i) The vertical momentum balance reduces to the cryostatic force balance between vertical pressure gradient and the gravity force. (ii) The horizontal momentum balance comprises force balances between the horizontal pressure gradient and the corresponding vertical gradient of the shear stresses. Together with the boundary conditions $(2.22)_{1,2,3}$, these equations can be integrated to yield the stress fields

$$\begin{aligned} p(x, y, z, t) &= \varrho g(h_s(x, y, t) - z), \\ \boldsymbol{\tau} &= \varrho g(h_s(x, y, t) - z)\nabla_H h_s(x, y, t), \end{aligned} \tag{2.25}$$

which depend on geometry but not on material properties. Provided the temperature distribution is known, $(2.20)_{1,6,7}$ together with (2.25) imply (through integration)

$$\begin{aligned} \mathbf{v_H}(x, y, z, t) &= \mathbf{v_H}(h_b) + C(z, t, \|\nabla_H h_s\|)\,\nabla_H h_s, \\ C(z, t, \|\nabla h_s\|) &= -2\varrho g\int_{h_b}^{z} EA(T_I'(z'))\,f(\tau^2(z'))\,(h_s - z')\,dz', \\ w(x, y, z, t) &= w(h_b) - \int_{h_b}^{z}\nabla_H\cdot\mathbf{v}_H(x, y, z')\,dz', \\ \tau(x, y, z, t)^2 &= (\varrho g(h_s(x, y, t) - z)\|\nabla_H h_s\|)^2, \\ \|\nabla_H h_s\| &= \left(\frac{\partial h_s(x, y, t)}{\partial x}^2 + \frac{\partial h_s(x, y, t)}{\partial y}^2\right), \\ \mathbf{v}_H(h_b) &= \begin{cases} \mathbf{0} & \text{(cold ice)}, \\ -c(\varrho g h)^{m-l}\|\nabla_H h_s\|\nabla_H h_s & \text{(temperate ice)}, \end{cases} \\ w(h_b) &= \mathbf{v}_H(h_b)\cdot\nabla_H h_b\,. \end{aligned} \tag{2.26}$$

It follows that the velocity field within the ice shield can be computed by mere quadratures (if the temperature field and the geometry are prescribed). The formulas $(2.25)_2$ and $(2.26)_{1,6}$, however, also imply the following important facts of the shallow ice approximation, which can be tested by observation and thus may be used as evidence whether the approximation is applicable in a particular case:

- The horizontal shear stress vector points in the direction of steepest descent of the free surface. It is zero parallel to the level lines.

- At any given position in the horizontal plane, the horizontal velocity vector $\mathbf{v}_H$ does not change direction with depth. Its direction at all depths is that of the steepest descent of the surface topography.

- A dome or a trough is the location of vanishing horizontal velocity.

These properties were first recognized by HUTTER [71].

(iii) The heat equation shows that, whereas heat advection is significant in all spatial directions, conduction is dominant in the vertical direction. This means that the heat equation is parabolic only with regard to the vertical coordinate, but has been hyperbolized in the horizontal directions. For very thick ice sheets([2]) vertical thermal diffusion is small ($\mathcal{D} \ll 1$) and dissipation large ($\mathcal{E} = \mathcal{O}(1)$) so that thermal diffusion essentially operates only in a near-basal boundary layer. For very thin ice sheets $\mathcal{D} = \mathcal{O}(1)$ and $\mathcal{E} \ll 1$, so vertical convection of heat is significant over the entire depth but dissipation is small. In ice sheet modelling through ice ages both situations must be expected, leaving no room for further simplifications.

This limiting equation set has been used by virtually all numerical modellers who deal in one way or another with the deformation and distribution of temperature in ice sheets. Isothermal plane and axisymmetric [134, 135] flows, thermomechanically uncoupled cases with prescribed temperature [136] and the full plane [35, 61, 62, 78, 102] and axisymmetric [79] coupled cases were analysed before the full three-dimensional theory was numerically implemented in FD-programs [16, 17, 18, 80, 90, 91]. With them the steady-state response of Greenland, Antarctica and other ice sheets were studied, but also their response to climate variations, including complete interglacial cycles [19–23, 59, 81, 82, 84, 86, 87, 88, 89, 103, 105, 125, 129, 158, 188]. Historical and hypothetical ice sheets were also studied [4, 85, 99]. Presently, the physical as well as theoretical weaknesses of this limiting model are recognized; the theory has been extended e.g. to handle polythermal ice [7, 47, 50–56, 68, 71], but the shallow ice approximation is also extended to overcome its mathematical shortcomings.

([2]) Compare the definitions of $\mathcal{D}$ and $\mathcal{E}$ in (2.17).

2.4. Limitations of the shallow ice approximation

These occur because the shallow ice approximation is, as an asymptotic theory, not uniformly valid in the entire domain over which the ice extends. Regions of its fallacy are near-margin zones and the vicinity of ice domes and ice divides. Both can be revealed by scrutinizing the ice-thickness-evolution equation (2.4), which upon using (2.5) and (2.26) takes the form

$$\begin{aligned}\frac{\partial h_s}{\partial t} &= \nabla_H\cdot(\mathcal{D}_{sg}\nabla_H h_s) + b_s + b_b - \frac{1}{\tau_l}\left(h_b - h_0 + \frac{\varrho}{\varrho_a}h\right)\\ &= \mathcal{D}_{sg}\triangle_H h_s + (\nabla_H\mathcal{D}_{sg})\cdot\nabla_H h_s + b_s + b_b - \frac{1}{\tau_l}\left(h_b - h_0 + \frac{\varrho}{\varrho_a}h\right),\end{aligned} \tag{2.27}$$

where

$$\begin{aligned}\mathcal{D}_{sg}(h_s, h_b, \|\nabla_H h_s\|) &= \mathcal{D}_s(h_s, h_b, \|\nabla_H h_s\|) + \mathcal{D}_g(h_s, h_b, \|\nabla_H h_s\|)\\ &= c(\varrho g)^{m-l}(h_s - h_b)^{m-l+1}\|\nabla_H h_s\|^{m-1}\\ &\quad + 2\varrho g E\int_{h_b}^{h_s} A(T'(z))f(\tau^2(z))(h_s - z)^2\,dz\\ &\overset{\text{Glen}}{=} c(\varrho g)^{m-l}(h_s - h_b)^{m-l+1}\|\nabla_H h_s\|^{m-1}\\ &\quad + 2(\varrho g)^n E\|\nabla_H h_s\|^{n-1}\int_{h_b}^{h_s} A(T'(z))(h_s - z)^{n+1}\,dz,\end{aligned} \tag{2.28}$$

in which (2.5) has been used and $(2.28)_2$ is valid for a power law fluid. $\mathcal{D}_{sg}$ is a diffusivity with $\mathcal{D}_s$ and $\mathcal{D}_g$ due to sliding and gliding, respectively, and formally $\mathcal{D}_s = 0$ for a cold base. Equation (2.27) is a parabolic advection-diffusion equation for h_s. For $A(T')$ as defined in (2.2) and for a positive-definite creep response function $f(x)$ (> 0 for $x > 0$, $= 0$ for $x = 0$), or for $n \geq 1$ (i.e. Newtonian or pseudoplastic behaviour) the integrals in (2.27) are bounded. The exact margin behaviour depends on the values of m, l and n and could be analysed as shown in [62]. We are satisfied here with a restricted analysis that discloses the difficulties and refer the reader to [44, 71].

2.4.1. Near margin behaviour. The behaviour of D_s, D_g and their gradients in the neighbourhood of the margin as $h_s \to h_b$ depends on the exact functional forms of A, f, on the exponents m, l (and n), as well as on the functional forms of b_s and b_b in the vicinity of the margin. This behaviour can be extracted from a local analysis and it turns out that, when $h_s(x, y, t) \to h_b(x, y, t)$ as the margin is approached, $\|\nabla_H h_s\|$ usually becomes unbounded. A finite marginal slope is only obtained (i) at a cold margin ($\mathcal{D}_s = 0$) when Newtonian behaviour at small

strain rates is permitted (i.e., for a power law with $n = 1$), and (ii) when sliding is permitted close to the margin if $m = 1$. None of these cases is usually assumed – one uses Glen's flow law with $n = 3$ and $m = 3$, $l = 2$ – and so computed margin slopes must be infinite. The detailed analysis of this for plane flow is given e.g. in [44, 62, 71, 134]. Morland and co-workers request the sliding law to be such that finite slope profiles at the margin are obtained in which case uniform validity of the shallow ice approximation is guaranteed, [62, 135, 136, 137]. In numerical implementations of all other authors except [78, 173], the singular marginal behaviour is assumed to be local, not affecting the solution away from it a great deal. All the more, the mesh size is usually considerably larger than the marginal boundary layer is thick; in other words, the numerics determine a finite marginal slope and thus regularize the margin by effectively introducing a mesh-dependent sliding law. Thus, this passive boundary layer does not seem to be a real problem.

2.4.2. Large surface curvature at ice divides. Consider next the vicinity of a dome which is characterized by $\nabla_H h_s = \mathbf{0}$. Thus, according to (2.25) and (2.26)

$$\mathbf{v}_H = \mathbf{0}, \qquad \boldsymbol{\tau} = \mathbf{0}, \qquad \tau^2 = 0 \ \text{(at dome)}.$$

Let us choose the Cartesian coordinate system with origin at the dome. It then follows from (2.26) locally, i.e., at $(x, y) = \mathbf{0}$

$$\nabla_H \cdot \mathbf{v}_H = -\Big\{ c(\varrho g)^{m-l}(h_s - h_b)\, \|\nabla_H h_s\|^{m-1} + 2\varrho g E f(0) \int_{h_s}^{z} A(T'(\bar{z}))(h_s - \bar{z})\, d\bar{z} \Big\} \triangle_H h_s \tag{2.29}$$

and from (2.4)

$$\frac{\partial h}{\partial t} + \int_{h_b}^{h_s} \nabla_H \cdot \mathbf{v}_H \, dz = b_s + b_b. \tag{2.30}$$

Combining (2.29) and (2.30) yields

$$\frac{\partial h}{\partial t} - \mathcal{D}_0 \triangle_H H = b_s + b_b \qquad \text{(at dome)}, \tag{2.31}$$

where $\mathcal{D}_o = \mathcal{D}_s + \mathcal{D}_{g_0}$ is defined in (2.28) and $\mathcal{D}_{g_0}$ is obtained from $\mathcal{D}_g$ by replacing $f(\tau^2)$ by $f(0)$ (which for Glen's flow law equals zero). In steady state (2.31) can be used to evaluate the mean surface curvature at the ice divide,

$$\triangle_H h_s = \frac{b_s + b_b}{\mathcal{D}_s + \mathcal{D}_{g_0}} \qquad \text{(at dome)}, \tag{2.32}$$

which explains why the shallow ice approximation may fail close to divides. Indeed, at a cold divide $\mathcal{D}_s = 0$ and otherwise $\mathcal{D}_s = 0$ unless $m = 1$. Furthermore, when $f(0) = 0$, $\mathcal{D}_{g_0} = 0$ as well, implying that $\triangle_H h_{s\,\mathrm{dome}} = \infty$ in this case, in violation with the shallowness assumption. Since basal sliding cannot be guaranteed at a dome, regularization of the kinematic surface equation at least requires a finite viscosity flow law ($f(0) \neq 0$). However, even with this incorporated, very large surface curvatures must be expected at a divide.

As was done for the margin regions, numerical integration can be performed and the divide zone formally regularized through discretization, however observations indicate that near-divide velocities and temperatures are not accurate in general.

In attempts to date the ice from ice cores in connection with isotope composition studies [1, 2, 3, 11, 12, 13, 93–101, 118, 119, 120, 157, 169–172], the necessity of incorporation of "longitudinal stresses" was recognized, but computations [28–31, 160, 161, 163, 166, 167] employ streamline models and steady state with diverging flow properties taken into account by a fudge factor. In short, the computational suggestions are *ad hoc*, not in conformity with a proper scaling, and not appropriate to the three-dimensional situation. First attempts at a systematic use of higher order terms in the perturbation expansion are due to BLATTER [6] and MANGENEY *et al.* [126–128]. Equations (2.15) and (2.16), however, clearly indicate how the shallow ice approximation can be improved either by formal perturbation expansion or iteration. This analysis is presently under way in a dissertation at TH Darmstadt.

3. Application of the model to the Greenland Ice Sheet

The above SIA equations have been computationally solved by using finite difference techniques by BUDD *et al.* [16, 17, 20], CALOV and HUTTER [25, 26], HUYBRECHTS *et al.* [80–89, 103] and FABRÉ *et al.* [36]. These programs are formidable undertakings; we shall not discuss their peculiarities. We present some computational results obtained with our model, the intention being to highlight the geophysical implications rather than to expose the numerical complexities.

Ice sheet dynamics is governed by external and internal parameters; the first contribute to their driving, the second affect their response. The most important external driving parameters are furnished by the implemented atmospheric model of which a very simple version will be presented. Other less direct external "forcings" are the interaction of the ice sheet with the solid earth through the geothermal heat, the bedrock sinking and through the handling of the calving mechanism at ocean boundaries. Internal parameters relate to the material behaviour, here most conspicuously expressed by the enhancement factor, the sliding law at the ice-bed interface and the dissipation associated with it.

We shall in this section describe these couplings and present some parameter studies using the Greenland Ice Sheet as a test case. Then simplified climate scenarios will be applied and, finally, a comparison of the computed with the measured velocity transect – the so-called EGIG line – will be made. These comparisons will not only delineate the difficulties that one encounters when trying to identify phenomenological parameters of such a large geophysical system, but equally demonstrate the sheer impossibility of achieving an objective comparison.

3.1. Simplified model-atmosphere

In the model, the *atmospheric surface temperature* will be prescribed in the form

$$T_a(x,y,t) = T_a(x,y)|_{\text{loc}} + T_D(t), \tag{3.1}$$

where $T_a(x,y)|_{\text{loc}}$ is the present local distribution of the mean atmospheric temperature, and $T_D(t)$ describes the long periodic climate changes. For Greenland, data of the local temperature was collected by OHMURA [154] and very well fit by the linear relation $T_a|_{\text{loc}} = \vartheta_0 + a_0\varphi + \gamma h_s$, $\vartheta_0 = 55.76$ [°C], $a_0 = -0.8471$ [°C °North^{-1}], $\gamma = -8$ [°C km^{-1}], in which φ is latitude and h_s surface height above sea level. $T_D(t)$ is the climate driving and will be selected according to which climate scenario is modelled.

The *accumulation-ablation-rate fuction*

$$b_s = S - M \qquad [\text{m a}^{-1}, \quad \text{ice equivalent}] \tag{3.2}$$

is divided into *snowfall* S and *melting* M. The present-day annual mean of the snowfall is represented as a polysurface deduced from data reported by OHMURA and REEH [155]; the annual mean snowfall at earlier times is modelled according to

$$\begin{aligned} S(t) &= S_{\min} + (S_{\text{today}} - S_{\min})\frac{T_D(t) - T_D^{\min}}{T_D^{\text{today}} - T_D^{\min}}, \\ S_{\min} &= 0.5\, S_{\text{today}}, \qquad T_D^{\min} = -10^\circ\text{C}, \qquad T_D^{\text{today}} = 0^\circ\text{C}. \end{aligned} \tag{3.3}$$

This assumes that the snowfall was half as large at the climate minimum as it is today.

To parameterize the melting, we employ BRAITHWAITE'S [10] "positive degree day" formula

$$M = \frac{\beta_2}{Y}\max\left(0, \Sigma_+ - \frac{P_{\max} Y}{\beta_1} S\right) \tag{3.4}$$

with

$$\Sigma_+ = \begin{cases} YT_a & T_A \le T_a, \\ \dfrac{Y}{\pi}\left(T_a \arccos\left(-\dfrac{T_a}{T_A}\right) + \sqrt{T_A^2 - T_a^2}\right) & -T_A < T_a < T_A, \\ 0 & -T_A \ge T_a, \end{cases}$$

$$\beta_1 = 0.9\,, \qquad \beta_2 = 2.6 \qquad [\text{m water equivalent a}^{-1}\,^{\circ}\text{C}^{-1}],$$
$$Y = 10\,\text{a}\,, \qquad P_{\max} = 0.6,$$

which accounts for the percolation and re-freezing of melt-water and superimposed ice, respectively. T_a is the mean annual air temperature and T_A its seasonal amplitude. For a detailed explanation, see CALOV and HUTTER [26].

3.2. Handling of the model ice margin

As long as the ice margin stays on the continent we let it freely evolve, either advancing or retreating, depending on whether there is net mass addition or subtraction. When the ice margin reaches the ocean, then all mass flowing through that margin position is treated as *calving* and is lost to the ice sheet. This mechanism is interrupted only when the ice is retreating again at sheet positions distant from the ocean.

In the simulations described below, the sea level will be held constant; however in more realistic modelling it should be a function of time.

3.3. Computations of ice thickness distribution under steady driving conditions

3.3.1. Variation of the amplitude of the annual temperature. We present here the results of computations of the steady-state geometry of the Greenland Ice Sheet subject to various external time-independent driving conditions. The model is integrated subject to various parameterizations, using today's ice thickness distribution and temperature distribution it obtains for today's thermal equilibrium as initial conditions. Computations are continued until the ice thickness and the ice margins as well as the temperature distribution no longer change. This happens at approximately 50 000 model years. In the standard run we use as geothermal heat $G = 42$ mW m^{-2}, as enhancement factor $E = 3$, and as seasonal air temperature amplitude $T_A = 14^{\circ}$C. Figure 2 a displays the level lines of the free surface and the ice margins obtained when also the no-slip condition is imposed on the entire basal surface. When compared to the observed present surface topography (see CALOV and HUTTER [26]), the ice extends too far to the North and does not extend enough in the South. Moreover, the computed Summit height is about 600 m too high.

If we enlarge or lower the amplitude of the annual temperature variation by 7°C, to $T_A = 21^{\circ}$C (Fig. 2 b) and $T_A = 7^{\circ}$C (Fig. 2 c), it is seen that the former results in a substantial ice sheet reduction while the changes in the latter scenario are far less dramatic. This non-symmetry in the behaviour is due to the boundary conditions at the ice-ocean margin: free evolution for ice retreat but full calving for advance.

3.3.2. Variation of the sliding parameter. By incorporating a sliding condition along the ice-bedrock interface, reduced ice thickness (close to reality) can be modelled; this is simply because ice flows more easily toward the margins. At

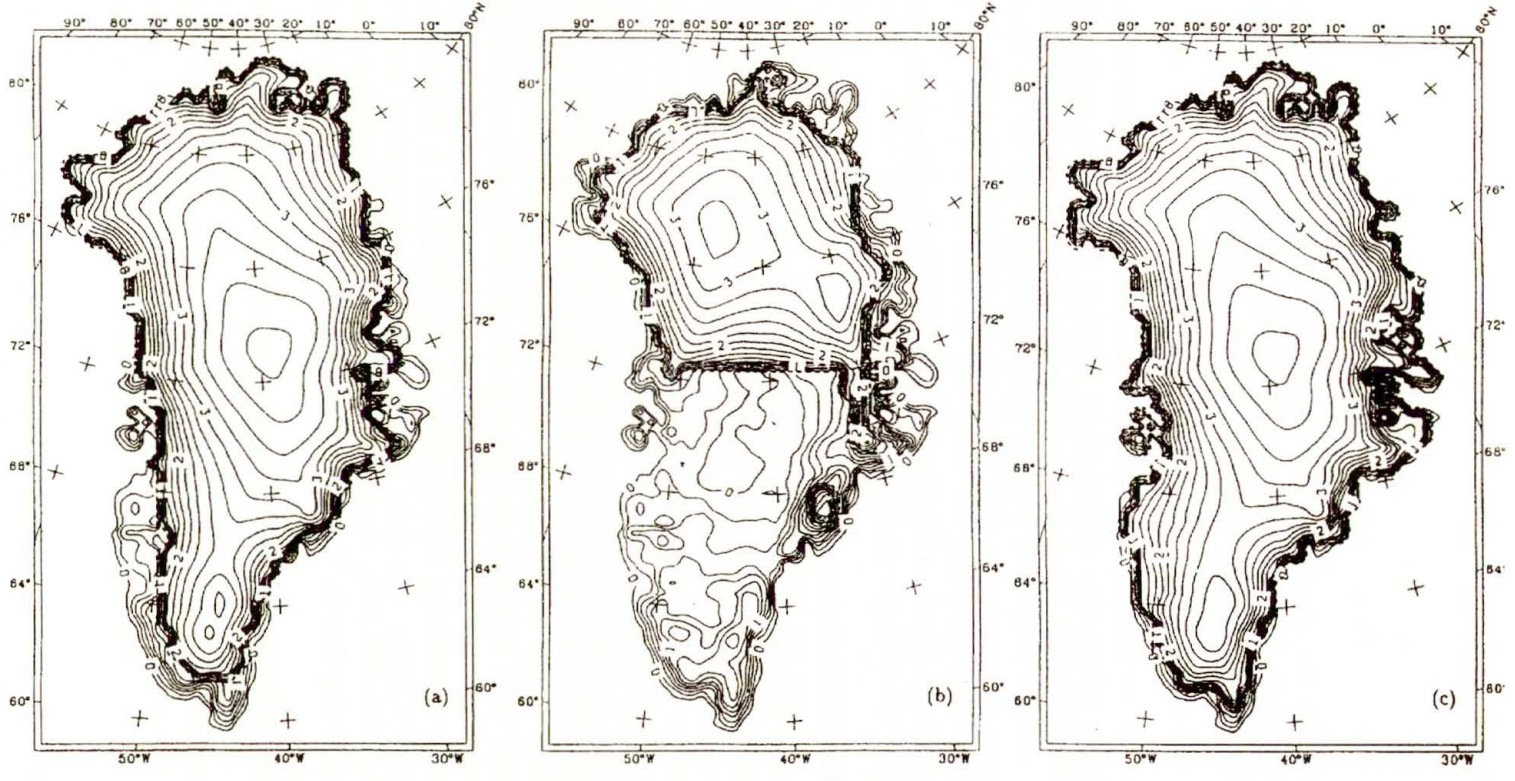

FIG. 2. Level lines of the free surface of the Greenland Ice Sheet (equidistance 200 m) for the steady-state computations under present conditions with the enhancement factor $E = 3$ using the amplitude of annual temperature $T_A = 14°C$ (a), $T_A = 21°C$ (b) and $T_A = 7°C$ (c).

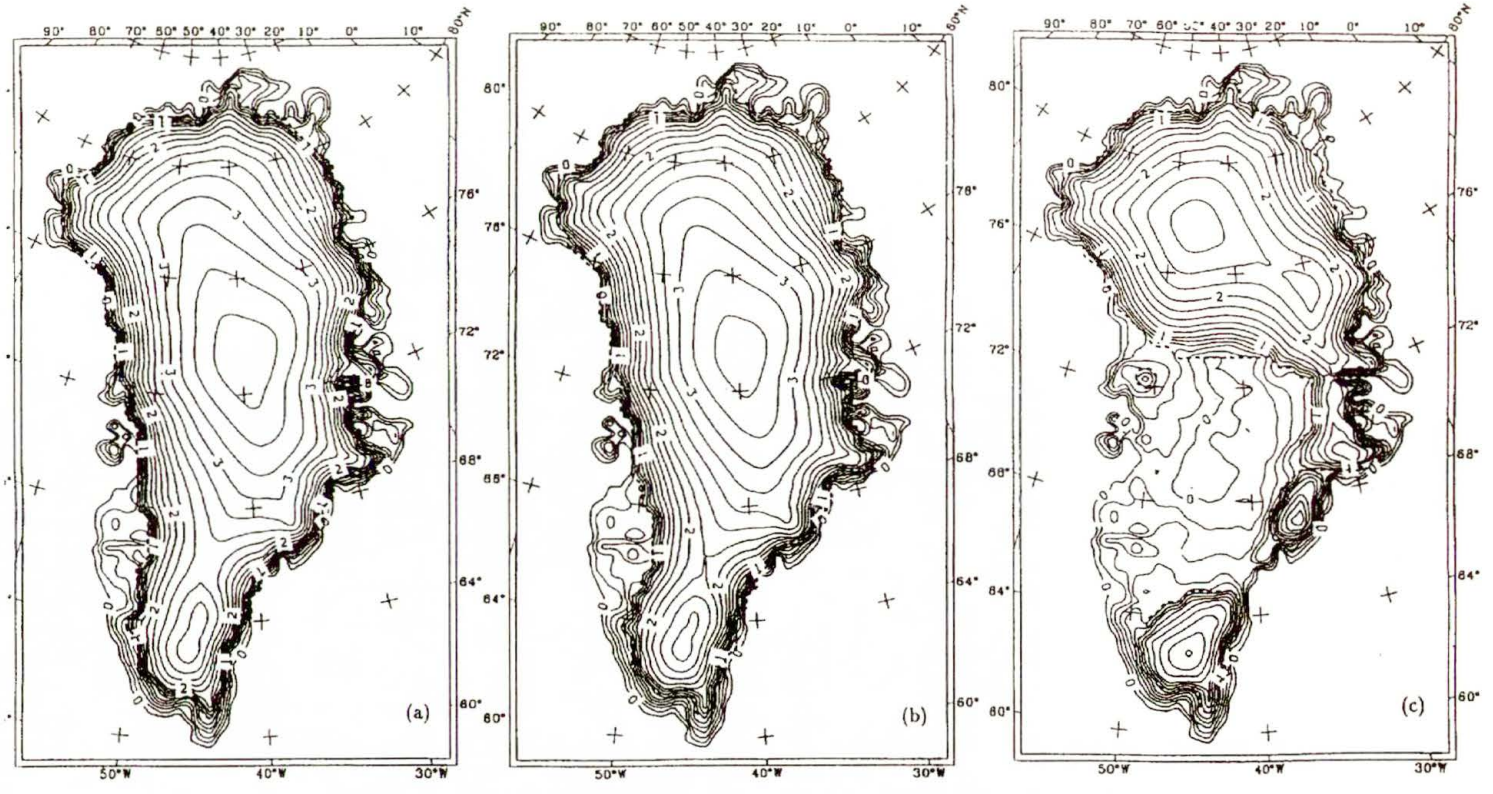

FIG. 3. Level lines of the free surface of the Greenland Ice Sheet in present steady-state using a latitude-dependent amplitude of temperature and incorporating sliding in the entire basal area with a sliding parameter $c_M = 2 \times 10^4\,\mathrm{a}^{-1}$ (a), $c_M = 6 \times 10^4\,\mathrm{a}^{-1}$ (b) and $c_M = 10 \times 10^4\,\mathrm{a}^{-1}$ (c).

a positive feedback margin slopes will be less steep and there is an increased ablation zone.

We shall use the sliding law

$$\mathbf{v}_H(h_b) = -c_M h \|\nabla_H h_s\|^2 \nabla_H h_s \,, \tag{3.5}$$

in which h is the ice thickness and h_s the surface height a.s.l. ∇_H is the horizontal gradient operator, $\mathbf{v}_H$ the horizontal velocity and c_M a coefficient with dimension a^{-1}.

Computations were performed for steady state using now a latitude-dependent amplitude of annual temperature $T_A = a + b\varphi$, $a = -23°\mathrm{C}$, $b = 0.55°\mathrm{C\,North}^{-1}$, and implementing sliding everywhere according to (3.5) with $c_M = (2;\ 6;\ 10) \times 10^4\,\mathrm{a}^{-1}$, and frictional heat due to sliding ignored, Figs. 3 a, b, c. It is seen that increasing the sliding coefficient causes a lowering of the North- and South domes of about 200 m, compare Fig. 3 a with Fig. 3 b. The results for $c_M = 10 \times 10^4\,\mathrm{a}^{-1}$ (Fig. 3 c) are obviously very unrealistic, but they demonstrate how catastrophically an ice sheet can develop when sufficient sliding is provided. The ice sheet has been split into essentially two parts with an ice-free 800 km wide zone in Middle-Greenland. The South cap exists, because it sits on high elevated ground but equally also because of the large snow accumulation rate there. If the frictional basal heat were incorporated, the two caps in Fig. 3 c would be even smaller; however, rebound of the substratum is a negative feedback and both may approximately balance.

Scenarios with sliding restricted to the basal melting zones, and frictional heat as well as bedrock sinking incorporated are analysed by WEIS *et al.* [188].

3.3.3. Variation of other parameters. We have also varied the snow melting parameters β_1, β_2 and the geothermal heat. While these also have some definite influences upon the steady-state geometry of an ice sheet, their variation about the most realistic values has indicated less dramatic sensitivity than with variations of the amplitude of the mean annual temperature T_A or the sliding coefficient c_M. However, variations in the geothermal heat flow changes the temperature distribution close to the base considerably.

3.4. Basal temperature evolution through the ice age

3.4.1. Glacial climate cycles. The external driving surface temperature T_D is constructed from the data of the Vostok ice core, Antarctica (BARNOLA *et al.* [1]), by selecting upper and lower bounds, Fig. 4,

$$T_D(t) = \begin{cases} T_D^{\mathrm{I}}(t) & \text{climate I,} \\ T_D^{\mathrm{II}}(t) & \text{climate II,} \end{cases} \tag{3.6}$$

respectively. These idealized cycles are prolonged by one period into the past in order that the model can be spun-up to appropriate initial conditions at the

end of the Illinoian Ice Age. The idealized climates I and II reproduce the steep warming from the climate minima to the interglacials very well, but model the slower decay from the Eemian Interglacial to the Wisconsin minimum relatively poorly. We thus expect different results for the two.

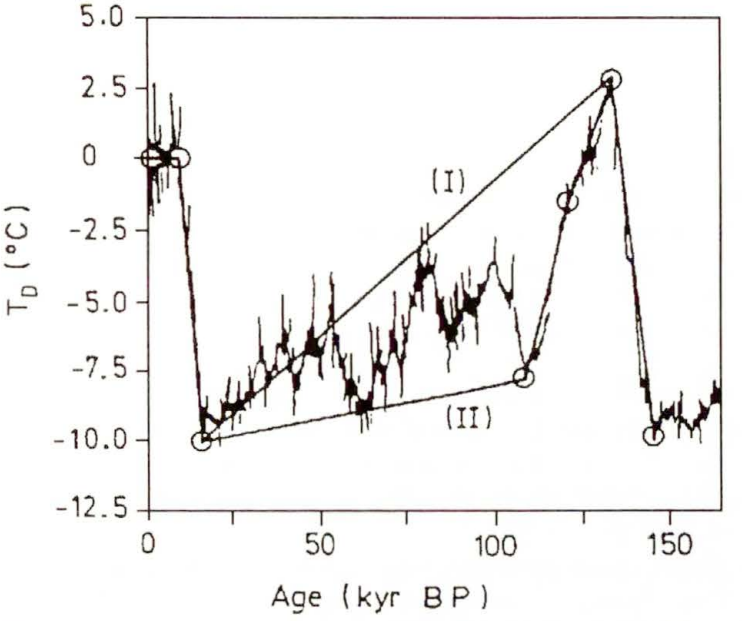

FIG. 4. Vostok δD-temperatures as taken from BARNOLA *et al.* [1] from present to 160 ka BP together with the model climate scenarios (I) and (II) that describe an approximate upper and lower bound to the Vostok data. Circles indicate points with abrupt climate changes or at climate maxima and minima, respectively.

Computional results are presented for the following scenarios:

• I or II: Response of the Greenland Ice Sheet under standard conditions (i.e., $E = 1$, $G = 42$ mW m^{-2}, no-slip) to the external climates I and II, respectively, while ignoring the thermal response of the substrate.

• I-S: Same as I, but now the response of the substrate is taken into account.

• I-S-E=3: Same as I-S, but now the enhancement factor of Wisconsinan ice is applied throughout.

In the first set of computations the ice thickness distribution will be held constant, the intention being to isolate the thermal response of the system substrate-inland ice. If the evolution of the geometry were varied, it would be very difficult to find the primary cause for the particular behaviour.

3.4.2. Basal temperatures at Dye 3, Summit and Camp Century. We discuss here the time series of temperature at the base which follow from computations according to the above idealized climate scenarios. The time series should not be

regarded as giving a realistic temperature distribution through 275 ka, but they disclose very significant behaviour that could not so well be identified with more realistic scenarios. The bore-hole positions are significant because extensive isotope studies have been performed (HANSEN and LANGWAY [57], DANSGAARD *et al.* [32], JOHNSEN *et al.* [92]). For these analyses it is of interest to know (i) how basal-temperature peaks lag behind the driving peaks, and (ii) whether the basal ice at these positions has at any time been at melting. Keeping the ice geometry fixed puts the results on the safe side in this regard, i.e., makes the base somewhat warmer.

For Dye 3, Summit and Camp Century time series are presented for the driving surface temperature (climate I), the homologous basal temperature of scenarios I, I-S and I-S-E=3, and the deviation of the geothermal heat flow into the ice from the "equilibrium" value $G_{\text{eq}} = 42\ \text{mW m}^{-2}$ of scenarios I-S and I-S-E=3. The sytem is driven by two ice age cycles as illustrated in Fig. 4, lasting from 275 ka BP to present.

a. Dye 3. Scenario I, computed without taking the thermal response of the rock bed into account and by using $E = 1$ (Fig. 5 b) shows that both maxima and minima of the homologous temperature at the base occur 11.6 ka, 6.5 ka and 3.2 ka, respectively, after the corresponding maxima of the driving time series $T_a(t)$. The second of the two phase lags of the minimum is smaller than the first because the temperature rise to the Holocene is faster than that to the Eemian Interglacial. The graph also shows that no spin-up is needed for this scenario, because the two maxima of the basal temperatures are the same. Today's basal temperatures are by 0.5°C lower than the present equilibrium temperature would be. Whereas the deviation of the basal homologous temperature from its corresponding equilibrium value is largest at the last Interglacial (at about 135 ka BP), this deviation is smallest at the climatic minimum.

If the thermal inertia of the rock bed is included (Fig. 5 c), the present homologous basal temperature is 1.69°C below the corresponding equilibrium value. The deviation from the equilibrium value at all times where it is calculated is here larger than for scenario I. The model is not completely spun-up after one cycle because the relative maximum at 110.2 ka BP is larger than that at 237.8 ka BP: The rock layer adds additional thermal inertia to the system. Furthermore, whereas the phase shifts of the minima (6.5 and 3.2 ka) are exactly the same as those of scenario I, those of the maxima are roughly doubled. Interesting to note is the temporal variation of the heat flow into the ice from the rock bed. Panel e) shows the deviation of this flow from its value at the lower boundary, $G_{\text{eq}} = 42\ \text{mW m}^{-2}$. This heat flow is either larger or smaller than its equilibrium value by up to 21%. The present value is by $4\ \text{mW m}^{-2}$ smaller than G_{eq}, and the tendency is falling. Also interesting is that the phase shifts of the maxima (and minima) differ from those of the temperatures. This is the manifestation of nonlinear effects.

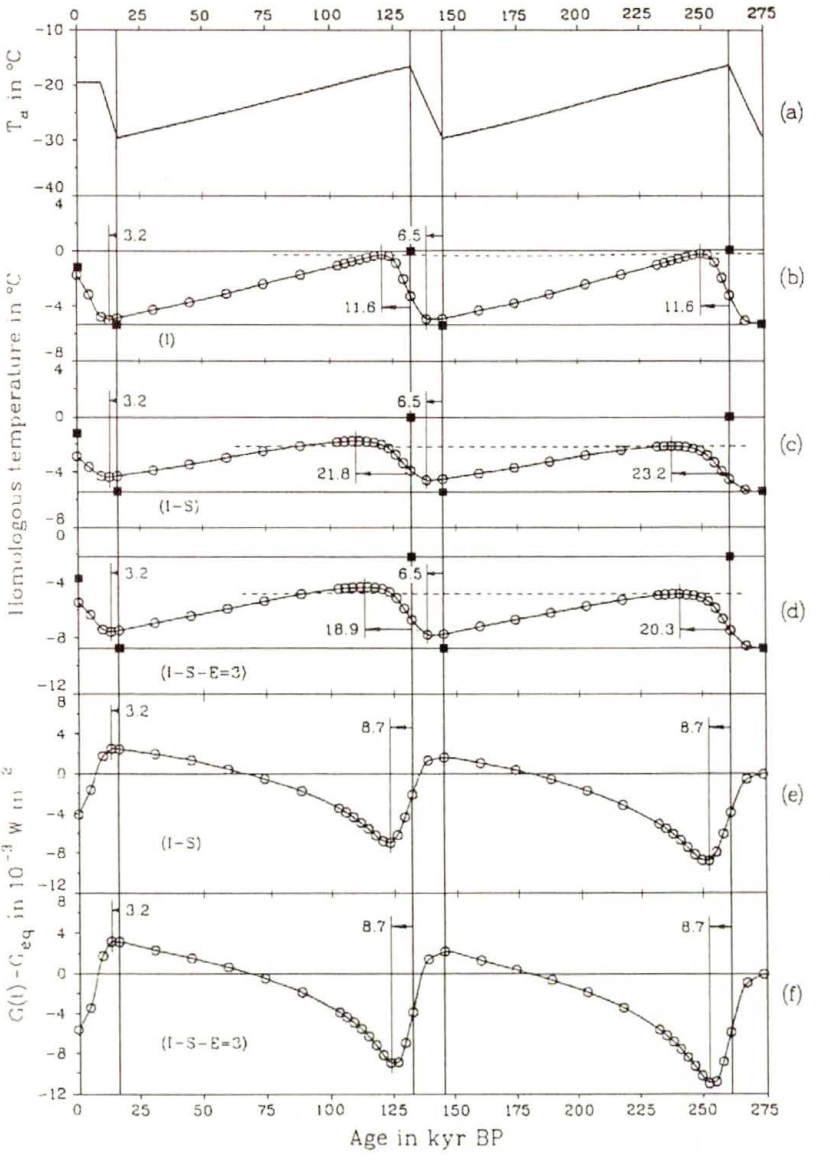

FIG. 5. "Dye 3": Variation of the athmosphere temperature $T_a(t)$ at Dye 3 from today to 275 kyears BP (a), basal homologous temperature for scenarios I (b), I-S (c), I-S-E=3 (d) and the difference of the actual heat flow through the ice-rock interface from the equilibrium value $G_{eq} = 42\,\mathrm{mW\,m^{-2}}$ for scenarios I-S (e) and I-S-E=3 (f). Symbols ○ are computed, solid lines interpolated. ■ mark computed equilibrium values of the homologous basal temperature if the climate were driven with the air temperature at that time. Inserted numbers with arrows show shifts between the relative maximum of the driving temperature and that of the basal homologous temperature or the corresponding minima of the heat flow. The dashed line marks the first relative maximum and compares it with the second.

Computations for a I-S-E=3 scenario, see Fig. 5 d, f, show that, because the ice is softer in this case, cold ice will be transported downward faster than with $E = 1$. Basal temperatures are now colder (by approximately 2°C), and phase shifts of the maximum basal temperatures shorter than for $E = 1$ (20.3 ka, 18.9 ka) while those of the minima remain the same. The variation of the heat flow through the ice-rock interface is also slightly enhanced. Thus the softness of the ice has a significant effect on the thermal regime of the Greenland Ice Sheet through time.

Calculations were also performed for scenario II (without a rock layer and for $E = 1$), but are not shown here. When compared with the results obtained with scenario I it is seen that the faster approach from the Eemian Interglacial to the Wisconsinan minimum is also visible in the temporal distribution of the basal temperature: The base is generally colder than for scenario I, but the maxima and minima of the homologous temperatures and their phase shifts are not very much different from those of scenario I, and, in particular, the present basal temperature is practically the same. The steep warming of the climate at the end of the last Ice Age seems to hide the detailed variations of the climate during the Ice Age.

b. Summit. Let us compare the results for this location with depth $h \approx 3200$ m (Fig. 6) with those of Dye 3, $h \approx 2000$ m. Again the phase shifts between the maxima of the homologous temperature are larger than those of the minima (Fig. 6 b, c, d). For scenario I one glacial cycle is enough to obtain the spun-up temperature distribution. Phase shifts of the maxima of the homologous basal temperature are far larger for scenario I-S than for scenario I. And for softer ice, $E = 3$, the basal temperature and phase shifts are generally smaller than for the corresponding computations with $E = 1$. The heat flow into the ice roughly agrees with the equilibrium value 42 mW m^{-2} but the tendency is falling. All phase shifts for Summit are larger than for Dye 3, and the corresponding amplitudes are smaller, both effects that are largely due to the larger thickness of the ice at "Summit".

c. Camp Century. Because the ice at Camp Century with its 1.4 km thickness is thinnest in comparison to the previous bore hole sites, it is expected that the corresponding phase shifts are smallest and the amplitudes largest, see Fig. 7. Whereas this is indeed so for the amplitudes, the phase shifts for Camp Century are in almost all scenarios and cases as large as (or even larger than) for Dye 3. Note that the phase shift for the first minimum in scenario I-S is larger than for Dye 3. A possible explanation could be that the model is still in the process of spin-up. On the other hand, the result indicates that thickness cannot be the only quantity that is responsible for the delay of basal processes from their climate forcing. Diffusion, advection and dissipation equally contribute. Among the three locations, the temporal variation of the heat flow into the ice deviates most from the equilibrium heat flow, and the present value is smaller than the equilibrium value by an amount of 6 – 8 mW m^{-2}.

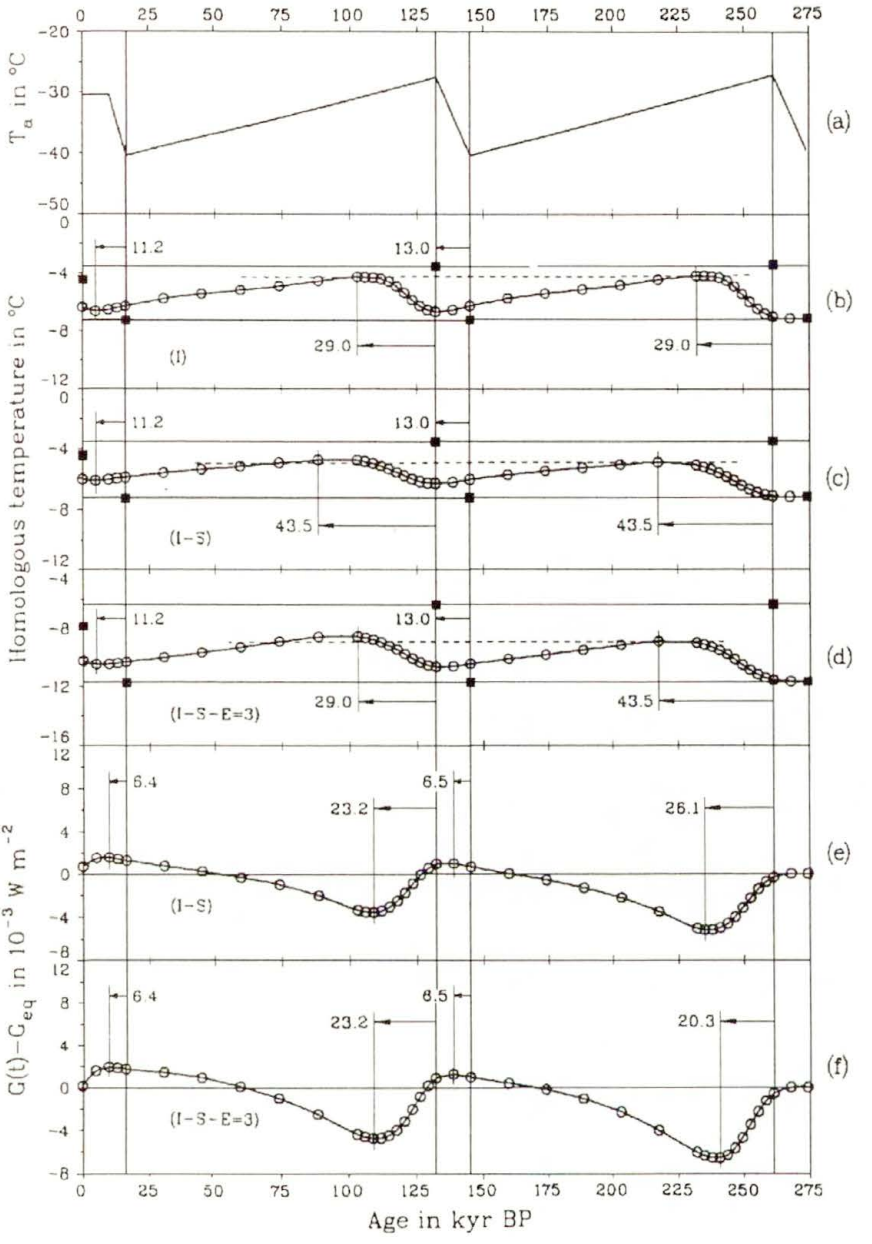

FIG. 6. "Summit". Same as for Fig. 5.

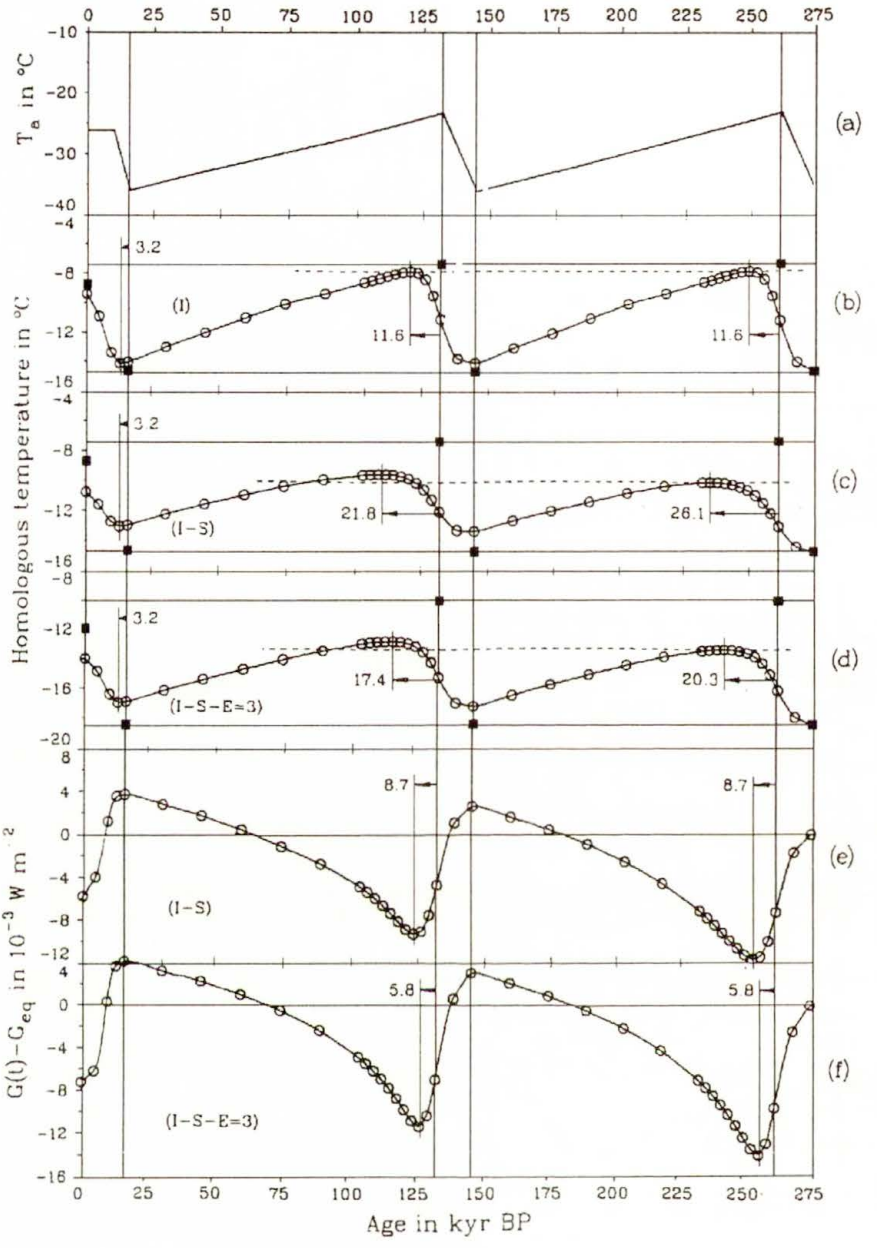

FIG. 7. "Camp Century". Same as for Fig. 5.

3.5. Comparison with the data

In this section we compare the ice-sheet-surface velocities that were measured along the EGIG (International Glaciological Greenland Expedition) traverse [64, 25].

3.5.1. The velocity data along the EGIG traverse. The EGIG traverse is the best known measuring traverse in Greenland and crosses Greenland approximately at the 70° N latitude from West to East (see Fig. 8). For our comparison, those measuring points listed in HOFMANN [64] with an approximate distance of 40 km will be considered, which corresponds to our numerical horizontal grid resolution. During the EGIG expedition the free surface velocity

$$v_H^{\text{meas}}(h_s) = |\mathbf{v}_H^{\text{meas}}(h_s)| = |v_x^{\text{meas}}(h_s)\mathbf{e}_x + v_y^{\text{meas}}(h_s)\mathbf{e}_y| \tag{3.7}$$

and the polar angle Θ^{meas} between the vectors $\mathbf{e}_x$ and $\mathbf{v}_H^{\text{meas}}$ were measured. Figure 8 displays the measured EGIG velocities (i.e. horizontal projections) as arrows at positions P 1 to P 17 along with the level lines of the free surface topography. These velocities decrease from $109.71\,\text{m}\,\text{a}^{-1}$ at position P 1 in the West to a minimum of $3.54\,\text{m}\,\text{a}^{-1}$ at position P 14 in the center and increase again to $12.46\,\text{m}\,\text{a}^{-1}$ at position P 17 in the East. Qualitatively, this is in conformity with the shallow ice approximation, which states that the horizontal velocities are pointing in the direction of steepest descent (i.e., orthogonally to the level lines) and are proportional to $(\partial h_s/\partial\sigma)^n$, where σ is the distance measured along the direction of steepest descent and $n = 3$ is the exponent in Glen's power law. Thus the velocities grow with increasing surface slope, corresponding to a reduction of the distance between the level lines, as shown.

3.5.2. Comparison of measured with computed EGIG-velocities using computations with fixed surface geometry. Table 3 summarizes the comparison of the measured and computed surface velocities along the EGIG traverse at points P 1 to P 17 as obtained with climate scenario I-S. This scenario drives the ice sheet evolution with an upper bound of the Vostok temperature data as explained in Sec. 3.4.1. The thermal inertia of a 4 km thick solid rock layer is accounted for and the no-slip condition at the ice-bedrock interface is applied. The enhancement factor in the flow law is $E = 1$ (i.e. Holocene ice conditions are applied throughout), and the geothermal heat is $G = 42 \times 10^{-3}\,\text{W}\,\text{m}^{-2}$. Columns 1, 2 and 3 of Table 3 list, respectively, the measuring point, the modulus of the horizontal components of the free surface velocity $v_H^{\text{meas}}(h_s)$ and its polar angle Θ^{meas} as inferred from the measurements. The corresponding quantities $v_H^{\text{mod}}(h_s)$ and Θ^{mod} are obtained from the computation and listed in Columns 4 and 5. In addition, Table 3 contains in columns 6 and 7 the relative deviations

$$\Delta A_r(h_s) = \frac{v_H^{\text{meas}}(h_s) - v_H^{\text{mod}}(h_s)}{v_H^{\text{mod}}(h_s)} \times 100 \text{ in } \% \tag{3.8}$$

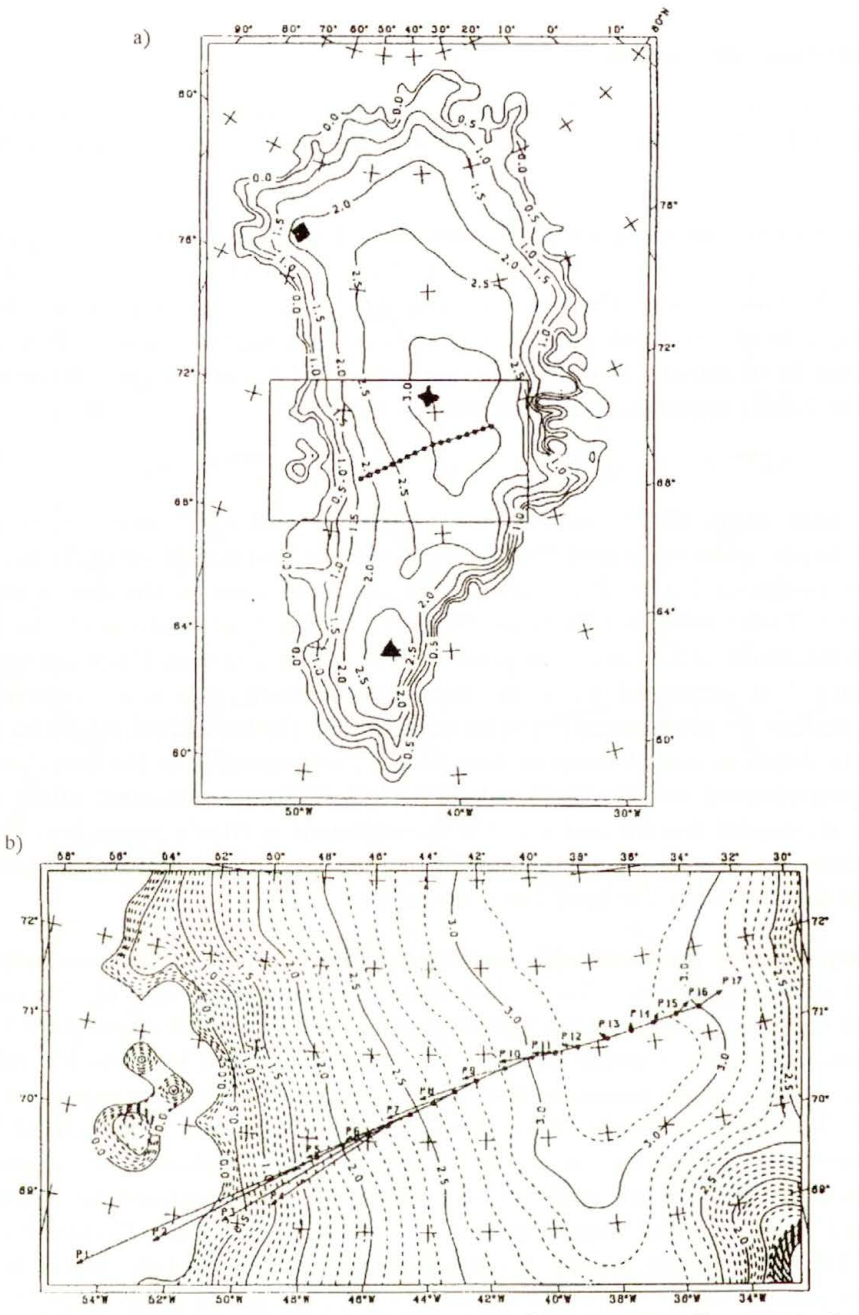

FIG. 8. Present surface topography of the Greenland Ice Sheet with the EGIG-traverse (a). The deep borehole positions are also indicated by a triangle (Dye 3), an asterisk (Summit) and a diamond (Camp Century). Measured velocity vectors at positions P 1 to P 17 along the EGIG-traverse (b) where the comparison with computational velocities is performed, see Tables 3 to 5.

of the measured and modelled EGIG-velocities, and the absolute deviations

$$\Delta\Theta = \Theta^{\text{meas}} - \Theta^{\text{mod}} \tag{3.9}$$

of the modelled from the measured polar angle.

Table 3. Comparison between measured and modelled EGIG-velocities as obtained for conditions of scenario I-S. Columns 1 to 7 list the position, measured surface speeds in $\mathrm{m\,a^{-1}}$, their polar angle in °, the modelled surface speeds and their polar angles and the relative error of the speeds in % and the absolute error in orientation as defined in (3.8) and (3.9).

Position	$v_H^{\text{meas}}(h_s)$ $[\mathrm{m\,a^{-1}}]$	Θ^{meas} [°]	$v_H^{\text{mod}}(h_s)$ $[\mathrm{m\,a^{-1}}]$	Θ^{mod} [°]	$\Delta A_r(h_s)$ [%]	$\Delta\Theta$ [°]
P 1	109.71	203.14	24.42	196.88	349	6.26
P 2	88.28	206.34	26.75	200.33	230	6.01
P 3	70.71	209.91	23.91	201.45	196	8.46
P 4	59.07	213.35	22.32	201.94	165	11.41
P 5	47.75	202.40	17.06	203.82	180	−1.42
P 6	39.96	202.17	13.60	199.39	194	2.78
P 7	31.40	200.60	11.59	202.18	171	−1.58
P 8	25.67	197.76	9.56	202.02	169	−4.26
P 9	18.76	194.73	6.93	200.83	171	−6.10
P 10	13.38	189.73	4.99	200.55	168	−10.82
P 11	9.88	182.79	3.50	200.03	182	−17.24
P 12	6.99	172.80	2.21	196.36	216	−23.56
P 13	4.21	144.46	0.71	190.05	493	−45.59
P 14	3.54	95.56	0.24	39.42	1375	56.14
P 15	4.83	62.10	1.29	24.64	274	37.46
P 16	7.58	44.47	2.87	22.89	164	21.58
P 17	12.46	33.73	4.50	17.42	177	16.31

Today's EGIG velocities of scenario I-S are all smaller than those of the measurements. This must certainly be in part due to the reduced deformability of the model ice with $E = 1$ that corresponds to Holocene conditions. In spite of this, a discussion of the results from scenario I-S reveals useful insight. Qualitatively, the EGIG velocities of scenario I-S show the right dependence on the position along the EGIG traverse. The relative minimum of the modelled velocities arises at position P 14, as in the observations. The computed velocities grow from position P 14 in both directions towards the ice margins in the West and the East. Overall the relative deviation $\Delta A_r(h_s)$ of the modelled from the observed EGIG-velocities is rather large. At position P 1, $\Delta A_r(h_s) = 349\%$; at P 8 it has a low of $\Delta A_r(h_s) = 169\%$ and at position P 14 it is as large as 1375%

(note that if $\Delta A_r(h_s)$ were normalized with $v_H^{\text{meas}}(h_s)$, this value would be 95%; so the discrepancy is highly exaggerated). The best agreement of the modulus of the velocity is reached at P 16 with $\Delta A_r(h_s) = 164\%$. The dependence of the relative velocity deviations $\Delta A_r(h_s)$ on the position of the EGIG-traverse is conspicuously correlated with the free surface height. The latter assumes at P 14 a relative maximum. In addition, in the vicinity of P 14, the gradient of the free surface is rather small. Therefore, there are two explanations for the large deviations of the measured from the computed velocities at P 13, P 14 and P 15. First, the shallow-ice approximation is an invalid approximation in the vicinity of a dome or ice divide and fails at the ice divide when a power flow law is used [44, 78, 71, 133, 159, 161, 173]. Second, small slopes of the free surface means that the numerical determination of these slopes from the height distribution requires the difference between two nearly equal numbers with consequent round-off error, and in turn the propagation of large errors in the evaluation of the velocities.

Overall, the differences $\Delta\Theta$ of the modelled and measured polar angles are not particularly large; this comes as no surprise, because in scenario I-S the smoothed surface topography is prescribed and held fixed during integration. This smoothed topography nearly agrees with the original topography provided by the data. Particularly small values of $|\Delta\Theta|$ arise at P 5, P 6, P 7 and, not surprisingly, the largest values of $|\Delta\Theta|$ occur close to the ice divide at P 14 ($\Delta\Theta = 56.14°$).

The EGIG-velocities, modelled with scenario I-S-E=3 – the computation equivalent to I-S but with an enhancement factor $E = 3$ – show the same qualitative behaviour as do those that were compared for scenario I-S. One would expect roughly a tripling of the modelled velocities; however, because of the thermomechanical coupling, the enlargement of the velocities is somewhat smaller because the basal ice is also colder. The modelled velocities along the EGIG traverse are now larger by a factor between 1.4 and 1.9., and the relative deviations $\Delta A_r(h_s)$ are smaller than for scenario I-S; in fact $\Delta A_r(h_s)$ generally lies below 100% except at P 1, P 12 – P 15, with a maximum of 941% at P 14. The differences in the polar angles, $|\Delta\Theta|$, remain essentially the same.

We conclude that whereas the enhanced apparent fluidity of the Pleistocene ice has moved the modelled velocities along the EGIG-traverse towards the observed values, the adjustment is not sufficient.

3.5.3. Comparison of measured with computed EGIG-velocities using computations with freely evolving surface geometry. Besides the above fixed domain simulations with the prescribed topography inferred from the data, computations were also performed with a freely evolving upper surface that is subject to prescribed snowfall and surface melting. The idea was to adjust certain free model parameters such that the modelled ice surface topographies would agree as far as possible with the observed surface topography. Such a procedure seems to be more appro-

priate anyhow, because the original topographic data needed smoothing in order that the computed velocities would not oscillate unrealistically. The reason for this was not numerical instability but lack of precision in the measured surface heights. In what follows, we shall describe results from two computations with free ice thickness, but with today's climatic conditions at the free surface held constant; thus, contrary to the preceding computations, the ice-age-temperature variations are not accounted for.

In the first computation we employ the following conditions: $E = 3$ and basal sliding throughout (i.e. at both temperate and cold basal points) with the frictional heat accounted for. The free surface geometry now differs from that of the measurements, but the horizontal surface velocities along the EGIG-traverse can still be evaluated. Table 4 compares the measured EGIG-velocities (speeds and polar angles) with those of the model at the positions P 1 to P 17. In addition to the previous Table 3 it contains in column 4 the modelled basal speeds, $v_H^{\mathrm{mod}}(h_b)$. This allows a direct comparison of the contributions of sliding and gliding (due to creep deformation over the depth). Overall, the EGIG-velocities $v_H^{\mathrm{mod}}(h_s)$ agree better with the measured EGIG-speeds than in the computations of scenario I-S-E=3. However, the polar angles now deviate more from the measured values because the free surface is free to evolve.

At position P 1, $v_H^{\mathrm{mod}}(h_s)$ is now larger than $v_H^{\mathrm{meas}}(h_s)$, a fact that is expressed by the negative sign in the relative deviation $\Delta A_r(h_s) = -8.5\%$, which for scenario I-S-E=3 was as large as 138%. This increase of the EGIG velocities at P 1 is, however, only in parts due to the sliding that is incorporated in this computation. The sliding velocity $v_H^{\mathrm{mod}}(h_b)$ at P 1 with its $22.97\,\mathrm{m\,a^{-1}}$ is only about 20% of the modelled EGIG-velocities there. The increase of the computed EGIG-velocity at P 1 can be traced back in this case to the change of surface topography. At positions P 2 to P 7 the relative deviations $|\Delta A_r(h_s)|$ are of the order of 5%, in excellent agreement with the observations. Somewhat striking is the large value $\Delta A_r(h_s) = 234.5\%$ at position P 12. It is at this location, where the computed surface height assumes its maximum along the EGIG-traverse. In the scenarios I-S and I-S-E=3 this role was played by position P 14, and $\Delta A_r(h_s)$ reached a maximum in this location for these scenarios. Here it is, however, no longer appropriate to attribute the large deviations to accidental errors in the ice topography, because the latter is now determined by computations. It is evident that the model is not ideally capable of reproducing regions with small free surface slopes close to domes, obviously a demonstration of the nonuniformity of the validity of the shallow ice approximation. At P 14 – P 17, $\Delta A_r(h_s)$ is approximately -50%; the computed EGIG-velocities are too large in these positions.

At P 13 and P 14 the difference of the polar angle as obtained from observations and computations is larger than 180°, but, of course, its complement to 360° is then smaller than 180° and precisely indicates the error in the orientation of the velocity. It also comes as no surprise that the maximum errors of the

orientation arise where the surface speeds are smallest. Overall, the agreement of the orientations of the computed velocieties along the EGIG-profile with those of the observations is fair.

Table 4. Same as in Table 3, but now as obtained under conditions for which the free surface has been freely evolving for 50 000 years under steady driving conditions. Columns are the same as in Table 3, except that column 4 has been added which lists the modelled basal ice speed in m a^{-1}. At P 13 and P 14 both, the polar angle and its complement to 360° are listed. For details see also caption to Table 3.

Position	$v_H^{\text{meas}}(h_s)$ [m a^{-1}]	Θ^{meas} [°]	$v_H^{\text{mod}}(h_b)$ [m a^{-1}]	$v_H^{\text{mod}}(h_s)$ [m a^{-1}]	Θ^{mod} [°]	$\Delta A_r(h_s)$ [%]	$\Delta\Theta$ [°]
P 1	109.71	203.14	22.97	119.91	193.32	−8.5	9.82
P 2	88.28	206.34	15.07	86.44	200.96	2.1	5.38
P 3	70.71	209.91	11.49	67.21	204.63	5.2	5.28
P 4	59.07	213.35	9.54	56.02	207.23	5.4	6.12
P 5	47.75	202.40	7.96	45.81	207.83	4.2	−5.43
P 6	39.96	202.17	6.83	37.18	205.42	7.5	−3.25
P 7	31.40	200.60	5.58	29.92	206.35	5.0	−5.75
P 8	25.67	197.76	4.23	23.20	208.70	10.7	−10.94
P 9	18.76	194.73	3.01	16.27	210.96	15.3	−16.23
P 10	13.38	189.73	2.06	10.45	215.04	28.0	−25.31
P 11	9.88	182.79	1.26	6.05	221.02	63.3	−38.23
P 12	6.99	172.80	0.45	2.09	239.75	234.5	−66.95
P 13	4.21	144.46	0.71	3.39	346.43	24.2	−201.97
P 13							158.03*
P 14	3.54	95.56	1.52	7.31	358.30	−51.6	−262.74
P 14							97.26*
P 15	4.83	62.10	2.76	11.99	4.07	−59.7	58.03
P 16	7.58	44.47	4.44	18.06	8.28	−58.0	36.19
P 17	12.46	33.73	6.06	24.91	9.96	−50.0	23.77

In the next computation the model conditions are the same as above except that sliding is now restricted to the temperate basal regions; the comparison between the modelled and measured EGIG-velocities is given in Table 5. The relative deviations $|\Delta A_r(h_s)|$ of the measured from the modelled EGIG-velocities are now in all positions less than 100% with a maximum of 71.9% at P 17 and a minimum of 0.2% at P 2. Over most of the EGIG-traverse the computed surface velocities are larger than those observed, the reason being that at the positions where this happens (P 5 – P 14) the free surface heights are too large. Because of the restricted sliding in this, as opposed to the previous, computation, less ice is

transported to the margin. Notice also the values of the basal velocities $v_H^{\mathrm{mod}}(h_b)$ in Column 4 of Table 5 which differ from zero only at the positions P 1 to P 3. At these positions, the ice thicknesses of the two computations are very similar, implying that the deviations $|\Delta A_r(h_s)|$ are relatively small. This is exactly the other way around at positions P 16 and P 17. Here, $\Delta A_r(h_s)$ have opposite signs, a fact that is likely due to the small surface slopes.

Table 5. Same as in Table 4 but now for sliding arising only at temperate basal spots. In P 14 – P 17 both the polar angle and its complement to 360° are listed. For details, see also caption to Table 3.

Position	$v_H^{\mathrm{meas}}(h_s)$ [m a^{-1}]	Θ^{meas} [°]	$v_H^{\mathrm{mod}}(h_b)$ [m a^{-1}]	$v_H^{\mathrm{mod}}(h_s)$ [m a^{-1}]	Θ^{mod} [°]	$\Delta A_r(h_s)$ [%]	$\Delta\Theta$ [°]
P 1	109.71	203.14	26.48	135.45	191.82	−19.0	11.32
P 2	88.28	206.34	15.39	88.41	203.03	−0.2	3.31
P 3	70.71	209.91	2.90	63.81	211.24	10.8	−1.33
P 4	59.07	213.35	0.00	52.89	216.96	11.7	−3.61
P 5	47.75	202.40	0.00	50.00	209.73	−4.5	−7.33
P 6	39.96	202.17	0.00	44.39	203.64	−10.0	−1.47
P 7	31.40	200.60	0.00	38.30	206.02	−18.0	−5.42
P 8	25.67	197.76	0.00	30.12	210.13	−14.8	−12.37
P 9	18.76	194.73	0.00	21.88	213.51	−14.3	−18.78
P 10	13.38	189.73	0.00	15.68	217.12	−14.7	−27.39
P 11	9.88	182.79	0.00	11.64	224.58	−15.1	−41.79
P 12	6.99	172.80	0.00	8.07	233.51	−13.4	−60.71
P 13	4.21	144.46	0.00	5.39	256.08	−21.9	−111.62
P 14	3.54	95.56	0.00	4.71	279.11	−24.8	−183.55
P 14							176.45*
P 15	4.83	62.10	0.00	4.47	300.86	8.1	−238.76
P 15							121.24*
P 16	7.58	44.47	0.00	5.01	331.49	51.3	−287.02
P 16							72.98*
P 17	12.46	33.73	0.00	7.25	350.48	71.9	−316.75
P 17							43.25*

The orientations of the computed EGIG-velocities at P 1 to P 8 are fairly well reproduced; however, the differences $|\Delta\Theta|$ are now somewhat larger. At P 14, there arises an almost perfect inversion ($\Delta\Theta = 176.45°$). This result is not surprising since position P 14 is where the surface height along the EGIG-traverse reaches its maximum. The agreement of the orientation of the surface velocities at P 15 to P 17 is also worse than in the previous computation, probably because the North dome has moved towards the NE.

To compare the last two computations objectively, we have calculated the means

$$\overline{|\Delta A_r(h_s)|} = \frac{\sum_{i=1}^{17} |\Delta A_r(h_s)|_i}{17}, \qquad \overline{|\Delta\Theta|} = \frac{\sum_{i=1}^{17} |\Delta\Theta|_i}{17} \tag{3.10}$$

over all 17 positions and found the results of Table 6. Accordingly, the moduli of the surface velocities are better reproduced in the second computation, and their orientations are in better agreement in the first. Because we regard the speeds as more significant, the conditions of the second computation are probably closer to reality.

Table 6. Mean values of the moduli of the relative deviations $\Delta A_r(h_s)$ and the absolute deviations $\Delta\Theta$ for the seventeen selected points along the EGIG-traverse (see Eqs. (3.8) and (3.9)) for the steady-state computations with sliding overall (a) and that with sliding restricted to the temperate basal spots (b).

	$\overline{\lvert\Delta A_r(h_s)\rvert}$ [%]	$\overline{\lvert\Delta\Theta\rvert}$ [°]
a	37.2	33.6
b	19.1	42.4

4. Concluding remarks and outlook

For the Greenland Ice Sheet and probably all large ice sheets, the equilibrium temperature distribution is an unrealistic concept to estimate the temperature distribution for present climatic conditions. This statement holds true for all times through the last glacial cycle except perhaps the climatic minimum at 16 ka BP. The present temperature distribution in the Greenland Ice Sheet is affected by the last glacial cycle (Wisconsinan Ice Age), and to some extent the Illinoian Ice Age, as well as by the thermal inertia of the uppermost part of the rock bed. The temporal variation of the surface (air) temperature contributes significantly to the temporal and spatial distribution of the heat flow across the ice-rock interface, as it may vary from 33 to 43 mW m^{-2}.

By using various scenarios it was shown (but is not demonstrated here) that some parts of the basal area – probably rather small – were and are temperate, but that the locations where ice cores were drilled were probably never temperate. This statement holds even when the free surface is varied along with the climate driving, because the base can only become colder in this instance. Furthermore, the exact temporal variation of the homologous temperature at the base of "Dye 3", "Summit" and "Camp Century" depends on the mechanical and thermal properties of the ice, the thermal response of the rigid rock bed and the climate driving force through the surface temperature through time.

These inferences are drawn by using a restricted number of scenarios. The climate driving temperature was drastically simplified from the Vostok data. The

rock bed was assumed to be rigid and so the deformation of the lithosphere and the astenosphere were ignored, and the free-surface geometry was held fixed. These effects were thought to be of negligible influence, and in any case a description is possible only on the basis of unreliable data.

This review explained the theory upon which the thermomechanical processes of land-based ice sheets are based, and how this theory is reduced by a scaling analysis to the so-called shallow ice approximation. This turned out to be the lowest order outer solution of a matched asymptotic perturbation scheme valid except in a near margin boundary layer and in the vicinity of ice divides([3]). Numerical solution of the governing equations are nevertheless generally constructed through the entire ice sheet on the premise that the two inner regions are passive. While this seems to be correct for the near-margin layer, comparison of computed velocities along the EGIG-profile (and obtained with various computational scenarios) with the measured ones indicates that this is not so for the ice divide region. This conclusion is justified because deviations of the computed and measured velocities are systematically larger close to the divide than elsewhere.

Of course, authors of papers on ice divide analysis are aware of this fact [6, 28–31, 44, 73, 78, 133, 166, 173], but no attempt has so far been made to construct near-ice-divide solutions of the full Stokes equations. BLATTER [6] has made a first attempt towards that end, but the works of DAHL-JENSEN [28–31], REEH [160–163] and RITZ [164–167] and associates, intended to achieve this and known under the terms "longitudinal stress" or "longitudinal stretching effects" [15, 67, 151] cannot, in general, be systematically extended to embrace eventually the full Stokes equations. The scaling analysis of this article shows how it should be done, either by a formal perturbation or – and numerically more efficiently – by iteration; we are presently doing this.

Ice shield analyses need other, equally important amendments. The constitutive model of this article is that of a fluid and therefore necessarily isotropic. However, ice at depth is strongly anisotropic [27], while at formation from sintered snow in the surface layer it is isotropic. This stress-induced transition has only recently been incorporated into the first models [49, 131, 174, 175]. Their incorporation into ice sheet analyses and, in particular, the construction of reduced model equations by implementing the shallowness assumption is still ahead of us.

Acknowledgments

The work of K. HUTTER was partly supported by the A. v. Humboldt Foundation and the Max Planck Society through the Max Planck prize, that of

([3]) In the terminology of perturbation theory the outer region is that part of the domain of integration in which the perturbation solution of the unstretched equation is a valid approximation. The inner region is where the perturbation expansion of the stretched equation is valid. These latter regions are here the marginal zone and the neighbourhood of the ice divide [44].

R. CALOV by the Deutsche Forschungsgemeinschaft. We thank Prof. L.W. MORLAND for his review of an earlier version of this paper and for his help with the English wording. The file with the digitized topography of the Greenland Ice Sheet was given to us by Dr. ANNE LETRÉGUILLY. We also acknowledge the help received from D. BARAL and Y. WANG in the production of the extensive reference list.

References

1. J.M. BARNOLA, D. RAYNAUD, Y.S. KOROTKEVICH and C. LORIUS, *Vostok ice core provides 160 000-year record of atmospheric* CO_2, Nature, **329**, 408–414, 1987.
2. J.M. BARNOLA, P. PIMIENTA, D. RAYNAUD and Y.S. KOROTKEVICH, CO_2*-climate relationship as deduced from the Vostok ice core: a re-examination based on new measurements and on a re-evaluation of the air-dating*, Tellus, **43B**, 83–90, 1991.
3. M. BENDER, L.D. LABEYRIE, D. RAYNAUD and C. LORIUS, *Isotropic composition of atmospheric* O_2 *in ice linked with deglaciation and global primary productivity*, Nature, **318**, 349–352, 1985.
4. G.E. BIRCHFIELD, J. WEERTMAN and A. LUNDE, *A Paleoclimate model of Northern Hemisphere ice sheets*, Quat. Res., **15**, 126–142, 1981.
5. H. BLATTER, *Effect of climate on the cryosphere*, Züricher Geographische Schriften, Geographisches Institut, ETH Zürich, **41**, 1991.
6. H. BLATTER, *Velocity and stress fields in grounded glaciers: a simple algorithm for including deviatoric stress gradients*, J. Glaciol., **41**, 333–344, 1995.
7. H. BLATTER and K. HUTTER, *Polythermal conditions in arctic glaciers*, J. Glaciol., **37**, 126, 261–269, 1991.
8. G.S. BOULTON, G.D. SMITH and L.W. MORLAND, *The reconstruction of former ice sheets and their mass balance characteristics using a nonlinearly viscous flow model*, J. Glaciol., **30**, 105, 140–152, 1984.
9. W.J. BÖHMER and K. HERTERICH, *A simplified 3-D ice sheet model including ice shelves*, Ann. Glaciol., **14**, 17–19, 1990.
10. R.J. BRAITHWAITE and O.B. OLESEN, *Calculation of glacier ablation from air temperature, West Greenland*, [in:] Glacier Fluctuations and Climatic Change, J. OERLEMANS [Ed.], Kluwer, 219–233, 1989.
11. A.J. BROCCOLLI and S. MANABE, *The influence of continental ice, atmospheric* CO_2*, and land albedo on the climate of the last glacial maximum*, Climate Dyn., **1**, 87–99, 1987.
12. W.S. BROECKER, *Carbon dioxide circulation through ocean and atmosphere*, *Nature*, **308**, 602, 1984.
13. W.S. BROECKER, D.M. PETEET and D. RIND, *Does the ocean-atmosphere system have more than one stable mode of operation*, Nature, **315**, 21–26, 1985.
14. W. BROECKER and G.H. DENTON, *The role of ocean-atmosphere reorganizations in glacial cycles*, Geochimica et Cosmochimica Acta, **53**, 2465–2501, 1989.
15. W.F. BUDD, *Ice flow over bedrock perturbations*, J. Glaciol., **9**, 55, 29–48, 1970.
16. W.F. BUDD and D. JENSSEN, *Numerical modelling of glacier systems*, IAHS Publ., **104**, 257–291, 1975.
17. W.F. BUDD and D. JENSSEN, *The dynamics of the Antarctic ice sheet*, Ann. Glaciol., **12**, 16–22, 1989.
18. W.F. BUDD, D. JENSSEN and I.N. SMITH, *A threedimensional time-dependent model of the West Antarctic ice sheet*, Ann. Glaciol., **5**, 29–36, 1984.

19. W.F. BUDD and U. RADOK, *Glaciers and other large ice massers*, Rep. Prog. Phys., **34**, 1–70, 1971.

20. W.F. BUDD and I.N. SMITH, *Large-scale numerical modelling of the Antarctic ice sheet*, Ann. Glaciol., **3**, 42–49, 1982.

21. W.F. BUDD, T.H. JACKA, D. JENSSEN, U. RADOK and N. YOUNG, *Derived physical characteristics of the Greenland ice sheet*, Publication no. 23, University of Melbourne, Meteorology Department, 1982.

22. W.F. BUDD and N.W. YOUNG, *Application of modelling techniques to measured profiles of temperature and isotopes*, [in:] The Climatic Record in Polar Ice Sheets, G. DE Q. ROBIN [Ed.], Cambridge University Press, Cambridge, UK. 150–157, 1983.

23. W.F. BUDD and I.N. SMITH, *The state of balance of the Antarctic ice sheet, an updated assessment 1984*, [in:] Glaciers, Ice Sheets and Sea Level: Effects of a CO_2-Induced Climatic Change, DOE/ER/60235-1, National Academy Press, Washington, 172–177, 1985.

24. W.F. BUDD and T.H. JACKA, *A review of ice rheology for ice sheet modelling*, Cold Reg. Sci. Technol., **16**, 107–144, 1989.

25. R. CALOV, *Das thermomechanische Verhalten des Grönländischen Eisschildes unter der Wirkung verschiedener Klimaszenarien – Antworten eines theoretisch-numerischen Modells*, Dissertation, Institut für Mechanik, TH Darmstadt, 1994.

26. R. CALOV and K. HUTTER, *The thermomechanical response of the Greenland Ice Sheet to various climate scenarios*, Climate Dyn., **12**, 243–260, 1996.

27. O. CASTELNAU, TH. THORSTEINSSON, S. KIPFSTUHL, P. DUVAL and G.R. CANOVA, *Modelling fabric developement along the GRIP ice core, central Greenland*, Ann. Glaciol., **23**, 194–201, 1996.

28. D. DAHL-JENSEN, *Steady thermomechanical flow along two-dimensional flow lines in large grounded ice sheets*, J. Geophys. Res., **94**, (B8), 10 355–10 362, 1989.

29. D. DAHL-JENSEN, *Two-dimensional thermo-mechanical modelling of flow and depth-age profiles near the ice divide in central Greenland*, Ann. Glaciol., **12**, 31–36, 1989.

30. D. DAHL-JENSEN and S.J. JOHNSEN, *Paleotemperature still exist in Greenland ice sheet*, Nature, **320**, 250–252, 1986.

31. D. DAHL-JENSEN and N.S. GUNDESTRUP, *Constitutive properties of ice at Dye 3, Greenland*, [in:] The Physical Basis of Ice Sheet Modelling, IAHS, **170**, 31–43, 1987.

32. W. DANSGAARD, H.B. CLAUSEN, N. GUNDESTRUP, C.U. HAMMER, S.F. JOHNSEN, P.M. KRISTINSDOTTIR and N. REEH, *A New Greenland Deep Ice Core*, Science, **218**, 1273–1277, 1982.

33. P. DUVAL, *The role of the water content on the creep rate of polycristalline ice. In isotopes and impurities in snow and ice*, IAHS, **118**, 29–33, 1977.

34. P. DUVAL, *Mécanisme de la déformation plastique de la glace polycristalline*, La Houille Blanche, **6/7**, 499–503, 1984.

35. M.B. ESCH and K. HERTERICH, *A two-dimensional coupled atmosphere-ice sheet-continent model designed for paleoclimatic simulations*, Ann. Glaciol., **14**, 55–57, 1990.

36. A. FABRÉ, A. LETRÉGUILLY, C. RITZ and A. MANGENEY, *Greenland under changing climates: sensitivity experiments with a new three-dimensional ice sheet model*, Ann. Glaciol., **21**, 1–7, 1995.

37. A.C. FOWLER, *The use of a rational model in the mathematical analysis of polythermal glacier*, J. Glaciol., **24**, 443–456, 1979.

38. A.C. FOWLER, *A theoretical treatment of the sliding of glaciers in the absence of cavitation*, Phil. Trans. R. Soc. London, **298**, 1445, 637–685, 1981.

39. A.C. FOWLER, *A sliding law of glaciers of constant viscosity in the presence of subglacial cavitation*, Proc. R. Soc. London, **407**, 147–170, 1981.
40. A.C. FOWLER, *Waves on glaciers*, J. Fluid Mech., **120**, 283–321, 1982.
41. A.C. FOWLER, *A sliding law for temperate glaciers in the presence of subglacial cavitation*, Proc. R. Soc. London, 1984.
42. A.C. FOWLER, *Sub-temperate basal sliding*, J. Glaciol., **32**, 110, 3–5, 1986.
43. A.C. FOWLER, *Sliding with cavity formation*, J. Glaciol., **33**, 115, 255–267, 1987.
44. A.C. FOWLER, *Modelling ice sheet dynamics*, Geophys. Astrophys. Fluid Dynamics, **63**, 29–65, 1992.
45. A.C. FOWLER and D.A. LARSON, *On the flow of polythermal glaciers. I. Model and preliminary analysis*, Proc. R. Soc. London, **363**, 217–242, 1978.
46. A.C. FOWLER and D.A. LARSON, *The uniqueness of steady state flows of glaciers and ice sheets*, Geophys. J. Roy. Astr. Soc., **63**, 333–345, 1980.
47. M. FUNK, K. ECHELMEYER and A. IKEN, *Mechanisms of fast flow in Jacobshavns Isbrae, West Greenland. Part II. Modeling of englacial temperatures*, J. Glaciol., **40**, 136, 569–585, 1994.
48. J.W. GLEN, *The creep of polycrystalline ice*, Proc. R. Soc. London, **228**, 1175, 519–538, 1955.
49. N. AZUMA and K. GOTO-AZUMA, *An anisotropic flow law for ice-sheet ice and its implications*, Ann. Glaciol., **23**, 202–208, 1996.
50. R. GREVE, *Thermomechanisches Verhalten Polythermer Eisschilde – Theorie, Analytik, Numerik*, Berichte aus der Geowissenschaft, Shaker Verlag, Aachen, Germany, Dissertation, Institut für Mechanik, Technische Hochschule Darmstadt, Germany 1995.
51. R. GREVE, *Application of a polythermal three-dimensional ice sheet model to the Greenland Ice Sheet: Response to steady-state and transient climate scenarios*, J. of Climate, **10**, 901–918, 1997.
52. R. GREVE, *A continuum-mechanical formulation for shallow polythermal ice sheets*, Phil. Trans. R. Soc. London, **A 355**, 921–974, 1997.
53. R. GREVE and K. HUTTER, *Polythermal three-dimensional modelling of the Greenland ice sheet with varied geothermal heat flux*, Ann. Glaciol., **21**, 8–12, 1995.
54. R. GREVE and D.R. MACAYEAL, *Dynamic/thermodynamic simulations of Laurentide ice sheet instability*, Ann. Glaciol., **23**, 328–335, 1996.
55. I. HANSEN and R. GREVE, *Polythermal modelling of steady states of the Antarctic Ice Sheet in comparision with the real world*, Ann. Glaciol., **23**, 382–387, 1996.
56. I. HANSEN, R. GREVE and K. HUTTER, *Application of a polythermal ice sheet model to the Antarctic Ice Sheet: Steady-state solution and response to Milankovic cycles*, Proc. Fifth International Symposium on Thermal Engineering and Science for Cold Regions, Y. LEE and W. HALLET [Eds.], 89–96, 1996.
57. B.L. HANSEN and C.C. LANGWAY, Jr., *Deep core drilling in ice and ice core analysis at Camp Century, Greenland*, Antarctic J., **1**, 207–208, 1966.
58. K. HERTERICH, *On the flow within the transition zone between ice sheet and ice shelf*, [in:] Dynamics of the West Antarctic Ice Sheet, C.J. VAN DER VEEN and J. OERLEMANS [Eds.], D. Reidel (Dordrecht), 185–202, 1987.
59. K. HERTERICH, *A three-dimensional model of the Antarctic ice sheet*, Ann. Glaciol., **11**, 32–35, 1988.
60. K. HERTERICH, *Modellierung eiszeitlicher Klimaschwankungen*, Habilitationsschrift, Fachbereich Geowissenschaften, Universität Hamburg, 1990.

61. R.C.A. HINDMARSH and K. HUTTER, *Numerical fixed domain mapping solution of free-surface flows coupled with an evolving interior field*, Int. J. Numer. Anal. Methods Geomech., **12**, 437–459, 1988.

62. R.C.A. HINDMARSH, L.W. MORLAND, G.S. BOULTON and K. HUTTER, *The unsteady plane flow of ice-sheets, a parabolic problem with two moving boundaries*, Geophys. Astrophys. Fluid Dynamics, **39**, 3, 183–225, 1987.

63. R.C.A. HINDMARSH, G.S. BOULTON and K. HUTTER, *Modes of operation of thermomechanically coupled ice sheets*, Ann. Glaciol., **12**, 57–69, 1989.

64. W. HOFMANN, *Die Internationale Glaziologische Grönland-Expedition* EGIG, Z. Gletscherkd. Glazialgeol., **5**, 217–224, 1974.

65. R. LEB. HOOKE, *Flow law for polycrystalline ice in glaciers: comparison of theoretical predictions, laboratory data, and field measurements*, Rev. Geophys. Space Phys., **19**, 4, 664–672, 1981.

66. K. HUTTER, *Time-dependent surface elevation of an ice slope*, J. Glaciol., **25**, 247–266, 1980.

67. K. HUTTER, *The effect of longitudinal strain on the shear stress of an ice sheet. In defence of using stretched coordinates*, J. Glaciol., **27**, 95, 39–56, 1981.

68. K. HUTTER, *A mathematical model of polythermal glaciers and ice sheets*, Geophys. Astrophys. Fluid Dynamics, **21**, 201–224, 1982.

69. K. HUTTER, *Dynamics of glaciers and large ice masses*, Ann. Rev. Fluid Mech., **14**, 87–130, 1982.

70. K. HUTTER, *Glacier flow*, Am. Sci., **70**, 1, 26–34, 1982.

71. K. HUTTER, *Theoretical glaciology; material science of ice and the mechanics of glaciers and ice sheets*, D. Reidel Publishing Company, Dordrecht, Holland 1983.

72. K. HUTTER, *Mathematical foundation of flow of glaciers and large ice masses*, [in:] Mathematical Models and Methods in Mechanics, Banach Center Publ., **15**, PWN-Polish Scientific Publishers, Warsaw. 277–322, 1985.

73. K. HUTTER, *Thermo-mechanically coupled ice sheet response. Cold, polythermal, temperate*, J. Glaciol., **39**, 131, 65–86, 1993.

74. K. HUTTER and H. ENGELHARDT, *How useful is continum thermodynamics to formulate concepts of ice sheet dynamics?* Eidg. Tech. Hochschule, Zürich. Versuchsanst. Wasserbau, Hydrol. Glaziol. Mitt., 94, 163–210, 1988.

75. K. HUTTER and H. ENGELHARDT, *The use of continuum thermodynamics in the formulation of ice sheet dynamics*, Ann. Glaciol., **11**, 46–51, 1988.

76. K. HUTTER, H. BLATTER and M. FUNK, *A model computation of moisture content in polythermal glaciers*, J. Geophys. Res., **93**, (B10), 12205–12214, 1988.

77. K. HUTTER and L. VULLIET, *Gravity driven slow creeping flow of a thermoviscous body at elevated temperatures*, J. Thermal Stresses, **8**, 99–138, 1985.

78. K. HUTTER, S. YAKOWITZ and F. SZIDAROVSZKY, *A numerical study of plane ice sheet flow*, J. Glaciol., **32**, 111, 139–164, 1986.

79. K. HUTTER, S. YAKOWITZ and F. SZIDAROVSKY, *Coupled thermomechanical response of an axi-symmetric cold ice sheet*, J. Water Resources Research, **23**, 1327–1339, 1987.

80. P. HUYBRECHTS, *A three-dimensional time-dependent numerical model for polar ice sheets: some basic testing with a stable and efficient finite difference scheme*, Geografisches Institute VUB Report 86-1, p. 39, 1986.

81. P. HUYBRECHTS, *Dynamics of the Antarctic ice cap. Part II. Sensitivity experiments with a numerical ice sheet model with full thermo-mechanical coupling*, Proc. of the Belgian National Colloquium on Antarctic Research, 226–239, 1987.

82. P. HUYBRECHTS, *A 3-D model for the Antarctic ice sheet: a sensitivity study on the glacial-interglacial contrast*, Climate Dyn., **5**, 79–92, 1990.

83. P. HUYBRECHTS, *The Antarctic ice sheet during the last glacial-interglacial cycle: A three-dimensional experiment*, Ann. Glaciol., **14**, 115–119, 1990.

84. P. HUYBRECHTS, *The Antarctic ice sheet and environmental change: a three-dimensional modelling study*, Berichte zur Polarforschung, **99**, Alfred-Wegener-Institut, Bremerhaven 1992.

85. P. HUYBRECHTS, *Glaciological modelling of the Late Cenozoic East Antarctic ice sheet: stability or dynamism?* Geografiska Annaler, **75 A**, 4, 221–238, 1993.

86. P. HUYBRECHTS, *The present evolution of the Greenland ice sheet: an assessment by modelling*, Global and Planetary Change, **9**, 39–51, 1994.

87. P. HUYBRECHTS, A. LETRÉGUILLY and N. REEH, *The Greenland ice sheet and greenhouse warming*, Palaeogeography, Palaeoclimatology, Palaeoecology, Global and Planetary Change Section, **89**, 399–412, 1991.

88. P. HUYBRECHTS and J. OERLEMANS, *Evolution of the East Antarctic ice sheet: A numerical study of thermo-mechanical response patterns with changing climate*, Ann. Glaciol., **11**, 52–59, 1988.

89. P. HUYBRECHTS and J. OERLEMANS, *Response of the Antarctic ice sheet to future greenhouse warming*, Climate Dyn., **5**, 93–102, 1990.

90. D. JENSSEN, *A three-dimensional polar ice-sheet model*, J. Glaciol., **18**, 80, 373–389, 1977.

91. D. JENSSEN and J.A. CAMPBELL, *Heat conduction studies*, [in:] The Climatic Record In Polar Ice sheets, G. DE Q. ROBIN [Ed.], . Cambridge University Press, Cambridge, UK., 150–157, 1983.

92. S.J. JOHNSEN, H.B. CLAUSEN, W. DANSGAARD, K. FUHRER, N. GUNDESTRUP, C.U. HAMMER, P. IVERSEN, J. JOUNZEL, B. STAUFFER and J.P. STEFFENSEN, *Irregular glacial interstadials recorded in a new Greenland ice core*, Nature, **359**, 311–313, 1992.

93. J. JOUZEL, L. MERLIVAT and C. LORIUS, *Deuterium excess in an East Antarctic ice core suggests higher relative humidity at the oceanic surface during the last glacial maximum*, Nature, **299**, 688–691, 1982.

94. J. JOUZEL and L. MERLIVAT, *Deuterium and Oxygen 18 in Precipitation: Modelling of the isotopic effects during snow formation*, J. Geophys. Res., **89**, D7, 11749–11757, 1984.

95. J. JOUZEL, L. MERLIVAT, J.R. PETIT and C. LORIUS, *Climatic information over the last century deduced from a detailed isotopic record in the South Pole snow*, J. Geophys. Res., **88**, C4, 2693–2703, 1983.

96. J. JOUZEL, C. LORIUS, J.R. PETIT, C. GENTHON, N.I. BARKOV, V.M. KOTLYAKOV and V.M. PETROV, *Vostok ice core: a continuous isotope temperature record over the last climatic cycle (160,000 years)*, Nature, **329**, 403–408, 1987.

97. J. JOUZEL, G.L. RUSSEL, R.J. SUOZZO, R.D. KOSTER, J.W.C. WHITE and W.S. BROECKER, *Simulation of the HDO and $H_2^{18}O$ atmospheric cycles using the NASA GISS general circulation model: The seasonal cycle for present-day conditions*, J. Geophys. Res., **92**, D 12, 14739–14760, 1987.

98. J. JOUZEL, G. RAISBECK, J.P. BENOIST, F. YIOU, C. LORIUS, D. RAYNAUD, J.R. PETIT, N.I. BARKOV, Y.S. KOROTKEVICH and V.M. KOTLYAKOV, *A comparison of deep Antarctic ice cores and their implications for climate between 65,000 and 15,000 years ago*, Quat. Res., **31**, 135–150, 1989.

99. M. KUHLE, K. HERTERICH and R. CALOV, *On the ice age glaciation of the Tibetan Highlands and its transformation into a 3-D model*, GeoJournal, **19**, 2, 201–206, 1989.

100. L.D. LABEYRIE, J.S. DUPLESSY and P.L. BLANC, *Variations in mode of formation and temperature of oceanic deep waters over the past 125,000 years*, Nature, **327**, 477–482, 1987.

101. K. LAMBECK and M. NAKADA, *Constraints on the age and duration of the last interglacial period and on sea-level variations*, Nature, **357**, 125–128, 1992.

102. R. LeB. HOOK, C. RAYMOND, R.L. HOTCHKISS and R.J. GUSTAFSON, *Calculation of velocity and temperature in a polar glacier using the finite-element method*, J. Glaciol., **24**, 90, 131–146, 1979.

103. A. LETRÉGUILLY, P. HUYBRECHTS and N. REEH, *Steady-state characteristics of the Greenland ice sheet under different climates*, J. Glaciol., **37**, 125, 149–157, 1991.

104. A. LETRÉGUILLY, N. REEH and P. HUYBRECHTS, *Topographical data for Greenland*, Report, Alfred-Wegener-Institut für Polar- und Meeresforschung, Bremerhaven 1990.

105. A. LETRÉGUILLY, N. REEH and P. HUYBRECHTS, *The Greenland ice sheet through the last glacial-interglacial cycle*, Palaeogeography, Palaeoclimatology, Palaeoecology, Global and Planetary Change Section, **90**, 4, 385–394, 1991.

106. R.C. LILE, *The effect of anisotropy on the creep of polycrystalline ice*, J. Glaciol., **21**, 85, 475–483, 1978.

107. L. LLIBOUTRY, *Traité de glaciologie. Tome I and II*, Masson, Paris 1964-1965.

108. L. LLIBOUTRY, *General theory of subglacial cavitation and sliding of temperate glaciers*, J. Glaciol., **7**, 49, 21–58, 1968.

109. L. LLIBOUTRY, *The dynamics of temperate glaciers from the detailed viewpoint*, J. Glaciol., **8**, 53, 185–205, 1969.

110. L. LLIBOUTRY, *Loi de glissement d'un glacier sans cavitation*, Ann. Géophys., **31**, 2, 207–226, 1975.

111. L. LLIBOUTRY, *Physical processes in temperate glaciers*, J. Glaciol., **16**, 74, 151–158, 1976.

112. L. LLIBOUTRY, *Local friction laws for glaciers. A critical review and new openings*, J. Glaciol., **23**, 89, 67–95, 1979.

113. L. LLIBOUTRY, *A critical review of analytical approximate solutions for steady state velocities and temperatures in cold ice-sheets*, Z. Gletscherkd. Glazialgeol., **15**, 2, 135–148, 1981.

114. L. LLIBOUTRY, *Tectonphysique et géodynamique. Une synthése. Géologie structurale. Géophysique interne*, Masson Ed., 1982.

115. L. LLIBOUTRY, *Very slow flow of solids: Basics of modelling in geodynamics and glaciology*, Martinus Nijhoff, Dordrecht, Netherlands 1987.

116. L. LLIBOUTRY, *Realistic, yet simple bottom boundary conditions for glaciers and ice sheets*, J. Geophys. Res., **92**, b 9, 9101–9109, 1987.

117. L. LLIBOUTRY and P. DUVAL, *Various isotropic and anisotropic ices found in glaciers and polar ice caps and their corresponding rheologies*, Annales Geophysicae, **3**, 2, 207–224, 1985.

118. C. LORIUS and L. MERLIVAT, *Distribution of mean surface stable isotope values in East Antarctica: observed changes with depth in the coastal area*, IAHS 118, Proc. of the Grenoble Symposium, 127–137, 1977.

119. C. LORIUS, L. MERLIVAT, J. JOUZEL and M. POURCHET, *A 30,000-yr isotope climatic record from Antarctic ice*, Nature, **280**, 644–648, 1979.

120. C. LORIUS, J. JOUZEL, C. RITZ, L. MERLIVAT, N.I. BARKOV, Y.S. KOROTKEVITCH and V. KOTLYAKOV, *A 150,000 year climatic record from Antarctic ice*, Nature, **316**, 591–596, 1985.

121. D.R. MACAYEAL, *Ice-shelf backpressure: form drag versus dynamic drag*, [in:] Dynamics of the West Antarctic Ice Sheet, C.J. VAN DER VEEN and J. OERLEMANS [Ed.], Reidel., 141–16, 1987.

122. D.R. MACAYEAL, *Large-scale ice flow over a viscous basal sediment: Theory and application to ice stream B, Antarctica*, J. Geophys. Res., **94**, B 4, 4071–4087, 1989.

123. D.R. MACAYEAL and R.H. THOMAS, *Numerical modelling of ice-shelf motion*, Ann. Glaciol., **3**, 189–194, 1982.

124. D.R. MACAYEAL and R.H. THOMAS, *The effects of basal melting on the present flow of the Ross Ice Shelf, Antarctica*, J. Glaciol., **32**, 110, 72–86, 1986.

125. M.W. MAHAFFY, *A three-dimensional numerical model of ice sheets: Test on the Barnes ice cap, Northwest Territories*, J. Geophys. Res., **81**, 6, 1059–1066, 1976.

126. A. MANGENEY, *Modélisation de l'écoulement de la glace dans les callottes palaires: prise en compte d'une loi comportement anisotrope*, Thèse de Doctorat de l'Université Pierre et Marie Curie – Paris VI, 1996.

127. A. MANGENEY and F. CALIFANO, *The shallow-ice approximation for anisotropic ice – formulation and limits*, J. Geophys. Res., 1997 [in press].

128. A. MANGENEY, F. CALIFANO and K. HUTTER, *A numerical study of anisotropic ice, low-Reynolds numbers, free surface flows for ice sheet modelling*, J. Geophys. Res., 1997 [in press].

129. B.J. MCINNES and W.F. BUDD, *A cross-sectional model for West Antarctica*, Ann. Glaciol., **5**, 95–99, 1984.

130. J. MEYSSONNIER and A. PHILIP, *A model for tangent viscous behaviour of anisotropic ice*, Ann. Glaciol., **23**, 253–261, 1996.

131. L.W. MORLAND, *Glacier sliding down an inclined wavy bed*, J. Glaciol., **17**, 77, 447–462, 1976.

132. L.W. MORLAND, *Glacier sliding down an inclined wavy bed with friction*, J. Glaciol., **17**, 77, 463–477, 1976.

133. L.W. MORLAND, *Thermo-mechanical balances of ice sheet flows*, Geophys. Astrophys. Fluid Dynamics, **29**, 237–266, 1984.

134. L.W. MORLAND and I.R. JOHNSON, *Steady motion of ice sheets*, J. Glaciol., **25**, 229–246, 1980.

135. L.W. MORLAND and I.R. JOHNSON, *Effect of bed inclination and topography on steady isothermal ice sheets*, J. Glaciol., **28**, 71–90, 1982.

136. L.W. MORLAND and G.D. SMITH, *Influence of non-uniform temperature distribution on the steady motion of ice sheets*, J. Fluid Mech., **140**, 113–930, 1984.

137. L.W. MORLAND, G.D. SMITH and G.S. BOULTON, *Basal sliding relations deduced from ice sheet data*, J. Glaciol., **30**, 105, 131–139, 1984.

138. J.F. NYE, *The flow of glaciers and ice-sheets as a problem in plasticity*, Proc. R. Soc. London, **207**, 554–572, 1951.

139. J.F. NYE, *The mechanics of glacier flow*, J. Glaciol., **2**, 82–93, 1952.

140. J.F. NYE, *A comparison between the theoretical and the measured long profile of the Unteraar Glacier*, J. Glaciol., **2**, 103–107, 1952.

141. J.F. NYE, *The flow law of ice from measurements in glacier tunnels, laboratory experiments and the Jungfraufirn borehole experiment*, Proc. R. Soc. London, **219**, 477–489, 1953.

142. J.F. NYE, *The distribution of stress and velocity in glaciers and ice-sheets*, Proc. R. Soc. London, **239**, 113–133, 1957.

143. J.F. NYE, *A theory of wave formation on glaciers*, IASH, **47**, 139–154, 1958.

144. J.F. NYE, *The deformation of a glacier below an ice fall*, J. Glaciol., **3**, 387–408, 1959.
145. J.F. NYE, *The response of glaciers and ice-sheets to seasonal and climatic changes*, Proc. R. Soc. London, **256**, 559–584, 1960.
146. J.F. NYE, *The influence of climatic variations on glaciers*, IASH, **54**, 297–404, 1961.
147. J.F. NYE, *On the theory of the advance and retreat of glaciers*, Geophys. J.R. Astron. Soc., **7**, 431–456, 1963.
148. J.F. NYE, *The response of a glacier to changes in the rate of nourishment and wastage*, Proc. R. Soc. London, **275**, 87–112, 1963.
149. J.F. NYE, *The flow of a glacier in a channel of rectangular, elliptic or parabolic cross-section*, J. Glaciol., **5**, 661–690, 1965.
150. J.F. NYE, *Plasticity solution for a glacier snout*, J. Glaciol., **6**, 695–715, 1967.
151. J.F. NYE, *The effect of longitudinal stress on the shear stress at the base of an ice sheet*, J. Glaciol., **8**, 53, 207–213, 1969.
152. J.F. NYE, *A calculation on the sliding of ice over a wavy surface using a Newtonian viscous approximation*, Proc. R. Soc. London, **311**, 445–467, 1969.
153. J.F. NYE, *Glacier sliding without cavitation in a linear viscous approximation*, Proc. R. Soc. London, **315**, 1522, 381–403, 1970.
154. A. OHMURA, *New temperature distribution maps for Greenland*, Z. Gletscherkd. Glazialgeol., **23**, 1–45, 1987.
155. A. OHMURA and N. REEH, *New precipitation and accumulation maps for Greenland*, J. Glaciol., **37**, 140–148, 1991.
156. W.S.B. PATERSON, *Why ice-age ice is sometimes "soft"*, Cold Reg. Sci. Technol., **20**, 75–98, 1991.
157. J.R. PETIT, L. MOUNIER, J. JOUZEL, V.I. KOTLYAKOV and C. LORIUS, *Paleoclimatological and chronological implications of the Vostok core dust record*, Nature, **343**, 56–58, 1990.
158. U. RADOK, T.J. BROWN, D. JENSSEN, I.N. SMITH and W.F. BUDD, *On the surging potential of polar ice streams*. Part IV. *Antarctic ice accumulation basins and their main discharge regions*, Boulder CO, University of Colorado, Cooperative Institute for Research in Environmental Sciences/Parkville, Victoria, University of Melbourne, Meteorology Department, 1986.
159. C.F. RAYMOND, *Deformation in the vicinity of ice divides*, J. Glaciol., **29**, 103, 357–373, 1983.
160. N. REEH, *A flow-line model for calculating the surface profile and the velocity, strain rate and stress fields in an ice sheet*, J. Glaciol., **34**, 116, 46–54, 1988.
161. N. REEH, *The age-depth profile in the upper part of a steady-state ice sheet*, J. Glaciol., **35**, 121, 406–417, 1989.
162. N. REEH, *Parameterization of melt rate and surface temperature on the Greenland ice sheet*, Polarforschung, **59**, 3, 113–128, 1991.
163. N. REEH, S.J. JOHNSEN and D. DAHL-JENSEN, *Dating the Dye 3 deep ice core by flow model calculations*, [in:] Greenland Ice Core: Geophysics, Geochemistry, and the Environment, Geophysical Monograph 33, C.C. LANGWAY, H. OESCHGER and W. DANSGAARD [Eds.], A. G. U., 57–65, 1985.
164. C. RITZ, *Exploitation du profil de températures mesuré dans la calotte glaciaire au Dôme C (Antarctide Orientale)*, Thése de Troisiéme Cycle de l'Université Scientifique et Médicale de Grenoble, 1980.
165. C. RITZ, *Time-dependent boundary conditions for calculation of temperature fields in ice sheets*, [in:] The Physical Basis of Ice Sheet Modelling, E.D. WADDINGTON and J.S. WALDER, IAHS Publication No. 170. 1987.

166. C. RITZ, *Interpretation of the temperature profile measured at Vostok, East Antarctica*, Ann. Glaciol., **12**, 138–144, 1989.
167. C. RITZ, L. LLIBOUTRY and C. RADO, *Analysis of a 870 m deep temperature profile at Dome C*, Ann. Glaciol., **3**, 284–289, 1982.
168. D.S. RUSSEL-HEAD and W.F. BUDD, *Ice-sheet flow properties derived from bore-hole shear measurements combined with ice-core studies*, J. Glaciol., **24**, 90, 117–130, 1979.
169. T.J.O. SANDERSON, *Equilibrium profile of ice shelves*, J. Glaciol., **22**, 88, 435–460, 1979.
170. N.J. SHACKLETON, *Oxygen isotopes, ice volume and sea level*, Quat. Sci. Rev., **6**, 183–190, 1987.
171. N.J. SHACKLETON, M.A. HALL and SHUXI CANG, *Carbon isotope data in core V19-30 confirm reduced carbon diobon dioxide concentration in the ice age atmosphere*, Nature, **306**, 319–322, 1983.
172. B. STAUFFER, *Dating of ice by radioactive isotope*, [in:] Dahlem Conference, The environmental Record in Glaciers and Ice Sheets, H. OESCHGER and C.C. LANGWAY Jr. [Eds.], 123–139, 1989.
173. F. SZIDAROVSZKY, K. HUTTER and S. YOKOWITZ, *Computational ice-divide analysis of a cold plane ice sheet under steady conditions*, Ann. Glaciol., **12**, 170–177, 1989.
174. B. SVENDSEN and K. HUTTER, *On the continuum modelling of induced anisotropy in polycrystals*, Quarterly of Applied Mathematics, 1995.
175. B. SVENDSEN and K. HUTTER, *A continuum approach for modelling-induced anisotropy in glaciers and ice sheets*, Ann. Glaciol., **23**, 262–269, 1995.
176. D.L. TURCOTTE and G. SCHUBERT, *Geodynamics*, John Wiley, New York, p. 440, 1982.
177. E.D. WADDINGTON, *Geothermal heat flux beneath ice sheets*, [in:] The Physical Basis of Ice Sheet Modeling, IAHS, **170**, 217–226, 1987.
178. J. WEERTMANN, *On the sliding of glaciers*, J. Glaciol., **3**, 21, 33–38, 1957.
179. J. WEERTMAN, *Deformation of floating ice shelves*, J. Glaciol., **3**, 38–42, 1957.
180. J. WEERTMAN, *Stability of ice-age ice sheets*, J. Geophys. Res., **66**, 11, 3783–3792, 1961.
181. J. WEERTMANN, *Mechanism for the formation of inner moraines found near the edge of cold ice caps and ice sheets*, J. Glaciol., **3**, 30, 965–978, 1961.
182. J. WEERTMANN, *The theory of glacier sliding*, J. Glaciol., **5**, 39, 287–303, 1964.
183. J. WEERTMANN, *An examination of the Lliboutry theory of glacier sliding*, J. Glaciol., **6**, 46, 489–494, 1967.
184. J. WEERTMAN, *Comparison between measured and theoritical temperature profiles of the Camp century, Greenland borehole*, J. Geophys. Res., **73**, 2691–2700, 1968.
185. J. WEERTMANN, *In defense of a simple model of glacier sliding*, J. Geophys. Res., **76**, 26, 6485–6487, 1971.
186. J. WEERTMANN, *General theory of water flow at the base of a glacier or ice sheet*, Rev. Geophys. Space Phys., **10**, 1, 187–333, 1972.
187. J. WEERTMANN, *The unsolved general glacier sliding problem*, J. Glaciol., **23**, 89, 97–115, 1979.
188. M. WEIS, K. HUTTER and R. CALOV, 250 000 *years in history of Greenland's ice sheet*, Ann. Glaciol., **23**, 359–363, 1996.

DEPARTMENT OF MECHANICS
TU DARMSTADT, DARMSTADT, GERMANY.
e-mail:hutter@mechanik.tu-darmstadt.de

Received February 21, 1997; new version May 28, 1997.

Arch. Mech., 49, 5, pp. 963–975, Warszawa 1997

Steady non-uniform extensional motions as applied to kinematic description of polymer fibre formation

S. ZAHORSKI (WARSZAWA)

IT IS SHOWN that the concept of steady non-uniform extensional motions (NUEM) can be used for kinematic description of polymer fibre formation, taking into account the variable geometry and shearing effects. To this end, pretty general, materially non-uniform constitutive equations, depending on temperature distributions, structure formations, etc., are applied and the linearized perturbation procedure is developed. Especially simple expressions describing the additional velocity fields are obtained for the first order approximation.

1. Introduction

IN OUR PREVIOUS PAPERS [1, 2], we discussed the concept of steady non-uniform extensional motions (called briefly NUEM) of materially non-uniform (non-homogeneous) fluids and solids. We also mentioned possible applicability of the above concept to various fibre-forming processes and certain flows realized in extensometers. An example of application to the case of cold drawing of polymer fibres was presented in [3].

In this paper, we use the concept of steady NUEM to describe many realistic fibre-forming processes, assuming that the fundamental motions are quasi-elongational and the shearing effects, resulting from the axial variability of fibre geometry, are taken into account. A motivation for the present description arises from the following requirements.

1. We want to apply relatively general constitutive equations describing various fundamental quasi-elongational motions. An assumption of particular rheological models, frequently made for description of fibre-forming processes, is not necessary. Such an approach to the problem enables effective application either of experimental data or numerical results calculated for simpler models (Newtonian, Maxwellian, etc.).

2. Material properties of fibres in the processes considered essentially depend on temperature distributions, crystallization effects, structure orientation etc. (cf. [4]). The concept of steady NUEM of materially non-uniform materials replaces, in some sense, arbitrary distributions of mechanical properties varying from position to position in media which are homogeneous in reality. Moreover, there exists some possibility of smooth transitions from viscous to elastic materials or from fluid-like to solid-like behaviour.

3. We try to apply a consequent linearization process throught the corresponding perturbation procedure. To this end, an asssumption of thin-thread (layer) approximation, usually satisfied in fibre processing, is very useful.

The concept considered generalizes, to some extent, that of steady flows with dominating extension (briefly called FDE) developed previously in [5] and applied to melt-spinning processes in [6]. We must emphasize, however, that the concept of steady FDE does not satisfy the requirement 1 and 3. The requirement 2 remains valid only for the properly defined viscosity function.

In Sec. 2 the general quasi-elongational motions and the corresponding constitutive equations are considered. Section 3 is entirely devoted to the additional superposed motions describing the variability of fibre geometry and the related shearing effects. Moreover, we introduce the auxiliary concept of thin-tread (layer) approximation. The continuity conditions in local and global forms are discussed in Sec. 4. Sections 5 and 6 contain the equilibrium equations and the boundary conditions presented for the first and second order approximations. In Sec. 7 the corresponding solutions of the previously derived governing equations are obtained for viscoelastic isotropic materials. Certain particular cases are discussed in greater detail. The main results are quoted in Sec. 8 in a form of final remarks.

2. Quasi-elongational motions treated as steady non-uniform extensional motions (NUEM)

Consider the isochoric, quasi-elongational motion for which the deformation gradient at the current time t, relative to a configuration at time 0, is of the diagonal form in cylindrical coordinates:

$$[\mathbf{F}(\mathbf{X},t)] = \begin{bmatrix} \lambda^{1/2} & 0 & 0 \\ 0 & \lambda^{-1/2} & 0 \\ 0 & 0 & \lambda \end{bmatrix}, \qquad \det \mathbf{F} = 1, \tag{2.1}$$

where the non-uniform stretch ratio $\lambda(\mathbf{X},t)$ depends on time t as well as on the position $\mathbf{X}$ of a particle in the reference configuration $\boldsymbol{\kappa}$ at time 0. We use the following definitions:

$$\lambda = V/V_0\,, \qquad \epsilon = \ln\lambda, \tag{2.2}$$

where ϵ is the Hencky measure of strain; V and V_0 denote the variable axial velocity and the velocity at the exit (feeding velocity), respectively. The above quasi-elongational motion is consistent with the definition of NUEM introduced in [2].

On the basis of Eq. (2.1), the velocity gradient (strain rate) can be written as

$$[\mathbf{L}(\mathbf{X},t)] = [\dot{\mathbf{F}}\,\mathbf{F}^{-1}] = \begin{bmatrix} -\frac{1}{2}V' & 0 & 0 \\ 0 & -\frac{1}{2}V' & 0 \\ 0 & 0 & V' \end{bmatrix}, \tag{2.3}$$

where V' denotes the axial component of the velocity gradient and the primes denote derivatives with respect to the axial coordinate z.

Equations (2.1) and (2.3) lead to the following forms of the left Cauchy – Green deformation tensor $\mathbf{B}$ and the first Rivlin – Ericksen kinematic tensor $\mathbf{A}_1$ (cf. [7]):

$$[\mathbf{B}(\mathbf{X},t)] = [\mathbf{F}\,\mathbf{F}^T] = \begin{bmatrix} \lambda^{-1} & 0 & 0 \\ 0 & \lambda^{-1} & 0 \\ 0 & 0 & \lambda^2 \end{bmatrix} = \begin{bmatrix} \frac{V_0}{V} & 0 & 0 \\ 0 & \frac{V_0}{V} & 0 \\ 0 & 0 & \frac{V^2}{V_0^2} \end{bmatrix}, \tag{2.4}$$

$$[\mathbf{A}_1(\mathbf{X},t)] = \begin{bmatrix} -\frac{\dot{\lambda}}{\lambda} & 0 & 0 \\ 0 & -\frac{\dot{\lambda}}{\lambda} & 0 \\ 0 & 0 & 2\frac{\dot{\lambda}}{\lambda} \end{bmatrix} = \begin{bmatrix} -V' & 0 & 0 \\ 0 & -V' & 0 \\ 0 & 0 & 2V' \end{bmatrix}, \tag{2.5}$$

respectively. In the above expressions we have used the relations:

$$\dot{\lambda} = V'\lambda, \qquad \dot{\epsilon} = V', \tag{2.6}$$

where the dots denote differentiation with respect to time.

For steady NUEM the gradient $\mathbf{L}$ as well as the kinematic tensor $\mathbf{A}_1$ do not depend on time. Thus, according to our previous considerations [2], the constitutive equations of materially non-uniform, simple, locally isotropic materials can be expressed in the form:

$$\mathbf{T}(\mathbf{X},t) = \mathbf{h}(\mathbf{A}_1(\mathbf{X}), \mathbf{B}(\mathbf{X},\mathbf{t}), \varrho(\mathbf{X}); \mathbf{X}), \tag{2.7}$$

where $\mathbf{T}$ is the non-uniform stress tensor, and $\mathbf{h}$ denotes the non-uniform isotropic function, depending on the reference configuration $\boldsymbol{\kappa}$. In the case of incompressible materials $\mathbf{T}$ should be replaced by the extra-stress tensor $\mathbf{T}_E$ and the dependence on the scalar density ϱ should be disregarded. The question whether Eq. (2.7) describes a fluid or solid can be answered having known the corresponding isotropy (internal symmetry) group (cf. [7]).

For steady quasi-elongational motions, describing the majority of fibre forming processes, in which material properties depend solely on the coordinate z, there exists a unique correspondence between the material Z (in the reference configuration $\boldsymbol{\kappa}$) and the spatial coordinate z. In particular, we may assume that

$$z = \frac{V}{V_0} Z, \qquad z = Vt, \qquad Z = V_0 t. \tag{2.8}$$

Thus, Eq. (2.7) can be written in the particular form:

$$\mathbf{T}(z) = \mathbf{k}(V'(z), V(z), \varrho(z); z), \tag{2.9}$$

where $\mathbf{k}$ is the tensor function of the indicated scalar arguments. If necessary, the pairs of arguments λ', λ or $\dot{\epsilon}, \epsilon$ can be used instead of V', V.

For our present purposes the way of reasoning leading to the constitutive equation (2.7) has not been presented with all details (to this end cf. [1, 2]); the simplified Eq. (2.9) can also be taken as a constitutive postulate. Therefore, we assume that the stress (or extra-stress) components in the motions considered depend on the velocity gradient V', the velocity V, the density ϱ and the coordinate z characterizing an explicit dependence of the material properties on the position along the axis.

Since for axisymmetric, quasi-elongational motions only normal components of stresses are meaningful, we can also write

$$\begin{aligned} T^{11} &= T^{22} = \sigma_1(V', V, \varrho; z), \\ T^{33} &= \sigma_3(V', V, \varrho; z), \\ T^{13} &= 0, \\ T^{33} - T^{11} &= \sigma_3 - \sigma_1 = \sigma(V', V, \varrho; z). \end{aligned} \tag{2.10}$$

3. Additional motion and shearing effects

In the motions considered, the inclination of fibre surface is usually a small quantity, i.e. $R' = 0(\varepsilon)$, $\varepsilon = R_0/L \ll 1$, where R, R_0 and L denote the outer radius of the filament, the outer radius at the exit (or the orifice radius) and the total length, respectively.

In what follows, we assume that some small additional velocity field, viz.

$$\mathbf{w}(r, z) = \mathbf{0}(\varepsilon) \tag{3.1}$$

is superposed on the fundamental, quasi-elongational motion described by the axial velocity $V(z)$. Under the above assumption all the quantities relevant for the motions considered undergo some small linear increments denoted by Δ. We have, in particular,

$$\mathbf{L}^* = \mathbf{L} + \Delta\mathbf{L}, \qquad \mathbf{F}^* = \mathbf{F} + \Delta\mathbf{F}, \quad \text{etc.} \tag{3.2}$$

For the deformation gradients, velocity gradients, deformation tensors and kinematic tensors, we obtain the following matrices:

$$[\Delta\mathbf{F}] = \begin{bmatrix} -\frac{1}{2}\frac{V_0}{V^2}w & 0 & \frac{u}{V_0} \\ 0 & -\frac{1}{2}\frac{V_0}{V^2}w & 0 \\ 0 & 0 & \frac{V}{V_0^2}w \end{bmatrix},$$

(3.3)

$$[\Delta\mathbf{B}] = \begin{bmatrix} -\frac{V_0}{V^2}w & 0 & \left(\frac{V_0}{V}\right)^{1/2}\frac{u}{V_0} \\ 0 & -\frac{V_0}{V^2}w & 0 \\ \left(\frac{V_0}{V}\right)^{1/2}\frac{u}{V_0} & 0 & 2\frac{V}{V_0^2}w \end{bmatrix},$$

and

$$[\Delta\mathbf{L}] = \begin{bmatrix} \frac{\partial u}{\partial r} & 0 & \frac{\partial u}{\partial z} \\ 0 & \frac{u}{r} & 0 \\ \frac{\partial w}{\partial r} & 0 & \frac{\partial w}{\partial z} \end{bmatrix}, \qquad [\Delta\mathbf{A}_1] = \begin{bmatrix} 2\frac{\partial u}{\partial r} & 0 & \frac{\partial u}{\partial z}+\frac{\partial w}{\partial r} \\ 0 & 2\frac{u}{r} & 0 \\ \frac{\partial u}{\partial z}+\frac{\partial w}{\partial r} & 0 & 2\frac{\partial w}{\partial z} \end{bmatrix},$$

(3.4)

where u and w denote the radial and axial components of the additional velocity $\mathbf{w}$, respectively. In the above formulae we have used the simple relations:

$$\Delta\lambda = \frac{w}{V_0}, \qquad \Delta\lambda' = \frac{1}{V_0}\frac{\partial w}{\partial z}, \qquad \Delta\lambda^{-1} = -\frac{V_0}{V^2}w. \tag{3.5}$$

The constitutive equations (2.10), after taking into account the increments resulting from the additional velocity field (3.1), can be presented in the following general form, linear with respect to u and w:

$$\begin{aligned} T^{*11} &= \sigma_1 + \frac{\partial\sigma_1}{\partial V}w + \frac{\partial\sigma_1}{\partial V'}\frac{\partial w}{\partial z} + \frac{\partial\sigma_1}{\partial\varrho}\Delta\varrho + \alpha\frac{\partial u}{\partial r}, \\ T^{*22} &= \sigma_1 + \frac{\partial\sigma_1}{\partial V}w + \frac{\partial\sigma_1}{\partial V'}\frac{\partial w}{\partial z} + \frac{\partial\sigma_1}{\partial\varrho}\Delta\varrho + \beta\frac{u}{r}, \\ T^{*33} &= \sigma_3 + \frac{\partial\sigma_3}{\partial V}w + \frac{\partial\sigma_3}{\partial V'}\frac{\partial w}{\partial z} + \frac{\partial\sigma_3}{\partial\varrho}\Delta\varrho, \\ T^{*13} &= \eta\left(\frac{\partial u}{\partial z}+\frac{\partial w}{\partial r}\right) + \gamma u, \\ T^{*33} - T^{*11} &= \sigma + \frac{\partial\sigma}{\partial V}w + \frac{\partial\sigma}{\partial V'}\frac{\partial w}{\partial z} + \frac{\partial\sigma}{\partial\varrho}\Delta\varrho - \alpha\frac{\partial u}{\partial r}, \end{aligned} \tag{3.6}$$

where α, β, γ and η are new, additional material functions, depending on the same arguments as σ, e.g.

$$\eta = \eta(V', V, \varrho; z). \tag{3.7}$$

The functions η, α and β have dimension of viscosity ($\mathrm{Ns/m^2}$), while γ, characterizing the shearing deformations of a material, has dimension of shear modulus divided by velocity ($\mathrm{Ns/m^3}$).

It is worth noting that the representations of constitutive equations in the form (3.6) can also be obtained in a different way. An application of linear perturbation procedure to the Rivlin–Ericksen constitutive equations (cf. [7]), involving 8 material functions (α_i, $i = 1, \ldots, 8$), leads to exactly the same result.

The next step in our perturbation procedure is connected with the so-called thin-thread (layer) approximation (cf. [6]). To this end, we assume again that $\varepsilon = R_0/L$ is a small quantity. Introducing the following dimensionless variables marked with overbars:

$$r = \overline{r} R_0\,, \qquad z = \overline{z} L, \qquad w = U\overline{w}, \qquad u = \varepsilon U \overline{u}, \tag{3.8}$$

where the characteristic velocity $U = V'(0)R_0$, or $U = V'_{\max} R_0$, we arrive at the following increments:

$$[\Delta B] = \begin{bmatrix} -\dfrac{\overline{V}_0}{\overline{V}^2}\overline{w} & 0 & \varepsilon \dfrac{\overline{u}}{\overline{V}_0}\left(\dfrac{\overline{V}_0}{\overline{V}}\right)^{1/2} \\ 0 & -\dfrac{\overline{V}_0}{\overline{V}^2}\overline{w} & 0 \\ \varepsilon \dfrac{\overline{u}_0}{\overline{V}_0}\left(\dfrac{\overline{V}_0}{\overline{V}}\right)^{1/2} & 0 & \dfrac{\overline{V}}{\overline{V}_0^2}\overline{w} \end{bmatrix}, \tag{3.9}$$

$$[\Delta A_1] = \begin{bmatrix} \varepsilon 2 \dfrac{\partial \overline{u}}{\partial \overline{r}} & 0 & \dfrac{\partial \overline{w}}{\partial \overline{r}} + \varepsilon^2 \dfrac{\partial \overline{u}}{\partial \overline{z}} \\ 0 & \varepsilon 2 \dfrac{\overline{u}}{\overline{r}} & 0 \\ \dfrac{\partial \overline{w}}{\partial \overline{r}} + \varepsilon^2 \dfrac{\partial \overline{u}}{\partial \overline{z}} & 0 & \varepsilon 2 \dfrac{\partial \overline{w}}{\partial \overline{z}} \end{bmatrix} \frac{U}{R_0}. \tag{3.10}$$

Since by assumption, the axial component w of the additional velocity field is of order ε, the radial component u under a thin-thread approximation is of order ε^2. This fact is taken into account when dealing with various terms in the corresponding governing equations (Sec. 5).

4. Continuity conditions

So far, we have not discussed any continuity conditions, assuming tacitly that they are satisfied in a local as well as in a global sense.

In the local form the continuity condition, valid for the fundamental, quasi-elongational motion, viz.

$$\dot{\varrho} + \varrho \operatorname{div} \mathbf{V} = 0, \tag{4.1}$$

implies that $\varrho = \text{const}$, if $\operatorname{div} \mathbf{V} = 0$ and the motion is steady ($\partial \varrho / \partial t = 0$). The same equation for quantities involving the corresponding increments ($\mathbf{V}^* = \mathbf{V} + \mathbf{w}$, $\varrho^* = \varrho + \Delta\varrho$) amounts to

$$V \frac{\partial \Delta\varrho}{\partial z} + \varrho \operatorname{div} \mathbf{w} = 0, \tag{4.2}$$

and after integration to

$$\Delta\varrho = -\int \frac{\varrho}{V} \left(\frac{1}{r} \frac{\partial}{\partial r}(ru) + \frac{\partial w}{\partial z} \right) dz + C(r), \tag{4.3}$$

where $C(r)$ is an arbitrary function of r only.

Since for our thin-thread approximation the radial components u are of order of magnitude less than the axial components w, we may use the approximate formula:

$$\Delta\varrho \cong -\int \frac{\varrho}{V} \frac{\partial w}{\partial z} dz + C(r). \tag{4.4}$$

On the other hand, in the global form the mass output W in a fundamental motion must be constant along the filament, viz.

$$W = \varrho \pi R^2 V = \text{const}. \tag{4.5}$$

Taking into account the corresponding mass output with small increments w and $\Delta\varrho$, we arrive at

$$2\pi \int_0^R (V + w)(\varrho + \Delta\varrho) r \, dr = \text{const}, \tag{4.6}$$

what leads to

$$V \int_0^R \Delta\varrho r \, dr + \varrho \int_0^R w r \, dr = 0. \tag{4.7}$$

If the additional velocity field is such that the second integral is identically equal to zero (cf. Sec. 6), the radial distribution of the density increment $\Delta\varrho$ is determined only by the vanishing first integral (4.7).

Another implication of the condition (4.5) are the following formulae:

$$\frac{R'}{R} = -\frac{1}{2} \frac{V'}{V} \qquad \text{or} \qquad \frac{d}{dz} \ln R = -\frac{1}{2} \frac{d}{dz} \ln V, \tag{4.8}$$

expressing useful relations between the fibre radius and the fundamental velocity V.

5. Equations of equilibrium

For axisymmetric deformations the inertialess equations of equilibrium, expressed in cylindrical coordinates, viz.

$$\begin{aligned} &\frac{\partial T^{*11}}{\partial r} + \frac{1}{r}(T^{*11} - T^{*22}) + \frac{\partial T^{*13}}{\partial z} = 0, \\ &\frac{\partial T^{*13}}{\partial r} + \frac{1}{r}T^{*13} + \frac{\partial T^{*33}}{\partial z} = 0, \end{aligned} \tag{5.1}$$

after taking into account Eqs. (3.6), lead to

$$\begin{aligned} &\frac{\partial \sigma_1}{\partial r} + \frac{\partial}{\partial r}\left(\frac{\partial \sigma_1}{\partial V}w + \frac{\partial \sigma_1}{\partial V'}\frac{\partial w}{\partial z} + \partial\sigma_1\partial\varrho\Delta\varrho\right) + \frac{\partial}{\partial z}\left(\eta\frac{\partial w}{\partial r}\right) + \frac{\partial}{\partial r}\left(\alpha\frac{\partial u}{\partial r}\right) \\ &\qquad + \frac{1}{r}\left(\alpha\frac{\partial u}{\partial r} - \beta\frac{u}{r}\right) + \frac{\partial}{\partial z}\left(\eta\frac{\partial u}{\partial z}\right) + \frac{\partial}{\partial z}(\gamma u) = 0, \\ &\frac{\partial \sigma_3}{\partial z} + \frac{\partial}{\partial z}\left(\frac{\partial \sigma_3}{\partial V}w + \frac{\partial \sigma_3}{\partial V'}\frac{\partial w}{\partial z} + \frac{\partial \sigma_3}{\partial \varrho}\Delta\varrho\right) \\ &\qquad + \frac{1}{r}\frac{\partial}{\partial r}\left(r\eta\frac{\partial w}{\partial r}\right) + \frac{\partial}{\partial r}\left(\eta\frac{\partial u}{\partial z}\right) + \frac{\eta}{\gamma}\frac{\partial u}{\partial z} + \frac{\gamma}{r}\frac{\partial}{\partial r}(ru) = 0. \end{aligned} \tag{5.2}$$

Differentiating the first Eq. (5.2) with respect to z and the second one with respect to r, and subtracting (this procedure also eliminates the hydrostatic pressure, if necessary), we arrive at

$$\begin{aligned} &\eta\frac{\partial}{\partial r}\left\{\frac{1}{r}\frac{\partial}{\partial r}\left(r\frac{\partial w}{\partial r}\right) + \frac{d}{dz}\left(\sigma + \frac{\partial \sigma}{\partial V}w + \frac{\partial \sigma}{\partial V'}\frac{\partial w}{\partial z} + \frac{\partial \sigma}{\partial \varrho}\Delta\varrho\right)\right\} \\ &\quad - \frac{\partial^2}{\partial z^2}\left(\eta\frac{\partial w}{\partial r}\right) + \frac{\partial}{\partial r}\left[\frac{\gamma}{r}\frac{\partial}{\partial r}(ru)\right] - \frac{\partial^2}{\partial z^2}(\gamma u) - \frac{\partial^2}{\partial r\partial z}\left(\alpha\frac{\partial u}{\partial r}\right) \\ &\quad - \frac{\partial}{\partial z}\left[\frac{1}{r}\left(\alpha\frac{\partial u}{\partial r} - \beta\frac{u}{r}\right)\right] + \frac{\partial^2}{\partial r\partial z}\left(\eta\frac{\partial u}{\partial z}\right) + \frac{\partial}{\partial r}\left(\frac{\eta}{r}\frac{\partial u}{\partial z}\right) \\ &\quad + \eta\frac{\partial}{\partial r}\left(\frac{1}{r}\frac{\partial u}{\partial z}\right) - \frac{\partial^2}{\partial z^2}\left(\eta\frac{\partial u}{\partial z}\right) = 0. \end{aligned} \tag{5.3}$$

The corresponding analysis of orders of magnitude determined by the powers of ε leads, after integration with respect to r, to the following governing equation:

$$\eta\frac{\partial}{\partial r}\left(r\frac{\partial w}{\partial r}\right) + r\frac{d}{dz}\left(\sigma + \frac{\partial \sigma}{\partial V}w + \frac{\partial w}{\partial V'}\frac{\partial w}{\partial z} + \frac{\partial \sigma}{\partial \varrho}\Delta\varrho\right) = Cr - \gamma\frac{\partial}{\partial r}(ru), \tag{5.4}$$

where only terms up to ϱ^2 have been retained and C is an integration constant. In the above equations as well as in our further considerations the symbol d/dz denotes the total derivative with respect to z.

Let us assume, in agreement with Eq. (3.1), that the additional velocity field can be written as

$$w = \varepsilon w_1 + \varepsilon^2 w_2 \,. \tag{5.5}$$

Under the above assumption the governing equations resulting from Eq. (5.4) take the following forms:

$$\eta \frac{\partial}{\partial r}\left(r \frac{\partial w_1}{\partial r}\right) = C_1 r - r \frac{d\sigma}{dz} \,, \tag{5.6}$$

for the first order approximation with respect to ε, and

$$\eta \frac{\partial}{\partial r}\left(r \frac{\partial w_2}{\partial r}\right) = C_2 r - r \frac{d}{dz}\left(\frac{\partial \sigma}{\partial V} w_1 + \frac{\partial \sigma}{\partial V'} \frac{\partial w_1}{\partial z} + \frac{\partial \sigma}{\partial \varrho} \Delta \varrho\right) - \gamma \frac{\partial}{\partial r}(ru) \tag{5.7}$$

for the second order approximation containing terms of order ε^2.

6. Boundary conditions

The governing equations (5.6), (5.7) are the second order partial differential equations which can be integrated with respect to r. To this end, at least two boundary conditions for the additional motions are necessary.

Because of Eq. (4.5) and the boundary conditions satisfied at the exit (feeding velocity) and the end of filament (take-up velocity, cf. [4]):

$$V(0) = V_0 \,, \qquad V(L) = V_L \,, \tag{6.1}$$

respectively, it is reasonable to assume that the additional velocity field only modifies the uniform velocity profile resulting from the fundamental motion. This means that we assume

$$\int_0^R wr \, dr = 0. \tag{6.2}$$

The above assumption can be justified *a posteriori* by the fact that the solutions for w_1 (cf. Sec. 7) are proportional to R'. Usually this latter quantity is small but finite at the exit and tends to zero for $z = L$ (cf. [4]).

On the free surface of the fibre all the forces acting have to be mutually balanced. Neglecting surface-tension effects, we arrive at the following condition (cf. [6]), earlier derived by KASE [8]:

$$R'\left(T^{*33} - T^{*11}\right)_{r=R} = T^{*13}|_{r=R} \,. \tag{6.3}$$

Introducing the corresponding stresses from Eqs. (3.6), we obtain

$$R'\left[\sigma+\frac{\partial\sigma}{\partial V}w+\frac{\partial\sigma}{\partial V'}\frac{\partial w}{\partial z}+\frac{\partial\sigma}{\partial\varrho}\Delta\varrho\right]_{r=R}=\eta\left(\frac{\partial w}{\partial r}+\frac{\partial u}{\partial z}\right)_{r=R}+\gamma u|_{r=R}\,. \tag{6.4}$$

Bearing in mind Eq. (5.5), we can write the following conditions:

$$R'\sigma=\eta\frac{\partial w_1}{\partial r}\bigg|_{r=R} \tag{6.5}$$

for the first order approximation, and

$$R'\left[\frac{\partial\sigma}{\partial V}w_1+\frac{\partial\sigma}{\partial V'}\frac{\partial w_1}{\partial z}+\frac{\partial\sigma}{\partial\varrho}\Delta\varrho\right]_{r=R}=\eta\frac{\partial w_2}{\partial r}\bigg|_{r=R}+\gamma u_1|_{r=R}\,, \tag{6.6}$$

for the second order approximation, respectively.

7. Solutions for isotropic viscoelastic materials

The governing equation (5.6) together with the boundary conditions (6.2) and (6.5) leads to the solution

$$w_1=\frac{\sigma}{2\eta}\frac{R'}{R}\left(r^2-\frac{R^2}{2}\right), \tag{7.1}$$

depending on the fibre geometry ($R'/R=d/dz(\ln R)$) as well as on two material functions σ and η.

Integrating the expression for u, resulting from the continuity condition (4.2), we arrive at

$$u_1=-\frac{V}{\varrho}\frac{d}{dz}\int\Delta\varrho\, r\,dr-\frac{1}{8}\frac{d}{dz}\left(\frac{\sigma}{\eta}\frac{R'}{R}(r^2-R^2)r\right), \tag{7.2}$$

where we have taken into account Eq. (7.1) and the requirement that $u_1|_{r=0}=0$. Moreover, we have

$$u_1|_{r=R}=-\frac{V}{\varrho}\frac{d}{dz}\int_0^R\Delta\varrho\, r\,dr=0, \tag{7.3}$$

where Eq. (4.7) has been used.

The second order governing equation (5.7) together with the boundary conditions (6.2) and (6.6) leads to the following expression, more complex than that

for the first approximation:

$$
\begin{aligned}
(7.4)\qquad w_2 = {} & \frac{1}{8}RR'\left\{\frac{\partial\sigma}{\partial V}\frac{\sigma}{\eta^2}\frac{R'}{R}+\frac{1}{\eta}\frac{\partial\sigma}{\partial V'}\left[\frac{d}{dz}\left(\frac{\sigma}{\eta}\frac{R'}{R}\right)\right]+2\frac{\sigma}{\eta}\frac{R'^2}{R^2}\right\}\left(r^2-\frac{R^2}{2}\right)\\
& -\frac{1}{32\eta}\frac{d}{dz}\left\{\frac{\partial\sigma}{\partial V}\frac{\sigma}{\eta}\frac{R'}{R}+\frac{\partial\sigma}{\partial V'}\frac{d}{dz}\left(\frac{\sigma}{\eta}\frac{R'}{R}\right)\right\}\left(r^4-2R^2r^2+3R^4\right)\\
& +\frac{1}{2\eta}\frac{R'}{R}\frac{\partial\sigma}{\partial\varrho}\Delta\varrho\left(r^2-\frac{R^2}{2}\right)+\frac{\gamma}{4\eta}\left(V\frac{\partial}{\partial z}(\ln\Delta\varrho)-\frac{\sigma}{2\eta}R'^2\right)\left(r^2-\frac{R^2}{2}\right)\\
& +\frac{\gamma}{32\eta}\frac{d}{dz}\left(\frac{\sigma}{\eta}\frac{R'}{R}\right)\left(r^4-2R^2r^2+\frac{2}{3}R^4\right).
\end{aligned}
$$

The solutions (7.1) and (7.4) are valid for isotropic viscoelastic materials (fluids or solids) described by the constitutive equations of the type (2.10) and (3.6) with three material functions σ, η, γ and the variable temperature-dependent increment of the density $\Delta\varrho$. For purely inviscid or viscous materials, we may disregard in Eq. (7.4) all the terms containing partial derivatives with respect to V' or V, respectively.

For the frequently applied case of viscous, generalized Newtonian fluids, for which

$$
(7.5)\qquad \frac{\partial\sigma}{\partial V}=0, \qquad \sigma=3\eta V', \qquad \gamma=0,
$$

we arrive at

$$
(7.6)\qquad w_1=\frac{3}{2}V'\frac{R'}{R}\left(r^2-\frac{R^2}{R}\right),
$$

and at

$$
\begin{aligned}
(7.7)\qquad w_2 = {} & \frac{9}{8}RR'\left\{\frac{d}{dz}\left(V'\frac{R'}{R}\right)+2V'\frac{R'^2}{R^2}\right\}\left(r^2-\frac{R^2}{2}\right)\\
& -\frac{9}{32\eta}\frac{d}{dz}\left[\eta\frac{d}{dz}\left(V'\frac{R'}{R}\right)\right]\left(r^4-2R^2r^2+3R^4\right)\\
& +\frac{1}{2\eta}\frac{R'}{R}\frac{\partial\sigma}{\partial\varrho}\Delta\varrho\left(r^2-\frac{R^2}{2}\right).
\end{aligned}
$$

A realistic shape of the additional velocity profiles can easily be predicted, assuming that the outer radius $R(z)$ of the filament may be approximated by the exponential function:

$$
R(z)=R_0\exp(-zb), \qquad b=-\frac{1}{L}\ln\frac{R_L}{R_0}=\text{const}.
$$

In such a case: $R'/R = -b$, and the velocity profiles (7.1) or (7.6) are proportional only to σ/η or V', respectively. It is well known from the experiments (cf. [4]) that V' takes small values for $z = 0$, increases rapidly reaching a maximum for $z = 0.15 \div 0.3L$, and tends to zero for $z = L$. It may be expected that possible σ/η profiles along the fibre axis are of the character similar to V'.

8. Final remarks

The linearized perturbation procedure developed in the paper enables determination of the realistic velocity fields taking into account the variable geometry of the elongated fibres as well as the appropriate shearing effects.

To this end some information on the material behaviour in steady quasi-elongational motions is necessary either on the basis of experimental data (measured radii, stresses, forces, etc.) or using various numerical results calculated for particular models of fluids or solids. The constitutive equations used in the paper are sufficiently general; the corresponding material functions (normal stresses, viscosity, etc.) all depend on the strain, strain rate (velocity gradient), variable density and explicitly on the axial coordinate. The latter dependence replaces distributions of temperature, crystallization effects, structure formation, etc. There exists a possibility for simultaneous description of fluid-like or solid-like behaviour along the same fibre-line.

The solutions corresponding to the first order approximation depend on two material functions only: the normal stress and viscosity functions, and the radius variable along the thread.

The additional velocity fields are simply expressed in the case of viscous, generalized Newtonian fluids. Then, a knowledge of such kinematic quantities as the variable radius and the velocity gradient is entirely sufficient.

An example of numerical and experimental results which could, in principle, be used in determining the additional velocity fields and the relevant shearing effects may be found in the paper by PAPANASTASIOU *et al.* [10]. They applied the so-called PSM model and the Newtonian model to calculate the properties of polypropylene, polystyrene and PET and to compare the results with available experiments.

References

1. S. ZAHORSKI, *Non-uniform stagnant motions of materially non-uniform simple fluids*, Arch. Mech., **48**, 577, 1996.
2. S. ZAHORSKI, *Non-uniform extensional motions of materially non-uniform simple solids*, Arch. Mech., **48**, 747, 1996.
3. S. ZAHORSKI, *Necking in steady-state drawing of polymer fibres*, Arch. Mech., **48**, 1101, 1996.
4. A. ZIABICKI, *Fundamentals of fibre formation. The science of fibre spinning and drawing*, Wiley, London 1976.

5. S. ZAHORSKI, *Viscoelastic flows with dominating extensions: application to squeezing flows*, Arch. Mech., **38**, 191, 1986.

6. S. ZAHORSKI, *An alternative approach to non-isothermal melt spinning with axial and radial viscosity distributions*, J. Non-Newtonian Fluid Mech., **36**, 71, 1990.

7. S. ZAHORSKI, *Mechanics of viscoelastic fluids*, Martinus Nijhoff, The Hague 1982.

8. S. KASE, *Studies on melt spinning.* III. *Velocity field within the thread*, J. Appl. Polym. Sci., **18**, 3267, 1974.

9. T. PAPANASTASIOU, S.M. ALAIE and Z. CHEN, *High-speed, non-isothermal fiber spinning*, Int. Polymer Processing, **9**, 148, 1994.

POLISH ACADEMY OF SCIENCES
INSTITUTE OF FUNDAMENTAL TECHNOLOGICAL RESEARCH
e-mail: szahor@ippt.gov.pl

Received April 25, 1997.

Arch. Mech., 49, 5, pp. 977–990, Warszawa 1997

Development of flow and heat transfer on a wedge with a magnetic field

M. KUMARI (BANGALORE)

THE DEVELOPMENT of the flow and heat transfer of an incompressible laminar viscous electrically conducting fluid on a stationary infinite wedge with an applied magnetic field has been studied when the fluid in the external stream is set into motion impulsively and at the same time, the surface temperature is suddenly raised from its ambient temperature. The effects of the induced magnetic field, viscous dissipation and Ohmic heating have been taken into account. The mathematical problem has been formulated in such a way that at time $t = 0$, it reduces to Rayleigh type of equation and as time $t \to \infty$, it tends to Falkner–Skan type of equation. The scale of time has been chosen such that the traditional infinite region of integration becomes finite which considerably reduces the computational time. The singular parabolic partial differential equations governing the flow have been solved numerically using an implicit finite difference scheme. There is a smooth transition from the Rayleigh solution at $\xi = 0$ ($t^* = 0$) to Falkner–Skan type of solution at $\xi = 1$ ($t^* \to \infty$ when the steady state is reached). The surface shear stress and the surface heat transfer increase or decrease with time when the pressure gradient parameter is greater or less than a certain value. However, the x component of the induced magnetic field at the surface decreases as time increases.

1. Introduction

FLUID DYNAMIC PHENOMENA involving unsteady boundary layers are of great theoretical and practical interest. Much of the work that has been done in this area is related to external aerodynamics. However, there are also several applications in biofluid dynamics, hydronautics and manufacturing. Excellent review papers on the unsteady boundary layers have been contributed by STUART [1], RILEY [2], TELIONIS [3] and MCCROSKEY [4].

When the external stream is impulsively set into motion at time $t = 0$ with uniform velocity along the plane of symmetry of the stationary infinite wedge, the inviscid flow over the wedge is developed instantaneously. But the viscous flow within the boundary layer develops slowly and it reaches a steady flow only after a certain period of time. The development of the boundary layer with time takes place in two stages. For small time, the flow is dominated by the viscous and pressure gradient forces and the unsteady acceleration. The convective acceleration plays only a minor role in the flow development. On the other hand, for large time the flow is dominated by the viscous forces, the pressure gradient and the convective acceleration. During this phase the unsteady acceleration plays only a minor role in the flow development. For $t = 0$, the flow

is governed by the Rayleigh equation and for $t \to \infty$ it is governed by the Falkner – Skan equation. This change in the character of the flow manifests itself mathematically as a change in character of the equations which describe the fluid motion.

STEWARTSON [5] first studied the impulsive motion over a flat plate and found that for $t > 1$, the flow undergoes a transition from Rayleigh flow to Blasius flow. He [5] noted certain difficulties in the mathematical formulation of the problem (i.e., the transition from the Rayleigh flow to Blasius flow is not smooth) and related it to the physics of the flow. Since then several authors [6 – 11] have studied this problem using different methods. SMITH [12] has studied the analogous wedge problem and encountered the same difficulties which arise in the case of the flat plate. In order to overcome this difficulty, WILLIAMS and RHYNE [13] have formulated the problem of impulsive motion over a wedge in a new set of scaled coordinates which includes both the short time solution (Rayleigh solution) and long time solution (Falkner – Skan solution) and there is a smooth transition from Rayleigh solution to Falkner – Skan solution. In the above studies, the effect of the magnetic field was not considered. INGHAM [14] has studied the effect of the magnetic field on the flow past an impulsively started semi-infinite plate.

The present investigation considers the development of boundary layer flow and heat transfer with time of an electrically conducting fluid over a stationary infinite wedge with a magnetic field when the fluid in the external stream is set into motion impulsively and at the same time the temperature of the wall is suddenly raised from that of the surrounding fluid. The effects of the induced magnetic field, viscous dissipation and Ohmic heating have been included in the analysis. The mathematical problem has been formulated in such a way that for time $t = 0$, it reduces to Rayleigh type of equations and for $t \to \infty$ it reduces to Falkner – Skan type of equation. The scale of time has been selected such that the traditional infinite region of integration becomes finite which considerably reduces the computational time. The singular parabolic partial differential equations governing the flow have been solved numerically using an implicit finite difference scheme. The particular cases of the present results have been compared with those of HALL [6], DENNIS [7], WATKINS [9], INGHAM [10, 14], TADROS and KIRKHOPE [11], WILLIAMS and RHYNE [13], NATH [16] and WATANABE [17].

2. Problem formulation

We assume that for $t < 0$, an infinite wedge lies in the (x, y) plane with the leading edge at $x = y = 0$ in the ambient fluid. The wall T_w is assumed to have the same temperature as that of the surrounding fluid (i.e., $T_w = T_\infty$) which is electrically conducting. A magnetic field H_0 is applied in the x direction at large distance from the surface of the wedge. At time $t = 0$, the external stream

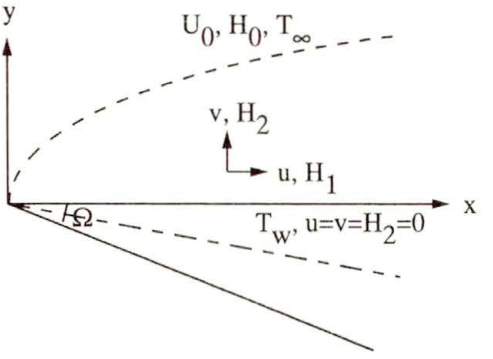

FIG. 1. Coordinate system.

away from the wedge is impulsively set into motion with velocity U_0 parallel to the surface of the wedge (Fig. 1). At the same time the temperature of the wall is raised to T_w from T_∞, the temperature of the surrounding fluid. The effects of the induced magnetic field, viscous dissipation and Ohmic heating have been included in the analysis but the Hall effect has been neglected. It is assumed that there is no applied voltage which implies the absence of an electric field ($E = 0$). The electrical currents flowing in the fluid give rise to an induced magnetic field which would exist if the fluid were an electrical insulator. It has been assumed that the normal component of the induced magnetic field H_2 vanishes at the wall and the parallel component H_1 approaches its given value H_0 at the edge of the boundary layer [15]. The free stream temperature is constant. The solution for small time is described by the Rayleigh's type of equation. For $t \to \infty$, the steady-state equations as given by GRIBBEN [15] and NATH [16] are obtained. Under the above assumptions, the boundary layer and Maxwell's equations governing the unsteady flow can be expressed as [14–17]

$$u_x + v_y = 0, \tag{2.1}$$

$$(H_1)_x + (H_2)_y = 0, \tag{2.2}$$

$$u_t + uu_x + vu_y = -\varrho^{-1}(p + \mu_0 H_0^2/2)_x + \nu u_{yy} + (\mu_0/\varrho)\,[H_1(H_1)_x + H_2(H_1)_y]\,, \tag{2.3}$$

$$(H_1)_t + u(H_1)_x + v(H_1)_y - H_1 u_x - H_2 u_y = \alpha_1 (H_1)_{yy}\,, \tag{2.4}$$

$$T_t + uT_x + vT_y = \nu \mathrm{Pr}^{-1} T_{yy} + (\nu/c_p)u_y^2 + (\varrho c_p \sigma)^{-1}\,[(H_1)_y]^2\,, \tag{2.5}$$

where

$$-\varrho^{-1}(p + \mu_0 H_0^2/2)_x = U_0(U_0)_x - (\mu_0/\varrho)H_0(H_0)_x\,, \qquad U_0 = Ux^m, \qquad H_0 = Hx^m, \qquad \mathrm{Pr} = \nu/\alpha\,. \tag{2.6}$$

The boundary conditions for $t \geq 0$ are given by

$$
\begin{aligned}
& u(x,0,t) = v(x,0,t) = H_2(x,0,t) = 0, \\
& \partial H_1(x,0,t)/\partial y = 0, \qquad T(x,0,t) = T_w\,, \\
& u(x,\infty,t_0) = U_0(x), \quad H_1(x,\infty,t) = H_0(x), \quad T(x,\infty,t) = T_\infty\,.
\end{aligned} \tag{2.7}
$$

The initial conditions at $t = t_0$ (< 0) are expressed in the form

$$
u(x,y,t_0) = 0, \qquad H_1(x,y,t_0) = H_0\,, \qquad T(x,y,t_0) = T_\infty\,. \tag{2.8}
$$

Here x and y are the distances along and perpendicular to the surface, respectively; u and v are the velocity components along the x and y directions, respectively; H_1 and H_2 are the components of the induced magnetic field along the x and y directions, respectively; U_0 and H_0 are the velocity and the applied magnetic field in the x direction, respectively; p is the pressure; Pr is the Prandtl number; T is the temperature; ϱ and ν are the density and kinematic viscosity, respectively; μ_0 is the magnetic permeability; α and α_1 are, respectively, the thermal diffusivity and magnetic diffusivity; U and H are the velocity and magnetic field in the free stream, respectively; m is the index in the power-law variation of velocity, wall temperature and applied magnetic field; the subscripts t, x and y denote derivatives with respect to t, x and y, respectively; and the subscripts w and ∞ denote conditions at the wall and in the free stream, respectively.

In order to reduce the number of independent variables from three to two in Eqs. (2.1)–(2.5) and to reduce these equations to dimensionless form, we apply the following transformations:

$$
\begin{aligned}
\eta &= (U/\nu)^{1/2}\, x^{(m-1)/2}\, \xi^{-1/2}\, y\,, \qquad \xi = 1 - \exp(-U_0 t/x), \\
t^* &= U_0 t/x\,, \quad u = \psi_y\,, \quad v = -\psi_x\,, \quad H_1 = \phi_y\,, \quad H_2 = -\phi_x\,, \\
\psi(x,y,t) &= (U\nu)^{1/2} x^{(m+1)/2}\, \xi^{1/2}\, f(\xi,\eta), \quad \mathrm{Ec} = U^2/[c_p(T_{w0} - T_\infty)], \\
\phi(x,y,t) &= (H^2\nu/U)^{1/2}\, x^{(m+1)/2}\, \xi^{1/2} g(\xi,\eta), \\
T(x,y,t) &= T_\infty + (T_w - T_\infty)\theta(\xi,\eta), \quad S = \mu_0 H^2/(\varrho U^2), \\
T_w - T_\infty &= (T_{w0} - T_\infty) x^{2m}, \qquad \lambda = \nu/\alpha_1\,, \qquad \alpha_1 = (\mu_0\sigma)^{-1}, \\
u &= U x^m f'(\xi,\eta), \qquad H_1 = H x^m g'(\xi,\eta), \\
\beta &= 2m/(m+1), \qquad m > -1,
\end{aligned} \tag{2.9}
$$

to Eqs. (2.1) – (2.5) and we find that Eqs. (2.1) and (2.2) are identically satisfied and Eqs. (2.3) – (2.5) reduce to

$$
\begin{aligned}
& f''' + 2^{-1}\left[(m+1)\xi + (1-m)(1-\xi)\ln(1-\xi)\right] f f'' \\
& + m\xi(1 - f'^2) + 2^{-1}\eta(1-\xi) f'' + (1-m)\xi(1-\xi)\ln(1-\xi) f''(\partial f/\partial\xi) \\
& - \xi m S(1 - g'^2) - 2^{-1}\left[(m+1)\xi + (1-m)(1-\xi)\ln(1-\xi)\right] S g g'' \\
& = \xi(1-\xi)\left[1 + (1-m)\ln(1-\xi) f'\right](\partial f'/\partial\xi) \\
& + S(1-m)\xi(1-\xi)\ln(1-\xi) g'(\partial g'/\partial\xi),
\end{aligned} \tag{2.10}
$$

$$
\begin{aligned}
(2.11)\qquad & \lambda^{-1}g'''+2^{-1}(m+1)\xi(fg''-f''g)+2^{-1}(1-m)(1-\xi)\ln(1-\xi)(fg''-f''g)\\
&\quad +2^{-1}(1-\xi)\eta g''+(1-m)\xi(1-\xi)\ln(1-\xi)g''(\partial f/\partial\xi)\\
&\quad -(1-m)\xi(1-\xi)\ln(1-\xi)f''(\partial g/\partial\xi)\\
&\quad =\xi(1-\xi)\left[1+(1-m)\ln(1-\xi)f'\right]\partial g'/\partial\xi\\
&\quad -(1-m)\xi(1-\xi)\ln(1-\xi)g'(\partial f'/\partial\xi),
\end{aligned}
$$

$$
\begin{aligned}
(2.12)\qquad & \mathrm{Pr}^{-1}\theta''+2^{-1}\left[(m+1)\xi+(1-m)(1-\xi)\ln(1-\xi)\right]f\theta'\\
&\quad -2mSf'\theta+2^{-1}(1-\xi)\eta\theta'+(1-m)\xi(1-\xi)\ln(1-\xi)\theta'(\partial f/\partial\xi)\\
&\quad +\mathrm{Ec}\left[(f'')^2+(S/\lambda)(g'')^2\right]=\xi(1-\xi)\left[1+(1-m)\ln(1-\xi)f'\right](\partial\theta/\partial\xi).
\end{aligned}
$$

The boundary conditions are given by

$$
\begin{aligned}
(2.13)\qquad & f(\xi,0)=f'(\xi,0)=g(\xi,0)=g''(\xi,0)=0, \qquad \theta(\xi,0)=1,\\
& f'(\xi,\infty)=g'(\xi,\infty)=1, \qquad \theta(\xi,\infty)=0.
\end{aligned}
$$

Here ξ and η are the transformed and dimensionless independent variables; t^* is the dimensionless time; ψ and ϕ are the dimensional fluid and magnetic stream functions, respectively; f' is the dimensionless velocity; g' is the dimensionless x component of the induced magnetic field; f and g are the dimensionless fluid and magnetic stream functions, respectively; θ is the dimensionless temperature; S is the dimensionless magnetic parameter; β is the pressure gradient parameter; Ec is the Eckert number; σ is the electrical conductivity; λ is the magnetic Prandtl number; T_{w0} is the value of T_w at $x=0$; and prime denotes derivative with respect to η.

Equations (2.11) – (2.13) are partial differential equations, but for $\xi=0$ and $\xi=1$ they reduce to ordinary differential equations. For $\xi=0$, the equations are

$$
(2.14)\qquad f'''+2^{-1}\eta f''=0,
$$

$$
(2.15)\qquad \lambda^{-1}g'''+2^{-1}\eta g''=0,
$$

$$
(2.16)\qquad \mathrm{Pr}^{-1}\theta''+2^{-1}\eta\theta'+\mathrm{Ec}\left[(f'')^2+(S/\lambda)(g'')^2\right]=0.
$$

For $\xi=1$, the equations are given by

$$
\begin{aligned}
(2.17)\qquad & f'''+2^{-1}(m+1)ff''+m(1-f'^2)-mS(1-g'^2)\\
&\quad -2^{-1}(m+1)Sgg''=0,
\end{aligned}
$$

$$
(2.18)\qquad \lambda^{-1}g'''+2^{-1}(m+1)(fg''-f''g)=0,
$$

$$
(2.19)\qquad \mathrm{Pr}^{-1}\theta''+2^{-1}(m+1)f\theta'-2mf'\theta+\mathrm{Ec}\left[(f'')^2+(S/\lambda)(g'')^2\right]=0.
$$

The boundary conditions for (2.14) – (2.19) are expressed as

$$
\begin{aligned}
(2.20)\qquad & f(0)=f'(0)=g(0)=g''(0)=0, \qquad \theta(0)=1,\\
& f'(\infty)=g'(\infty)=1, \qquad \theta(\infty)=0.
\end{aligned}
$$

It may be remarked that Eq. (2.10) for $S = 0$ reduces to that of WILLIAMS and RHYNE [13]. Equations (2.10) and (2.11) for $m = 0$ are essentially the same as those of INGHAM [14]. Also, Eq. (2.10) for $m = S = 0$ is the same as that of HALL [6], DENNIS [7], WATKINS [9], INGHAM [10] and TADROS and KIRKHOPE [11]. When $\xi = 1$, the self-similar equations (2.17) and (2.18) are the same as those of NATH [16] if we apply the following transformations

$$\eta = (2-\beta)^{1/2}\eta_1\,, \qquad f(\eta) = (2-\beta)^{1/2} f_1(\eta_1), \qquad \beta < 2, \tag{2.21}$$
$$g(\eta) = (2-\beta)^{1/2} g_1(\eta_1), \qquad \beta = 2m/(m+1).$$

Also, for $S = \mathrm{Ec} = 0$ and for constant wall temperature case (the term $2mf'\theta = 0$), Eqs. (2.17) and (2.19) reduce to those of WATANABE [17] if we apply the transformations

$$\eta = [2/(m+1)]^{1/2}\eta_1\,, \qquad f(\eta) = [2/(m+1)]^{1/2} f_1(\eta_1), \tag{2.22}$$
$$\theta(\eta) = \theta_1(\eta_1).$$

3. Analytical solution

Equations (2.14) – (2.16) under boundary conditions (2.20) admit closed-form solution. The solution of Eq. (2.14) under conditions (2.20) is expressed as

$$f = \eta\,\mathrm{erf}\,(\eta/2) + (\pi)^{-1/2}\left[\exp(-\eta^2/4) - 1\right], \tag{3.1}$$

hence

$$f' = \mathrm{erf}\,(\eta/2), \qquad f'' = (\pi)^{-1/2}\exp(-\eta^2/4), \qquad f''(0) = (\pi)^{-1/2}. \tag{3.5}$$

Equation (2.15) is integrated once to yield the equation

$$\lambda^{-1} g'' + 2^{-1}\eta g' - 2^{-1} g = 0, \tag{3.3}$$

where the constant of integration is zero by virtue of the conditions $g(0) = g''(0) = 0$. Equation (2.22) under conditions (2.20) has the solution of the form [14]:

$$g = \eta\,. \tag{3.4}$$

Equation (2.16) under conditions (2.20) for $\mathrm{Pr} = 1$ yields the followng solution:

$$\theta = \mathrm{erfc}\,(\eta/2) + (\mathrm{Ec}/2)\,\mathrm{erf}\,(\eta/2)\,\mathrm{erfc}\,(\eta/2). \tag{3.5}$$

Hence

$$\theta' = -\mathrm{Ec}\,(\pi)^{-1/2}\exp(-\eta^2/4)\,\mathrm{erf}\,(\eta/2) + (\pi)^{-1/2}(\mathrm{Ec}-1)\exp(-\eta^2/4), \tag{3.6}$$

$$\theta'(0) = (2^{-1}\mathrm{Ec}-1)(\pi)^{-1/2}. \tag{3.7}$$

Also, Eq. (2.16) under conditions (2.20) for Ec = 0 has the solution of the form (3.7)

$$\theta = \mathrm{erfc}\,(\mathrm{Pr}^{1/2}\eta/2). \tag{3.8}$$

Hence

$$\theta' = -(\mathrm{Pr}/\pi)^{1/2}\exp(-\mathrm{Pr}\,\eta^2/4), \qquad \theta'(0) = -(\mathrm{Pr}/\pi)^{1/2}. \tag{3.9}$$

4. Numerical solution

It may be noted that Eqs. (2.10) and (2.11) are coupled nonlinear partial differential equations of parabolic type, whereas Eq. (2.12) is an uncoupled linear parabolic partial differential equation. Equations (2.10) – (2.12) under boundary conditions (2.13) and initial conditions (2.14) – (2.16) can be solved numerically. Equations (2.10) – (2.12) can be rewritten as

$$\frac{\partial^2 W_1}{\partial\eta^2} + a_1\frac{\partial W_1}{\partial\eta} + a_2 W_1 + a_3\frac{\partial W_2}{\partial\eta} + a_4 W_2 + a_5 = a_6\frac{\partial W_1}{\partial\xi} + a_7\frac{\partial W_2}{\partial\xi}, \tag{4.1}$$

$$\lambda^{-1}\frac{\partial^2 W_2}{\partial\eta^2} + a_1\frac{\partial W_2}{\partial\eta} + a_8\frac{\partial W_1}{\partial\eta} = a_6\frac{\partial W_2}{\partial\xi} + a_9\frac{\partial W_1}{\partial\xi}, \tag{4.2}$$

$$\mathrm{Pr}^{-1}\frac{\partial W_3}{\partial\eta^2} + a_1\frac{\partial W_3}{\partial\eta} + a_{10}W_3 + a_{11}W_1 + a_{12}W_2 = a_6\frac{\partial W_3}{\partial\xi}, \tag{4.3}$$

where

$$\begin{aligned}
W_1 &= f' = \partial f/\partial\eta, \qquad W_2 = g' = \partial g/\partial\eta, \qquad W_3 = \theta,\\
a_1 &= \left[2^{-1}(m+1)\xi + 2^{-1}(1-m)(1-\xi)\ln(1-\xi)\right] f\\
&\quad +2^{-1}\eta(1-\xi) + (1-m)\xi(1-\xi)\ln(1-\xi)(\partial f/\partial\xi),\\
a_2 &= -m\xi f',\\
a_3 &= -\left[2^{-1}(1+m)\xi + 2^{-1}(1-m)(1-\xi)\ln(1-\xi)\right] g,\\
a_4 &= \xi m S g', \qquad a_5 = m\xi(1-\xi),\\
a_6 &= \xi(1-\xi)\left[1+(1-m)\ln(1-\xi)f'\right],\\
a_7 &= S(1-m)\xi(1-\xi)\ln(1-\xi)g',\\
a_8 &= -\left[2^{-1}(m+1)\xi + 2^{-1}(1-m)(1-\xi)\ln(1-\xi)\right] g\\
&\quad -(1-m)\xi(1-\xi)\ln(1-\xi)(\partial g/\partial\xi),\\
a_9 &= -(1-m)\xi(1-\xi)\ln(1-\xi)g',\\
a_{10} &= -2mSf', \qquad a_{11} = \mathrm{Ec}\,f'', \qquad a_{12} = \mathrm{Ec}\,(S/\lambda)g''.
\end{aligned} \tag{4.4}$$

The boundary conditions (2.20) can be expressed as

$$
\begin{aligned}
&W_1(\xi,0) = f(\xi,0) = W_2'(\xi,0) = g(\xi,0) = 0, \qquad W_3(\xi,0) = 1,\\
&W_1(\xi,\infty) = W_2(\xi,\infty) = 1, \qquad W_3(\xi,\infty) = 0.
\end{aligned} \tag{4.5}
$$

It may be remarked that a_6 which is the coefficient of $\partial W_i/\partial\xi$, $i = 1,2,3$ in Eqs. (4.1) – (4.3) will be positive when $\xi < 1 - \exp[(m-1)^{-1}]$ as $f' > 0$ $(0 < f' \leq 1)$ in $(0 < \eta \leq \eta_\infty)$. However a_6 becomes negative for some η when $\xi > 1 - \exp[(m-1)^{-1}]$. When a_6 is positive, Eqs. (4.1) – (4.3) are parabolic partial differential equations and well-posed. Equations (4.1) – (4.3) under initial conditions given by Eqs. (2.14) – (2.16) and boundary conditions (4.5) can be solved by using an implicit finite-difference scheme. When $a_6 < 0$, the problem is no longer well-posed and the forward integration method fails [13]. Such equations are called singular parabolic partial differential equations [10]. Physically, the change in the sign of a_6 is attributed to the change in the direction of flow of information as explained in [13].

In order to overcome the difficulty mentioned above, in the finite-difference scheme we have used either forward or backward differences in ξ direction consistent with the direction of the flow of information. In the η direction, we have used the central difference scheme. This solution technique is based on the technique used by CARTER [18] and the detailed description of this technique is given by WILLIAMS and RHYNE [13]. Hence it is not presented here. Figure 2 shows the computational region and the behaviour of the coefficient a_6.

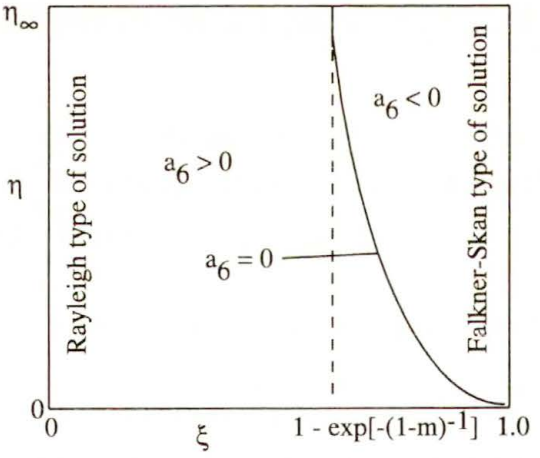

FIG. 2. Schematic representation of computational region.

We have also studied the effect of step sizes $\Delta\eta$ and $\Delta\xi$ and the edge of the boundary layer represented by η_∞ on the solution in order to optimize them. Consequently, the step sizes $\Delta\eta = 0.05$, $\Delta\xi = 0.01$ and $\eta_\infty = 10$ have been used for the computation.

5. Results and discussion

In order to verify the analysis and to check the accuracy of the present method, we have compared our dimensionless surface shear stress parameter $(f''(\xi,0))$ for $S = 0$ (no magnetic field) with that of WILLIAMS and RHYNE [13] and for $S = m = 0$ (flat plate case without magnetic field) with that of HALL [6], DENNIS [7], WATKINS [9], INGHAM [10], TADROS and KIRKHOPE [11] and WILLIAMS and RHYNE [13]. Also, we have compared our dimensionless surface shear stress parameter $(f''(t^*,0))$ and the x-component of the induced magnetic field on the surface $(g'(t^*,0))$ for $m = 0$ (flat plate case) with those of INGHAM [14]. For $\xi = 1$, we have compared the surface shear stress $(f''(0))$ and the x-component of the induced magnetic field $(g'(0))$ with those of NATH [16]. For $\xi = 1$, $S = 0$, $\mathrm{Pr} = 0.73$ we have compared the surface shear stress $(f''(0))$ and the surface heat transfer $(-\theta'(0))$ with those of WATANABE [17]. In all the cases the results are found to be in excellent agreement. Hence for the sake of brevity, the comparison is not shown here. It may be noted that for direct comparison with NATH [16] we have to multiply the shear stress parameter $f''(0)$ by $(2-\beta)^{1/2}$ where $\beta = 2m/(m+1)$ and with WATANABE [17], we have to multiply $f''(0)$ and $\theta'(0)$ by $[2/(m+1)]^{1/2}$.

We have obtained the solution of (4.1) – (4.3) for the pressure gradient parameter $m(\beta)$ in the range $m_1 \leq m \leq 1$ $(\beta_1 \leq \beta \leq 1)$ and for several values of the magnetic parameter S $(0.125 \leq S \leq 0.75)$.

The solution for $m = 1$ $(\beta = 1)$ is of interest because for this case a_6, which is the coefficient of $\partial W_i/\partial\xi$, $i = 1,2,3$, in (4.1) – (4.3), is positive for all $\xi < 1$. In this case, it takes an infinite time for a signal from the line $x = 0$ to reach any point x downstream. The flow develops under the influence of the unsteady acceleration, the viscous forces and magnetic field and the imposed pressure gradient. This type of flow has been discussed in detail by STEWARTSON [19].

For $m_1 \leq m < 1$ $(m_1 < 0)$, a_6 changes sign between $\xi = 0$ and $\xi = 1$ (Fig. 2). The region where $a_6 < 0$ represents the region where the flow at a given x station is affected by conditions at $x = 0$. The case $m = m_1$ $(m_1 < 0)$ represents the unsteady development of the incipient separation profile [13]. $m_1 = -0.0842$, -0.0773, -0.0667 and -0.0508 for $S = 0.125$, 0.25, 0.50 and 0.75.

The variation of the surface shear stress $(f''(\xi,0))$, the x component of the induced magnetic field at the surface $(g'(\xi,0))$ and the heat transfer at the surface $(-\theta'(\xi,0))$ with the dimensionless time ξ for various values of the pressure gradient parameter m and the magnetic parameter S are shown in Figs. 3 – 8. From the results it is evident that there is a smooth transition from the Rayleigh solution at $\xi = 0$ (i.e., at $t^* = 0$) to the Falkner – Skan type of solution at $\xi = 1$ (i.e., as $t^* \to \infty$ when the steady-state is reached). For the pressure gradient parameter $m > m_0$, which depends on the magnetic parameter S, the surface shear stress $(f''(\xi,0))$ increases when ξ increases from zero to 1, but for $m < m_0$ it decreases. On the other hand, the x component of the induced magnetic field at

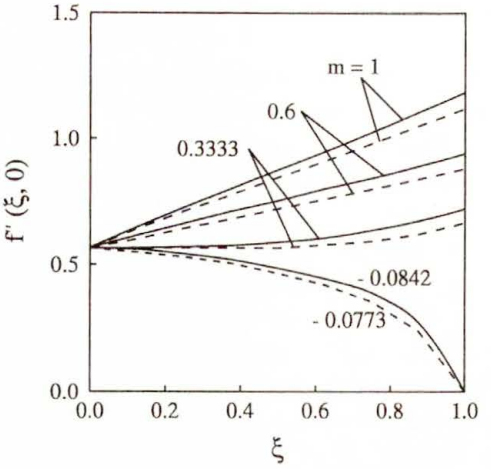

FIG. 3. Variation of the surface shear stress $f''(\xi, 0)$ with ξ for $S = 0.125$ and 0.25. ——, $S = 0.125$; – – – –, $S = 0.25$.

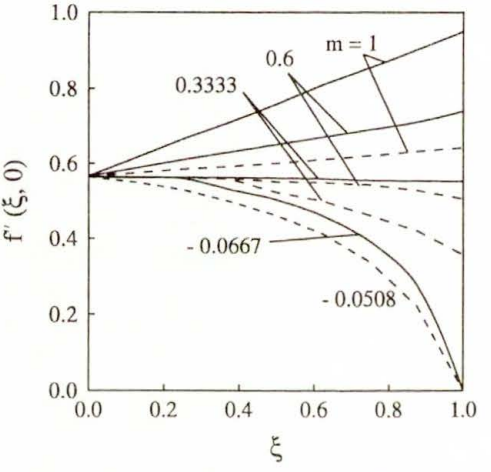

FIG. 4. Variation of the surface shear stress $f''(\xi, 0)$ with ξ for $S = 0.5$ and 0.75. ——, $S = 0.5$; – – – –, $S = 0.75$.

the wall ($g'(\xi, 0)$) and the surface heat transfer ($-\theta'(\xi, 0)$) decrease for all values of m and S when ξ increases from zero to 1 except for $m = 1$ and $S \leq 0.125$ when $-\theta'(\xi, 0)$ slightly increases with ξ. For $m = 1$, $S = 0.5$, Pr = 0.73 $f''(\xi, 0)$ increases by about 68% when ξ increases from zero to 1, but $g'(\xi, 0)$ and $-\theta'(\xi, 0)$ decrease by about 28% and 21%, respectively. For $m = 0.3333$ $f''(\xi, 0)$, $g'(\xi, 0)$ and $-\theta'(\xi, 0)$ decrease, respectively, by about 2.3%, 41% and 40% as ξ increases from zero to 1. Also for all ξ, the shear stress, the x component of the induced magnetic field and the heat transfer ($f''(\xi, 0)$, $g'(\xi, 0)$, $-\theta'(\xi, 0)$) decreases as the magnetic parameter S increases. For example, when $\xi = 0.5$, $m = 0.3333$,

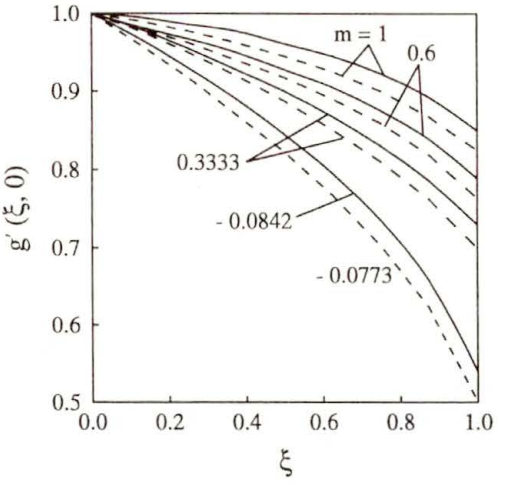

FIG. 5. Variation of the x-component of the induced magnetic field $g'(\xi, 0)$ with ξ for $S = 0.125$ and 0.25. ——, $S = 0.125$; – – – –, $S = 0.25$.

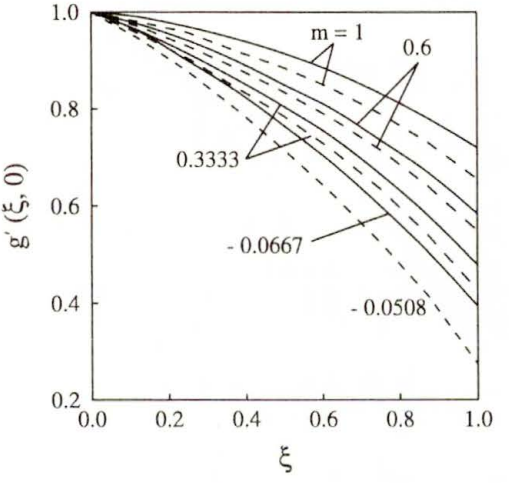

FIG. 6. Variation of the x-component of the induced magnetic field $g'(\xi, 0)$ with ξ for $S = 0.5$ and 0.75. ——, $S = 0.5$; – – – –, $S = 0.75$.

Pr = 0.73, $f''(\xi, 0)$, $g'(\xi, 0)$ and $-\theta'(\xi, 0)$ decrease by about 29%, 17% and 22%, respectively, as S increases from 0.125 to 0.75. For a given value of ξ ($\xi > 0$), S and Pr, $f''(\xi, 0)$, $g'(\xi, 0)$ and $-\theta'(\xi, 0)$ decreases as the pressure gradient parameter m decreases from 1 to -0.0408. The percentage reduction in $f''(\xi, 0)$, $g'(\xi, 0)$ and $-\theta'(\xi, 0)$ for $\xi = S = 0.5$, Pr = 0.73 is about 54, 14 and 21, respectively, as m decreases from 1 to -0.0408. Finally it may be remarked that the effect of variation of m or S on $f''(\xi, 0)$, $g'(\xi, 0)$ and $-\theta'(\xi, 0)$ is most pronounced for $\xi = 1$ (i.e., when the steady state is attained).

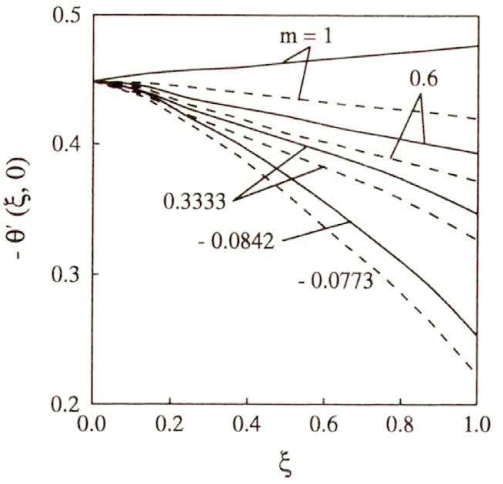

FIG. 7. Variation of the heat transfer parameter at the surface $-\theta'(\xi, 0)$ with ξ for $S = 0.125$ and 0.25, Pr = 0.73, Ec = 0.1. ——, $S = 0.125$; – – – –, $S = 0.25$.

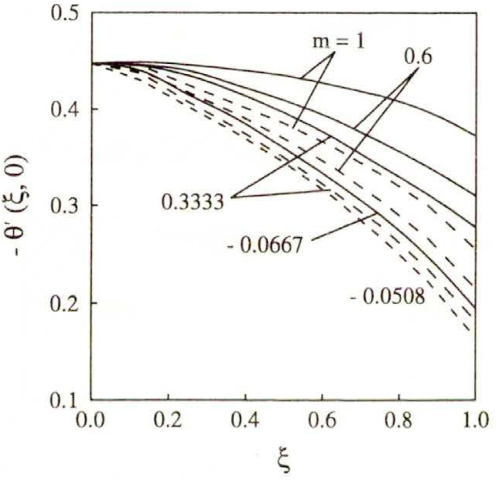

FIG. 8. Variation of the heat transfer parameter at the surface $-\theta'(\xi, 0)$ with ξ for $S = 0.5$ and 0.75, Pr = 0.73, Ec = 0.1. ——, $S = 0.5$; – – – –, $S = 0.75$.

The physical problem considered here depends on the magnetic field H, electrical conductivity σ and thermal diffusivity α. These parameters enter the dimensionless equations (2.10) – (2.12) as magnetic parameter α (which is the square of the ratio of the Alfven speed to the free stream velocity), magnetic Prandtl number α (which is the ratio of the viscous to magnetic diffusivities), and the fluid Prandtl number Pr (which is the ratio of the kinematic viscosity to the thermal diffusivity), respectively. Here, we qualitatively discuss the effects of these parameters (S, λ, Pr) on our problem.

At the start of the motion (i.e., at $\xi = 0$), the flow is independent of the magnetic parameter S and the magnetic Prandtl number λ, and the effect of these parameters increases with ξ. For fixed values of λ and Pr, the viscous, magnetic and thermal boundary layers continue to thicken and the surface shear stress $(f''(\xi,0))$, x-component of the induced magnetic field on the surface $(g'(\xi,0))$ and the surface heat transfer $(-\theta'(\xi,0))$ decrease as the magnetic parameter S increases until at $S = 1$ the entire flow is plugged (i.e., f, g, θ all tend to zero as $S \to 1$). This is due to the induced current which produces a magnetic counter-field that annuls the entire flow field. Similar trend has been observed by GLAUERT [20], TAN and WANG [21] and DAS [22] for the flat plate case.

The effect of the magnetic Prandtl number λ on the flow field is significant. For zero electrical conductivity $\lambda = 0$ and the problem reduces to the classical boundary layer case. For infinite electrical conductivity, $\lambda \to \infty$. For this case the magnetic lines of forces are frozen into the fluid and no interaction between the magnetic field and flow field takes place. For small λ, the viscous boundary layer is much thinner than the magnetic boundary layer, and for large λ it is the other way around. The surface shear stress $(f''(\xi,0))$, x-component of the induced magnetic field $(g'(\xi,0))$ at the surface and the surface heat transfer $(-\theta'(\xi,0))$ decrease with increasing magnetic Prandtl number λ.

The fluid Prandtl number Pr affects only the thermal field. For small Pr (Pr < 1), the thermal boundary layer is thicker than the viscous boundary layer, and for large Pr (Pr $\gg 1$) the thermal boundary layer is much thinner than the viscous boundary layer, consequently, the surface heat transfer $(-\theta'(\xi,0))$ increases with Pr.

6. Conclusions

It is evident from the results that there is a smooth transition from the Rayleigh solution at $\xi = 0$ ($t^* = 0$) to the Falkner–Skan type of solution at $\xi = 1$ ($t^* \to \infty$ when the steady state is reached). The surface shear stress and the surface heat transfer parameters increase or decrease with time when the pressure gradient parameter is greater or less than a certain value. However, the x-component of the induced magnetic field at the surface decreases as time increases whatever may be the value of the pressure gradient parameter. The surface shear stress, the x-component of the induced magnetic field at the surface and the surface heat transfer decrease as the pressure gradient parameter decreases or the magnetic parameter or the magnetic Prandtl number increases. However, the effect is more pronounced for large times.

References

1. J.T. STUART, *Unsteady boundary layers*, [in:] Recent Research of Unsteady Boundary Layers, Vol. 1, E.A. EICHELBRENNER [Ed.], University of Arizona, Tucson, 1–46, 1971.

2. N. RILEY, *Unsteady laminar boundary layers*, SIAM Review, **17**, 274–297, 1975.
3. D.P. TELIONIS, *Calculations of time-dependent boundary layers*, [in:] Unsteady Aerodynamics, Vol. 1, R.B. KINNEY [Ed.], Laval University Press, Quebec, 155–190, 1975.
4. W.J. MCCROSKEY, *Some current research in unsteady fluid dynamics*, J. Fluid Engng., **99**, 3–38, 1979.
5. K. STEWARTSON, *On the impulsive motion of a flat plate in a viscous fluid*, Quart. J. Mech. Appl. Math., **4**, 182–198, 1951.
6. M.G. HALL, *The boundary layer over an impulsively started flat plate*, Proc. Roy. Soc., **310 A**, 401–414, 1969.
7. S.C.R. DENNIS, *The motion of a viscous fluid past an impulsively started semi-infnite flat plate*, J. Inst. Math. Applics., **10**, 105–117, 1972.
8. K. STEWARTSON, *On the impulsive motion of a flat plate in a viscous fluid – II* Quart. J. Mech. Appl. Math., **26**, 143–153, 1973.
9. C.B. WATKINS, *Heat transfer in the boundary layer over an impulsively started fat plate*, J. Heat Transfer, **97**, 482–484, 1975.
10. D.B. INGHAM, *Singular parabolic partial differential equations that arise in impulsive motion problems*, J. Appl. Mech., **44**, 396–400, 1977.
11. R.N. TADROS and J. KIRKHOPE, *Unsteady boundary layer over an impulsively started flat plate using finite elements, computers and fluids*, **6**, 285–292, 1978.
12. S.H. SMITH, *The impulsive motion of a wedge in a viscous fluid*, ZAMP, **18**, 508–522, 1976.
13. J.C. WILLIAMS III and T.H. RHYNE, *Boundary layer development on a wedge impulsively set into motion*, SIAM J. Appl. Math., **38**, 215–224, 1980.
14. D.B. INGHAM, *Flow past an impulsively started semi-infinite flat plate in the presence of a magnetic field*, J. Inst. Maths. Applics., **20**, 459–469, 1977.
15. R.J. GRIBBEN, *The magnetohydrodynamic boundary layer in the presence of a pressure gradient*, Proc. Roy. Soc., **287 A**, 123–141, 1965.
16. G. NATH, *Magnetohydrodynamic boundary layer with pressure gradient and suction*, Def. Sci. J., **26**, 153–156, 1976.
17. T. WATANABE, *Thermal boundary layers over a wedge with uniform suction or injection in forced flow*, Acta Mech., **83**, 119–126, 1990.
18. J.E. CARTER, *Inverse solutions for laminar boundary layer flows with separation and attachment*, NASA TR-R447, Washington, D.C. 1975.
19. K. STEWARTSON, *The theory of unsteady laminar boundary layers*, Advances in Applied Mechanics, Academic Press, New York, **6**, pp. 1–37, 1960.
20. M.B. GLAUERT, *A study of the magnetohydrodynamic boundary layer on a plate*, J. Fluid Mech., **10**, 276–288, 1961.
21. C.W. TAN and C.T. WANG, *Heat transfer in aligned-field magnetohydrodynamic fow past a flat plate*, Int. J. Heat Mass Transfer, **11**, 299–319, 1968.
22. U.N. DAS, *A small unsteady perturbation on the steady hydromagnetic boundary layer flow past a semi-infinite flat plate*, Proc. Camb. Soc., **68**, 509–528, 1970.

DEPARTMENT OF MATHEMATICS
INDIAN INSTITUTE OF SCIENCE, BANGALORE, INDIA.
e-mail: mkumari@math.iisc.ernet.in

Received November 4, 1996; new version June 16, 1997.

NATO ADVANCED RESEARCH WORKSHOP

– SMART STRUCTURES – REQUIREMENTS AND POTENTIAL APPLICATIONS IN MECHANICAL AND CIVIL ENGINEERING

SMART – 98

16 – 19 June 1998
Pułtusk, Poland

Scope of the Workshop

The aim of the meeting is evaluation of needs and potential applications of *smart structure* concept in mechanical and civil engineering i.e. determination of regional (Central/East Europe, European Union, USA&Canada) priority problems, transfer of technology & information between the regions, between Academia and Industry and between researchers from different scientific areas. Multi-disciplinary interaction of topics like: active and hybrid control of structures, vibration isolation, sensors, actuators, smart materials, structural identification and damage monitoring in mechanical and civil engineering applications will be discussed.

Scientific Program

• The following Key Lectures given by members of the ARW Scientific Committee will be presented:

P. Ballardini, ISMES, Bergamo, Italy – *to be announced*

Ken P. Chong, NSF, U.S.A. – *Smart Structures Research in the U.S.*

P. Destuynder, St.Cyr L'Ecole, France – *On the Application of Piezo-electric Devices for Improving the Aerodynamic Properties of an Airfoil*

G. Farkas, Technical University of Budapest, Hungary – *Supervision, Maintenance and Renovation of Reinforced and Prestressed Bridges*

J. Holnicki-Szulc, IFTR, Warsaw, Poland – *Adaptive Structures*

A. Jarosevic, Comenius University, Bratislava, Slovakia – *Magnetoelastic Method of Stress Measurement in Steel*

L. Jezequel, Ecol Central de Lyon, Ecully, France – *to be announced*

G.C. Lee, State University of New York at Buffalo, U.S.A. – *Development of a Bridge Monitoring System*

J. Rodellar, Universitat Politechnica de Catalunya, Barcelona, Spain – *Control Theory Sources in Active Control of Structures*

T.T. Soong, State University of New York at Buffalo, U.S.A. – *Full-scale Structural Applications of Intelligent Protective Systems in North America*

Ming L. Wang, University of Illinois at Chicago, U.S.A. – *Advanced Monitoring System for Large Structures*

• *Sessions* with oral presentations selected from the Call for Papers

• and *Panel Discussions* will be organized.

Official Language

English will be used for lectures, presentations and publishing proceedings.

Location

The Workshop will be held in the Conference Center in Pułtusk (historical castle in the vicinity of Warsaw) with transportation arranged directly from the international Warsaw airport and also from the center of the city. Accompanying guest program (tourist trips, tennis courts, horse riding, rowing boats) is being planned.

Proceedings

Presentations at the Workshop are expected to be accompanied by a full paper which will be due in camera-ready format at the Workshop days. These papers will be reviewed and those accepted will be included, together with conclusions from panel discussions in the Proceedings published in the NATO Science Series. Further details regarding submission of camera-ready papers will be provided with the notification of acceptance for the Workshop. The extended version of selected papers will be published in the Journal of Structural Control.

Registration

No registration fee is planned. Partial support for the living costs in Pułtusk (including banquet and social events) will be available.

Organizing Committee

Prof. J. Holnicki-Szulc	Co-Chairman, Institute of Fundamental Technological Research
Prof. J. Rodellar	Co-Chairman, Universitat Politecnica de Catalunya
Prof. G. Kawiecki	University of Tennessee
Mr. P. Kołakowski	Secretary, Institute of Fundamental Technological Research

Collaborating Institutions

- NATO
- National Science Foundation, U.S.
- European Panel of the Association for the Control of Structures
- National Research Committee, Poland
- Institute of Fundamental Technological Research, Polish Academy of Sciences, Warsaw
- Applied Research Group – Epsilon Ltd., Poland

Address for Correspondence

Prof. Jan Holnicki-Szulc, Smart Structures Group
Institute of Fundamental Technological Research, Polish Academy of Sciences
Świętokrzyska 21, 00-049 Warsaw, Poland
Fax: (48) 22 826 98 15
Tel: (48) 22 826 12 81 ext. 355
E-mail: smart98@ippt.gov.pl

Information about the Workshop is also available through the Internet:
www.ippt.gov.pl/~pkolak/smart98.html